

University of Windsor

## Scholarship at UWindor

---

Electronic Theses and Dissertations

Theses, Dissertations, and Major Papers

---

2017

# Enhancing Convective Heat Transfer over a Surrogate Photovoltaic Panel

Fama Fouladi  
*University of Windsor*

Follow this and additional works at: <https://scholar.uwindsor.ca/etd>

---

### Recommended Citation

Fouladi, Fama, "Enhancing Convective Heat Transfer over a Surrogate Photovoltaic Panel" (2017).  
*Electronic Theses and Dissertations*. 5981.  
<https://scholar.uwindsor.ca/etd/5981>

This online database contains the full-text of PhD dissertations and Masters' theses of University of Windsor students from 1954 forward. These documents are made available for personal study and research purposes only, in accordance with the Canadian Copyright Act and the Creative Commons license—CC BY-NC-ND (Attribution, Non-Commercial, No Derivative Works). Under this license, works must always be attributed to the copyright holder (original author), cannot be used for any commercial purposes, and may not be altered. Any other use would require the permission of the copyright holder. Students may inquire about withdrawing their dissertation and/or thesis from this database. For additional inquiries, please contact the repository administrator via email ([scholarship@uwindsor.ca](mailto:scholarship@uwindsor.ca)) or by telephone at 519-253-3000ext. 3208.

# **Enhancing Convective Heat Transfer over a Surrogate Photovoltaic Panel**

By

**Fama Fouladi**

A Dissertation  
Submitted to the Faculty of Graduate Studies  
through the Department of Mechanical, Automotive & Materials Engineering  
in Partial Fulfillment of the Requirements for  
the Degree of **Doctor of Philosophy**  
at the University of Windsor

Windsor, Ontario, Canada

2017

© 2017 Fama Fouladi

# **Enhancing Convective Heat Transfer over a Surrogate Photovoltaic Panel**

by

**Fama Fouladi**

APPROVED BY:

---

K. Siddiqui

Department of Mechanical and Materials Engineering, Western University

---

A. Edrisy

Department of Mechanical, Automotive & Materials Engineering

---

J. Johrendt

Department of Mechanical, Automotive & Materials Engineering

---

A. Fartaj

Department of Mechanical, Automotive & Materials Engineering

---

D.S.-K Ting, Co-Advisor

Department of Mechanical, Automotive & Materials Engineering

---

P. Henshaw, Co-Advisor

Department of Civil and Environmental Engineering

March 17, 2017

## DECLARATION OF CO-AUTHORSHIP / PREVIOUS PUBLICATION

### I. Co-Authorship Declaration

I hereby declare that this thesis incorporates material that is result of joint research in collaboration with Mr. Steve Ray, Essex Energy Corporation under the supervision of Dr. David S.-K Ting and Dr. Paul Henshaw, University of Windsor. In chapters 2-7, the key ideas, primary contributions, experimental designs, data analysis and interpretation, were performed by the author, and the contribution of Dr. Ting and Dr. Henshaw was primarily through the provision of supervision. Mr. Ray collaboration is covered in chapters 5 and 7 of the thesis, which was primarily through the provision of data.

I am aware of the University of Windsor Senate Policy on Authorship and I certify that I have properly acknowledged the contribution of other researchers to my thesis, and have obtained written permission from each of the co-author(s) to include the above material(s) in my thesis.

I certify that, with the above qualification, this thesis, and the research to which it refers, is the product of my own work.

### II. Declaration of Previous Publication

This thesis includes 4 original papers that have been previously published/submitted for publication in peer reviewed journals, as follows:

Thesis Chapter	Publication title/full citation	Publication status*
<i>Chapter 2</i>	Fouladi, F., Henshaw, P. and Ting, D. S-K., 2013, "Enhancing Smart Grid realization with accurate prediction of photovoltaic performance based on weather forecast," <a href="#">International Journal of Environmental Studies</a> , 70(5), pp. 754-764	<i>Published</i>
<i>Chapter 3</i>	Fouladi, F., Henshaw, P. and Ting, D. S-K., 2014, "Turbulent flow over a flat plate downstream of a finite height perforated plate," <a href="#">Journal of Fluids Engineering</a> , 137 (2), pp. 021203-12	<i>Published</i>
<i>Chapter 4</i>	Fouladi, F., Henshaw, P. and Ting, D. S-K., 2015, "Effect of a triangular rib on a flat plate boundary layer," <a href="#">Journal of Fluids Engineering</a> , 138 (1), pp. 011101-11	<i>Published</i>
<i>Chapter 5</i>	Fouladi, F., Henshaw, P., Ting, D. S-K. and Ray, S., 2013, "Flat plate convection heat transfer	<i>Published</i>

	enhancement via a square rib,” <a href="#">International Journal of Heat and Mass Transfer</a> , 104, pp. 1202-1216	
<i>Chapter 6</i>	Fouladi, F., Henshaw, P. and Ting, D. S-K., “Partial grid’s turbulence analysis by wavelet transform,” <i>Experimental Thermal and Fluid Science</i>	<i>To be submitted</i>
<i>Chapter 7</i>	Fouladi, F., Henshaw, P., Ting, D. S-K. and Ray, “Flat Plate Heat Convection Enhancement by a Discrete Transverse Rib ,” <i>Journal of Heat Transfer</i>	<i>Under review</i>

I certify that I have obtained a written permission from the copyright owner(s) to include the above published material(s) in my thesis. I certify that the above material describes work completed during my registration as graduate student at the University of Windsor.

I declare that, to the best of my knowledge, my thesis does not infringe upon anyone’s copyright nor violate any proprietary rights and that any ideas, techniques, quotations, or any other material from the work of other people included in my thesis, published or otherwise, are fully acknowledged in accordance with the standard referencing practices. Furthermore, to the extent that I have included copyrighted material that surpasses the bounds of fair dealing within the meaning of the Canada Copyright Act, I certify that I have obtained a written permission from the copyright owner(s) to include such material(s) in my thesis.

I declare that this is a true copy of my thesis, including any final revisions, as approved by my thesis committee and the Graduate Studies office, and that this thesis has not been submitted for a higher degree to any other University or Institution.

## ABSTRACT

This research is particularly focused on studying heat transfer enhancement of a photovoltaic (PV) panel by putting an obstacle at the panel's windward edge. The heat transfer enhancement is performed by disturbing the airflow over the surface and increasing the heat and momentum transfer. Different objects such as triangular, square, rectangular, and discrete rectangular ribs and partial grids were applied at the leading edge of a surrogate PV panel and flow and the heat transfer of the panel are investigated experimentally. This approach was selected to expand understanding of effect of these different objects on the flow and turbulence structures over a flat surface by analyzing the flow comprehensively. It is observed that, a transverse object at the plate's leading edge would cause some flow blockage in the streamwise direction, but at the same time creates some velocity in the normal and cross stream directions. In addition to that, the obstacle generates some turbulence over the surface which persists for a long downstream distance. Also, among all studied objects, discrete rectangular ribs demonstrate the highest heat transfer rate enhancement (maximum  $Nu/Nu_0$  of 1.5). However, ribs with larger gap ratios are observed to be more effective at enhancing the heat transfer augmentation at closer distances to the rib, while at larger downstream distances from the rib, discrete ribs with smaller gap ratios are more effective. Furthermore, this work attempted to recognize the most influential flow parameters on the heat transfer enhancement of the surface. It is seen that the flow structure over a surface downstream of an object (flow separation-reattachment behaviour) has a significant effect on the heat transfer enhancement trend. Also, turbulence intensities are the

most dominant parameters in enhancing the heat transfer rate from the surface;  
however, flow velocity (mostly normal velocity) is also an important factor.

## DEDICATION

To my family



## ACKNOWLEDGEMENTS

Many people contributed to this work and made it possible. I would like first to sincerely thank my advisors Dr. David S.-K. Ting and Dr. Paul Henshaw for their inspiration, guidance and support during my PhD study at the University of Windsor. Also, I would like to thank Mr. Andy Jenner for his technical assistance.

This work is made possible by the Ontario Trillium Foundation for an Ontario Trillium Scholarship and Essex Energy Corporation for the financial support. Also, the Department of Mechanical, Automotive and Materials Engineering in the form of Graduate Assistantships is also acknowledged.

# TABLE OF CONTENTS

DECLARATION OF CO-AUTHORSHIP / PREVIOUS PUBLICATION .....	iii
ABSTRACT.....	v
DEDICATION.....	vii
ACKNOWLEDGEMENTS.....	viii
LIST OF TABLES.....	xiii
LIST OF FIGURES .....	xiv
LIST OF APPENDICES.....	xxii
<b>CHAPTER 1 INTRODUCTION .....</b>	<b>1</b>
<i>1.1. Motivation and Background .....</i>	<i>1</i>
<i>1.2. Thesis Objective and Overview.....</i>	<i>2</i>
<i>References.....</i>	<i>5</i>
<b>CHAPTER 2 ENHANCING SMART GRID REALIZATION WITH ACCURATE PREDICTION OF PHOTOVOLTAIC PERFORMANCE BASED ON WEATHER FORECAST.....</b>	<b>7</b>
<i>2.1. Introduction .....</i>	<i>7</i>
<i>Nomenclature.....</i>	<i>7</i>
<i>2.2 Panel Efficiency.....</i>	<i>8</i>
<i>2.3. Cell Temperature (T<sub>c</sub>).....</i>	<i>9</i>
<i>2.4. Studied Photovoltaic Array.....</i>	<i>11</i>
<i>2.5. Calculation Procedure.....</i>	<i>12</i>
<i>2.6. Results and discussion .....</i>	<i>13</i>
<i>2.7. Conclusions.....</i>	<i>17</i>
<i>Acknowledgements.....</i>	<i>17</i>
<i>References.....</i>	<i>17</i>
<b>CHAPTER 3 TURBULENT FLOW OVER A FLAT PLATE DOWNSTREAM OF A FINITE HEIGHT PERFORATED PLATE.....</b>	<b>21</b>
<i>3.1. Introduction .....</i>	<i>21</i>
<i>Nomenclature.....</i>	<i>22</i>

3.2 Experimentation .....	22
3.2.3. Hot-wire Anemometer .....	24
3.3. Methodology .....	24
3.3.1. Studied Parameters .....	24
3.4. Results and Discussion .....	26
3.4.1. Velocity Profile .....	26
3.4.2. Turbulence Intensity.....	30
3.4.3. Turbulence Higher Moments (Skewness and Flatness Factors).....	34
3.4.4. Turbulence Length Scales .....	37
3.5. Conclusion .....	41
Acknowledgment .....	42
References .....	42

**CHAPTER 4 EFFECT OF A TRIANGULAR RIB ON A FLAT PLATE BOUNDARY LAYER.....**

46	
4.1. Introduction .....	46
Nomenclature .....	47
4.2. Apparatus and Instrumentation .....	48
4.3. Results and Discussion .....	49
4.3.1. Velocity profiles .....	49
4.3.1.1. Time-averaged Velocity Profiles.....	49
4.3.1.2. Logarithmic Velocity Profiles .....	53
4.3.2. Turbulence Intensity.....	57
4.3.3. Fast Fourier Transform (FFT) .....	59
4.3.4. Turbulence Length Scales .....	60
4.4. Conclusion .....	64
Acknowledgment .....	64
References .....	65

**CHAPTER 5 FLAT PLATE CONVECTION HEAT TRANSFER ENHANCEMENT VIA A SQUARE RIB .....**

69	
5.1. Introduction .....	69
Nomenclature .....	71
5.2. Apparatus and Instrumentation .....	71
5.3. Results and Discussion .....	75

5.3.1. Heat Transfer Results .....	76
5.3.2. Flow Measurement Results .....	77
5.3.2.1. Hot-wire Data Modification in the Recirculation Region.....	78
5.3.2.2. Velocity Profiles.....	80
5.3.2.3. Turbulence Parameters.....	84
5.3.2.3.1. Turbulence Intensities .....	84
5.3.2.3.2. Reynolds Shear Stress .....	87
5.3.2.4. Energy Spectrum .....	90
5.4. Conclusion .....	91
Acknowledgement .....	92
References .....	92

CHAPTER 6 WAVELET ANALYSIS OF PARTIAL GRID INDUCED TURBULENCE OVER A FLAT PLATE .....	95
6.1. Introduction .....	95
Nomenclature .....	96
6.2. Experimentation.....	97
6.2.1. Methodology .....	99
6.3. Wavelet Fundamentals.....	99
6.3.1. Continuous Wavelet Transform .....	99
6.3.1.1. Intermittency Measure .....	100
6.3.2. Discrete (orthogonal) Wavelet Transforms .....	100
6.4. Results and Discussion .....	101
6.4.1. Flow under Study .....	101
6.4.2. Power Spectra .....	103
6.4.3. Wavelet analysis.....	105
6.4.3.1. Discrete wavelet analysis.....	107
6.4.3.1.1. Skewness and Flatness Factors.....	110
6.4.3.2. Continuous wavelet analysis .....	115
6.4.3.2.1. Intermittency analysis .....	118
6.5. Conclusion .....	120
Acknowledgements.....	120
References .....	120

CHAPTER 7 FLAT PLATE HEAT CONVECTION ENHANCEMENT BY A DISCRETE TRANSVERSE RIB .....	123
7.1. Introduction .....	123
Nomenclature .....	124
7.2. Experimentation .....	125
7.3. Results and Discussion .....	128
7.3.1. Heat transfer results .....	128
7.3.2. Time-averaged flow field results .....	132
7.3.2.1. Velocity .....	132
7.3.2.2. Turbulence Intensity and Shear Stress .....	137
7.4. Conclusion .....	147
Acknowledgment .....	148
References .....	148
CHAPTER 8 CONCLUSION.....	151
Nomenclature .....	151
8.1. Concluding Remarks .....	151
8.2. Future Work Recommendations.....	156
References .....	156
APPENDICES .....	157
Appendix A. Heat transfer enhancement and flow measurements of a heated flat plate after a partial grid with different heights .....	157
Appendix B. Uncertainty Analysis .....	161
Appendix C. Air Flow Quality in the Wind Tunnel .....	165
Appendix D. Turbulent Flow behind a Partially Blocking Grid.....	166
Appendix E. Wavelet Analysis OF Finite Height Grid Turbulence over a Flat Plate ..	174
VITA AUCTORIS .....	190

## LIST OF TABLES

2.1 Some experimental relations for heat transfer over a flat plate.....	10
2.2 Characteristics of tested PV panels [37].....	12
4.1 Average integral length scale at streamwise locations of the ribbed wall.....	64
6.1 Turbulence scales (length and frequency) at Points 1 to 4.....	105
6.2 Discrete wavelet transform levels and frequencies.....	107
6.3 Frequency range corresponding to each discrete wavelet decomposition level.....	112
E.1. Frequency range of different levels of discrete wavelet analysis.....	178

## LIST OF FIGURES

2.1 Schematic drawing of the studied PV array.....	12
2.2 Meteorological data for April 13, 2011.....	13
2.3 Comparison between measured and calculated efficiencies using Equations (2.2) and (2.4), with different relations for convective heat loss.....	14
2.4 Comparison between measured and calculated efficiencies using Equations (2.3) and (2.4), with different relations for convective heat loss.....	15
2.5 Comparison between measured and calculated efficiencies using Equations (2.2) and (2.5), with different relations for convective heat loss.....	15
2.6 Cell Temperature calculated from Equation (2.4), with different relations for convective heat loss.....	16
2.7 Calculated efficiencies based on Test et al. relation versus calculated cell temperatures.....	16
2.8 Absolute deviations of efficiencies calculated using the Test et al. heat loss correlation, Equation (2.9), from measured efficiencies.....	17
3.1 Flat plate and perforated plate isometric.....	23
3.2 Test section isometric.....	24
3.3 Velocity profiles at $H = 11$ cm and (a) 4.5 m/s (b) 5.5 m/s (c) 6.5 m/s free stream velocity.....	28
3.4 Dynamic pressure profiles at $H = 11$ cm (a) upstream of the grid (b) downstream of the grid.....	29
3.5 Velocity profiles for different heights of perforated plate, 5.5 m/s free stream velocity and (a) $X/D = 10$ (b) $X/D = 20$ (c) $X/D = 30$ . The circles signify $H = 3$ cm, the squares $H = 7$ cm, and the triangles $H = 11$ cm.....	30
3.6 Turbulence intensity for $H = 11$ cm at (a) 4.5 m/s (b) 5.5 m/s (c) 6.5 m/s free stream velocity. The circles signify $X/D = 10$ , the squares $X/D = 20$ , and the triangles $X/D = 30$ .....	30
3.7 Turbulence intensity for $X/D = 20$ and different free stream velocities. The circles signify $U_{\infty} = 4.5$ m/s, the squares $U_{\infty} = 5.5$ m/s, and the triangles $U_{\infty} = 6.5$ m/s.....	32

3.8 Turbulence intensity for different heights of perforated plate, 5.5 m/s free stream velocity and (a)  $X/D = 10$  (b)  $X/D = 20$  (c)  $X/D = 30$ , The circles signify  $H = 3$  cm, the squares  $H = 7$  cm, and the triangles  $H = 11$ cm.....33

3.9 Turbulence intensity at different downstream distances, 5.5 m/s free stream velocity and (a)  $H = 3$  cm (b)  $H = 7$  cm (c)  $H = 11$ cm. The circles signify  $X/D = 10$ , the squares  $X/D = 20$ , and the triangles  $X/D = 30$ .....33

3.10 Skewness factor for  $H = 11$  cm at (a) 4.5 m/s (b) 5.5 m/s (c) 6.5 m/s free stream velocity. The circles signify  $X/D = 10$ , the squares  $X/D = 20$ , and the triangles  $X/D = 30$ .....34

3.11 Velocity fluctuation vs. Time for  $H = 11$  cm,  $U_\infty = 4.5$  m/s,  $X/D = 30$  and points (a)  $Y = 10.8$  cm,  $S = 1.28$  (b)  $Y = 15.8$  cm,  $S = -1.95$  (c)  $Y = 5.2$  cm,  $S = 0$ .....35

3.12 Flatness factors for  $H = 11$  cm at (a) 4.5 m/s (b) 5.5 m/s (c) 6.5 m/s free stream velocity. The circles signify  $X/D = 10$ , the squares  $X/D = 20$ , and the triangles  $X/D = 30$ .....36

3.13 Autocorrelation coefficient for  $H = 11$ cm,  $Y = 5.5$  cm and  $U_\infty = 4.5$  m/s, solid line ( — ) signifies  $X/D = 10$ , dash dot ( - · )  $X/D = 20$ , dash ( - - )  $X/D = 30$  and round dot ( ····· ) the parabola fitted curve to the first five points of  $R(\tau)$  at  $X/D = 10$ .....37

3.14 Taylor micro scale for  $H = 11$  cm and  $U_\infty = 5.5$  m/s. The circles signify  $X/D = 10$ , the squares  $X/D = 20$ , and the triangles  $X/D = 30$ .....38

3.15 Taylor micro scale for different perforated plate's height and 5.5 m/s free stream velocity and at (a)  $X/D = 10$  (b)  $X/D = 20$  (c)  $X/D = 30$ . The circles signify  $H = 3$  cm, the squares  $H = 7$  cm, and the triangles  $H = 11$  cm.....39

3.16 Integral length scale for  $H = 11$  cm and (a) 4.5 m/s (b) 5.5 m/s (c) 6.5 m/s free stream velocity. The circles signify  $X/D = 10$ , the squares  $X/D = 20$ , and the triangles  $X/D = 30$ .....40

3.17 Integral length scale for different perforated plate's height and 6.5 m/s free stream velocity and at (a)  $X/D = 10$  (b)  $X/D = 20$  (c)  $X/D = 30$ . The circles signify  $H = 3$  cm, the squares  $H = 7$  cm, and the triangles  $H = 11$ cm.....40

3.18 Integral length scale for  $H = 11$  cm at  $X/D = 10$  and different free stream velocities. The circles signify  $U_\infty = 4.5$  m/s, the squares  $U_\infty = 5.5$  m/s, and the triangles  $U_\infty = 6.5$  m/s.....41

4.1 Rib mounted flat plate schematic.....48



4.2 Test section side view.....	49
4.3 Velocity profiles for smooth and ribbed wall at (a) $U_\infty = 4$ m/s (b) $U_\infty = 6.8$ m/s (c) $U_\infty = 9$ m/s.....	51
4.4 Flow over a (a) square ribbed surface [14] (b) wedge ribbed surface [3].....	52
4.5 Liu et al. [14] velocity profile over a square ribbed surface.....	53
4.6 Normalized velocity profiles inside the boundary layer at $U_\infty = 9$ m/s for the (a) smooth and (b) ribbed wall.....	55
4.7 Turbulent boundary layer normalized velocity profile of DeGraaff and Eaton [32].....	56
4.8 Wake parameter at $U_\infty = 9$ m/s.....	57
4.9 Turbulence intensity profiles for smooth and ribbed wall at (a) $U_\infty = 4$ m/s (b) $U_\infty = 6.8$ m/s (c) $U_\infty = 9$ m/s.....	58
4.10 Wall normal location of maximum streamwise $Tu$ (a) present study at $U_\infty = 9$ m/s (b) Liu et al. [14].....	59
4.11 FFT of velocity fluctuation signal at $Y/H = 1$ .....	60
4.12 Autocorrelation coefficient for ribbed wall at $X/H = 20$ , $Y/H = 2.2$ and $U_\infty = 9$ m/s, the dashed line shows the parabola fitted curve to the first five points of $R(\tau)$ .....	61
4.13 Ribbed wall integral length scale at $U_\infty = 9$ m/s.....	62
4.14 Ribbed wall Integral length scale at (a) $U_\infty = 4$ m/s (b) $U_\infty = 6.8$ m/s (c) $U_\infty = 9$ m/s.....	63
4.15 Taylor micro-scale in the boundary layer at $U_\infty = 9$ m/s.....	63
5.1 Set-up schematic.....	72
5.2 Set-up close view.....	73
5.3 Streamwise Nusselt number enhancement at different Reynolds numbers.....	76
5.4 Streamwise instantaneous velocity (a) hot-wire data (b) modified hot-wire data.....	78
5.5 Streamwise velocity profile (a) Liu et al. [11] (b) present study's modified hot-wire data (c) present study's raw hot-wire data.....	79

5.6 (a) Streamwise and (b) normal velocities of the flow over the ribbed plate at $Re_H = 2.6 \times 10^3$ .....	81
5.7 Streamwise velocity over the smooth and ribbed plate at (a) $Re_H = 1.3 \times 10^3$ and (b) $Re_H = 6.3 \times 10^3$ .....	82
5.8 Normal velocity over the smooth and ribbed plate at (a) $Re_H = 1.3 \times 10^3$ and (b) $Re_H = 6.3 \times 10^3$ .....	83
5.9 Turbulence intensities (a) $u_{rms}/U_\infty$ and (b) $v_{rms}/U_\infty$ , for the flow over the ribbed plate at $Re_H = 2.6 \times 10^3$ .....	85
5.10 Turbulence intensity in X direction ( $u_{rms}/U_\infty$ ) at (a) $Re_H = 1.3 \times 10^3$ and (b) $Re_H = 6.3 \times 10^3$ .....	86
5.11 Turbulence intensity in Y direction ( $v_{rms}/U_\infty$ ) at (a) $Re_H = 1.3 \times 10^3$ and (b) $Re_H = 6.3 \times 10^3$ .....	87
5.12 Non dimensional turbulent shear stress ( $\overline{uv}/U_\infty^2$ ) for the flow over ribbed plate at $Re_H = 2.6 \times 10^3$ .....	88
5.13 Normalized shear stress at (a) $Re_H = 2.6 \times 10^3$ and (b) $Re_H = 6.3 \times 10^3$ .....	89
5.14 Spectra of $v^2$ ( $m^2/s^2$ ) at $Y/H = 0.7$ and different streamwise locations and (a) $Re_H = 1.3 \times 10^3$ (b) $Re_H = 6.3 \times 10^3$ .....	91
6.1 Schematic of the partial grid-flat plate setup .....	98
6.2 Wind tunnel test section with the experimental set-up .....	98
6.3 Normalized (a) streamwise (b) normal velocities, (c) $u_{rms}$ (d) $v_{rms}$ and (e) Reynolds shear stress ( $uv$ ) profiles. The triangles signify $X/H = 8.75$ and circles $X/H = 17.75$ .....	102
6.4 Four selected points after the grid for analysis .....	103
6.5 Power spectra of u and v signals ( $P_{uu}$ and $P_{vv}$ ) at points: (a) 1 ( $X/H = 8.75$ , $Y/H = 0.55$ ), (b) 2 ( $X/H = 8.75$ , $Y/H = 1.05$ ), (c) 3 ( $X/H = 17.75$ , $Y/H = 0.55$ ) and (d) 4 ( $X/H = 17.75$ , $Y/H = 1.05$ ) .....	104
6.6 Comparison between the filtered signal (a), and wavelet transforms with different functions: (b) dmey (c) Haar (d) db10 performed on the u signal at point 1 ( $X/H = 8.75$ , $Y/H = 0.55$ ) .....	106
6.7 Discrete wavelet analysis of u (m/s) and v (m/s) signals at $X/H = 8.75$ and $Y/H = 0.55$ .....	108

6.8 Discrete wavelet analysis of $u$ (m/s) and $v$ (m/s) signals at $X/H = 8.75$ and $Y/H = 1.05$ .....	109
6.9 Discrete wavelet analysis of $u$ (m/s) and $v$ (m/s) signals at $X/H = 17.75$ and $Y/H = 0.55$ .....	110
6.10 Discrete wavelet analysis of $u$ (m/s) and $v$ (m/s) signals at $X/H = 17.75$ and $Y/H = 1.05$ .....	110
6.11 Skewness factor at (a) point 1 ( $X/H = 8.75$ , $Y/H = 0.55$ ), (b) point 2 ( $X/H = 8.75$ , $Y/H = 1.05$ ), (c) point 3 ( $X/H = 17.75$ , $Y/H = 0.55$ ) and (d) point 4 ( $X/H = 17.75$ , $Y/H = 1.05$ ).....	112
6.12 (a) PDF curves of $u$ and $v$ signals at Points 1 ( $u_1$ and $v_1$ at $X/H = 8.75$ , $Y/H = 0.55$ ) and 3 ( $u_3$ and $v_3$ at $X/H = 17.75$ , $Y/H = 0.55$ ) (b) fluctuating velocities at Point 1 ( $u_1$ and $v_1$ ).....	113
6.13 Flatness factor at (a) point 1 ( $X/H = 8.75$ , $Y/H = 0.55$ ), (b) point 2 ( $X/H = 8.75$ , $Y/H = 1.05$ ), (c) point 3 ( $X/H = 17.75$ , $Y/H = 0.55$ ) and (d) point 4 ( $X/H = 17.75$ , $Y/H = 1.05$ ).....	114
6.14 PDF curves of (1) $u$ and (2) $v$ signals at the point 1 ( $X/H = 8.75$ , $Y/H = 0.55$ ).....	115
6.15 Continuous wavelet transform of $u$ and $v$ signals at (a.1, a.2) Point 1 ( $X/H = 8.75$ , $Y/H = 0.55$ ), (b.1, b.2) Point 2 ( $X/H = 8.75$ , $Y/H = 1.05$ ), (c.1, c.2) Point 3 ( $X/H = 17.75$ , $Y/H = 0.55$ ) and (d.1, d.2) Point 4 ( $X/H = 17.75$ , $Y/H = 1.05$ ).....	117
6.16 Local intermittency factor of (a.1) $u$ (a.2) $v$ signals at Point 1 ( $X/H = 8.75$ , $Y/H = 0.55$ ), (b.1) $u$ and (b.2) $v$ signals at Point 2 ( $X/H = 8.75$ , $Y/H = 1.05$ ), (c.1) $u$ and (c.2) $v$ signals at Point 3 ( $X/H = 17.75$ , $Y/H = 0.55$ ) and (d.1) $u$ and (d.2) $v$ signals at Point 4 ( $X/H = 17.75$ , $Y/H = 1.05$ ).....	119
7.1 Set-up layers' close view.....	126
7.2 Set-up schematic.....	126
7.3 The five different tested ribs, Rib L1-L2, L1 signifies the tooth width and L2 the gap width, Rib F-0 signifies the full rib.....	127
7.4 Heat transfer enhancement at (a) $U_\infty = 4$ m/s and: (a.1) $H = 0.5$ cm, (a.2) $H = 1$ cm and (a.3) $H = 2$ cm and (b) $U_\infty = 10$ m/s and: (b.1) $H = 0.5$ cm, (b.2) $H = 1$ cm, (b.3) $H = 2$ cm.....	129

7.5 Heat transfer enhancement at $U_\infty = 4$ m/s and $H = 1$ cm (a) ribs 1-1-1 and 1-0.5-1 (b) ribs 0.5-0.5-1 and 0.5-1-1.....	131
7.6 Heat transfer enhancement comparison for different grids at two different rib's heights and free stream velocities (a) Rib 1-1 (b) Rib 0.5-0.5 (c) Rib 0.5-1 (d) Rib 1-0.5 and (e) Rib F-0.....	132
7.7 Rib F-0-1, Rib 1-1-1 and Rib 1-0.5-1 streamwise velocity profiles ( $U/U_\infty$ ) at different downstream distances.....	134
7.8 Rib F-0-1, Rib 1-1-1 and Rib 1-0.5-1 normal velocity profiles ( $V/U_\infty$ ) at different downstream distances.....	135
7.9 Rib F-0-1, Rib 1-1-1 and Rib 1-0.5-1 cross stream velocity profiles ( $W/U_\infty$ ) at different downstream distances.....	136
7.10 Time-averaged overall flow profile in the XY plane after the rib.....	137
7.11 Streamwise turbulence intensity profiles ( $u_{rms}/U_\infty$ ) of Rib F-0-1, Rib 1-1-1 and Rib 1-0.5-1 at different downstream distances.....	138
7.12 Normal turbulence intensity profiles ( $v_{rms}/U_\infty$ ) of Rib F-0-1, Rib 1-1-1 and Rib 1-0.5-1 at different downstream distances.....	139
7.13 Cross stream turbulence intensity profiles ( $w_{rms}/U_\infty$ ) for Rib F-0-1, Rib 1-1-1 and Rib 1-0.5-1 at different downstream distances.....	140
7.14 Shear stress profiles ( $uv/U_\infty^2$ ) for Rib F-0-1, Rib 1-1-1 and Rib 1-0.5-1 at different downstream distances.....	141
7.15 Shear stress profiles ( $uw/ U_\infty^2$ ) of Rib F-0-1, Rib 1-1-1 and Rib 1-0.5-1 at different downstream distances.....	142
7.16 Shear stress profiles ( $vw/ U_\infty^2$ ) of Rib F-0-1, Rib 1-1-1 and Rib 1-0.5-1 at different downstream distances.....	143
7.17 The streamwise distribution of (a) $Nu/Nu_0$ versus (b) $U/U_\infty$ (b) $V/ U_\infty$ (c) $W/ U_\infty$ for Rib1-1-1, Rib 1-0.5-1 and Rib F-0-1.....	145
7.18 The streamwise distribution of (a) $Nu/Nu_0$ versus (b) $u_{rms}/U_\infty$ (b) $v_{rms}/ U_\infty$ (c) $w_{rms}/ U_\infty$ for Rib 1-1-1, Rib 1-0.5-1 and Rib F-0-1.....	146
7.19 The streamwise distribution of (a) $Nu/Nu_0$ versus (b) $uv/U_\infty^2$ (b) $vw/ U_\infty^2$ (c) $uw/ U_\infty^2$ for Rib 1-1-1, Rib 1-0.5-1 and Rib F-0-1.....	146

7.20 Nu/Nu <sub>0</sub> correlation with different flow and turbulence parameters; triangles correspond to $u_{rms}/U_{\infty}$ , x's to $v_{rms}/U_{\infty}$ , diamonds to $\text{abs}(V/U_{\infty})$ and circles to $U/U_{\infty}$ .....	147
8.1 Comparing heat transfer enhancements of the surface after different objects at the leading edge at $U_{\infty} = 4\text{m/s}$ and $H = 1\text{cm}$ .....	152
8.2 Flow velocity and turbulence intensity profiles in streamwise direction at $U_{\infty} = 4\text{ m/s}$ and (a) $X/H \approx 9$ (b) $X/H \approx 20$ .....	154
A.1 Schematic of the experimental setup and the partial grid.....	157
A.2 Heat transfer enhancement after the partial grid with different heights and free stream velocities (a) $U_{\infty} = 4\text{ m/s}$ (b) $U_{\infty} = 7.5\text{ m/s}$ (c) $U_{\infty} = 10\text{ m/s}$ .....	158
A.3 Flow turbulence parameters after the partial grid with $H = 2\text{ cm}$ and $U_{\infty} = 4\text{ m/s}$ .....	159
A.4 Oval-shaped grid with two different small and large dimensions.....	160
A.5 Heat transfer enhancement after the oval-shaped partial grid with two different hole lengths (small = 1.5 cm and Large = 3 cm) and different heights at $U_{\infty} = 7.5\text{ m/s}$ .....	160
B.1 Uncertainty in $U/U_{\infty}$ and boundary layer thickness.....	163
C.1 Flow measurement in an empty wind tunnel test section.....	165
D.1 Test section isometric.....	167
D.2 Velocity profiles after grid.....	168
D.3 Turbulence intensity profiles after grid.....	169
D.4 Integral length scale profiles after grid.....	170
D.5 Taylor micro-scale profiles after grid.....	171
E.1 Flat plate and perforated plate isometric.....	175
E.2 Test section isometric.....	176
E.3 Velocity Profile at 4.5 m/s free stream velocity for: (a) $X/D = 10$ , (b) $X/D = 20$ , and (c) $X/D = 30$ .....	179
E.4 Turbulence intensity at 4.5 m/s free stream velocity, the circles signify $X/D = 10\text{ cm}$ , the squares $X/D = 20\text{ cm}$ , and the triangles $X/D = 30\text{ cm}$ .....	180

E.5 Fourier transform for the points $X/D=10$ (a) $Y = 5.7$ cm (b) $Y = 10.7$ cm.....	181
E.6 Fourier transform for the points $X/D=30$ (a) $Y = 5.7$ cm (b) $Y = 10.7$ cm....	181
E.7 continues wavelet analysis for points $X/D = 10$ and: (a) $Y = 5.7$ cm (b) $Y = 10.7$ cm, Frequency range: 13746 - 27.05 Hz.....	182
E.8 continues wavelet analysis for point $X/D = 30$ and: (a) $Y = 5.7$ cm (b) $Y = 10.7$ cm, Frequency range: 13746-27.05 Hz.....	183
E.9 discrete wavelet analysis for point $X/D = 10$ and $Y = 5.7$ cm (a) original signal (b) approximation levels (A1-A9) (c) detail levels (D1-D9).....	185
E.10 Signal reconstruction.....	186

## LIST OF APPENDICES

Appendix A. Heat Transfer Enhancement and Flow Measurements of a Heated Flat Plate after a Partial Grid with Different Heights.....	157
Appendix B. Uncertainty Analysis.....	161
Appendix C. Wind Tunnel Flow Quality.....	165
Appendix D. Turbulent Flow Behind a Partially Blocking Grid.....	166
Appendix E. Wavelet Analysis of Finite Height Grid Turbulence over a Flat Plate.....	174

# CHAPTER 1

## INTRODUCTION

### ***1.1. Motivation and Background***

The direct conversion of solar energy to electricity via photovoltaic (PV) systems is one of the most promising renewable energy technologies. The electricity generated by a PV system can compete with other sources of electricity for bulk power on the grid at times of peak demand, especially in areas where the peak electricity energy source is oil products. Based on the International Energy Agency's (IEA), solar photovoltaic energy technology roadmap in 2014, PV's share of global electricity will reach 16% by 2050, with a projected PV capacity of 4600 GW. Also, PV generation would contribute 17% to all clean electricity, and 20% of all renewable electricity [1]. In the USA, based on a Solar Energy Association (SEAI) report, the cost to install solar panels has dropped by more than 70% over the last 10 years, leading the industry to expand into new markets and deploy thousands of systems nationwide. It is predicted that, there will be robust growth across all three different PV market segments (residential, non-residential and utility) through the end of this decade, and eventually a 20 GW annual solar market in USA will be achieved [2].

However, this technology suffers from low efficiency, as a major part of the absorbed energy is converted into heat and only a small part (13-22%), is converted into electricity [3]. The heat which is added to the PV panel would lead to an increase in the cell temperature. The rise in cell temperature has a negative effect on the operation of the photovoltaic cell and thus cooling the photovoltaic panel can significantly improve its performance [4].

Several active and passive methods have been utilized for cooling PV panels' surface and consequently enhancing their efficiency, such as air cooling, water film or spray cooling, using alternative materials, etc. [5-7]. In air cooled systems heat can be removed by either natural or forced convection of air. These systems offer less expensive cooling of PV systems as air is the preferred media for low-cost cooling despite its poor thermo-physical characteristics [3,5]. The convective heat transfer rate of the surface is characterized by the flow dynamics over the surface, which is a combination of several parameters. One approach to enhance the convective heat transfer rate could be disturbing the flow over the surface by applying some wall attached roughness elements. This passive method is utilized in different industrial applications such as heat exchangers and solar air and water collectors [8-14]. Placing an obstacle or rib over the surface would lead to an enhancement in the heat transfer rate by affecting the flow structure. The flow separation and then reattachment, high turbulence level and existence of some vortices over the ribbed surfaces would cause more flow mixing and enhance the heat transfer from the surface [12-14].

Applying turbulence promoter objects on the PV panels could be an affordable and easy to implement method for enhancing the heat transfer rate. However, in most industrial applications, multiple rows of ribs are applied all over the surface which is definitely more effective in terms of the heat transfer enhancement but increases the friction factor at the same time [15-18]. Unfortunately for PV panels, turbulence elements cannot be applied over the panel's entire surface as they may block the sun's radiation and interfere with the panels' performance. Thus, for this



specific application, just one row of the turbulence element could be placed at the leading edge of each panel. Studying the effect of such an element, and modifying the element so that it has an effect for a large downstream distance is the subject of this dissertation.

## ***1.2. Thesis Objective and Overview***

The ultimate objective of the current research is to enhance the heat transfer rate from a heated plate that acts as a surrogate PV panel. One method to reach this goal is enhancing the flow mixing rate over the surface by disturbing the flow. To do so, a set-up was designed and constructed, and different objects were placed at the leading edge in order to affect the flow structure over the surface with the intent of enhancing the heat transfer rate. The scope of this research work includes:

1. Identify the parameters affecting the PV panel's temperature and consequently its efficiency. Derive a predictive relation for PV efficiency based on commonly measured meteorological parameters.
2. Describe the flow and turbulence structures in detail after a partial grid. The concept of the partial grid which is introduced in this research is basically different from that of a continuous transverse rib as it is a perforated plate with a certain height. The concept originated from conventional grid turbulence studies where nearly isotropic free stream turbulence is created in a wind tunnel in a laboratory. In conventional grid studies, the grid covers the whole test section area. But in this study, as it is intended to utilize a more applicable method for generating the turbulence, a grid with a certain height is placed at the leading edge of the simulated PV panel.
3. Investigate the flow physics behind ribs. Measure and interpret the flow and turbulence over a flat plate downstream of several rib shapes such as triangular, square and rectangular (full and discrete).
4. Understand the heat transfer rate enhancement after different grids and rib shapes and try to correlate flow and turbulence parameters with the heat transfer augmentation to identify the most effective flow dynamics factors on the heat transfer enhancement.

In this study, flow was measured by the hot-wire anemometer system and for heat transfer measurements a heat flux sensor was designed and embedded inside the flat plate. Different steps of this research work are explained in the chapters of this dissertation. An overview of these chapters is as follows:

### **Chapter 1 (Introduction, current chapter)**

The motivation, objective and an overview of the thesis are presented.

### **Chapter 2**

This chapter introduces the PV panels' thermal issue and investigates different parameters affecting the panel's temperature and heat loss. It also summarizes relevant relationships in the literature between the cell temperature and the efficiency and develops a method for calculating the cell temperature and efficiency of the PV panels. The method was applied to a real PV power plant and results were compared with the real plant's measurements. PV cell temperature was assumed to be

approximately equal to the PV surface temperature (at a typical large heat transfer rate, the difference between the cell temperature and the top surface tempered glass temperature was calculated to be less than 1.5 °C).

### **Chapter 3**

In this section, a partial grid was placed at the leading edge of a flat plate and the flow physics over the flat plate surface were investigated experimentally. A partial grid with diamond-shaped holes was proposed. Other shapes of the grid such as perforated plate with circular hole pattern and orificed opening were studied in other graduate projects [19-21]. Wishing to produce more turbulence on the flat plate, a perforated plate with diamond pattern and sharp edge was designed. Different flow and turbulence parameters were analyzed downstream of this partial grid extended to different heights above the level of the flat plate. From this work, it was conceived that a fundamental study of the effect of flow disturbance on heat transfer would be applicable to many different flow disrupting objects.

The convective heat transfer rate of the surface after a diamond-shaped grid and an oval-shaped partial grid was later tested at different grid heights and free stream velocities which are discussed in Appendix A. It was observed that partial grids were not as effective as other tested objects in enhancing the heat transfer rate from the plate.

### **Chapter 4**

In the next step, the flow physics after a solid rib were investigated. A triangular shape was chosen in this step for the rib as flow structure after this specific rib shape had not been explored in detail in the literature. The rib was designed with a small size (0.5 cm height and 0.5 cm base) to alter the inner layer of the boundary layer, but large enough so that its effect could be measured by a single wire probe. Also, in the previous study on the partial grid, it was seen that the grid with smaller height created a single thick shear layer and higher turbulence near the surface behind the grid. Other than these factors, some practical aspects of utilizing these objects at the leading edge of a PV panel were considered; thus a large height was avoided to reduce the shading effect and possible snow drifting. The effect of the rib on the flow and boundary layer structure were investigated. The boundary layer shape, thickness and turbulence parameters after this triangular rib until a large downstream distance are analyzed precisely.

### **Chapter 5**

A new set-up was designed and constructed, which is a (scaled-down) surrogate PV panel. This set-up contains an electrical heater layer to heat the upper surface evenly, and an embedded heat flux sensor. Thus, the heat transfer rate from the set-up surface in different flow conditions could be tested. The set-up surface temperature during these and subsequent experiments ranged from 30°C to 40°C, which is in the range of a PV panel surface temperature in a typical summer day. Also, the air temperature was around 22 °C during tests, which caused a convection temperature difference between the surface and flow between 8 to 18 °C. A square rib was placed at the leading edge of the set-up to disturb the flow over the surface. Larger rib size (1 cm) compared to the previous step was tested to have more extended altered flow over the surface behind the rib for

easier measurements with a X-wire probe. A square rib with its simple design has a complex flow mechanism [22-24]. While, many studies investigated the effect of the square rib on the flow and heat transfer over the surface, a detailed study on the impact of a single rib on the flow physics would seem to be helpful in understanding the mechanisms associated with ribbed surfaces' heat transfer enhancement. Thus, the effect of the square rib on different flow and turbulence parameters was studied and those that most correlated to the surface heat transfer enhancement were identified in this section.

## **Chapter 6**

To better understand the turbulence structure after the partial grid as used in Chapter 3 (diamond-shaped), a novel data analysis method was applied in this section. Wavelet analysis, which is mostly utilized for interpreting intermittent events, was used to explore the flow and turbulence after the partial grid over time and frequency domains.

## **Chapter 7**

It was seen that creating gaps inside the rib breaks the wake vortex and generate a higher level of turbulence downstream compared to the full rib [25]. In this chapter, the effect of creating a gap in a transverse rectangular rib on the flow and heat transfer of the downstream surface was studied in detail. The heat transfer rate of the surrogate PV panel after full and different discrete ribs with different heights was tested experimentally. Flow and turbulence parameters after ribs were investigated and the most influential flow parameters on the heat transfer enhancement of the plate were identified.

## **Chapter 8 (Conclusion)**

The final chapter attempts to synthesize the work in previous chapters and summarize the state-of-the-science on convective heat transfer enhancement over a flat plate utilizing an obstacle at the leading edge. It also tries to develop some strategies for next steps.

Furthermore, five different appendices are also included to provide additional information and support the thesis main body:

**Appendix A.** This section studies the heat transfer enhancement and flow parameters of the set-up which is utilized in chapters 5-7 after a partial grid with different heights. Two different patterns of partial grid (diamond and oval-shaped) are tested.

**Appendix B.** This part includes the uncertainty analysis of different parameters which are measured or calculated from the measured parameters.

**Appendix C.** This section shows the results of the air flow quality test which was performed in the University of Windsor's closed-loop wind tunnel. All experiments in this research work are carried out in the mentioned wind tunnel.

**Appendix D.** The flow after a partial grid which is hanged at the middle of the wind tunnel test section is experimentally investigated in this section. This was intended to establish turbulence parameters in the absence of the surrogate PV panel.

**Appendix E.** In this section a wavelet analysis is performed on the partial grid turbulence over a flat plate. The data used in this study are from one-dimensional turbulence measurements.

### ***References***

- [1] “Technology Roadmap Solar Photovoltaic Energy”, 2014 edition, International Energy Agency, accessed December 10, 2016, [https://www.iea.org/publications/freepublications/publication/TechnologyRoadmapSolarPhotovoltaicEnergy\\_2014edition.pdf](https://www.iea.org/publications/freepublications/publication/TechnologyRoadmapSolarPhotovoltaicEnergy_2014edition.pdf).
- [2] “Solar Industry Data Solar Industry Growing at a Record Pace”, accessed December 10, 2016, <http://www.seia.org/research-resources/solar-industry-data>.
- [3] Touni, J.K., Tripanagnostopoulos, Y., 2007, “Air-cooled PV/T Solar Collectors with Low Cost Performance Improvements,” *Solar Energy*, 81 (4), pp. 498-511.
- [4] Spectrolab, Inc., Sylmar, C.A., 1977, “Photovoltaic Systems Concept Study: Final Report,” (ALO-2748-12) U.S. Dept. of Energy, Division of Solar Energy, Springfield, VA.
- [5] M. Hasanuzzaman, M., Malek, A.B.M.A., Islam, M.M., Pandey, A.K., Rahim, N.A., 2016, “Global Advancement of Cooling Technologies for PV Systems: A Review,” *Solar Energy*, 137, pp. 25–45.
- [6] Kane, A., Verma, V., Singh, B., 2016, “Optimization of Thermoelectric Cooling Technology for an Active Cooling of Photovoltaic Panel,” *Renewable and Sustainable Energy Reviews*, in press, Available online 16 November 2016.
- [7] Irwan, Y.M., Leow, W.Z., Irwanto, M., Fareq, M., Amelia, A.R., Gomesh, N., Safwati, I., 2015, “Indoor Test Performance of PV Panel through Water Cooling Method. 2015 International Conference on Alternative Energy in Developing Countries and Emerging Economies,” *Energy Procedia*, 79, pp. 604 – 611.
- [8] Yadav, A.S., Bhagoria, J.L., 2014, “A CFD Based Thermo-Hydraulic Performance Analysis of an Artificially Roughened Solar Air Heater Having Equilateral Triangular Sectioned Rib Roughness on the Absorber Plate,” *International Journal of Heat and Mass Transfer*, 70, pp. 1016–1039.
- [9] Saha, A.K., Acharya, S., 2005, “Unsteady RANS Simulation of Turbulent Flow and Heat Transfer in Ribbed Coolant Passages of Different Aspect Ratios,” *International Journal of Heat and Mass Transfer*, 48 (23-24), pp. 4704–4725.
- [10] Panigrahi, P.K., Acharya, S., 2004, “Multi-modal Forcing of the Turbulent Separated Shear Flow Past a Rib,” *ASME Journal of Fluid Engineering*, 126 (1), pp. 22–31.
- [11] Bhagoria, J.L., Saini, J.S., Solanki, S.C., 2002, “Heat Transfer Coefficient and Friction Factor Correlations for Rectangular Solar Air Heater Duct Having Transverse Wedge Shaped Rib Roughness on the Absorber Plate,” *Renewable Energy*, 25 (3), pp. 341–369.

- [12] Mittal, M.K., Varun, Saini, R.P., Singal, S.K., 2007, "Effective Efficiency of Solar Air Heaters Having Different Types of Roughness Elements on the Absorber Plate," *Energy*, 32 (5), pp. 739–745.
- [13] Chamoli, S., Thakur, N.S., Sain, J.S., 2012, "A Review of Turbulence Promoters Used in Solar Thermal Systems," *Renewable and Sustainable Energy Reviews*, 16 (5), pp. 3154–3175.
- [14] Greig, D., Siddiqui, K., Karava, P., 2012, "An Experimental Investigation of the Flow Structure Over a Corrugated Waveform in a Transpired Air Collector," *International Journal of Heat and Fluid Flow*, 38, pp. 133–144.
- [15] Liou, T.M., Chen, C. C., Tsai, T.W., 2000, "Heat Transfer and Fluid Flow in a Square Duct with 12 Different Shaped Vortex Generators," *ASME Journal of Heat Transfer*, 122, pp. 327–335.
- [16] Kumar, A., Kim, M.H., 2015, "Effect of Roughness Width Ratios in Discrete Multi V-rib with Staggered Rib Roughness on Overall Thermal Performance of Solar Air Channel," *Solar Energy*, 119, pp. 399–414.
- [17] Kumar, A., Kim, M.H., 2014, "Numerical Optimization of Solar Air Heaters Having Different Types of Roughness Shapes on the Heated Plate-Technical Note," *Energy*, 72, pp. 731–738.
- [18] Tang, X.Y., Zhu, D.S., 2013, "Flow Structure and Heat Transfer in a Narrow Rectangular Channel with Different Discrete Rib Arrays," *Chemical Engineering and Processing*, 69, pp. 1– 14.
- [19] Liu, R., Ting, D.S-K., and Rankin, G.W., 2004, "On the generation of turbulence with a perforated plate," *Experimental Thermal Fluid Science*, 28(4), pp. 307–316.
- [20] Liu, R., and Ting, D. S.-K., 2007, "Turbulent flow downstream of a perforated plate: sharp-edged orifice versus finite-thickness holes," *ASME J. Fluid Eng.* 129(9), pp. 1164–1171.
- [21] Arianmehr, I., Ting, D.S-K., and Ray, S., 2013, "Assisted turbulence convective heat transfer for cooling the photovoltaic cells," *Proceedings of the ASME 2013 summer Heat Transfer Conference*, Paper HT2013-17210, DOI:10.1115/HT2013-17210, Minneapolis, MN, USA.
- [22] Liu, Y.Z. Kang, W., and Sung, H.J., 2005, "Assessment of the organization of a turbulent separated and reattaching flow by measuring wall pressure fluctuations," *Experiments in Fluids* 38 (4), pp. 485–493.
- [23] Liu, Y.Z., Ke, F., and Sung, H.J., 2008, "Unsteady separated and reattaching turbulent flow over a two-dimensional square rib," *Journal of Fluids and Structures* 24 (3), pp. 366–381.
- [24] Acharaya, S., Dutta, S., Myrum, T.A., and Baker, R.S., 1994, "Turbulent flow past a surface-mounted two-dimensional rib," *ASME Journal of Fluids Engineering* 116 (2), pp. 238–246.
- [25] Kumar, A., Saini, R.P., and Saini, J.S., 2013, "Development of Correlations for Nusselt Number and Friction Factor for Solar Air Heater with Roughened Duct having Multi V-shaped with Gap Rib as Artificial Roughness," *Renewable Energy*, 58, pp. 151–163.

## CHAPTER 2

# ENHANCING SMART GRID REALIZATION WITH ACCURATE PREDICTION OF PHOTOVOLTAIC PERFORMANCE BASED ON WEATHER FORECAST

### 2.1. Introduction

Global energy demand will increase by one-third from 2010 to 2035 [1]. One option to handle such a huge demand is to manage more efficiently distributed energy resources including traditional and renewable energies. Development of the Smart Grid – the next-generation power system - helps to attain this goal. It is expected that Smart Grids will enhance the usefulness and reliability of renewable energy resources [2], but an element in making these systems “smart” is the predictability of the output we expect from intermittent renewable power systems.

The sun is the ultimate source of most renewable energy. From the  $3.8 \times 10^{23}$  kW energy emitted by the sun, only around  $1000 \text{ W/m}^2$  hits the earth on a sunny day when the incident angle is normal to the surface [3,4] Photovoltaic (PV) systems convert solar energy directly to electricity. Currently, the efficiency of PV panels ranges from 5.4% for polymer and organic solar cells to more than 40% in multi-junction cells [5,6]. The efficiency and operation of PV systems is affected by absorbed irradiance, PV cell temperature and technology, and ancillary equipment. Estimating the cell efficiency requires accurately estimating the cell temperature, which depends on environmental factors that affect heat transfer, such as ambient and sky temperatures, solar irradiance, and wind speed, fluctuation and direction. Many attempts have been made to relate the efficiency of solar PV cells to their temperature [7-11] and to model the cell temperature based on different environmental factors [12-15]. Yet, there seems to remain much discrepancy from study to study.

Numerous efforts have been made to find an appropriate heat loss correlation for a PV panel: experimentally, analytically and numerically [16-18]. Some of the experimental studies are based on lab experiments of surrogate models [19-21]. Others are based on in-situ experimental measurements under particular local environmental conditions [22-24]. Heat loss from the PV panel can be deduced from relations that have been derived from idealized studies on forced convection of a heated flat plate [25-33]. The qualitative trend of decreasing panel temperature with decreasing irradiance and environmental temperature, increasing wind speed and/or turbulence not disputed. On the other hand, the quantitative results can vary significantly from one study to another.

In this paper an attempt is made to apply previous pertinent research on deriving a predictive relation for PV efficiency based on commonly measured meteorological parameters.

### Nomenclature

$A$	panel area ( $\text{m}^2$ )	$T_{a,NOCT}$	Air temperature at NOCT condition ( $^{\circ}\text{C}$ )
$C_P$	specific heat ( $\text{J/kg}\cdot\text{K}$ )	$T_b$	back surface temperature ( $^{\circ}\text{C}$ )
$D$	hydraulic diameter (m)	$T_C$	cell temperature ( $^{\circ}\text{C}$ )
$F$	view factor	$T_g$	ground temperature ( $^{\circ}\text{C}$ )

$F_{front-ground}$	view factor of the front surface of the PV panel to the ground	$T_r$	roof temperature ( $^{\circ}\text{C}$ )
$F_{front-sky}$	view factor of the front surface of the PV panel to the sky	$T_{ref}$	reference temperature ( $^{\circ}\text{C}$ )
$G_T$	irradiance on the plane of the panel (W)	$T_s$	sky temperature ( $^{\circ}\text{C}$ )
$G_{T,NOCT}$	solar radiation at the standard reference environment (W)	$U_L$	thermal loss coefficient of the photovoltaic panel ( $\text{W}/\text{m}^2\cdot\text{K}$ )
$h$	convective heat loss coefficient ( $\text{W}/\text{m}^2\text{K}$ )	$U_{L,NOCT}$	thermal loss coefficient of the photovoltaic panel at NOCT condition ( $\text{W}/\text{m}^2\text{K}$ )
$I$	output current (A)	$V$	output voltage (V)
$k$	thermal conductivity ( $\text{W}/\text{m}\cdot\text{K}$ )	$V_w$	wind velocity (m/s)
$L$	panel length (m)	$\alpha$	coefficient of the solar absorptance of the PV layer
$NOCT$	Nominal Operation Cell Temperature ( $^{\circ}\text{C}$ )	$\beta$	temperature coefficient
$\overline{Nu}_L$	average Nusselt number ( $hL/k$ ) over the plate with total length of $L$	$\gamma$	solar irradiance coefficient
$P$	power output (W)	$\varepsilon$	emissivity constant
$P_{max}$	maximum power output (W)	$\eta$	panel efficiency
$Pr$	Prandtl number ( $C_p\mu/k$ )	$\eta_{ref}$	cell efficiency at the reference temperature
$q_{rad}$	radiation heat loss from the panel (W)	$\theta$	PV tilt angle
$q_{rad,front}$	radiation from the front surface of the panel to the sky and/or ground (W)	$\mu$	dynamic viscosity of the fluid ( $\text{kg}/\text{m}\cdot\text{s}$ )
$q_{rad,back}$	radiation from the rear surface of the panel to the sky and/or ground (W)	$\rho$	density of the fluid ( $\text{kg}/\text{m}^3$ )
$Re_L$	Reynolds number ( $\rho VL/\mu$ ) of the flow over a plate with total length of $L$	$\sigma$	Stefan-Boltzmann constant
$Re_D$	Reynolds number ( $\rho VD/\mu$ ) of the flow in a duct	$\tau$	coefficient of the solar transmittance of glazing
$T_a$	air temperature ( $^{\circ}\text{C}$ )		

## 2.2 Panel Efficiency

The efficiency of a PV panel is defined as electric power output over irradiance power input:

$$\eta = \frac{P}{AG_T} = \frac{VI}{AG_T} \quad (2.1)$$

where the  $I$  and  $V$  are the output current and voltage.  $A$  is the panel area. This efficiency is influenced by cell temperature and irradiance, and can be estimated by relating the existing environmental conditions to a reference condition [11]:

$$\eta = \eta_{ref} \left[ 1 - \beta(T_C - T_{ref}) + \gamma \text{Log} \frac{G_T}{1000} \right] \quad (2.2)$$

where  $\eta_{ref}$  is cell efficiency at the reference temperature,  $T_{ref}$  (typically 25°C), and reference solar irradiance of 1000 W/m<sup>2</sup>.  $\beta$  and  $\gamma$  are the temperature coefficient and solar irradiance coefficient, respectively, which are dependent on the PV materials.  $\eta_{ref}$  and  $\beta$  are normally given by manufacturers. It can be seen that an increase in cell temperature ( $T_C$ ) would lead to a decrease in efficiency. The value of  $\gamma$  is often assumed to be zero, which simplifies the efficiency expression to [8]:

$$\eta = \eta_{ref} [1 - \beta(T_C - T_{ref})] \quad (2.3)$$

### 2.3. Cell Temperature ( $T_C$ )

Increasing the cell temperature causes the output voltage to decrease significantly and the current to increase slightly. Hence, the overall effect is a decrease in output power [34]. Direct measurements of cell temperature inside the PV module pose serious manufacturing challenges. One method for estimating cell temperature is using the Nominal Operation Cell Temperature (NOCT), which is the cell temperature of an open-rack module under an open circuit condition and in a standard reference environment: the solar radiation is typically 800 W/m<sup>2</sup> ( $G_{T,NOCT}$ ) and the panel is tilted 45° from the horizontal and subjected to 20°C air ( $T_{a,NOCT}$ ) at 1 m/s [35]. Cell temperature can then be expressed as [12]:

$$T_C = T_a + (NOCT - T_{a,NOCT}) \left( \frac{G_T}{G_{T,NOCT}} \right) \left( \frac{U_{L,NOCT}}{U_L} \right) \left( 1 - \frac{\eta}{\tau\alpha} \right) \quad (2.4)$$

where  $U_L$  is the thermal loss coefficient of the photovoltaic panel which consists of convection and radiation from both sides of the panel and conduction to the mounting frame [12].  $T_a$  and  $G_T$  are the air temperature and irradiance on the plane of the panel, respectively. Coefficients  $\tau$  and  $\alpha$  are the solar transmittance of glazing and the solar absorptance of the PV layer, respectively.  $\eta$  is the electrical efficiency.

According to Duffie and Beckman [12], the term  $\left(\frac{\eta}{\tau\alpha}\right)$  is typically small, so the equation may be simplified to:

$$T_C = T_a + (NOCT - 20) \left( \frac{G_T}{800} \right) \left( \frac{U_{L,NOCT}}{U_L} \right) \quad (2.5)$$

#### 2.3.1. Heat Loss from the PV Panel ( $U_L$ )

Ignoring conduction from the PV panel to the mounting frame, which depends on the installation conditions, the overall heat loss coefficient for the panel,  $U_L$ , may be expressed as:

$$U_L = h + \frac{q_{rad}}{T_C - T_a} \quad (2.6)$$



where  $h$  and  $q_{rad}$  are the convective heat loss coefficient and radiation heat loss from the panel, respectively.

### 2.3.1.1. Convection

The following relations by Incropera and DeWitt [27] apply to a flat plate with uniform temperature:

Laminar flow:

$$\overline{Nu}_L = 0.664Re_L^{1/2}Pr^{1/3} \quad Pr \geq 0.6, \quad Re_L < 5 \times 10^5 \quad (2.7)$$

Turbulent flow:

$$\overline{Nu}_L = 0.037Re_L^{4/5}Pr^{1/3} \quad 0.6 \leq Pr \leq 60, \quad 5 \times 10^5 \leq Re_L \leq 10^7 \quad (2.8)$$

$\overline{Nu}_L$ ,  $Re_L$  and  $Pr$  are the average Nusselt number ( $hL/k$ ) and Reynolds number ( $\rho VL/\mu$ ) of the flow over the plate with total length of  $L$ , and the Prandtl number ( $C_p\mu/k$ ), respectively. Table 2.1 summarizes additional experimental studies. One of these studies is based on indoor tests and two were performed in outdoor conditions with natural wind.

Table 2.1 Some experimental relations for heat transfer over a flat plate

Study	Proposed relation	Test conditions
Test et al. [33]	$h (W/m^2\text{C}) = 2.56V_w(m/s) + 8.55$ (2.9)	outdoor test with natural wind heated plate: 1.22 m × 0.81 m 1.5 m/s < wind velocity ( $V_w$ ) < 5.6 m/s attack angle $\geq 40^\circ$
Sharples and Charlesworth [24]	$h(W/m^2\text{C}) = 3.3V_w(m/s) + 6.5$ (2.10) (wind parallel to the plate)	outdoor test with natural wind heated plate: 1.81 m × 0.89 m mounted on a roof with a pitch of $35^\circ$ 0.8 m/s < $V_w$ < 6.2 m/s
Kumar et al. [20]	$h(W/m^2\text{C}) = 4.687V_w(m/s) + 10.03$ (2.11)	indoor test, fans used to simulate wind heated aluminum plate: 4 mm thick, 0.368 m <sup>2</sup> 1 m/s < $V_w$ < 4 m/s, parallel to the plate

To accommodate convective heat loss from the back of the PV panel, an additional heat loss coefficient may be added to Equation (2.6). The heat loss due to turbulent flow in the space underlying the PV panel is similar to the case of air flow between parallel plates with heat transfer from one plate, for which the following relation has been proposed [29]:

$$Nu = 0.0186Re_D^{0.787} \quad 10^4 \leq Re_D \leq 10^6 \quad (2.12)$$

where  $D$  is the hydraulic diameter. For flow between two parallel plates the hydraulic diameter is simply twice the gap [16].

### 2.3.1.2. Radiation

The radiation heat loss from the PV panel can be defined as follows:

$$q_{rad} = q_{rad,front} + q_{rad,back} \quad (2.13)$$

where  $q_{rad,front}$  is radiation from the front surface of the panel to the sky and/or ground, and  $q_{rad,back}$  is radiation from the rear surface of the panel to the sky and ground or roof (depending on the installation condition). By assuming the glass temperature is equal to the cell temperature, radiation from the front and rear surfaces would be [36]:

$$q_{rad,front/back} = \varepsilon\sigma FA(T_c^4 - T_{s/g/r}^4) \quad (2.14)$$

where  $T_s$ ,  $T_g$ ,  $T_b$  and  $T_r$  are the sky, ground, back surface and roof temperatures, respectively.  $\varepsilon$  and  $\sigma$  are the emissivity and Stefan-Boltzmann constant, respectively.  $A$  is the panel's surface area. Sky temperature may be estimated as [12]:

$$T_s = 0.0552(T_a)^{1.5} \quad (2.15)$$

The view factor,  $F$ , is a function of PV tilt angle,  $\theta$  [36]. For example, the view factor of the front surface of the PV panel to the sky is:

$$F_{front-sky} = \frac{1}{2}(1 + \cos\theta) \quad (2.16)$$

## 2.4. Studied Photovoltaic Array

The PV array in this study consists of 2186 ClearPower CS6P-230P panels (Canadian Solar, Guelph, Ontario, Canada) with characteristics listed in Table 2.2, and is located on Tecumseh Arena near Windsor, Ontario, Canada with latitude of 42°18'. As portrayed in Figure 1, panels are installed on east and west slopes of a roof with an open-ended gap of around 90 mm. Global solar irradiance, wind velocity and ambient temperature at the site were measured by a Satcon Weather Station (model PM00447; Boston, USA), every 15 minutes.

Table 2.2 Characteristics of tested PV panels [37]

	Technology	Frame and dimensions	<i>NOCT</i>	Temperature coefficient of maximum power ( $\beta$ )	Nominal maximum power ( $P_{max}$ )	Cell reference efficiency ( $\eta_{ref}$ )
ClearPower CS6P-230P	poly-crystalline	Anodized silver aluminum, 1638 x 982 x 40 mm	45±2°C	0.43%	230 W	14.3%

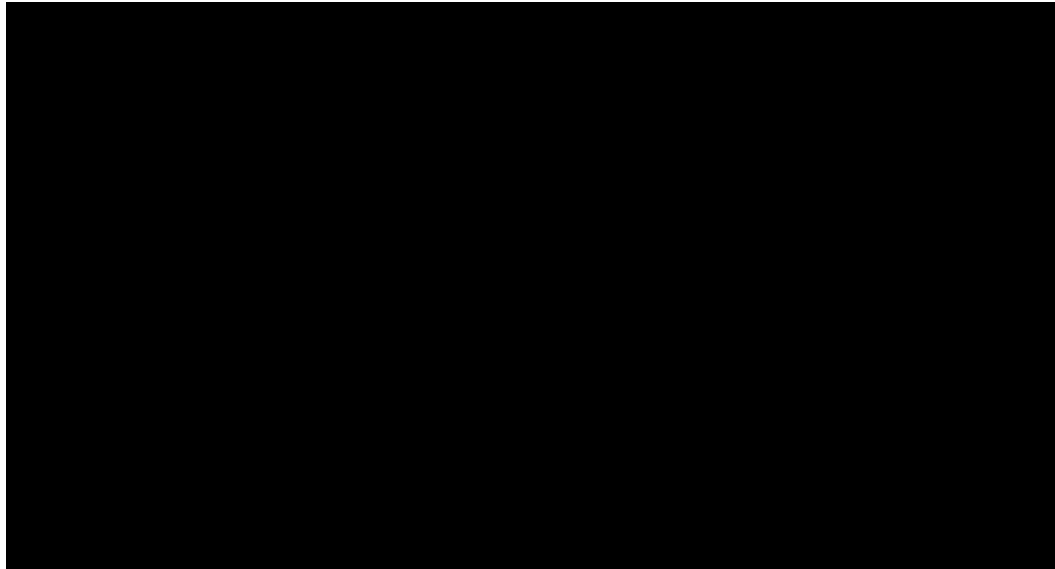


Figure 2.1 Schematic drawing of the studied PV array

### 2.5. Calculation Procedure

Based on meteorological data from the array site, panel efficiencies have been computed using Equations (2.2) or (2.3), (2.4) or (2.5), (2.6), and (2.8)-(2.16), and compared to the measured efficiency calculated from Equation (2.1). As can be seen in Equation (2.1), the measured efficiency has to be calculated from the measured output power divided by incident solar irradiance on the plane of the panel. The amount of solar irradiance is different for east and west panels. It was computed from measurements of total solar radiation on a horizontal surface and the geometric factor,  $R_b$ , which is the ratio of beam radiation on the tilted surface to that on a horizontal surface [12]. Using Equation (2.4) requires an iterative calculation. The following simplifications were assumed:

- Conduction and radiation from the rear surface of the PV panel are negligible
- Temperature is uniform throughout the 2186 module array
- Temperature of cell, glass cover and rear surface are equal
- $\tau\alpha$  is 0.9 [7]
- $\varepsilon$  is 0.91, for glass surface [38]  $\gamma$  is 0.025, for crystalline and poly-crystalline silicon modules [17]
- $\theta$  is  $5^\circ$ ,  $F_{front-ground} = 0.0019$ ; therefore this radiation component is negligible

Flow over this array was assumed to be turbulent because of the length of the array and the fact that the natural wind itself is very turbulent. The typical range of turbulence intensity in natural wind is 20%~50% [33]. The prevailing wind direction on the selected day was from the south [39]. Therefore, the Reynolds number was based on a characteristic length of 59 m. Flow in the underlying gap was also assumed to be turbulent.

The overall heat loss coefficient in the NOCT situation,  $U_{L,NOCT}$ , was calculated by the same procedure as the studied panel, based on NOCT conditions (Section 2.3) and with the assumption of turbulent flow.

## 2.6. Results and discussion

Figure 2.2 shows the plots for solar irradiance, ambient temperature and wind velocity for April 13, 2011 from 7:45 AM to 6:45 PM. Sunrise and sunset on April 13, 2011 were 6:55 AM and 8:11 PM, respectively. East panels saw the sun from sunrise to 7:37 PM and west panels saw it from 7:29 AM to sunset.

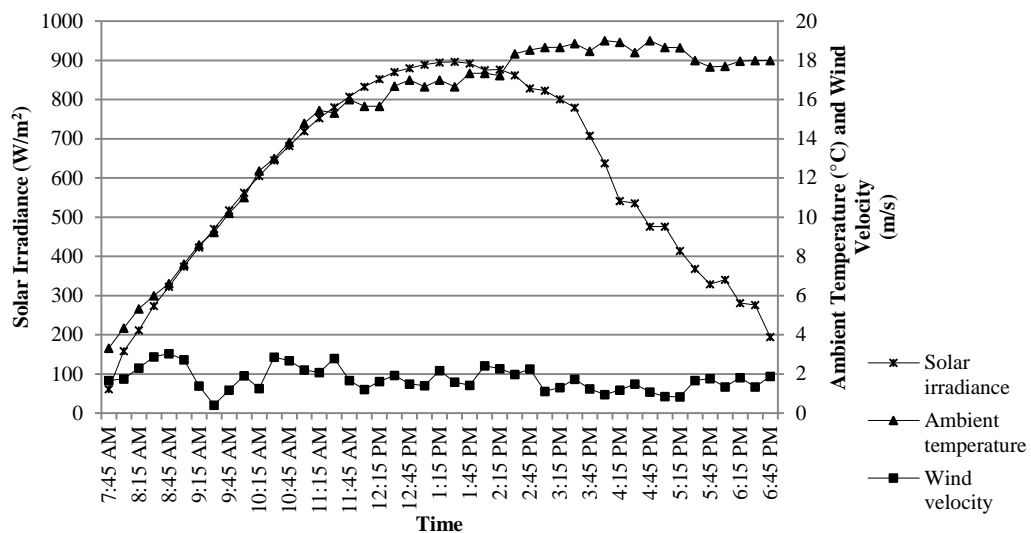


Figure 2.2 Meteorological data for April 13, 2011

Figure 2.3 shows the good agreement between the calculated and measured efficiencies. Deviations are not larger than 0.62% in absolute efficiency between 9 AM and 6 PM. The real efficiencies at many points are larger than the calculated values, probably because the radiation heat loss from the back of the panels has been ignored. This would result in an over-estimate of the cell temperature and hence, an under-estimate of the efficiency. It is noted that Equations (2.8)-(2.12) were derived from experimental studies that were performed in conditions different from the present field study. Moreover, a different mounting situation from the *NOCT* test conditions may cause some errors in using Equation (2.4) or (2.5) for cell temperature.

Figure 2.3 shows that the measured efficiencies decrease drastically in the early morning and late evening, perhaps because of lower inverter efficiencies at very low irradiance [40]. Another reason might be that the parameter  $\tau\alpha$  would be smaller at large incident angles, although constant values were used in Equation 2.4 [12]. Hence, the actual direct irradiance penetrating to the cells would be smaller in the morning and evening than what is reported by the radiometer, which has a wider range of acceptable angles. Accordingly, the actual power output was less, but the measured  $G_T$  was unaffected at high incident angles. Finally, the difference in the morning and evening might be because of underestimating  $\gamma$ , which is not given by the manufacturer of the PV panel. In spite of these differences, the predictions corroborate well with the measured values. The similarity of results using the different heat transfer correlations may be caused by the fact that each equation in Section 2.3.1.1. is used in both the numerator and denominator of  $\left(\frac{U_{L,NOCT}}{U_L}\right)$  in Equations (2.4) and (2.5), and thus the effect on cell temperature from any particular equation is reduced.

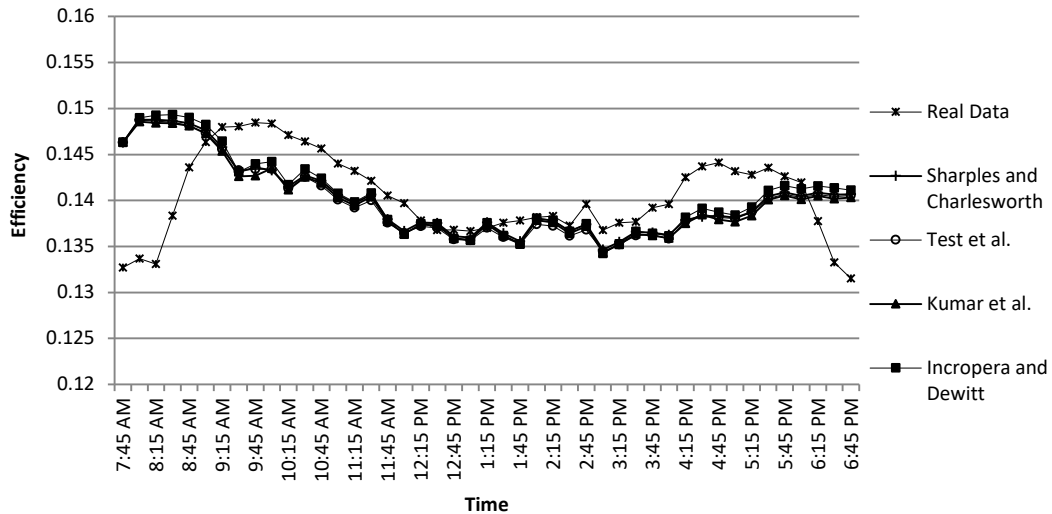


Figure 2.3 Comparison between measured and calculated efficiencies using Equations (2.2) and (2.4), with different relations for convective heat loss

Figure 2.4 shows the comparison between the efficiencies calculated using Equation (2.3) and measured efficiencies. Comparing Figures 2.3 and 2.4, it can be seen that the calculated efficiencies have been increased by considering  $\gamma$  as zero. In the morning and evening this rise is around 1% and 0.7% (absolute), respectively, but at other times of the day is around 0.2% (absolute). A comparison of Figures 2.3 and 2.5 shows that ignoring the term  $\left(1 - \frac{\eta}{\tau\alpha}\right)$  in the *NOCT* equation causes a 0.1%~0.4% (absolute) reduction in the calculated efficiency.

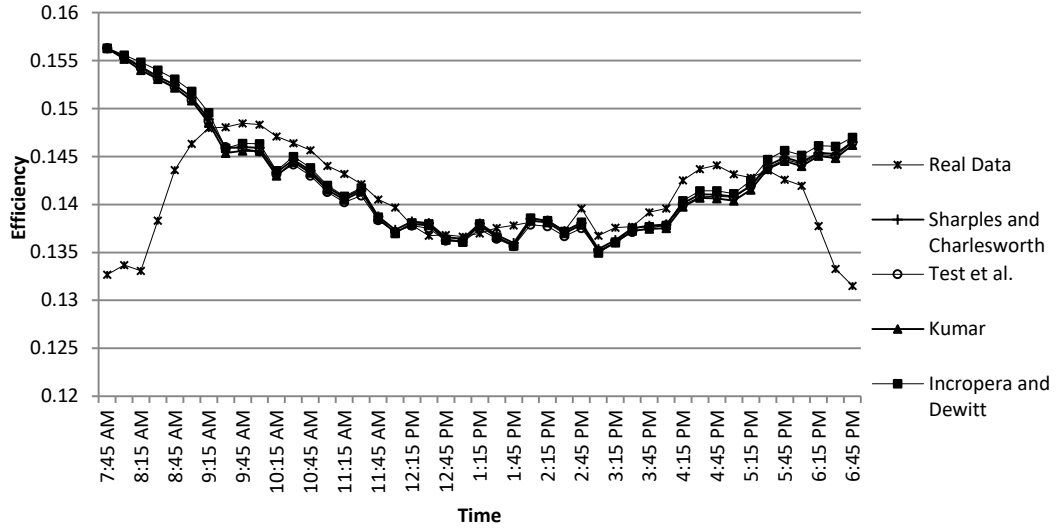


Figure 2.4 Comparison between measured and calculated efficiencies using Equations (2.3) and (2.4), with different relations for convective heat loss

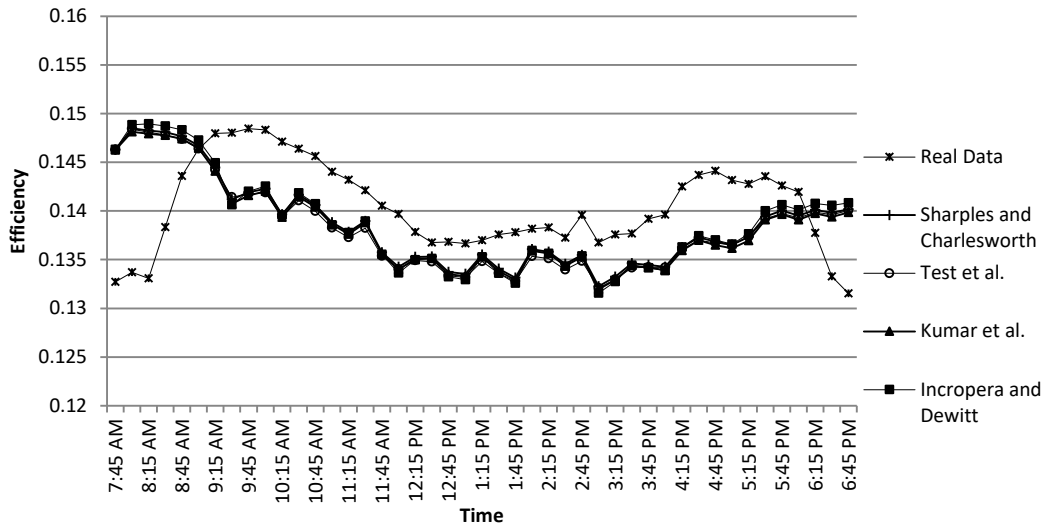


Figure 2.5 Comparison between measured and calculated efficiencies using Equations (2.2) and (2.5), with different relations for convective heat loss

Figure 2.6 illustrates that cell temperature increases from the morning, with increasing irradiance and ambient temperature. The peak in cell temperature approximately coincides with maximum solar irradiance. Upon examination of Figures 2.3 and 2.6, it can be concluded that when the cell temperature experiences its highest value, the efficiency is minimum. This minimum is normally masked by the increase in array power output, because of maximum solar radiation.

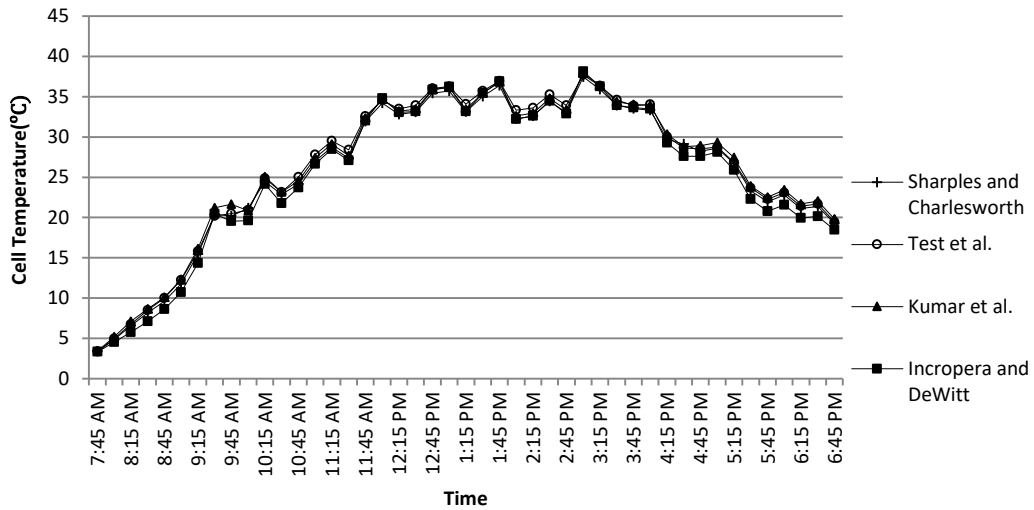


Figure 2.6 Cell Temperature calculated from Equation (2.4), with different relations for convective heat loss

The adverse effect of cell temperature on its efficiency can be clearly observed in Figure 2.7. Note that the negative slope of this graph is greater at lower cell temperatures. This slope is a reflection of  $\beta$  in Equations (2.2) and (2.3), which is clearly higher at lower cell temperatures.

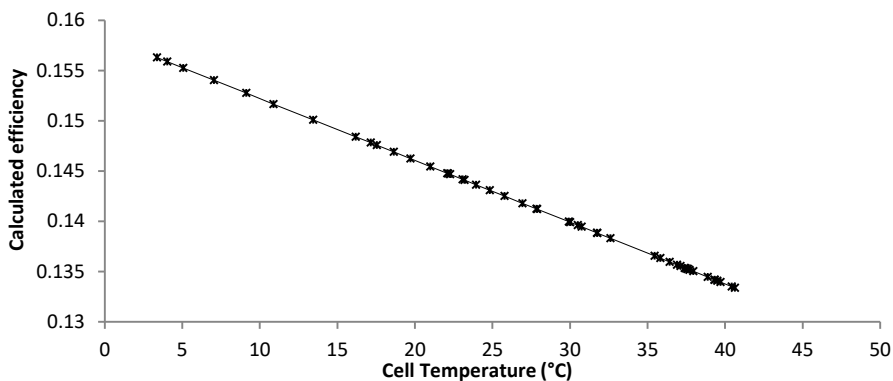


Figure 2.7 Calculated efficiencies based on Test et al. relation versus calculated cell temperatures

Figure 2.8 shows the deviation of efficiencies, calculated by Equations (2.2) and (2.4) and the heat loss correlation from Test et al. [33], from the measured efficiencies. When all points are considered, the deviations are less than 1.6%. Except for the three points in the morning, deviations are less than 1%. And the mean deviation, with all points, is -0.05%. This is sufficiently accurate for efficiency predictions, in light of the simplifications made in our calculations.

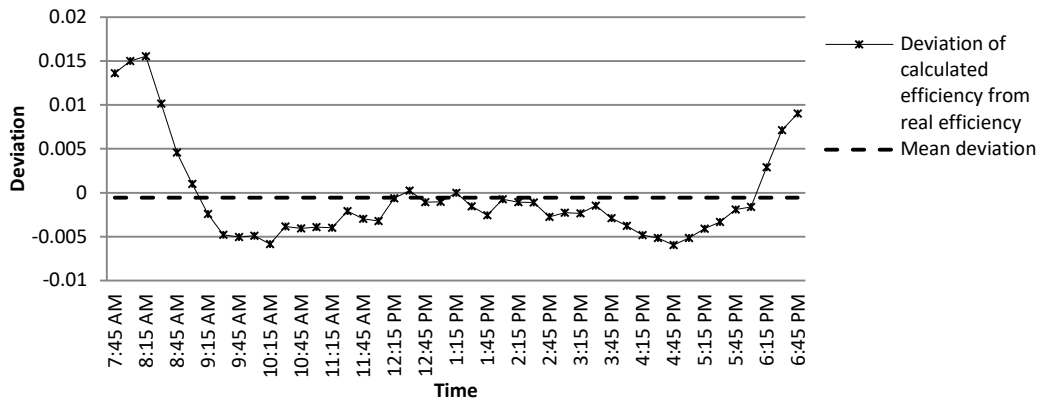


Figure 2.8 Absolute deviations of efficiencies calculated using the Test et al. heat loss correlation, Equation (2.9), from measured efficiencies

## 2.7. Conclusions

Based on comparison to measured field data, Equation (2.2) [11] is adequate to predict PV array efficiency using panel-specific coefficients. The cell temperature in this equation can be calculated from the *NOCT* equation (Equation (2.4); [12]) using generic coefficients and including only sky-to-panel radiation and convection from the front and back of the panel. Several equations may be used to estimate the convective heat transfer coefficient, without much loss in accuracy. When the equation by Test et al. [33] was used, the PV array efficiency was estimated with 1.6% accuracy at any point in time and with 0.05% accuracy over time. Thus the PV efficiency may be estimated simply from field measurements of solar irradiance, ambient temperature and wind speed. This predictive ability may be used to integrate solar energy into a Smart Grid.

## Acknowledgements

This work was made possible by the Ontario Trillium Foundation and Natural Sciences and Engineering Research Council of Canada.

## References

- [1] International Energy Agency (IEA). 2013 [online] [http://www.iea.org/publications/freepublications/publication/worldwide\\_engagement.pdf](http://www.iea.org/publications/freepublications/publication/worldwide_engagement.pdf) [accessed on March 21, 2013]
- [2] Wang, W. and Lu, Z., 2013, "Cyber security in the Smart Grid: Survey and challenges," *Computer Networks*, 57(5), pp. 1344–1371.



- [3] Khullar, V. and Tyagi, H., 2012, "A study on environmental impact of nanofluid-based concentrating solar water heating system," *International Journal of Environmental Studies*, 69 (2), pp. 220–232.
- [4] Lovegrove, K. and Dennis, M., 2006, "Solar energy systems in Australia," *International Journal of Environmental Studies*, 63(6), pp. 791–802.
- [5] Friedman, D.J., 2010, "Progress and challenges for next-generation high-efficiency multijunction solar cells," *Current Opinion in Solid State and Materials Science*, 14(6), pp. 131–138.
- [6] Meral, M.E. and Diner, F., 2013, "A review of the factors affecting operation and efficiency of photovoltaic based electricity generation systems," *Renewable and Sustainable Energy Reviews*, 15(5), pp.2176-2184.
- [7] Aste, N., Chiesa, G. and Verri, F., 2008, "Design, development and performance monitoring of a photovoltaic-thermal (PV/T) air collector," *Renewable Energy*, 33(5), pp. 914-927.
- [8] Evans, D.L., 1981, "Simplified method for predicting photovoltaic array output," *Solar Energy*, 27(6), pp. 555–560.
- [9] Evans, D.L. and Florschuetz, L.W., 1977, "Cost studies on terrestrial photovoltaic power systems with sunlight concentration," *Solar Energy*, 19(3), pp. 255–262.
- [10] Siegel, M.D., Klein, S.A. and Beckman, W.A., 1981, "A simplified method for estimating the monthly-average performance of photovoltaic systems," *Solar Energy*, 26(5), 413-418.
- [11] Spectrolab, Inc., Sylmar, C.A., 1977, "Photovoltaic Systems Concept Study: Final Report," (ALO-2748-12) U.S. Dept. of Energy, Division of Solar Energy, Springfield, VA.
- [12] Duffie, J.A. and Beckman, W.A., 1980, *Solar Engineering of Thermal Processes*, 2<sup>nd</sup> ed., John Wiley and Sons, New York, USA.
- [13] Hove, T., 2000, "A method for predicting long-term average performance of photovoltaic systems," *Renewable Energy*, 21(2), pp. 207-229.
- [14] King, D.L., Boyson, W.E. and Kratochvil, J.A., 2004, "Photovoltaic Array Performance Model," Sandia National Laboratories Report, SAND2004-3535.
- [15] Kou, Q., Klein, S.A. and Beckman, W.A., 1998. "A method for estimating the long-term performance of direct-coupled PV pumping systems," *Solar Energy*, 64(1-3), pp. 33-40.
- [16] Brinkworth, B.J., 2000, "Estimation of flow and heat transfer for the design of PV cooling duct," *Solar Energy*, 69(5), pp. 413-420.
- [17] Mittelman, G., Alshare, A. and Davidson, J.H., 2009, "A model and heat transfer correlation for rooftop integrated photovoltaics with a passive air cooling channel," *Solar Energy*, 83(8), pp. 1150-1160.

- [18] Sandberg, M. and Moshfegh, B., 2002, "Buoyancy-induced air flow in photovoltaic facades, Effect of geometry of the air gap and location of solar cell modules," *Building and Environment*, 37(3), pp. 211-218.
- [19] Brinkworth, B.J. and Sandberg, M., 2006, "Design procedure for cooling ducts to minimise efficiency loss due to temperature rise in PV arrays," *Solar Energy*, 80(1), pp. 89–103.
- [20] Kumar, S., Sharma, V.B., Kandpal, T.C. and Mullick, S.C., 1997, "Wind induced heat losses from outer cover of solar collectors," *Renewable Energy*, 10(4), pp. 613-616.
- [21] Liu, C.H. and Sparrow, E.M., 1980, "Convective-radiative interaction in a parallel plate channel- application to air-operated solar collectors," *International Journal of Heat and Mass Transfer*, 23(8), pp. 1137-1146.
- [22] Francey, J.L.A. and Papaioannou, J., 1985, "Wind-related heat losses of a flat-plate collector," *Solar Energy*, 35(1), pp. 15–19.
- [23] Kumar, S. and Mullick, S.C., 2010, "Wind heat transfer coefficient in solar collectors in outdoor conditions," *Solar Energy*, 84(6), pp. 956-963.
- [24] Sharples, S. and Charlesworth, P.S., 1998, "Full scale measurement of wind induced convective heat transfer from a roof mounted flat plate solar collector," *Solar Energy*, 62(2), pp. 69–77.
- [25] Bejan, A., 1995, *Convective Heat Transfer*, 2<sup>nd</sup> ed., John Wiley and Sons, New York, USA.
- [26] Brinkworth, B.J., 2000, "A procedure for routine calculation of laminar free and mixed convection in inclined ducts," *International Journal of Heat and Fluid Flow*, 21(4), pp. 456-462.
- [27] Incropera, F.P. and DeWitt, D.P., 1996, *Fundamentals of heat and mass transfer*, 3<sup>rd</sup> ed., John Wiley and Sons, New York, USA.
- [28] Kays, W.M. and Crawford, M.E., 1976, *Convective Heat and Mass Transfer*, 2<sup>nd</sup> edn., McGraw-Hill, New York, USA.
- [29] Kays, W.M. and Leung, E.Y., 1963, "Heat transfer in annular passages: hydrodynamically developed turbulent flow with arbitrarily prescribed heat flux," *International Journal of Heat and Mass Transfer*, 6(7), pp. 537-557.
- [30] Osborne, D.G. and Incropera, F.P., 1985, "Laminar, mixed convection heat transfer for flow between horizontal parallel plates with asymmetric heating," *International Journal of Heat and Mass Transfer*, 28(1), pp. 207-217.
- [31] Osborne, D.G. and Incropera, F.P., 1985, "Experimental study of mixed convection heat transfer for transitional and turbulent flow between horizontal, parallel plates," *International Journal of Heat and Mass Transfer*, 28(7), pp. 1337-1344.
- [32] Sartori, E., 2006, "Convection coefficient equations for forced air flow over flat surfaces," *Solar Energy*, 80(9), pp. 1063–1071.

- [33] Test, F.L., Lessmann, R.C.L. and Johary, A., 1981, "Heat transfer during wind flow over rectangular bodies in natural environment," *Journal of Heat Transfer*, 103(2), pp. 262–267.
- [34] Kalogirou, S., 2009, *Solar Energy Engineering: Process and Systems*, Elsevier Inc.
- [35] International Electrotechnical Commission, 1993, *Crystalline Silicon Terrestrial Photovoltaic Modules – Design Qualification and Type Approval*, 2<sup>nd</sup> ed, International Standard EN-61215, 1993-04.
- [36] Armstrong, S. and Hurley, W.G., 2010, "A thermal model for photovoltaic panels under varying atmospheric condition," *Applied Thermal Engineering*, 30(11-12), pp. 1488-1495.
- [37] Canadian Solar Inc., 2012. ClearPower CS6P 230/235/240/245/250P. [Online] <http://www.canadiansolar.com/en/products/standard-modules/cs6-series.html> [accessed on September 1, 2012]
- [38] Notton, G., Cristofari, C., Mattei, M. and Poggi, P., 2005, "Modelling of a double-glass photovoltaic module using finite differences," *Applied Thermal Engineering*, 25(17-18), pp. 2854-2877.
- [39] Environment Canada, 2012. *Canadian climate normals 1971-2000* [Online] [http://climate.weatheroffice.gc.ca/climate\\_normals/results\\_e.html?stnID=4716andlang=eandCode=1andStationName=WINDSORandSearchType=Containsandprovince=ALLandprovBut=andmonth1=0andmonth2=12](http://climate.weatheroffice.gc.ca/climate_normals/results_e.html?stnID=4716andlang=eandCode=1andStationName=WINDSORandSearchType=Containsandprovince=ALLandprovBut=andmonth1=0andmonth2=12) [accessed on October 1, 2012]
- [40] Chen, S., Li, P., Brady, D. and Lehman, B., 2013, "Determining the optimum grid-connected photovoltaic inverter size," *Solar Energy*, 87(1), pp. 96–116.

## CHAPTER 3

### TURBULENT FLOW OVER A FLAT PLATE DOWNSTREAM OF A FINITE HEIGHT PERFORATED PLATE

#### ***3.1. Introduction***

Photovoltaic (PV) panels are a method to harvest renewable solar energy directly as electricity. Maintaining the PV panels at temperatures close to or less than ambient is critical because their efficiency decreases as the temperature increases [1-5]. The ultimate goal behind this study is to enhance the heat transfer rate from a PV panel's surface by perturbing the flow over it via a finite height perforated plate (grid). To do so, this paper focuses on detailing the perturbed flow with respect to the height of the grid.

Grid-generated turbulence has been investigated for over seventy years. Taylor [6] was the first to introduce the idea of generating nearly-isotropic turbulence via a perforated plate in a wind tunnel. Just downstream of the grid, the turbulence is neither homogeneous, nor isotropic. It becomes homogeneous in the lateral direction and quasi isotropic after some distance downstream of the grid [7]. Based on extensive examination of the decay of the turbulent kinetic energy downstream of the grid, there are stages of the turbulent flow downstream of a grid: the initial developing region, and the initial and final decay regions [8, 9, 10]. The initial developing region is where fully developed, nearly homogenous turbulence is formed. For conventional grids, this length has been determined to range from 20 D [9] to 10 - 15 D by Hinze [7]. However, it has been pointed out by many researchers [11-19] that, even at larger distances, grid-generated turbulence can deviate from an isotropic and homogenous state and the amount of this deviation varies from study to study.

In recent years conventional grid-generated turbulence has been discussed in many studies. Murzyn and Be'lorgey [20] experimentally investigated the time and length scales of grid-generated turbulence occurring in a flume with a free surface flow. In Liu et al.'s study [21], homogeneous, nearly isotropic turbulence was experimentally produced and discussed using an orificed, perforated plate in a wind tunnel. Llor [22] studied the decay of homogeneous isotropic turbulence theoretically. Liberzon et al. [23] investigated the turbulent dissipation rate in a decaying grid turbulent flow using particle image velocimetry and laser Doppler velocimetry. George [24] reviewed the experimental, theoretical and numerical studies for the asymptotic effect of initial and upstream conditions on turbulence. Horender [25] discussed the turbulent flow downstream of a large-solidity (96%) perforated plate at 1m/s bulk velocity.

The effect of grid geometry and solidity on turbulence parameters has also been investigated by many other researchers. Uberio and Wallis [26] studied the effect of grid geometry on turbulent decay. Lavoie et al. [27] investigated the effect of grid geometry and solidity on turbulence parameters by using different shapes of bars. Liu et al. [28] also studied the effect of perforated plate solidity and hole diameter on turbulence parameters in a wind tunnel. Liu and Ting [29] performed a comparative experimental study on the turbulence produced by perforated plates with sharp-edged orificed openings and finite-thickness straight openings in a wind tunnel.

In almost all of these previous grid turbulence studies, the perforated plate covered the whole cross section area of the wind tunnel. One exception to this was Judd et al. [30] who performed wind-tunnel experiments on the flow around single and multiple porous windbreaks with a finite height and different solidities, which was sheltering a model plant canopy with lower height. In their work, the experimental emphases were on the interactions of flow with the underlying plant canopy. In the present study also, the perforated plate (grid) has a finite height, and was placed at the leading edge of the flat plate, in order to simulate an accoutrement to a PV panel. Accordingly, it is important to see the effect of panel height on the flow and turbulence over the panel.

### ***Nomenclature***

D	grid mesh size (m)	X	streamwise distance from the plate's leading edge (cm)
F	flatness factor, $\overline{u^4}/u'^4$	Y	normal distance from the plate (cm)
H	grid height above the flat plate	Y <sup>+</sup>	normalized distance from the wall, $\frac{Y \cdot u_\tau}{\nu}$
N	sampling size (2 x 10 <sup>6</sup> )	Z	distance along the width of the plate from the plate's centerline (cm)
R( $\tau$ )	autocorrelation function between turbulence velocities	$\delta$	boundary layer thickness (cm)
Re <sub>L</sub>	Reynolds number based on the total length of the plate, $\rho UL/\mu$	$\delta^*$	boundary layer displacement thickness, $\int_0^Y \left(1 - \frac{U}{U_\infty}\right) dy$ (cm)
S	skewness factor, $\overline{u^3}/u'^3$	$\lambda$	Taylor micro-scale length (mm)
Tu	turbulence intensity, $u'/U_\infty$	$\mu$	dynamic viscosity (N·s/m <sup>2</sup> )
u	velocity fluctuations (m/s)	$\nu$	kinematic viscosity (m <sup>2</sup> /s)
u'	root-mean-square of the velocity fluctuations (m/s)	$\tau$	time difference (s)
u <sub><math>\tau</math></sub>	shear velocity, $\sqrt{\frac{\tau_w}{\rho}}$ (m/s)	$\tau_\lambda$	Taylor time scale (s)
U	local velocity (m/s)	$\tau_\Lambda$	integral time scale (s)
U <sub>i</sub>	instantaneous velocity (m/s)	$\tau_w$	viscous stress at the wall, $-\mu \left. \frac{du}{dy} \right _{y=0}$ (N/m <sup>2</sup> )
U <sub><math>\infty</math></sub>	free stream velocity (m/s)	$\Lambda$	integral length scale (cm)

## ***3.2 Experimentation***

### ***3.2.1. Wind Tunnel***

The experiment was conducted in a closed-loop wind tunnel with a 180 cm long test section (76 cm high and 77 cm wide). The maximum free stream velocity in the wind tunnel is around 30 m/s when the test section is empty. The background turbulence level of the wind tunnel was measured to be around 0.4%.

### 3.2.2. Experimental Setup

The experimental setup consists of a flat, horizontal plate with a vertical perforated plate (grid) mounted normal to the flow, at the leading edge of the flat plate. Figure 3.1 presents an isometric view of the flat plate and perforated plate. X, Y and Z are the streamwise, normal to the plate and widthwise directions, respectively, with the origin located at the center of leading edge of the flat plate. A perforated plate with circular hole pattern and orificed opening was studied in another graduate project [28, 29, 31]. Wishing to produce more turbulence on the flat plate, a new perforated plate with diamond pattern and sharp edge was designed. It was cut from an aluminum plate of 0.3 cm thickness by a computer numerical controlled machine. The outside dimensions of the perforated plate were 16 cm x 62 cm. After cutting diamond-shaped holes with a diagonal distance (D) of 1.4 cm, the resulting solidity was 0.545. The grid is connected to the flat plate by a support and it can be shifted vertically. So, the height of the grid above the flat plate (H) can be adjusted.

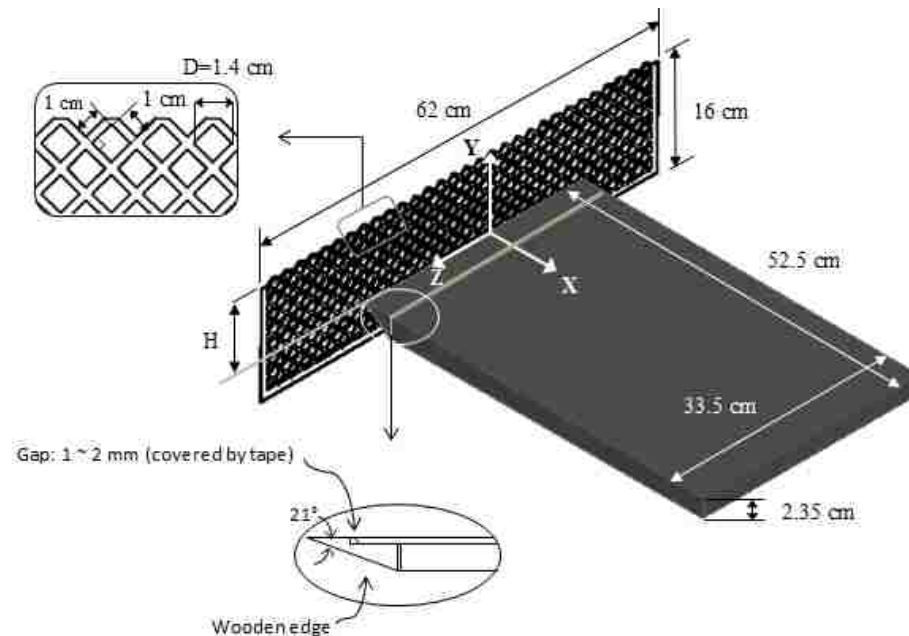


Figure 3.1 Flat plate and perforated plate isometric

The flat plate was a 1.5 mm thick aluminum plate with dimensions of 33.5 cm (width) x 52.5 cm (length) on a 0.2 cm layer of carbon fiber over a 2 cm layer of wood, bringing the total thickness to 2.35 cm. The windward cross-sectional area of the flat plate is around 1% of the total wind tunnel cross-section, so it is not expected to have a significant effect on the flow. However, in an attempt to reduce the effect of the blunt leading edge, a wooden wedge with a 21° bevel was attached to the main wood piece by glue and the small gap between two edges (1 - 2 mm) was covered by tape. The flat plate was placed at the grid half-height and in the middle of the test section. Figure 3.2 shows the test section setup.

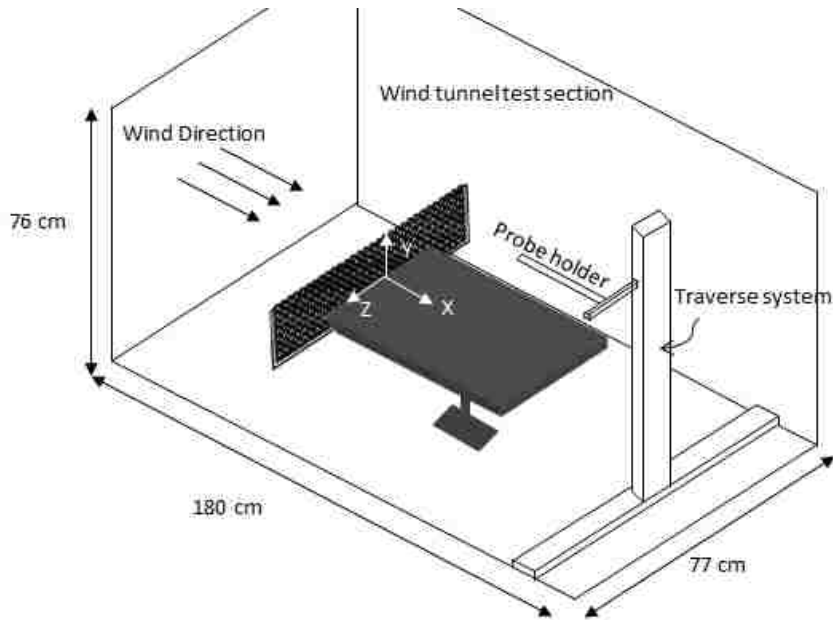


Figure 3.2 Test section isometric

### 3.2.3. Hot-wire Anemometer

The velocity at different points downstream of the plate was measured using a 1-D boundary layer hot-wire probe (type 55P15) as part of a Dantec streamline 55C90 constant-temperature anemometer (CTA). The probe had a platinum-plated tungsten wire with a diameter of  $5 \mu\text{m}$  and a length of  $1.25 \text{ mm}$ . Signals were low-passed at  $30 \text{ kHz}$  and then sampled at  $80 \text{ kHz}$  over a period of around  $25 \text{ s}$ , resulting in  $2 \times 10^6$  data points per measurement. A 12-bit PCI-6071E National Instrument data acquisition card was used to convert the analog data into digital ones. A computer-controlled 2-D traverse system was used to position the probe at each specified location (Figure 2). The computer-controlled traverse system can move through the widthwise direction of the test section (Z) and normal direction to the plate (Y) in  $3.2 \text{ mm}$  ( $0.125 \text{ inch}$ ) steps.

### 3.3. Methodology

Measurements were performed at  $Z = 0$  (Figure 3.1) and at 50 points in the Y direction (from  $Y = 0.6$  to  $25.6 \text{ cm}$ ) at each of three streamwise (X) locations ( $X/D = 10, 20$  and  $30$ ). X, Y and Z are the streamwise, normal to the plate, and widthwise directions, respectively (Figure 3.2). Tests were repeated at three different free-stream velocities,  $4.5, 5.5$  and  $6.5 \text{ m/s}$ . Reynolds numbers at the end of the flat plate ( $Re_L$ ) at these velocities were  $1.5 \times 10^5, 1.9 \times 10^5$  and  $2.2 \times 10^5$ , respectively, which indicates that at all of these velocities, the flow over an ideal smooth flat plate would be laminar [32].

#### 3.3.1. Studied Parameters

Local velocity is the time average of the instantaneous velocities at that point [33]:

$$U = \frac{1}{N} \sum_{i=1}^N U_i \quad (3.1)$$

where  $N$  is the number of instantaneous measurements ( $N = 2 \times 10^6$ ).

Turbulence intensity is defined as the normalized standard deviation, or root-mean-square (rms), of the velocity fluctuations [33]:

$$Tu = \frac{u'}{U_\infty} \quad (3.2)$$

where  $U_\infty$  is the free stream velocity; and  $u'$  is calculated from [33]:

$$u' = \sqrt{\sum_{i=1}^N \frac{(u_i)^2}{N-1}} \quad (3.3)$$

where  $u_i$  is the velocity fluctuation, which is the deviation of the instantaneous from the time-averaged velocity.

The normalized third moment of the velocity fluctuations is the skewness factor [34]:

$$S = \frac{\overline{u^3}}{u'^3} \quad (3.4)$$

This factor is an indication of the symmetrical distribution of the turbulence velocities ( $u$ ) or the symmetry in the probability density function (PDF). A perfectly symmetrical distribution of  $u$  gives  $S = 0$ .

It has been shown that isotropic turbulence has a PDF close to Gaussian [35]. Flatness factor is an indicator to measure how close a distribution is to the perfectly random Gaussian one [34]:

$$F \equiv \frac{\overline{u^4}}{u'^4} \quad (3.5)$$

For a true Gaussian PDF the flatness factor is 3 [34].

The integral length scale and Taylor micro-scale have been derived from the Eulerian autocorrelation function between turbulence velocity fluctuations [7]:

$$R(\tau) \equiv \frac{\overline{u(t)u(t')}}{u'^2} \quad (3.6)$$

where  $\tau = t' - t$ . In discrete form it would be:

$$R(m\Delta t) \equiv \frac{\frac{1}{N-1} \sum_{i=1}^{N-m} u_i u_{i+m}}{\frac{1}{N} \sum_{i=1}^N u_i^2}, \quad 0 < m < N \quad (3.7)$$



Based on Taylor's frozen hypothesis, if the velocity fluctuations are small compared to the flow velocity which carries eddies, the spatial rates could be approximated from the measured temporal rates as follows [36]:

$$\frac{\partial}{\partial t} = -U_c \frac{\partial}{\partial x} \quad (3.8)$$

where  $U_c$  is the convection velocity or the velocity at which flow is convected. There has been much discussion on the validity of Taylor's hypothesis in the turbulent boundary layer [37-39]. It has been shown that Taylor's approximation could be applied to a turbulent boundary layer by approximating the local mean velocity as the convection velocity [37].

The integral time scale is the integral of the autocorrelation function during the time [7]:

$$\tau_\Lambda = \int_0^\infty R(\tau) d\tau \quad (3.9)$$

Integration was truncated when  $R(\tau)$  crosses zero (the first time it becomes negative). Beyond the first zero crossing, the  $\tau_\Lambda$  value is not physically reliable [40]. The integral time scale for discrete samples is:

$$\tau_\Lambda = \frac{\frac{1}{N-m} \sum_{i=1}^{N-m} u_i u_{i+m}}{\frac{1}{N} \sum_{i=1}^N u_i^2}, \quad 0 < m < N \quad (3.10)$$

The integral length scale, which indicates the measure of the correlation distance between the velocities at two points of the flow field, could be deduced as [7]:

$$\Lambda = U \cdot \tau_\Lambda \quad (3.11)$$

The Taylor time scales ( $\tau_\lambda$ ) are derived from the intersection of a parabola, fitted to the first three to five points of the correlation curve, with the  $\tau$ -axis. Taylor length scales are then calculated as follows [7]:

$$\lambda = U \cdot \tau_\lambda \quad (3.12)$$

### 3.4. Results and Discussion

#### 3.4.1. Velocity Profile

Figure 3.3 shows the velocity profiles at three different downstream distances and velocities with the perforated plate (grid) positioned at 11 cm height. A second Y axis on the right side of the graphs is the dimensionless distance in the normal direction ( $Y/H$ ). As can be seen, the perforated plate causes the flow to be retarded such that the velocity downstream of the plate is approximately one half the free stream velocity. Two boundary layers can be distinguished in these profiles: one is next to the flat plate surface and the other is at the perforated plate edge. The growth of these boundary layers' thicknesses with downstream distance can also be observed in these graphs (dotted lines in Figure 3.3 (a)). The wall boundary layer thickness grows from around 1.6 to 3.2 cm.

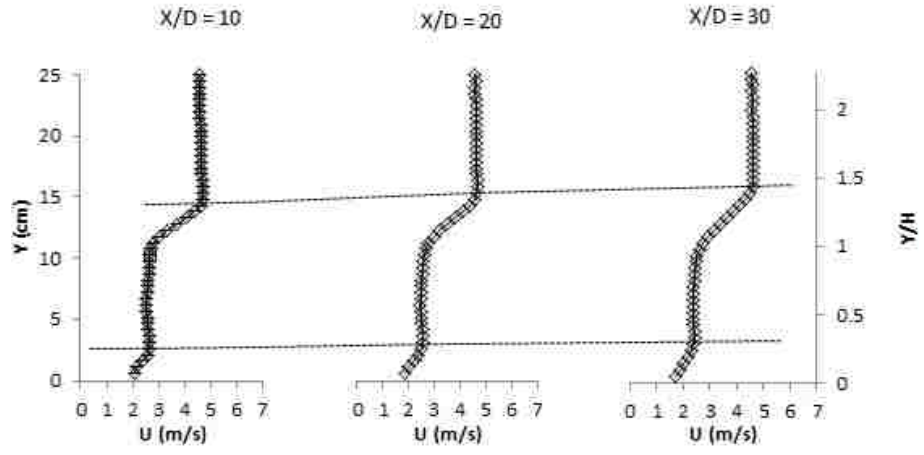
Compared with the laminar boundary layer thickness predicted by the Blasius equation and also the turbulent boundary layer predicted by Prandtl using the one-seventh power law [41], the wall boundary layer in this study is observed to be thicker. For example, for  $X/D = 20$  and  $U_\infty = 5.5$  m/s, it can be seen in Figure 3.3 (b) that the boundary layer thickness is around 2.63 cm which is which is around 5.5 times thicker than the predicted laminar boundary layer thickness (0.45 cm) and 2.8 times thicker than the predicted turbulent boundary layer (0.91 cm). Even if one considers the velocities at  $Y = 5 - 10$  cm to be the free stream velocities for calculation purposes, the prediction is still low. For example, considering new lower velocities (for  $X/D = 20$  and  $U_\infty = 5.5$  m/s the blocked velocity above the plate is around 2.8 m/s) in calculations, laminar (0.63 cm) and turbulent boundary layer thicknesses (1 cm) are still lower than that which has been observed (2.63 cm). The jet/wake flow and/or the increased flow turbulence caused by the grid appear to cause some thickening of the boundary layer over the flat plate [42, 43]. As mentioned before, at larger downstream distances, the grid's edge boundary layer thickens and the velocity gradient decreases, causing the flow to reach the free stream velocity more gradually. The same trend has been observed in the wind tunnel study by Judd et al. [30] on the flow around a windbreak.

It is also worth noting that by considering the blockage effect of the flat plate and perforated plate in the wind tunnel (around 10%), it is expected that the free stream velocity above the perforated plate to be higher than the incoming free stream upstream of the perforated plate [30]. The pressure measurements before and after the perforated plate also confirm this. As it can be seen in Figure 3.4, the dynamic pressure ( $\rho U_\infty^2/2$ ) above the perforated plate increased compared with the area upstream of the perforated plate. The pressure at different points in the normal ( $Y$ ) direction upstream and downstream of the perforated plate is measured by a Pitot tube.

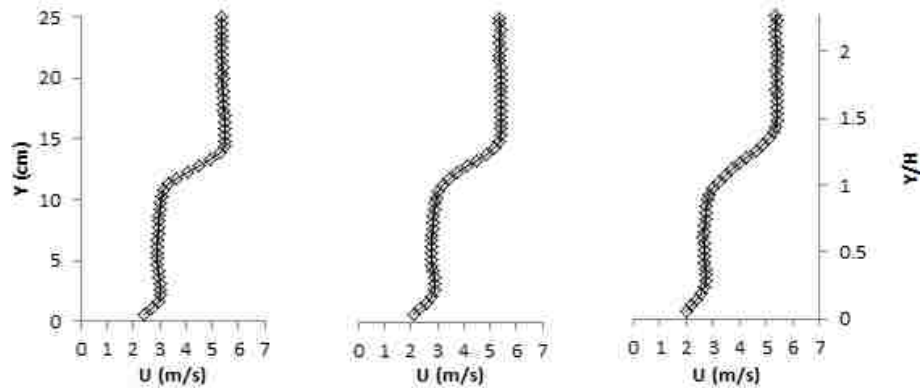
Also, it seems that the velocity has a local maximum value near the edge of the wall boundary layer and after that it decreases. This phenomenon is attributed to the Richardson annular effect, which is caused by the pressure oscillations due to a perforated plate. This effect would cause an overshoot in near-wall velocity [44].

Comparing Figures 3.3 (a), (b) and (c), it can be observed that the difference between the velocity behind the perforated plate and that in the free stream is greater at higher velocities, which indicates that the flow is routed around the perforated plate more at higher velocities. This might be due to higher flow resistance or friction through the perforated plate at higher velocities [45].

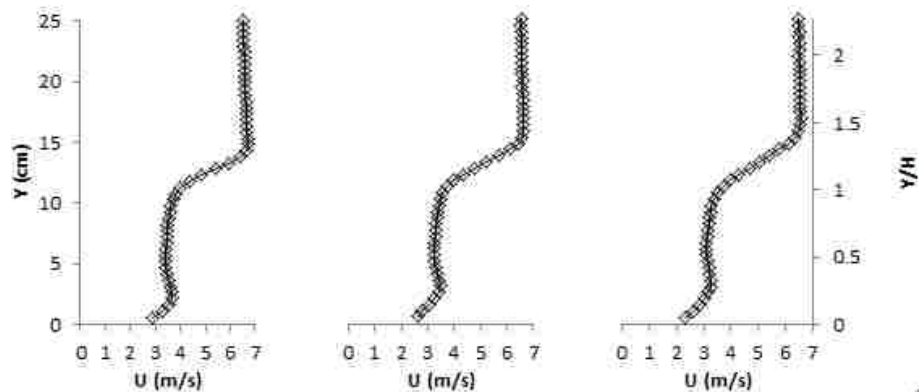
Many velocity measurements other than that at the centerline had been acquired to check the development of the flow downstream of the grid. These are not shown, but indicate that the flow is homogenous across the plate, in the range of studied conditions.



(a)



(b)



(c)

Figure 3.3 Velocity profiles at  $H = 11$  cm and (a) 4.5 m/s (b) 5.5 m/s (c) 6.5 m/s free stream velocity

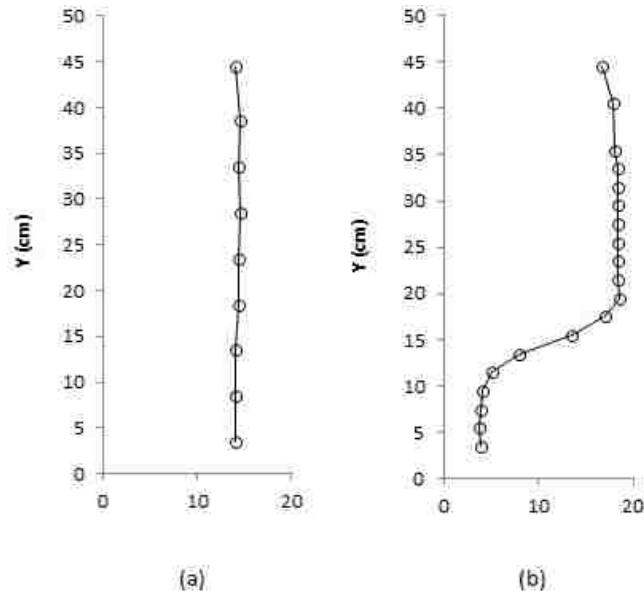


Figure 3.4 Dynamic pressure profiles at  $H = 11$  cm (a) upstream of the grid (b) downstream of the grid

The total uncertainty associated with each parameter consists of bias and precision uncertainties [33, 46] and are shown as error bars for a single point in the graphs. Bias or systematic uncertainty of the hotwire-measured instantaneous velocities has been calculated using information available in Ref. [33]. Bias in other parameters has been determined from the instantaneous velocity bias. Precision uncertainty, which concerns the repeatability of the test, has been derived from the Student's  $t$  distribution method with a 95% confidence interval [46]. The uncertainty in velocity at point  $Y=9.2$  cm in Figure 3.3 (a) (4.5 m/s free stream velocity and  $X/D = 10$ ) is estimated to be around  $\pm 0.3$  m/s, which is mostly because of the precision uncertainty. In addition, the uncertainty in position in the normal direction ( $Y$ ) of the hot-wire is estimated to be around 2 mm.

Lowering the height of the perforated plate lowers the shear layer boundary layer as shown in Figure 3.5. It can be seen from the figure that the retardation of flow near the flat plate surface (wall) increases with decreasing grid height but the flow resumes the free stream velocity at a much lower height from the plate. In terms of cooling a PV panel, a higher surface velocity is preferred, which occurs at higher perforated plate heights. But velocity is not the only parameter affecting the rate of heat transfer; other items such as turbulence intensity and shear should also be considered. The graphs in Figure 3.5 show how much the perforated plate's height has an inverse relationship with the wall boundary layer thickness. Examining Figure 3.5 (a), at  $H = 11$  cm two distinct boundary layers are visible, with the wall boundary layer reaching a height of 1.6 cm. When  $H$  was lowered to 7 cm, the wall boundary layer thickness increased to 5.1 cm, and the wall and grid boundary layers remained separate but close together. When the grid was lowered further to 3 cm, there was only one boundary layer visible, which reached a height of 5.7 cm. It is likely that at the lowest grid height, the two boundary layers merged into something like a single boundary layer. However, at greater grid heights, there was still an influence of the grid boundary layer on the wall boundary layer.

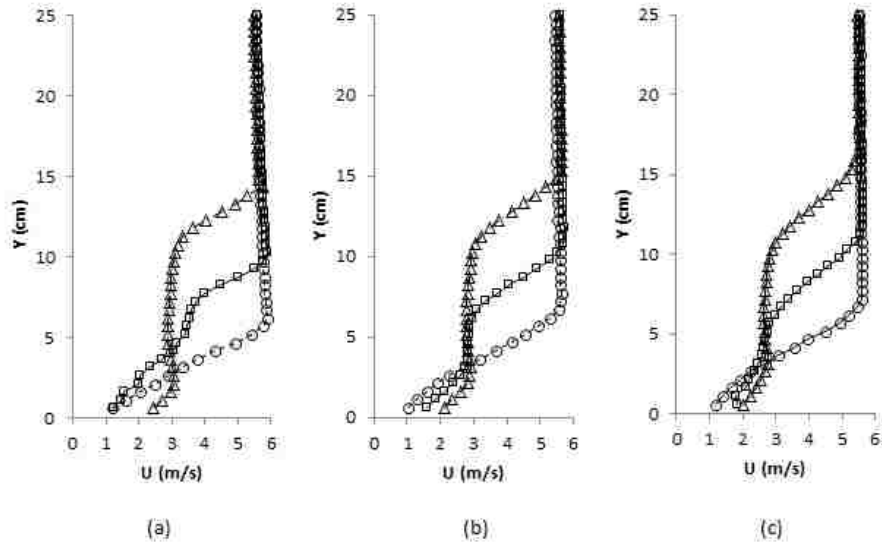


Figure 3.5 Velocity profiles for different heights of perforated plate, 5.5 m/s free stream velocity and (a)  $X/D = 10$  (b)  $X/D = 20$  (c)  $X/D = 30$ . The circles signify  $H = 3$  cm, the squares  $H = 7$  cm, and the triangles  $H = 11$  cm

### 3.4.2. Turbulence Intensity

Other than flow velocity, turbulence intensity is other key parameter dictating convection heat transfer rate. The local turbulence intensity is an indicator of the amount of turbulent kinetic energy available for enhancing energy transport. In Figure 3.6, the variations of  $Tu$  with downstream distance for the case of  $H = 11$  cm are shown.

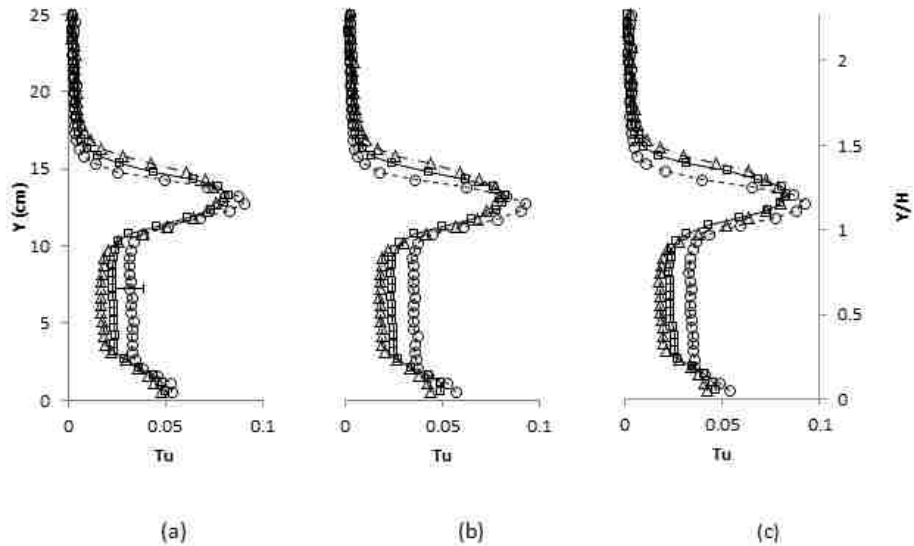


Figure 3.6 Turbulence intensity for  $H = 11$  cm at (a) 4.5 m/s (b) 5.5 m/s (c) 6.5 m/s free stream velocity. The circles signify  $X/D = 10$ , the squares  $X/D = 20$ , and the triangles  $X/D = 30$

As it can be clearly seen in these graphs, turbulence intensity adjacent to the flat plate surface is around 5% and decreases through the normal distance from the wall. Generally, in wall-bounded turbulent flows, the root mean square (rms) of the velocity fluctuations ( $u'$ ) has a peak value close to the wall. This peak has been reported to be at around  $Y^+ = 15$  (which would be around  $Y = 0.7$  cm in this study) [47], and at a  $Y/\delta^*$  value around 1.3 to 1.5 ( $Y = 0.7$  to 1.5 cm in the case shown) [48, 49], where  $\delta^*$  is the boundary layer displacement thickness, which is around  $\delta/3$  [41]. In our study, the characteristic, nearly parabolic shape of  $Tu$  as a function of  $Y$  was not observed clearly in the turbulence intensity plots [47]. This is mostly due to the limitation in our measurements, which were no closer than 6 mm to the flat plate, or due the interaction between the effects of the perforated plate and the wall, which caused the boundary layer to behave in a different way than simple wall-bounded turbulence. Above the wall boundary layer, turbulence intensity approached a nearly constant value of less than 4% until the edge of the perforated plate. At this point, turbulence intensity increased drastically to a value around 10% and then decreased with almost the same slope to the free stream turbulence intensity ( $\sim 0.4\%$ ). By comparing these plots to the velocity profiles (Figure 3.3), it can be seen that the turbulence intensity increase happened at the beginning of the perforated plate edge's boundary layer ( $Y = 10.7$  cm), reached a peak at  $Y = 12.8$  cm, and approached the free stream's  $Tu$  at the end of the grid boundary layer. The mentioned trend demonstrates the high degree of turbulence that was caused by the edge of the perforated plate. The growth of the shear boundary layers' thickness with downstream distance can also be easily seen by comparing the different symbols in a given plot. Furthermore, a general tendency of decreasing  $Tu$  with distance from the perforated plate is observed for the area behind the grid (until  $Y = 11$  cm) which indicates the decay of the turbulence kinetic energy in this area [48]. However, this conclusion may not be accurate for  $X/D = 20$  to 30 since the change in  $Tu$  was of the same order as the uncertainty. The uncertainty for a specific point ( $Y = 7.2$  cm) is shown in Figure 3.6 (a), which is around  $\pm 0.7\%$   $Tu$ .

In addition, it can be observed that in spite of increasing the velocity, the normalized turbulence intensity ( $Tu$ ) remained almost constant. This shows that increasing the free stream velocity leads to a proportional increase in the value of the root-mean-square of the velocity fluctuations ( $u'$ ). This phenomenon can be seen more clearly in Figure 3.7, where the  $Tu$  values at three different velocities are shown for  $X/D = 20$ . The superposition of these curves clearly depicts the self-similarity of the turbulence intensity profile with respect to the range of tested velocities.

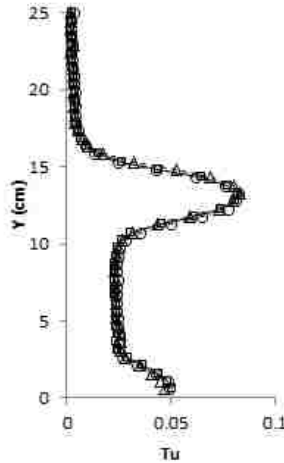


Figure 3.7 Turbulence intensity for  $X/D = 20$  and different free stream velocities. The circles signify  $U_\infty = 4.5$  m/s, the squares  $U_\infty = 5.5$  m/s, and the triangles  $U_\infty = 6.5$  m/s

The effect of the perforated plate's height on turbulence intensity at different downstream distances is portrayed in Figure 3.8. It can be seen that the  $Tu$ , at the point measured closest to the surface of the wall, gradually increased by decreasing the grid's height. This seems to show that at lower heights of the perforated plate, disturbances caused by its edge would interact with the flow over the flat plate surface and cause the turbulence intensity to be higher close to the plate. This might explain the lower velocities on the wall surface for the two lower grid heights compared with  $H = 11$  cm (Figure 3.5); the greater disturbance in the flow at the plate surface at these two lower grid heights may have caused the overall velocity in the  $X$  direction to be lower. In terms of PV panel cooling, it remains to be seen if the effect of higher  $Tu$  at lower heights will overcome the effect of lower velocity near the surface. The verdict of the best height is yet to be determined. It was also observed that the maximum turbulence intensity caused by the edge of the perforated plate is higher and closer to the surface at  $H = 3$  and  $7$  cm than at  $11$  cm. Another important observation is the number of peak values of turbulence intensities inside the boundary layers: two peaks in two boundary layers (wall and grid) can be distinguished for  $H = 7$  cm (for  $X/D = 10$  and  $20$  they can be seen clearly) and  $H = 11$  cm, while for  $H = 3$  cm, just one peak with its single boundary layer can be observed. This further confirms the mingling of disturbances into a single boundary layer for the lowest  $H$  case.

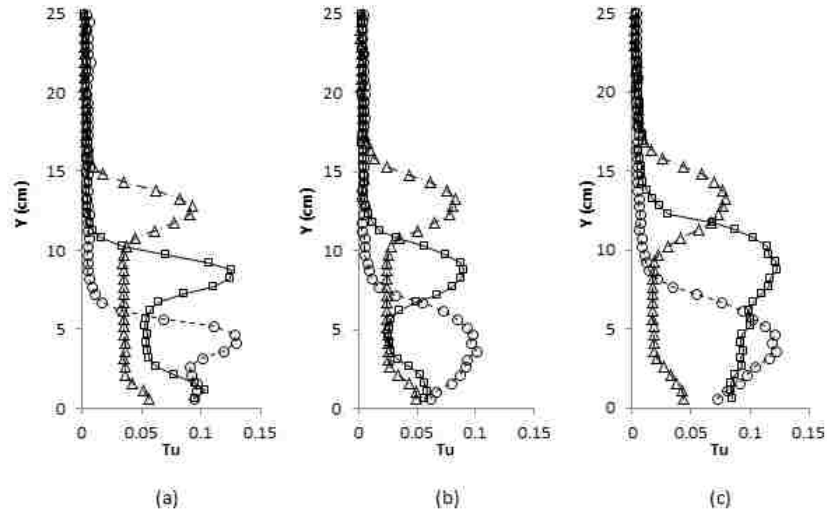


Figure 3.8 Turbulence intensity for different heights of perforated plate, 5.5 m/s free stream velocity and (a)  $X/D = 10$  (b)  $X/D = 20$  (c)  $X/D = 30$ , The circles signify  $H = 3$  cm, the squares  $H = 7$  cm, and the triangles  $H = 11$  cm

The trend of  $Tu$  with downstream distance was also studied for all grid heights (Figure 3.9). It is noted that no specific decreasing trend in  $Tu$  with downstream distance is distinguished for the two lower heights over the range of studied conditions. In fact, for  $H = 7$  cm a significant increase from  $X/D = 10$  to 30 can be observed. Maintaining a high level of turbulence over the surface of a solar PV panel would be advantageous in terms of enhanced convective cooling over the entire panel's row.

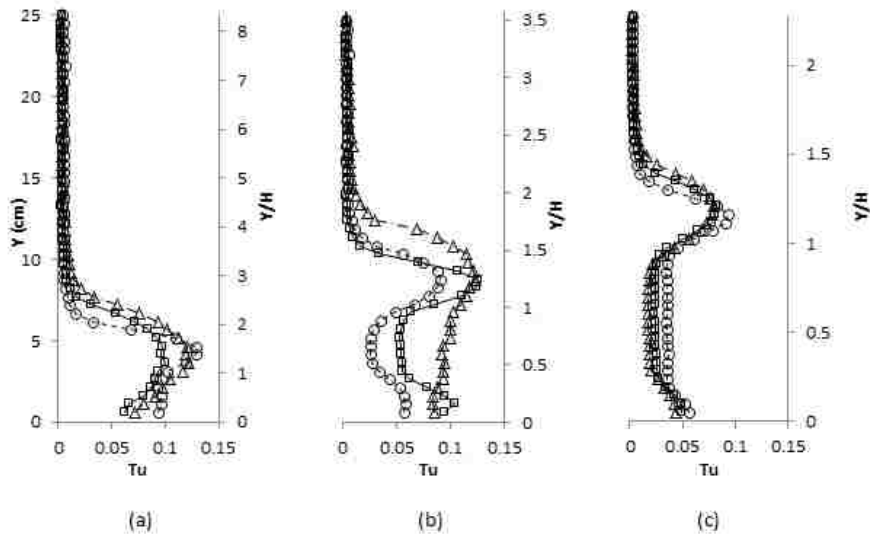


Figure 3.9 Turbulence intensity at different downstream distances, 5.5 m/s free stream velocity and (a)  $H = 3$  cm (b)  $H = 7$  cm (c)  $H = 11$  cm. The circles signify  $X/D = 10$ , the squares  $X/D = 20$ , and the triangles  $X/D = 30$



### 3.4.3. Turbulence Higher Moments (Skewness and Flatness Factors)

To have a better understanding of the turbulence in the domain behind the grid and also a better view of the effect of grid height on the distribution of the turbulence velocities, skewness and flatness factors have been analyzed in this section. Figure 3.10 shows the skewness factors for turbulence velocities after the perforated plate with  $H = 11$  cm at different velocities and downstream distances. As can be seen, near the plate surface ( $Y = 0.6$  cm), this factor was zero but when it became close to the edge of the boundary layer it deviated from zero to a negative peak value. The reason behind this is the interference of free stream fluid into the boundary layer, which results in a negatively skewed intermittently turbulent signal near the edge of the boundary layer with a high flatness (will be seen in Figure 3.14) [50]. In the area between the two boundary layers, the skewness factor was zero, which shows that the grid turbulence distribution is symmetrical. There were also two peak points above  $Y = 10$  cm, one positive and one negative, which were situated at the lower and upper extents of the grid edge's boundary layer respectively. At these two points the distribution of the turbulence fluctuation was very asymmetric. From the turbulence intensity graphs (Figure 3.6), it can be seen that at these two skewness peak points,  $Tu$  was at a minimum while in between these peak points at  $Y = 12.8$  cm where  $S = 0$ ,  $Tu$  had its highest value. In the free stream region - above the area which is under the effect of the edge - it can be observed that the skewness factor was close to zero but with significant variation. This is because there was very little turbulence in the free stream (around 0.4%) and hence the skewness factor was sensitive to minute changes in velocity distribution. In other words, there is little meaning associated with the magnitude or sign of the skewness factor regarding the turbulence fluctuation distribution in that area.

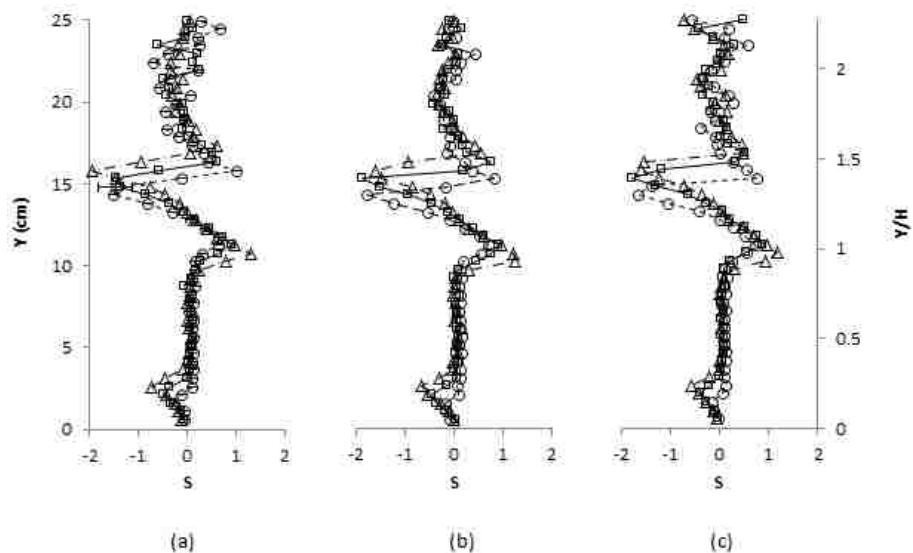


Figure 3.10 Skewness factor for  $H = 11$  cm at (a) 4.5 m/s (b) 5.5 m/s (c) 6.5 m/s free stream velocity. The circles signify  $X/D = 10$ , the squares  $X/D = 20$ , and the triangles  $X/D = 30$

The sign of the skewness factor in a sufficiently turbulent flow field such as that below the grid shear layer depicts the general tendency of the velocity fluctuations: whether they are in the positive or negative direction. To demonstrate this, the  $u$ - $t$  graph at the two peak points ( $Y = 10.8$  and  $15.8$  cm) and one point where  $S = 0$  ( $Y = 5.8$  cm) for 1 s duration were plotted in Figure 3.11. Figure 3.11 (a) shows the fluctuating velocity time trace for  $Y = 10.8$  cm where  $S$  was equal to  $+1.28$ . As can be seen, most of the large fluctuations were on the positive side. Figure 3.11 (b) presents the velocity fluctuations for the point  $Y = 15.8$  cm where the skewness factor was equal to  $-1.95$ . In this graph it can be seen that turbulence velocities were skewed to negative values. So in this region, the sign of  $S$  indicates the direction of the largest velocity fluctuations while the magnitude of  $S$  shows the degree of asymmetry in the distribution of the fluctuations. Figure 3.11 (c) portrays the turbulence velocities through time for the point  $Y = 5.8$  cm where the skewness factor was zero. It can be seen that turbulence velocities are distributed evenly around the zero value.

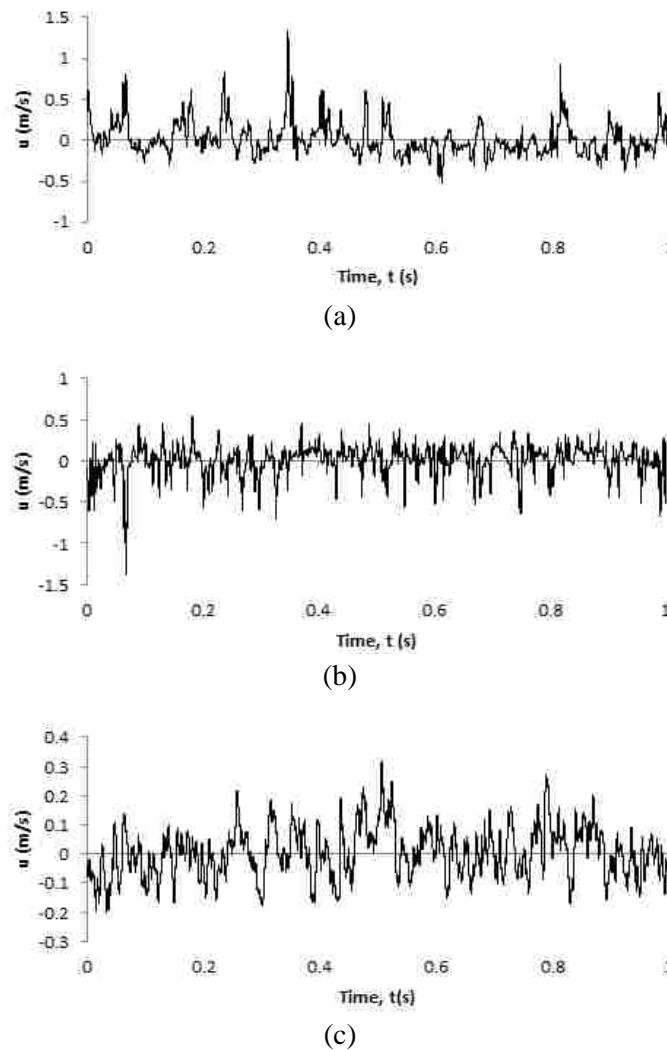


Figure 3.11 Velocity fluctuation vs. Time for  $H = 11$  cm,  $U_\infty = 4.5$  m/s,  $X/D = 30$  and points (a)  $Y = 10.8$  cm,  $S = 1.28$  (b)  $Y = 15.8$  cm,  $S = -1.95$  (c)  $Y = 5.2$  cm,  $S = 0$

Flatness factors for the grid height of 11 cm and three different velocities and downstream distances are shown in Figure 3.12. As can be seen, the flatness factor was equal to 3 near the plate surface and was somewhat greater than 3 as it went through the wall boundary layer edge. Above this region it resumed a value of 3 until the beginning of the shear boundary layer. At the edge of grid shear boundary layer, it exhibited a peak value of approximate 16 to 18. This indicates that in the area behind the grid, the velocity fluctuation had a Gaussian distribution, confirming the near-isotropic turbulence behind the perforated plate. At the beginning and end of the shear boundary layer,  $F$  had peaks; but at the middle of the boundary layer it had values around 3. This shows that the isotropy level decreased at the starting and ending points of the boundary layer. The same trend has been seen in skewness factor diagrams, but because flatness factor is an even-numbered power of the turbulence velocity, the  $F$  peaks all have positive signs. Above that, in the free stream, the flatness factor approached 3 but still deviated from 3 at some points. However, the turbulence level in the free stream was very low, so insignificant fluctuations in turbulence quantities were accentuated when the fourth moment is calculated. These graphs indicate that in the region behind the grid, turbulence was already isotropic from  $X/D = 10$  and the isotropy level does not change significantly downstream. It can be seen in these graphs that the deviation from 3 at the edge of the perforated plate decreased as the flow moved downstream but these differences may be insignificant when uncertainties are taken into account.

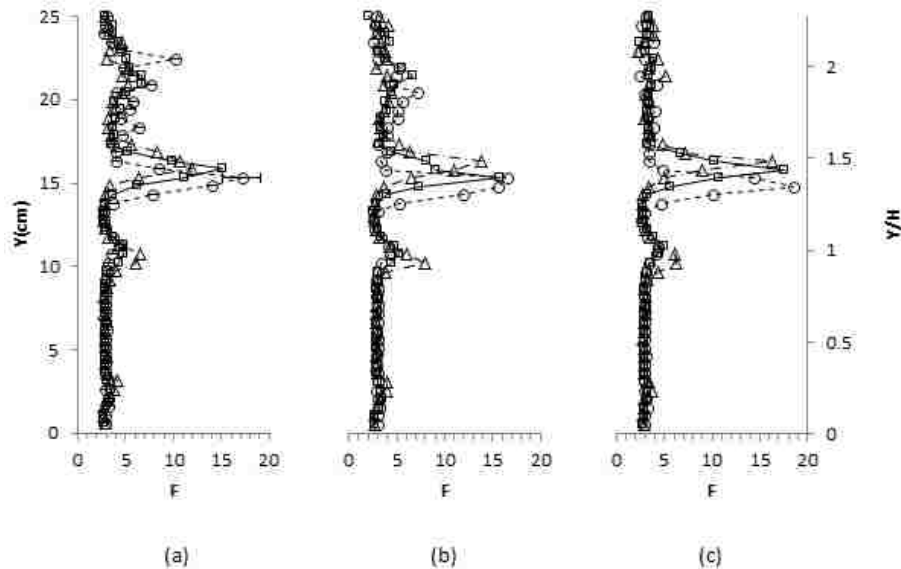


Figure 3.12 Flatness factors for  $H = 11$  cm at (a) 4.5 m/s (b) 5.5 m/s (c) 6.5 m/s free stream velocity. The circles signify  $X/D = 10$ , the squares  $X/D = 20$ , and the triangles  $X/D = 30$

Skewness and flatness factors for other grid heights also were studied but the results are not shown in the figures. For  $H = 7$  cm, the same trend as at  $H = 11$  cm was observed for skewness factor. In terms of flatness factor, there were two peaks: a first at the beginning point of the grid boundary

layer (or the edge of the wall boundary layer, because at some point they merged together) and a second one at the end of the grid boundary layer. For  $H = 3$  cm, one negative peak in skewness factor and one positive peak in flatness factor was seen at the edge of its single boundary layer ( $Y = 6.2$  to  $7.7$  cm). It is also worth noting that as the height of the grid decreased, the skewness factor on the wall surface tended to increase. This might be again because of the interference of the free stream with the flow near the wall surface, which restricted velocity fluctuations in one direction while augmenting them in another.

### 3.4.4. Turbulence Length Scales

Other than the fluctuating intensity, studies [51-53] have shown the importance of turbulent length scales in momentum and heat transportation. It is expected the turbulent length scale that is of the same order of magnitude as the corresponding existing sizes are most likely coupled. In the case of flow over a flat plate, the boundary layer thickness would be a likely candidate. For a solar PV panel, another likely candidate is the thermal boundary layer thickness. At the larger end, the width and length of the PV panel under consideration would also be other important characteristic lengths. The key turbulent length scales are not easily deducible. As a first step, the large and a small turbulent length scales were estimated. It is a common practice to pick the integral length scale to represent the large scale and the Taylor micro-scale to represent the smaller, dissipative eddies.

A sample of autocorrelation functions are presented in Figure 3.13. As can be seen, the area underneath the  $R(\tau)$  increased with the downstream distance, indicating increasing integral time and length scales. The parabola fitted to the first five points of the  $X/D = 10$  correlation curve can be seen. As was mentioned before, the Taylor time scale ( $\tau_\lambda$ ) is obtained from the intersection of the fitted curve with the  $\tau$ -axis. As can be seen in this figure, at higher distances from the grid, the  $R(\tau)$  curve at  $\tau = 0$  would be flatter, which indicates that  $\tau_\lambda$  would increase.

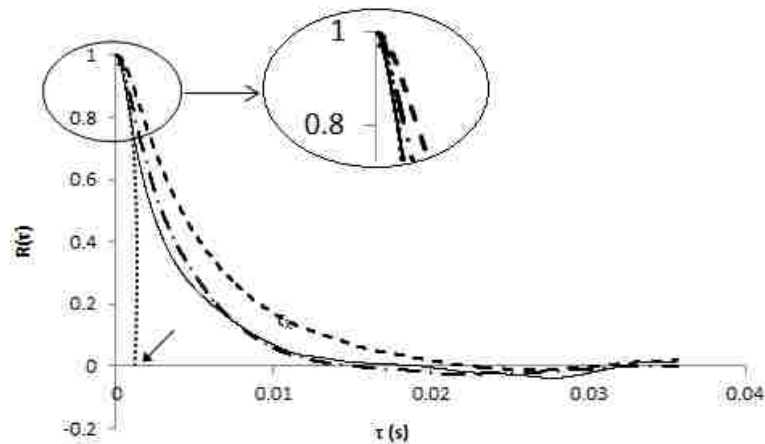


Figure 3.13 Autocorrelation coefficient for  $H = 11$  cm,  $Y = 5.5$  cm and  $U_\infty = 4.5$  m/s, solid line (—) signifies  $X/D = 10$ , dash dot (— · —)  $X/D = 20$ , dash (— —)  $X/D = 30$  and round dot (·····) the parabola fitted curve to the first five points of  $R(\tau)$  at  $X/D = 10$

In Figure 3.14, the Taylor micro scales for  $H = 11$  cm and  $U_\infty = 5.5$  m/s for different free stream distances are shown. A general trend of increasing Taylor micro scales with streamwise distance was observed at all tested velocities, although the estimated uncertainty (error bars) is relatively large which precludes a statistically significant trend for all studied cases. Nevertheless, it can be seen that for  $H = 11$  cm in the area behind the grid, Taylor micro scales increased with downstream distance (average values were 0.36, 0.46 and 0.53 cm for  $X/D = 10, 20$  and  $30$  respectively). This has been observed in conventional grid studies [9], signifying the decay of the turbulence.

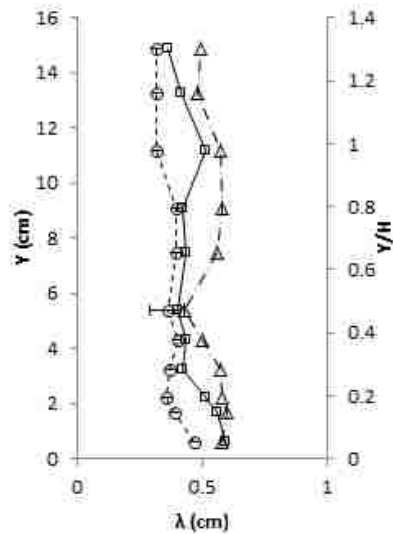


Figure 3.14 Taylor micro scale for  $H = 11$  cm and  $U_\infty = 5.5$  m/s. The circles signify  $X/D = 10$ , the squares  $X/D = 20$ , and the triangles  $X/D = 30$

Figure 3.15 shows the Taylor micro scale profile at  $U_\infty = 5.5$  m/s for different grid heights. The general trend of increasing eddy size with decreasing grid height was observed for  $H = 11$  cm. For  $H = 7$  cm and especially  $H = 3$  cm, there are large fluctuation in the Taylor micro scale which make it difficult to draw conclusions about the effect of grid height.

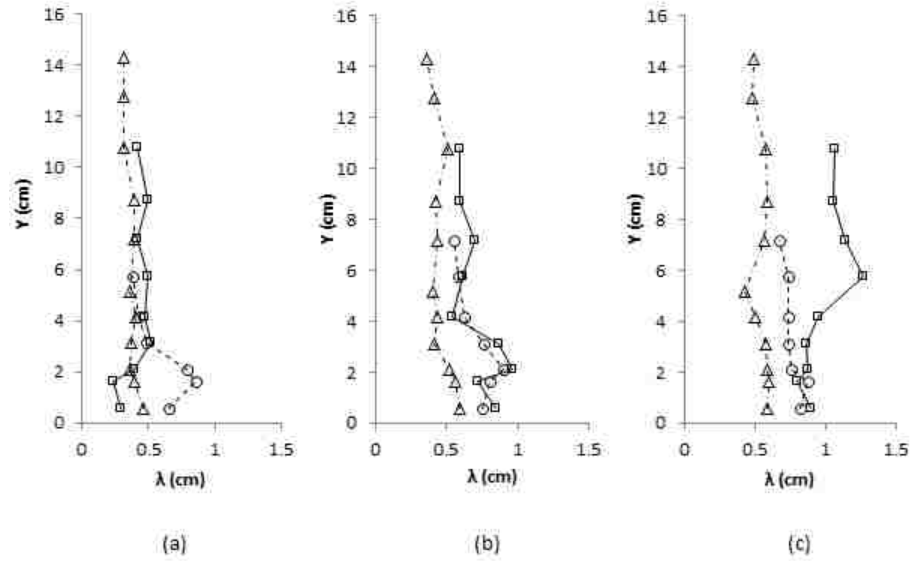


Figure 3.15 Taylor micro scale for different perforated plate's height and 5.5 m/s free stream velocity and at (a)  $X/D = 10$  (b)  $X/D = 20$  (c)  $X/D = 30$ . The circles signify  $H = 3$  cm, the squares  $H = 7$  cm, and the triangles  $H = 11$  cm

Figure 3.16 presents the integral length scale profile at different downstream distances. The calculation for a specific point was shown in Figure 3.13. At all velocities, the integral time and hence length scale increased with distance downstream of the plate (Figure 3.16). It has to be mentioned that the uncertainty in integral length scale value was around 0.3 cm. Furthermore, values of length scales above the shear layer were ill-defined since the free stream has little turbulence. The trend of increasing  $\Lambda$  with downstream distance has also been observed in conventional grid turbulence [9]. As can be seen in Figure 3.16, the integral length scale had higher values near the wall. For ideal wall turbulence, the integral length scale should have a peak value near the wall at  $Y/\delta = 0.2$  [40]. This peak was not observed in all plots in this figure, which might be because of the interference of the wall and grid turbulence and/or the fact that measurements could not be made closer than  $Y = 0.6$  cm ( $Y/\delta = 0.38$  to  $0.19$ ) to the flat plate. Nevertheless, the higher amount of  $\Lambda$  at the wall surface and the decreasing trend through the boundary layer edge was consistently observed.

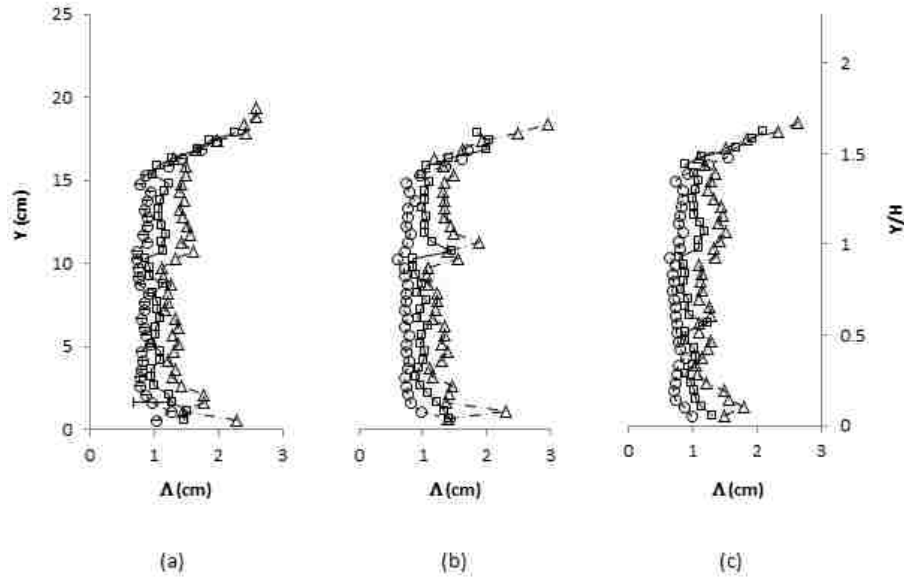


Figure 3.16 Integral length scale for  $H = 11$  cm and (a) 4.5 m/s (b) 5.5 m/s (c) 6.5 m/s free stream velocity. The circles signify  $X/D = 10$ , the squares  $X/D = 20$ , and the triangles  $X/D = 30$

Figure 3.17 compares the integral length scales for different perforated plate heights. A general tendency of decreasing integral length scales with decreasing height of the perforated plate was observed for  $H = 11$  cm and 7 cm at  $X/D = 20$  and 30. For  $H = 3$  cm, no general trend was observed. For all grid heights,  $\Lambda$  was generally higher at the wall surface and decreased through the wall boundary layer edge. Beyond the upper grid boundary layer, it increased to a very large value as expected.

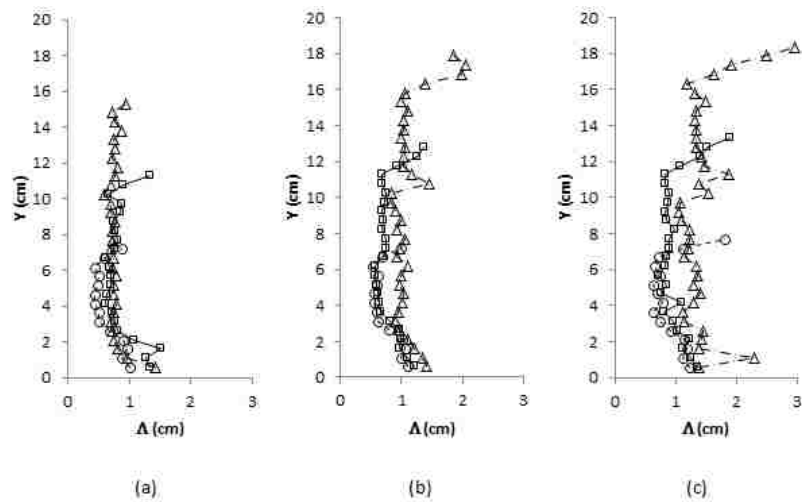


Figure 3.17 Integral length scale for different perforated plate's height and 6.5 m/s free stream velocity and at (a)  $X/D = 10$  (b)  $X/D = 20$  (c)  $X/D = 30$ . The circles signify  $H = 3$  cm, the squares  $H = 7$  cm, and the triangles  $H = 11$  cm

Figure 3.18 depicts the variation of the integral length scale along the normal (vertical) direction to the flat plate for different velocities. It can be seen that increasing the velocity from 4.5 to 6.5 m/s had an insignificant effect on the integral length scale. This indicated self-similarity over the range of velocities (Reynolds numbers) considered in these experiments. In the presence of the perforated plate, the flow was consistently fully developed turbulent, and the results seem to have indicated that the integral length scale was not affected by the velocity, but presumably by the size of the mesh.

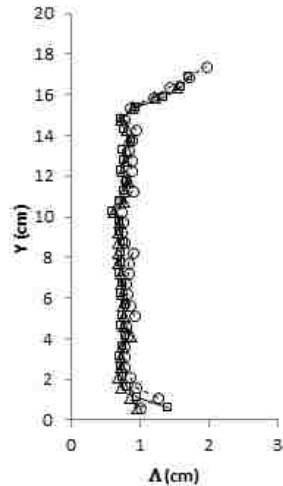


Figure 3.18 Integral length scale for  $H = 11$  cm at  $X/D = 10$  and different free stream velocities. The circles signify  $U_\infty = 4.5$  m/s, the squares  $U_\infty = 5.5$  m/s, and the triangles  $U_\infty = 6.5$  m/s

### 3.5. Conclusion

Flow over a flat plate downstream of a perforated plate with a finite height has been analyzed as the first phase of enhancing the heat transfer rate from a PV panel's surface. Two boundary layers have been distinguished in the velocity profiles: one next to the flat plate surface and another one around the upper edge of the perforated plate. The perforated plate's height was varied ( $H = 11, 7$  and  $3$  cm), and different turbulence parameters were studied. It has been observed that for a grid height of  $11$  cm, the turbulence at the region behind the grid behaved as for conventional grid turbulence; from  $X/D = 10$ , turbulence seemed to be isotropic and  $Tu$  decreased and turbulence length scales increased with downstream distance, which showed that the turbulence was decaying. The two other heights did not exhibit the same trend in their turbulence intensities, which have been observed to increase with downstream distance at some points. This shows that due to interference of the flow over the edge of the finite height grid, the turbulence was not in its continuous decaying mode as was the case for  $H = 11$  cm. Also, the Taylor micro scale for  $H = 3$  cm in the region behind the grid (until  $Y \sim 3$  cm) decreased with downstream distance which is again an indication of turbulence generation in this region. Over the studied conditions, it may be said that short height turbulence generators can be utilized to enhance convection of heat from the PV panels. An optimum height along with decreased grid solidity ratio appears to be needed to



boost heat convection by creating higher turbulence without a significant reduction in near surface wind speed.

### ***Acknowledgment***

This work was made possible by the Ontario Trillium Foundation and the Natural Sciences and Engineering Research Council of Canada.

### ***References***

- [1] Evans, D.L., and Florschuetz, L.W., 1977, "Cost studies on terrestrial photovoltaic power systems with sunlight concentration," *Solar Energy*, 19, pp. 255–262
- [2] Spectrolab, Inc., Sylmar, C.A., 1977, "Photovoltaic systems concept study: Final report," (ALO-2748-12) U.S. Dept. of Energy, Division of Solar Energy, Springfield, VA
- [3] Evans, D.L., 1981, "Simplified method for predicting photovoltaic array output," *Solar Energy* 27(6), pp. 555–560
- [4] Aste, N., Chiesa, G., and Verri, F., 2008, "Design, development and performance monitoring of a photovoltaic-thermal (PV/T) air collector," *Renewable Energy*, 33(5), pp. 914-927
- [5] Fouladi, F., Henshaw, P., and Ting, D. S-K., 2013, "Enhancing Smart Grid realisation with accurate prediction of photovoltaic performance based on weather forecast," *Int. J. Enviro. Studies*, 70(5), pp. 754-764
- [6] Taylor, G.I., 1935, "Statistical theory of turbulence," *Proc. R. Soc. London, Series A, Math. and Phys. Sci.*, 151, pp. 421–478
- [7] Hinze, J.O., 1975, *Turbulence*, 2nd edition, McGraw-Hill, New York, USA, ISBN 0-07-029037-7
- [8] Batchelor, G.K., 1948, "Energy decay and self-preserving correlation functions in isotropic turbulence," *Quart. Appl. Math.*, 6, pp. 97-116
- [9] Batchelor, G.K., and Townsend, A.A., 1948, "Decay of isotropic turbulence in the initial period," *Proc. R. Soc. London A.*, 193, pp. 539-558
- [10] Batchelor, G.K., and Townsend, A.A., 1948, "Decay of isotropic turbulence in the final period," *Proc. R. Soc. London A.*, 194, pp. 527-543
- [11] Grant, H. L., and Nisbet, I.C.T., 1957, "The inhomogeneity of grid turbulence," *J. Fluid Mech.*, 2(3), pp. 263-272
- [12] Grant, H.L., 1958, "The large eddies of turbulent motion," *J. Fluid Mech.*, 4(2), pp. 149-190
- [13] Uberoi, M.S., 1963, "Energy transfer in isotropic turbulence," *Phys. Fluids*, 6(8), pp. 1048-1056
- [14] Uberoi, M.S., Wallis, S., 1966, "Small axisymmetric contraction of grid turbulence," *J. Fluid Mech.*, 24(3), pp. 539-543

- [15] Comte-Bellot, G., and Corrsin, S., 1966, "The use of a contraction to improve the isotropy of grid-generated turbulence," *J. Fluid Mech.*, 25(4), pp. 657-682
- [16] Uberoi, M.S., and Wallis, S., 1967, "Effect of grid geometry on turbulence decay," *Phys. Fluids*, 10(6), pp. 1216-1222.
- [17] Van Atta, C.W., and Chen, R., 1968, "Correlation measurements in grid turbulence using digital harmonic analysis," *J. Fluid Mech.*, 34(3), pp. 497-515
- [18] Uberoi, M.S., and Wallis, S., 1969, "Spectra of grid turbulence," *Phys. Fluids*, 12(7), pp. 1355-1358
- [19] Van Atta, C.W., and Chen, R., 1969, "Measurements of spectral energy transfer in grid turbulence," *J. Fluid Mech.*, 38(4), pp. 743-763
- [20] Murzyn, F., and Bergey, M., 2005, "Experimental investigation of the grid-generated turbulence features in a free surface flow," *Exper. Thermal Fluid Sci.*, 29(8), pp. 925-935
- [21] Liu, R., Ting, D.S-K., and Checkel, M.D., 2007, "Constant Reynolds number turbulence downstream of an orificed perforated plate," *Exper. Thermal Fluid Sci.*, 31(8), pp. 897-908
- [22] Llor, A., 2011, "Langevin equation of big structure dynamics in turbulence: Landau's invariant in the decay of homogeneous isotropic turbulence," *Euro. J. Mechanics B/Fluids*, 30(5) pp. 480-504
- [23] Liberzon, A., Gurka, R., Sarathi, P., and Kopp, G.A., 2012, "Estimate of turbulent dissipation in a decaying grid turbulent flow," *Exper. Thermal Fluid Sci.*, 39, pp. 71-78
- [24] George, W.K., 2012, "Asymptotic effect of initial and upstream conditions on turbulence," *ASME J. Fluid Eng.*, 134(6), pp. 061203-1-27
- [25] Horender, S., 2013, "Turbulent flow downstream of a large solidity perforated plate: near-field characteristics of interacting jets," *Fluid Dyn. Res.*, 45(2), pp. 025501-1-22
- [26] Uberoi, M.S. and Wallis, S., 1967, "Effect of grid geometry on turbulence decay," *Phys. Fluids*, 10, pp. 1216-1224
- [27] Lavoie, P., Antonia, R.A., and Djenidi, L., 2004, "Effect of grid geometry on the scale-by-scale budget of decaying grid turbulence," *15th Australasian Fluid Mechanics Conference*, University of Sydney, Sydney, Australia
- [28] Liu, R., Ting, D.S-K., and Rankin, G.W., 2004, "On the generation of turbulence with a perforated plate," *Exper. Thermal Fluid Sci.*, 28(4), pp. 307-316
- [29] Liu, R., and Ting, D. S.-K., 2007, "Turbulent flow downstream of a perforated plate: sharp-edged orifice versus finite-thickness holes," *ASME J. Fluid Eng.* 129(9), pp. 1164-1171

- [30] Judd, M., Raupach, J.M.R., and Finnigan, J.J., 1996, "A wind tunnel study of turbulent flow around single and multiple windbreaks, Part I: Velocity Fields," *Boundary-Layer Meteorology*, 80, pp. 127-165
- [31] Arianmehr, I., Ting, D.S-K., and Ray, S., 2013, "Assisted turbulence convective heat transfer for cooling the photovoltaic cells," *Proceedings of the ASME 2013 summer Heat Transfer Conference*, Paper HT2013-17210, DOI:10.1115/HT2013-17210, Minneapolis, MN, USA
- [32] Incropera, F.P., and DeWitt, D.P., 1996, *Fundamentals of heat and mass transfer*, 3rd ed. John Wiley and Sons, New York, USA
- [33] Jørgensen, F. E., 2002, "How to measure turbulence with hot-wire anemometers - a practical guide," Dantec Dynamics
- [34] Ting, D. S. K., 2013, "Some basics of engineering flow turbulence," 2013, revised edition, Naomi Ting's Book, Windsor, Canada, ISBN: 978-0-9869355-3-4
- [35] Van Atta, C.W., and Chen, W.Y., 1969, "Measurements of spectral energy transfer in grid turbulence," *J. Fluid Mech.*, 38(4), pp. 43-763
- [36] Taylor, G.I., 1938, "The spectrum of turbulence," *Proc. R. Soc. London, Series A*, 164, pp. 476-490
- [37] Dennis D. J. C., and Nickels, T. B., 2008, "On the limitations of Taylor's hypothesis in constructing long structures in a turbulent boundary layer," *J. Fluid Mech.* 614, pp. 197-206
- [38] Lin, C.C., 1953, "On Taylor's hypothesis and the acceleration terms in the Navier-Stokes equation," *Quart. Appl. Math.*, 10, pp. 295-306
- [39] Lumley, J.L., 1965, "Interpretation of time spectra measured in high-intensity shear flows," *Phys. Fluids*, 8(6), pp. 1056-1062
- [40] Builtjes, P.J.H., 1975, "Determination of the Eulerian longitudinal integral length scale in a turbulent boundary layer," *Appl. Sci. Res.*, 31(5), pp. 397-399
- [41] White, F. M., 2003, *Fluid mechanics*, 5th edition, Mc Graw Hill, New York, USA, ISBN: 0-07-20217-2
- [42] Kline, S. J., Lestin, A.V., and Waitman, B. A., 1960, "Preliminary experimental investigation of effects of free-stream turbulence on turbulent boundary layer growth," NASA TN D-368
- [43] Evans, R. L., 1972, "Free stream turbulence effect on the turbulent boundary layer," Dep. Of Engineering, University of Cambridge, Report CUED/A Turbo/TR41
- [44] White, F., 1991, *Viscous Fluid Flow*, 2nd edition, McGraw-Hill, New York, USA, ISBN: 0071009957, 9780071009959
- [45] Vafai, K., and Tien, C. L., 1981, "Boundary and inertia effects on flow and heat transfer in porous," *Int. J. Heat Mass Transfer*, 24, pp. 195-203

- [46] Figliola, R.S., and Beasley, D.E., 2011, *Theory and Design for Mechanical Measurements*, 5th edition, John Wiley and Sons, Inc., New York, USA
- [47] Alfredsson, P.H., Örlü, R., and Segalini, A., 2012, “A new formulation for the streamwise turbulence intensity distribution in wall-bounded turbulent flows,” *Euro. J. Mechanics B/Fluids*, 36, pp. 167–175
- [48] Patten, N., Griffin, P., and Young, T.M., 2013, “Effects of freestream turbulence on the characteristics in the boundary layer near the transition onset location,” *ASME J. Fluid Eng.*, 135(7), pp. 071203-1-9
- [49] Westin, K. J. A., Bakchinov, A. A., Kozlov, V. V., and Alfredsson, P. H., 1998, “Experiments on localized disturbances in a flat plate boundary layer. Part 1. The receptivity and evolution of a localized free stream disturbance,” *Euro. J. Mechanics B/Fluids*, 17, pp. 823–846
- [50] Alving, A. E., and Fernholz, H.H., 1996, “Turbulence measurements around a mild separation bubble and downstream of reattachment,” *J. Fluid Mech.*, 322, pp. 297-328
- [51] Barrett, M. J., and Hollingsworth, D. K., 2001, “On the calculation of length scales for turbulent heat transfer correlation,” *J. Heat Transfer*, 123(5), pp. 878-883
- [52] Carullo, J. S., Nasir, S., Cress, R. D., Ng, W. F., Thole, K. A., Zhang, L. J., and Moon, H. K., 2011, “The effects of freestream turbulence, turbulence length scale, and exit Reynolds number on turbine blade heat transfer in a transonic cascade,” *J. Turbomach.* 133(1), pp. 011030-1-11
- [53] Peyrin, F., and Kondjoyan, A., 2002, “Effect of turbulent integral length scale on heat transfer around a circular cylinder placed cross to an air flow,” *Exper. Thermal Fluid Sci.*, 26, pp. 455–460

## CHAPTER 4

### EFFECT OF A TRIANGULAR RIB ON A FLAT PLATE BOUNDARY LAYER

#### ***4.1. Introduction***

Rib turbulators for enhancing convective heat transfer have been the subject of numerous investigations over the years as applied in various industries, such as gas turbines [1], heat exchangers [2] and solar air heaters [3-5]. Separation, recirculation followed by reattachment of the flow over the rib can lead to a significant enhancement in the surface heat transfer. Some strong unsteady behaviors such as rolled-up vortices, shedding of large-scale vortices and a flapping separation bubble were observed to be the fundamental behaviors of the separated and reattaching flow over forward and backward steps [7, 8] or a surface-mounted rib [9, 10, 11, 12]. These unsteady behaviors were shown to have a strong influence on the heat transfer rate [9, 12-14]. The cost of heat transfer enhancement using a rib is an increase in friction or pressure drop [6]. Thus, effort should be made to maximize the enhancement without a significant increase in pressure loss.

Rib geometry and arrangement, among other parameters, have been manipulated to alter the flow and consequently the heat transfer and friction of the surface [4, 15, 16]. The effect of rib shape has also been of interest in many studies [15, 17-19]. Some studies have argued that the rectangular [18], trapezoidal with decreasing height in the flow direction [15], or wedge-ribbed surfaces [17] result in a higher heat transfer rate than the triangular one. A few studies [17, 19], nonetheless, seem to indicate that the thermal performance in terms of the ratio of heat transfer to friction increase of the triangular-ribbed surface is superior. It can be seen that there is a discrepancy in the literature concerning the best rib shape for optimal performance. Furthermore, as was mentioned, the heat transfer rate and friction factor both rely on the flow structure. Thus, better understanding of the flow behavior around the rib is essential in systematically devising appropriate ribs for the best thermal performance.

The flow mechanism over a surface mounted rectangular rib has been investigated in numerous studies [2, 14, 20-22]. In the numerical study by Hwang et al. [21] it was seen that the flow characteristics depended on the streamwise length to height ratio of the rib ( $B/H$ ). For  $B/H < 4$ , the flow separated from the wall before the rib, hit the top leading corner, passed over the rib and then reattached downstream. Consequently, there were two recirculation regions, one before the rib and another one that started from the top upstream corner of the rib and extended downstream of the rib. By increasing  $B/H$  to 4, the separated flow formed at the top upstream corner would reattach twice, first on the top surface and then downstream of the rib [21]. Also, it was seen that the length of the recirculation zones in front of and behind the rib depended on the approaching flow boundary layer thickness to rib height ratio, and the length to height ratio of the rib, respectively [21, 22]. When  $B/H < 4$ , the reattachment length decreased linearly with increasing rib length ( $B$ ); while for  $B/H > 4$ , it was almost independent of the rib length [21].

The flow over a square rib, which is a special case of the rectangular rib, also has been studied quite extensively [8-10, 13, 20, 22]. The square rib is like short rectangular ribs ( $B/H = 1 < 4$ ), in that the flow separates at about  $1 \sim 2H$ , sweeps past the rib and then reattaches at  $5.5 \sim 10H$  downstream [8-10, 22]. In the study by Acharya et al. [20] it was seen that the turbulence in the recirculation

zone of a square rib was not in equilibrium and this non-equilibrium behavior lasted until 7 rib heights downstream of the reattachment point.

For triangular or wedge-ribbed surfaces however, the overall effect of a rib or ribs on the heat transfer or friction factor has been explored to some extent but without any detailed study of the underlying mechanisms. Because of the specific shape of this rib, the (second) recirculation zone starts from the apex and extends to the downstream side of the triangle or until some distance along the wall [15]. The reattachment length is predicted to strongly depend on the height to base ratio of the triangle. Also it is expected that for a triangle with a low height (compared to its base), the reattachment length may be shorter than that of rectangular or square ribs. The shorter wake region was also postulated to be effective in enhancing the heat transfer from the ribbed surfaces [9, 23]. Thus, it is clear that a study detailing the flow structure downstream of a surface-mounted triangular rib is overdue.

In the present study, the flow over a triangular-ribbed wall is studied with the ultimate objective of enhancing the heat transfer from a photovoltaic panel's (PV) surface to decrease its temperature and increase its efficiency. To this end, the flow mechanism over a single triangular rib placed on a flat plate was examined. The effect of this triangular rib on the velocity profiles, turbulence intensity, and length scale inside the wall boundary layer were studied. With the long term objective of applying rib turbulators on PV panels, the flow characteristics at streamwise locations up to 80 times the height of the rib were quantified to investigate the extent of the perturbation on the boundary layer downstream.

### ***Nomenclature***

$B$	rectangular rib streamwise length	$U_C$	convection velocity, m/s
$C_f$	wall skin friction coefficient	$U_\infty$	free stream velocity, m/s
$D_h$	duct hydraulic diameter	$X$	streamwise distance from the rib downstream's edge, m
$f$	Frequency, Hz	$Y$	normal distance from the plate, m
$H$	rib height, 0.5 cm	$Y^+$	normalized distance from the wall ( $\frac{Y \cdot U_\tau}{\nu}$ )
$N$	sampling size ( $2 \times 10^6$ )	$Z$	distance along the width of the plate from the plate's centerline, m
$R(\tau)$	autocorrelation function between turbulence velocities	$\delta$	boundary layer thickness, cm
$Re_H$	Reynolds number based on the rib height ( $\rho U H / \mu$ )	$\theta$	momentum thickness ( $\int_0^Y (1 - \frac{u}{U_\infty}) \times \frac{u}{U_\infty} dy$ ), m
$Re_L$	Reynolds number based on the length of the plate ( $\rho U L / \mu$ )	$\lambda$	integral length scale, cm
$Re_X$	Reynolds number based on the streamwise distance from the plate leading edge ( $\frac{\rho U X}{\mu}$ )	$\lambda$	Taylor micro-scale, cm

$Re_\theta$	Reynolds number based on the momentum thickness ( $\rho U \theta / \mu$ )	$\mu$	dynamic viscosity, $N \cdot s / m^2$
$Tu$	turbulence intensity ( $u_{rms} / U_\infty$ )	$\nu$	kinematic viscosity, $m^2 / s$
$u_i$	instantaneous velocity fluctuations, m/s	$\Pi$	wake parameter
$u_{rms}$	root-mean-square of the velocity fluctuations, m/s	$\tau$	time difference, s
$U_\tau$	shear velocity, $\sqrt{\frac{\tau_w}{\rho}}$ , m/s	$\tau_A$	integral time scale, s
$U$	local time averaged velocity, m/s	$\tau_\lambda$	Taylor time scale, s

#### 4.2. Apparatus and Instrumentation

All experimental data for the present investigation were obtained in a wind tunnel with a 180 cm long, 76 cm high and 77 cm wide test section. The maximum free stream velocity is around 30 m/s. The flow quality was tested with an empty test section at  $U_\infty = 7.8$  m/s. The background turbulence intensity was around 0.4% and the velocity varied only  $\pm 0.2$  m/s for the area outside the test section wall boundary layer.

As shown in Figure 4.1, the setup consisted of a flat, horizontal plate with an isosceles triangular rib having a 0.5 cm base and height, located 5 cm from the leading edge. X, Y and Z were the streamwise, normal to the plate and widthwise directions, respectively, with the origin located at the middle of the downstream edge of the rib. The flat aluminum plate was 1.5 mm thick, 30 cm wide and 60 cm long. As can be seen in Figure 1, an angle of  $30^\circ$  was machined at both surfaces of the leading edge of the flat plate in order to reduce the effect of the blunt edge. The flat plate was placed at mid-height in the middle of the test section. Figure 4.2 shows the ribbed flat plate, stand, measuring and traverse systems, and test section walls. The streamwise area of the flat plate and stand was around 1% of the wind tunnel cross-sectional area.

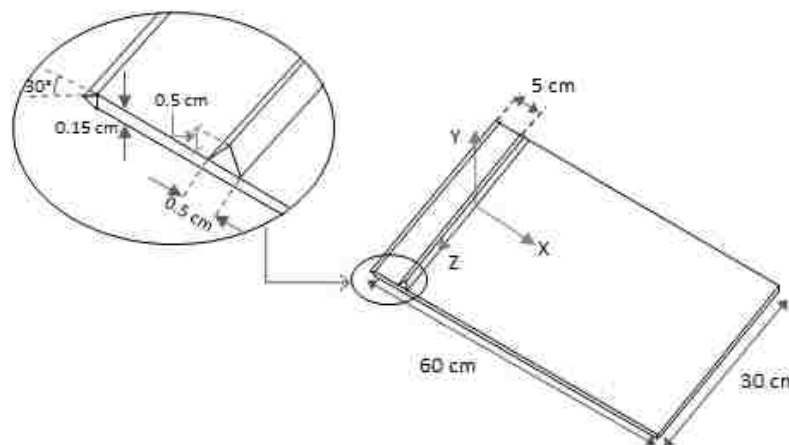


Figure 4.1 Rib mounted flat plate schematic

A 1-D boundary layer hot-wire probe (type 55P15) with a Dantec streamline 55C90 constant-temperature anemometer (CTA) was applied to measure the velocity at different points downstream of the rib. The probe had a platinum-plated tungsten wire with a diameter of  $5\ \mu\text{m}$  and a length of 1.25 mm. Signals were low-passed at 30 kHz and then sampled at 80 kHz over a period of around 25 s, resulting in  $2 \times 10^6$  data points per measurement. A 12-bit PCI-6071E National Instrument data acquisition card was used to convert the analog data into a digital one. A computer-controlled 2-D traverse system was used to position the probe at each specified location (Figure 2). The computer-controlled traverse system can move through the widthwise direction of the test section (Z) and normal direction to the plate (Y) in 2 mm steps.

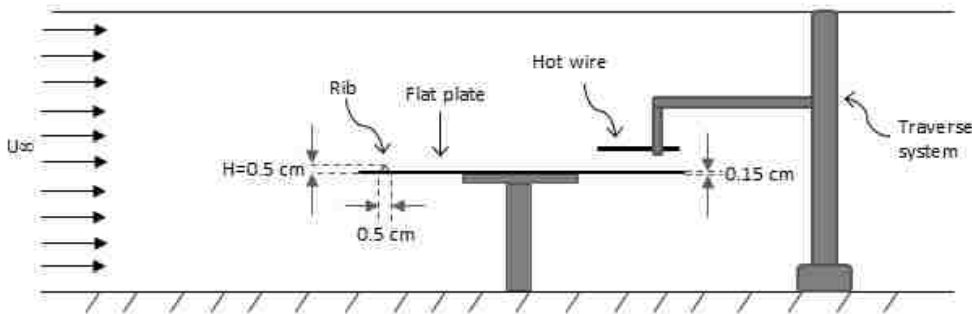


Figure 4.2 Test section side view

Measurements were performed at  $Z = 0$  (Figure 4.1) and at 30 points in the Y direction (from  $Y = 0.2$  to  $5.9$  cm) at each of the six streamwise (X) locations ( $X/H = 2, 10, 20, 40, 60$  and  $80$ ). Tests were repeated at three different free-stream velocities: 4, 6.8 and 9 m/s.

### 4.3. Results and Discussion

#### 4.3.1. Velocity profiles

The overall flow behavior behind the rib, such as flow separation, reattachment and boundary layer behavior can be detected from the streamwise velocity profiles. The boundary layer thickness is the lowest Y value that corresponds to  $U/U_\infty = 0.99$ . It was obtained by drawing a horizontal line at  $U/U_\infty = 0.99$  through the velocity profile curve in Figure 3 (shown in the next sub-section). The boundary layer thicknesses at  $X = 0$  for smooth (no rib) wall cases at  $U_\infty = 4$  m/s, 6.8 m/s and 9 m/s were 0.2 cm, 0.27 cm and 0.3 cm, respectively. The corresponding  $H/\delta$  values were 2.5, 1.85 and 1.7. These values are somewhat larger than those in Refs [3, 14] where the flow was observed to be affected strongly by the rib. So, the rib in the present study was also expected to significantly disturb the flow pattern over the surface.

##### 4.3.1.1. Time-averaged Velocity Profiles

Normalized time-averaged streamwise velocity profiles over the smooth and ribbed surfaces at different downstream distances and free stream velocities are presented in Figure 4.3. Recall (Figure 4.1) that X is a coordinate measured from the downstream lower edge of the rib. These



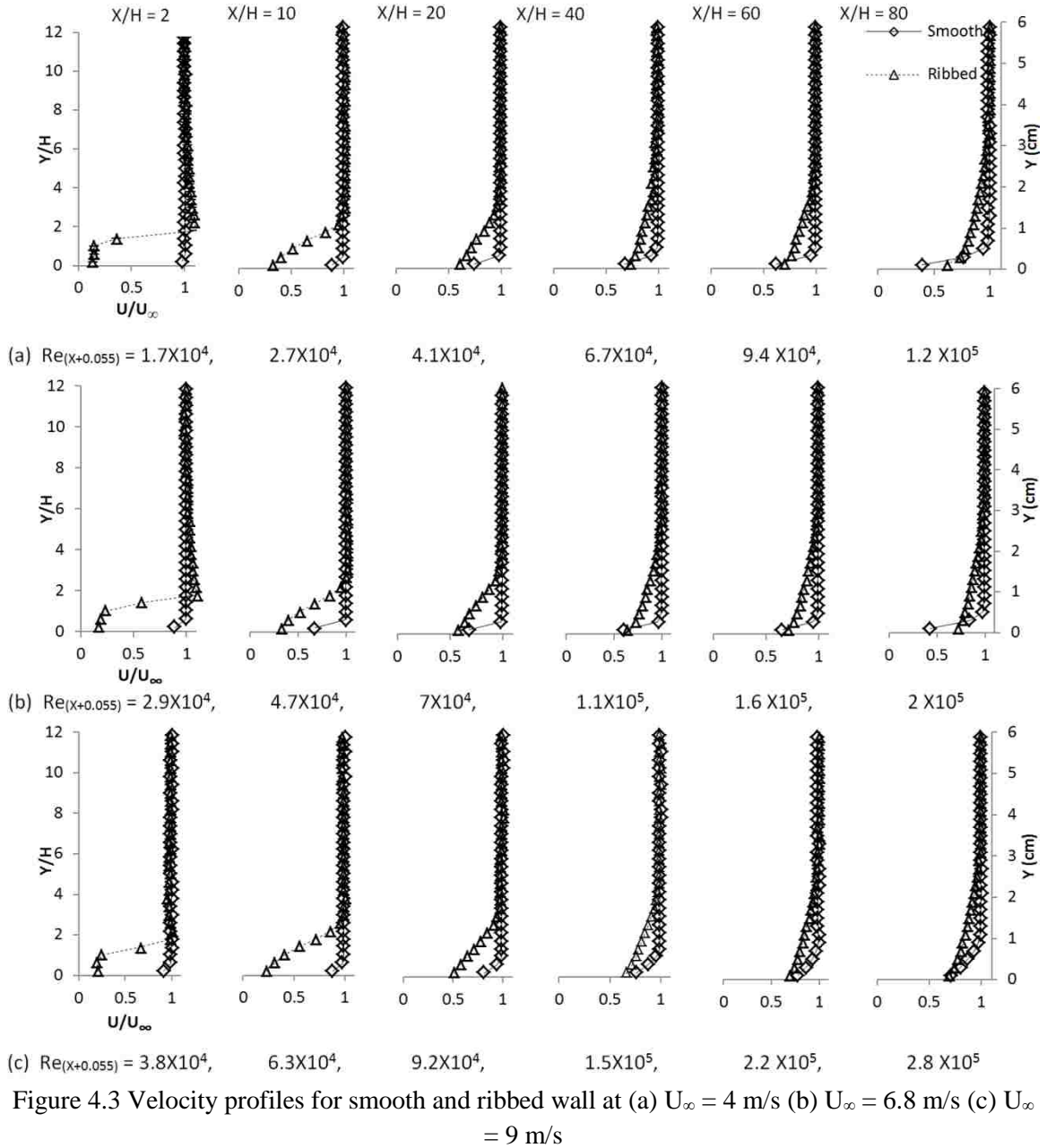
profiles span from  $Y/H = 0.2$  to 12. The corresponding Reynolds number based on the distance from the leading edge of the plate ( $Re_{(X+0.055m)}$ ) are provided for each graph.

For the smooth wall, the boundary layer growth downstream ( $X/H = 2$  to 80) can be clearly observed for all three free stream velocities. For  $U_\infty = 4$  and 6.8 m/s (Figure 4.3 (a) and (b)),  $\delta$  increases from 0.2 and 0.27 cm to 0.7 and 0.9, respectively. The value of  $\delta$  at these two free stream velocities is close to the predicted laminar boundary layer thickness [24]. Hence, it can be said that for the smooth wall at these free stream velocities, the boundary layer remains laminar until  $X/H \approx 80$ . For  $U_\infty = 9$  m/s (Figure 4.3 (c)),  $\delta$  increases from 0.3 to 1.3 cm. For this velocity, at  $X/H = 80$  ( $Re_{(X+0.055m)} = 2.8 \times 10^5$ ), the predicted laminar and fully turbulent boundary layer thicknesses for a smooth flat plate are 0.42 cm and 1.41 cm, respectively [24]. But, as can be seen in Figure 4.3 (c), the smooth wall  $\delta$  in the present study is around 1.3 cm. Therefore, it can be concluded that for  $U_\infty = 9$  m/s after  $X/H = 60$ , the smooth wall boundary layer starts to become turbulent though it may not be fully turbulent even at the farthest downstream location studied. The  $Re_x$  at which the flow starts to become turbulent is less than the typical critical  $Re$  for the flow over a smooth flat plates ( $5 \times 10^5$ ) [24]. This might be because of: minor disturbances in the approaching flow ( $\sim 0.4\%$  background turbulence intensity); leading edge imperfection; and/or vibrations of the supporting platform attached to the floor of the wind tunnel, causing the transition to the turbulent boundary layer to happen at a lower  $Re$ . During the experiment, it was noted that the vibrations were somewhat more severe at the highest tested wind speed  $U_\infty = 9$  m/s.

The total uncertainty associated with each parameter consists of bias and precision uncertainties [25, 26]. Bias or systematic uncertainty of the hotwire-measured instantaneous velocities has been estimated according to Jørgensen [25]. Bias consisted of calibration, data acquisition and data reduction uncertainties. Precision uncertainty, which concerns the repeatability of the test, has been derived from Student's  $t$  distribution method with a 95% confidence interval [26]. The uncertainty in velocity ( $U$ ) and normalized velocity ( $U/U_\infty$ ) at point  $Y/H = 0.6$  in Figure 4.3 (a) (4 m/s free stream velocity and  $X/H = 2$ ) were estimated to be around  $\pm 0.33$  m/s and  $\pm 0.02$ , mostly due to the precision uncertainty. The uncertainty value is very small compared to the symbols in these graphs, so error bars were not added. The uncertainty in probe positioning in the  $Y$  direction (which was also the boundary layer thickness uncertainty) was estimated to be 1.2 mm.

The disturbance of the rib on the flow over the surface should lead to a distinct growth in the boundary layer thickness compared with its smooth wall counterpart. This can be clearly seen in Figure 4.3. Also it can be observed that the effect of the rib on the boundary layer shape and characteristics is still detectable at the farthest studied streamwise location of  $X/H = 80$ . For the ribbed wall at  $U_\infty = 4$  m/s,  $\delta$  grows from 0.9 cm at  $X/H = 2$  to around 3.3 cm at  $X/H = 80$ . Compared with the smooth wall boundary layer thickness, the rib causes the boundary layer to be 4.5 ~ 4.7 times thicker. Almost the same trend is seen for  $U_\infty = 6.8$  m/s at all studied streamwise distances and for  $U_\infty = 9$  m/s until  $X/H = 60$ . For  $U_\infty = 9$  m/s at  $X/H = 80$ , the ribbed wall boundary layer thickness is around 2.8 cm which is only twice the smooth wall boundary layer thickness. Here, the effect of the rib on the two shear layers is lower because the corresponding smooth wall boundary layer started to become turbulent. However, the ribbed wall shear layer is still much thicker than that of a classical fully turbulent boundary layer over a smooth flat plate (1.46 cm [24]). As the working fluid in the present study is air ( $Pr = 0.7$ ), the hydrodynamic and thermal boundary layers

will be similar in thickness. So increasing the hydrodynamic boundary layer thickness corresponds to a growth in the thermal boundary layer, which alone can lead to a reduction in the heat transfer rate.



To discuss the overall flow mechanism after a triangular rib it might be helpful to look at the more extensively studied flow over a square rib [14, 27]. Based on flow visualization on a square ribbed surface, flow separation happens at the rib corners, which would cause a recirculation zone behind

the rib, followed by flow reattachment to the surface [27]. In the schematic diagram of the flow configuration around a square rib provided in Ref. [14] (Figure 4.4 (a)), the flow separated from the leading edge of the square rib is swept past the rib and directly reattached to the bottom wall downstream of the rib. So for square ribs, a layer of reverse flow forms above the rib.

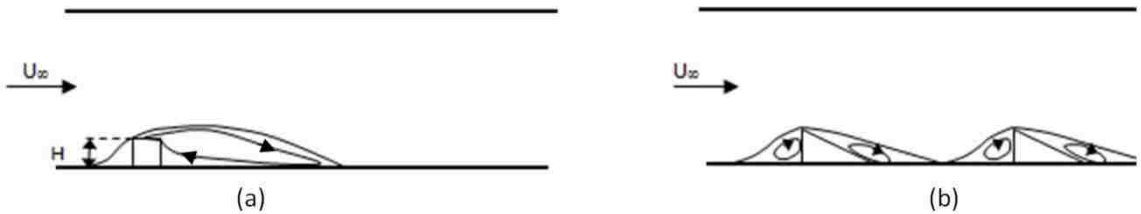


Figure 4.4 Flow over a (a) square ribbed surface [14] (b) wedge ribbed surface [3]

In the present study, due to the more gradual incline-decline associated with a triangular rib, the recirculation area downstream of the rib was predicted to be smaller and limited to a narrow region next to the wall. An approximate schematic of the flow over a wedge shaped rib is provided in Bhagoria et al. [3] (Figure 4.4 (b)), which shows that the reattachment point is supposed to happen at an earlier distance behind the rib, compared to a rectangular rib. However, in a numerical study by Kamali and Binesh [15] on the internal flow in a ribbed square duct, it was observed that the reattachment length of an equilateral-triangular rib is higher than that of a square one. Their study may not be directly comparable with the present case, external flow over a ribbed flat plate, as the ratio of the rib height to the duct hydraulic diameter was relatively large ( $H/D_h = 0.1$ ) and it was an internal flow case.

The reattachment point was defined in the literature [12, 14] as the location corresponding to the zero streamwise velocity at the closest measurement to the surface (2 mm away from the surface in Ref. [12]). To have a better view of the velocity profile shapes around the reattachment point, the profiles over a square ribbed surface before and after the reattachment point ( $X/H = 9.75$ ) from Liu et al. [14] are provided in Figure 4.5. In their study the rib size was rather large. Using the same definition for reattachment point and comparing the velocity profiles in Figure 4.3 with Figure 4.5, one may conclude that the reattachment in this study occurred before the first studied streamwise distance  $X/H = 2$ . This is much earlier than that associated with the square rib in Liu et al. [14]. As was mentioned before, the reported reattachment length for square ribs in different studies with different flow situations and rib heights, ranged from 5.5 to 10 times the rib height downstream [8-10, 22]. Different experimental situations in different studies make it difficult to draw a definite conclusion; nevertheless, the reattachment length in the present study for the flow over a triangular ribbed wall appeared to be much smaller than the range of square rib reattachment lengths provided in the literature. In the study by Acharya et al. [23], it was observed that in the recirculation zone downstream of a square rib, the heat transfer rate was very low. So, it appears that a shorter reattachment length can more effectively enhance the heat transfer rate of the surface [9]. However, further experimental studies are required to verify this conclusion.

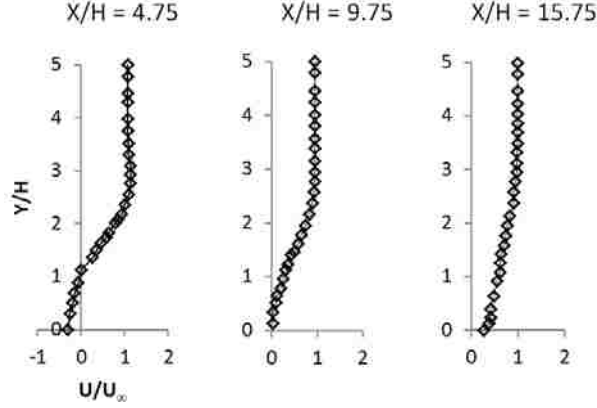


Figure 4.5 Liu et al. [14] velocity profile over a square ribbed surface

Also, Figure 4.3 shows that up to  $X/H = 40$  for all studied free stream velocities, the velocity near the ribbed wall at the closest solid surface measurement point ( $Y/H = 0.2$ ) is lower compared with that associated with the smooth wall. Farther downstream however, it becomes higher. Hence, it can be concluded that even though the flow may have been attached to the surface before  $X/H = 2$ , the streamwise velocity is not fully recovered until  $X/H$  around 40. Similar results were observed in the study on square rib by Liu et al. [14] and they attributed this to turbulent boundary layer redevelopment in the post reattachment zone, where the decay trend of the large scale vortical structures is slow [2, 14].

#### 4.3.1.2. Logarithmic Velocity Profiles

Figure 4.6 shows the normalized logarithmic time-averaged velocity profiles for smooth and ribbed walls at different downstream distances. The free stream velocity  $U_\infty = 9$  m/s was chosen because of the thicker wall boundary layer, so the logarithmic area could be better captured. But even at this velocity, the boundary layer for the smooth wall at  $X/H \leq 10$  was still very thin, limiting the number of data points and the quality of the measurement, so they are not included in these graphs. The Reynolds numbers based on the momentum thicknesses ( $Re_\theta$ ) and distances from the leading edge ( $Re_{(X+0.055 \text{ m})}$ ) are also provided in the graphs to put current results into proper perspective with the literature. Higher  $Re_\theta$  values indicate higher boundary layer thicknesses. For  $X/H = 20$  to 80 at  $U_\infty = 9$  m/s, the corresponding  $Re_{(X+0.055 \text{ m})}$  values were in the range of  $9.8 \times 10^4 \sim 2.8 \times 10^5$ . At different downstream distances,  $Re_X$  for the smooth and ribbed walls was the same because of how  $Re_X$  is defined, while  $Re_\theta$  was much higher for the ribbed wall, due to a thicker boundary layer. The solid line in these profiles shows the log law function [28]:

$$\frac{U}{u_\tau} = 1/k \cdot \ln\left(\frac{yU_\tau}{\nu}\right) + C \quad (4.1)$$

where  $k$  is the von Karman constant with a value of 0.41, and  $C$  is a constant taken to be 5. Friction velocity  $u_\tau$  was determined from the Clauser fit [28] for both cases by assuming that the log law remains valid even for the velocity profile in the presence of the rib.

The accuracy of using the Clauser fit for deducing the ribbed wall's friction may be debatable. Clauser showed that when the surface is rough there is an additional term in the log law that is a function of the wall roughness [28], this defect in velocity profile was also seen in other experimental studies [29, 30]. But a single rib on a surface may not be categorized as a rough wall. Antonia and Luxton [31] showed that the logarithmic mean velocity distribution is valid for the near-wall region immediately after a rough-smooth junction but with a much higher  $C$  value than the “universal” smooth wall value. So as Antonia and Luxton [31] mentioned for their case, downstream of a rough-smooth junction (here also because of the non-universality of  $k$  and  $C$  values), the determination of the skin friction coefficient from the Clauser chart for a single ribbed wall case may not be appropriate. However, in this research the same equation (Eqn 4.1) was used for both smooth and ribbed walls to portray the relative effect of the rib on different internal layers of the boundary layer.

For the smooth wall case in Figure 4.6 (a), progressing downstream (higher  $Re_{(X+0.055)}$  and higher  $Re_\theta$ ), the log law fit the data over an increasing broader region. However, for smaller  $X/H$  values the boundary layer was still laminar so the log law fit over very few points. This trend was also seen in Figure 4.6 (b) for the ribbed wall. After the log region, it is seen that the profile deviated from the solid line that follows the log law: this region is the outer region of the boundary layer, which is called the wake region. Comparing Figures 4.6 (a) and (b) demonstrates the significant effect of the rib on the velocity profile in both the logarithmic and wake regions. It can be seen that for the ribbed wall, the log law region was much more extended, which illustrates the expansion of the shear layer in the ribbed wall.

The velocity profile for a classical flat plate turbulent boundary layer from DeGraaff and Eaton at different  $Re_\theta$  [32] is presented in Figure 4.7 for comparison. Because of the higher  $Re_\theta$  values in Figure 4.7 compared to the present study, Figure 4.7 might be comparable just with the turbulent boundary layer profile of the smooth wall ( $X/H = 80$  in Figure 4.6 (a)) and with the ribbed wall (Figure 4.6 (b)). As can be seen, the overall shapes of the profiles are almost the same for  $X/H = 80$  in Figure 4.6 (a), Figure 4.6 (b) and Figure 4.7, except for the  $X/H = 20$  values in Figure 4.6 (b) where the turbulence is still being generated. The most comparable profiles are for  $Re_\theta = 1400$  in Figure 4.6 (a) and  $Re_\theta = 1430$  in Figure 4.7, where the log law fit well until  $Y^+ \cong 200$ . Also, for  $Re_\theta = 3240$  in Figure 4.6 (b) and  $Re_\theta = 2900$  in Figure 4.7; the log law fit these two profiles until  $Y^+ \cong 300$ .

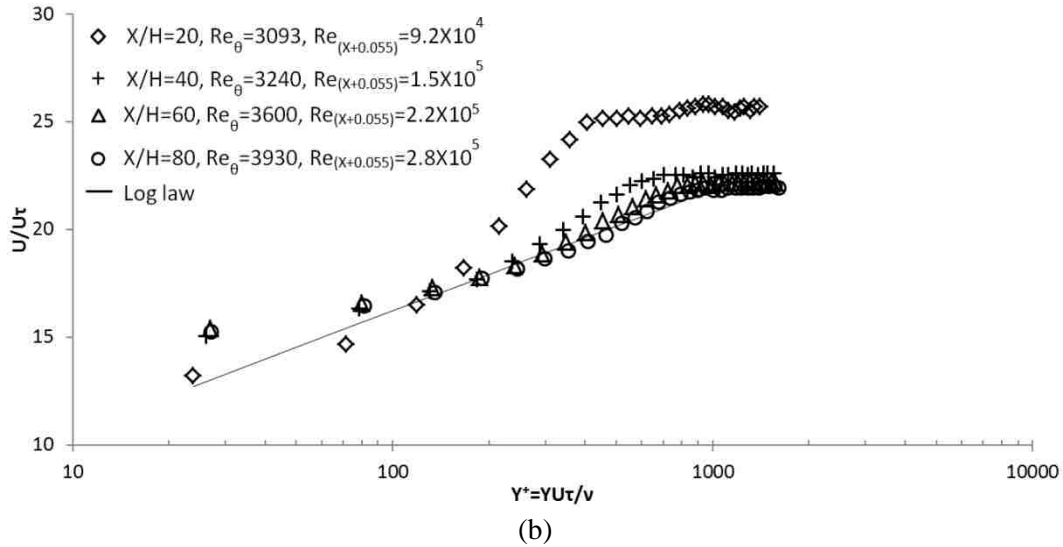
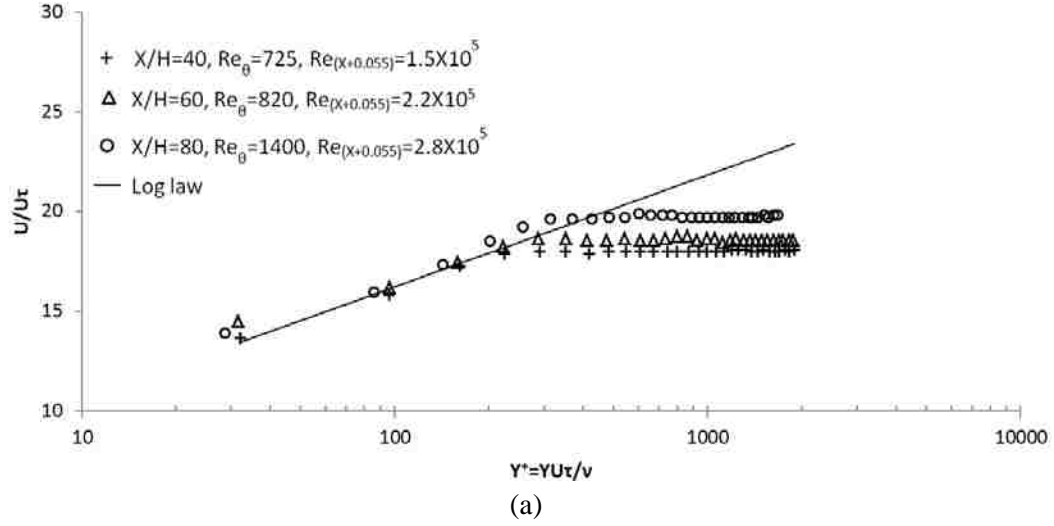


Figure 4.6 Normalized velocity profiles inside the boundary layer at  $U_\infty = 9$  m/s for the (a) smooth and (b) ribbed wall

As it is seen in the velocity profiles in Figure 4.6, the presence of the rib also affects the wake region of the wall boundary layer. This effect can be quantified by the wake parameter ( $\Pi$ ), described in the following paragraphs. The velocity profile in the wake region was defined by the wake law of Hancock and Bradshaw [33]:

$$\frac{U}{U_\tau} = \frac{1}{k} * \ln(U_\tau Y / \vartheta) + C + 1/k * g(\Pi, Y/\delta) \quad (4.2)$$

The wake component “g” is given as [33]:

$$g\left(\Pi, \frac{Y}{\delta}\right) = (1 + 6\Pi) \left(\frac{Y}{\delta}\right)^2 - (1 + 4\Pi) \left(\frac{Y}{\delta}\right)^3 \quad (4.3)$$

The wake defect can also be qualified by means of the wake parameter,  $\Pi$ :

$$\Pi = \frac{k}{2} * \left( \frac{U_\infty}{U_\tau} - \frac{1}{k} * \ln(U_\tau \delta / \vartheta) - C \right) \quad (4.4)$$

Wake strength is the parameter which demonstrates a velocity profile's shape in the wake region. This parameter shows the degree of deviation of the velocity profile from the logarithmic line at the edge of the boundary layer. It was observed that this parameter depends on the  $Re_\theta$  and pressure gradient [34]. In this work,  $\Pi$  at different  $X/H$  for  $U_\infty = 9$  m/s were calculated and shown in Figure 4.8. The corresponding  $Re_\theta$  values for each  $X/H$  were also provided in the graph. A positive  $\Pi$  means that at  $Y = \delta$ , the profile lies above the log law line (higher than log law velocity; solid line in Figure 4.6) while a negative  $\Pi$  signifies that the profile is under the log law line. For instance, for the ribbed wall at  $X/H = 20$ ,  $\Pi$  is +6.83 (Figure 4.8) and it can also be seen in Figure 4.6 (b) that, in the wake region the profile deviates positively from log law and lies above this line. As seen in Figure 4.8,  $\Pi$  has negative values for the smooth wall but it is positive for the ribbed wall at all studied  $Re_\theta$ . These results are consistent with velocity profiles (Figure 4.6), where the smooth wall's data in the wake region are under the log law line and that of the ribbed wall above the log law line. Saturdi and Ching [35] found a strong correlation between the wake parameter and local skin friction, such that a reduction in  $C_f$  leads to an increase in  $\Pi$  and vice versa. Regarding heat convection, the higher velocity than log law local velocity associated with positive  $\Pi$  is expected to enhance the heat transfer rate.

As can be observed in Figure 4.8, the calculated absolute wake strength for both ribbed and smooth wall cases decreased (approached zero) progressing downstream or by increasing the  $Re_\theta$ . For the ribbed wall from  $X/H = 20$  to 80 the absolute value of  $\Pi$  decreased from 6.8 to 0.3, and from 1.2 to 0.1 for the smooth wall. This means that in both cases the velocity profile approaches the log law profile in the streamwise direction. This trend also can be observed in Figure 4.6. In short, both ribbed and smooth wall cases illustrate an expanding log law region farther downstream. But as seen in Figure 8, the rate of the reduction in the wake strength absolute value is very significant for the ribbed wall for the region  $X/H = 20$  to 40.

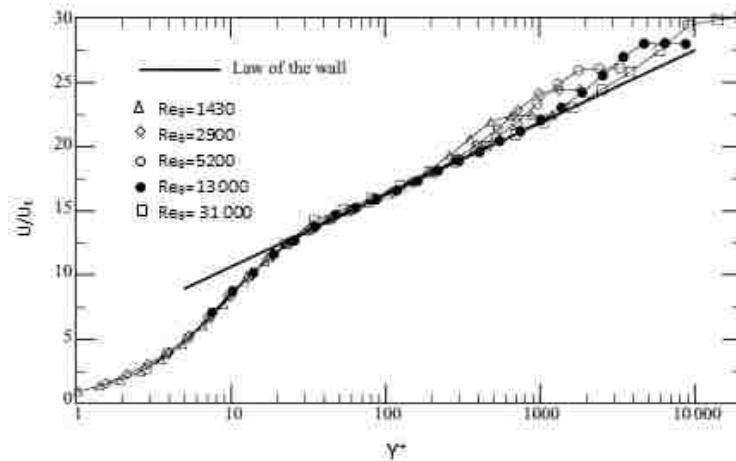


Figure 4.7 Turbulent boundary layer normalized velocity profile of DeGraaff and Eaton [32]

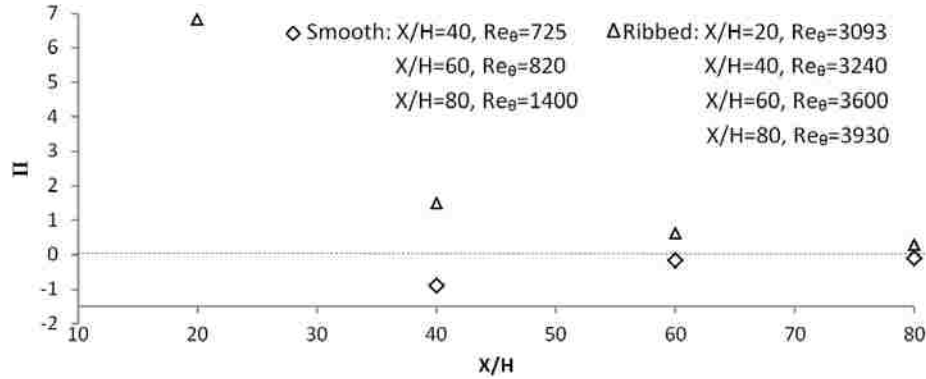


Figure 4.8 Wake parameter at  $U_\infty = 9$  m/s

### 4.3.2. Turbulence Intensity

Velocity fluctuations are associated with gradients in time-averaged flow, which can cause increased mixing in the fluid and heat transfer enhancement. So, it is anticipated that there is a positive correlation between heat transfer rate and the total generated turbulence behind the rib [27].

Streamwise turbulence intensities ( $Tu = u_{rms}/U_\infty$ ) for smooth and ribbed walls at various streamwise locations and free stream velocities are presented in Figure 4.9. The corresponding Reynolds number based on the distance from the leading edge of the plate ( $Re_{(X+0.055m)}$ ) are also provided. For the smooth wall,  $Tu$  was higher near the wall and decreased to the free stream  $Tu$  (less than 0.4%) at the boundary layer edge.

The rib caused a high level of disturbance in the area close to the wall and this effect lasts beyond  $X/H = 80$ , the farthest streamwise distance considered. Also, by comparing these graphs with the velocity profiles (Figure 4.3) it can be observed that the rib-generated turbulence lasted far beyond the boundary layer in the normal direction. As can be seen in Figure 4.9 for the ribbed wall at all studied  $U_\infty$ , for the region  $X/H = 2$  to 20, turbulence increased in the normal direction from the wall, reached a peak and subsequently reduced to the free stream value. The same increasing-decreasing trend in the normal direction from the wall in  $Tu$  was also seen in studies with a square-ribbed wall [9, 14, 27]. Also it can be observed that up until  $X/H = 20$ , the peak  $Tu$  value had an increasing trend, which showed that turbulence was still being generated. The maximum turbulence level peak occurred at  $X/H = 20$ , coinciding with the weakening shear layer in Figure 4.3. Beyond  $X/H = 20$  the peak  $Tu$  level diminished slowly and the  $Tu$  profile started to flatten [14].

It is noted that the smooth wall's  $Tu$  corresponding to the highest free stream velocity case ( $U_\infty = 9$  m/s) was higher, specifically for the couple of points close to the wall, compared to those of the two lower velocities for the same Reynolds number. This is presumably due to the somewhat increased vibrations in the plate at higher velocities, as mentioned earlier. The uncertainty for turbulence intensity ( $Tu$ ) at point  $X/H = 2$  and  $Y/H = 0.6$  at 4 m/s free stream velocity were estimated to be 0.8%. The uncertainty value was not shown on Figure 9 because it is smaller than symbols used in the plots.



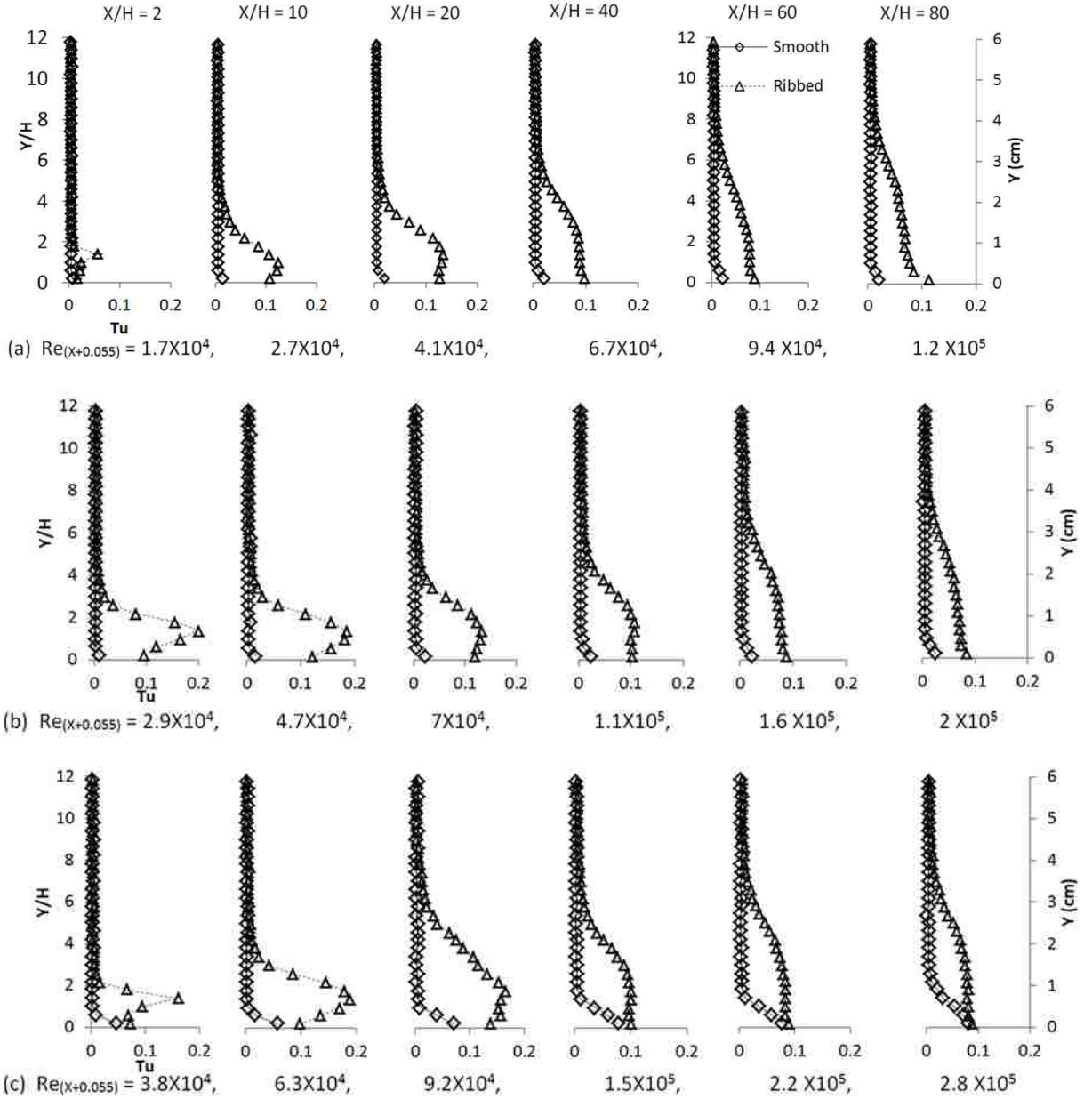


Figure 4.9 Turbulence intensity profiles for smooth and ribbed wall at (a)  $U_\infty = 4$  m/s (b)  $U_\infty = 6.8$  m/s (c)  $U_\infty = 9$  m/s

The wall-normal positions of the local maximum streamwise turbulence intensities were plotted in Figure 4.10 (a) for the three studied free stream velocities. This method was also used in Liu et al. [14], as shown in Figure 4.10 (b), to describe the trail of the convecting vortices in the reattaching turbulent flow after a square rib. Although the experimental conditions in their study, such as rib shape and size (square rib,  $H = 2$  cm) and free stream velocity ( $U_\infty = 10$  m/s), were quite different from the present work, the general trend is comparable. As can be seen in the present results (Figure 4.10 (a)), the location of the maximum  $Tu$  in the normal direction occurs at around  $Y/H = 1.4$  for

$X/H$  up until 20, beyond which the  $Tu$  peak location moves towards the wall. The same general trend was seen in Ref. [14] (Figure 4.10 (b)), and it was proposed that the gradual decrease in the position of the maximum  $Tu$  from the solid wall after the reattachment point ( $X/H = 9.75$ ) for the range of  $9.75 \leq X/H \leq 12$  demonstrated the persistence of the large scale vortical structures in the redeveloping turbulent boundary layer behind the rib. It was also argued that the rapid shift in this peak point toward the wall after  $X/H = 11$  was due to the decay of the vortices under the wall effect [14]. However, in the present study, due to the gradual incline-decline of the rib and the small size of the rib, the reattachment appears to occur much earlier, and the weak vortex shedding downstream of the rib may not be well defined. Also, the maximum  $Tu$  may or may not correspond to the position of these vortices. Nevertheless, it can be seen that the maximum  $Tu$  location moved towards the wall after  $X/H = 20$  in this study.

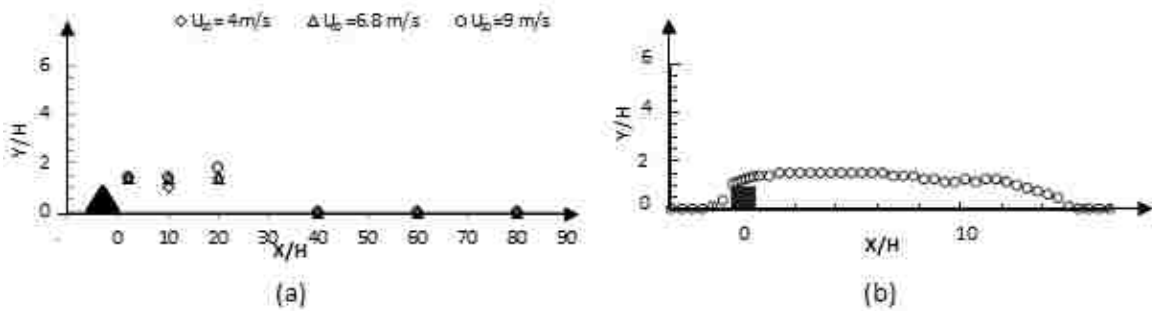


Figure 4.10 Wall normal location of maximum streamwise  $Tu$  (a) present study at  $U_\infty = 9 \text{ m/s}$  (b) Liu et al. [14]

### 4.3.3. Fast Fourier Transform (FFT)

To catch the large vortex shedding in the shear layer downstream of the rib, a FFT analysis was applied to the velocity fluctuation signals at different downstream and normal locations and free stream velocities. Figure 4.11 illustrates the FFT results at  $Y/H = 1$  and different free stream velocities. For each velocity the streamwise location was chosen at which the peak of the graph was clearest. For almost all free stream velocities and streamwise locations between  $X/H = 2$  and 40, the magnitude of the fluctuations peaked at  $f^*H/U_\infty \approx 0.013$  to 0.02. This, along with the maximum  $Tu$  plot (Figure 4.10), seems to indicate the presence of a large-scale vortical structure. The frequency at which the maximum flow magnitude occurred is close to the vortex shedding frequency captured by Liu et al. [14] for a square rib. They measured the wall-pressure autospectra at various streamwise locations which peaked at  $f^*H/U_\infty$  around 0.03. They associated this value with the frequency of the shedding of the large-scale vortical structure after the rib [14]. The velocity fluctuations' FFT value in the present study increased from  $U_\infty = 4 \text{ m/s}$  to  $9 \text{ m/s}$ , indicating the growing energy of the signal with increasing the free stream velocity.

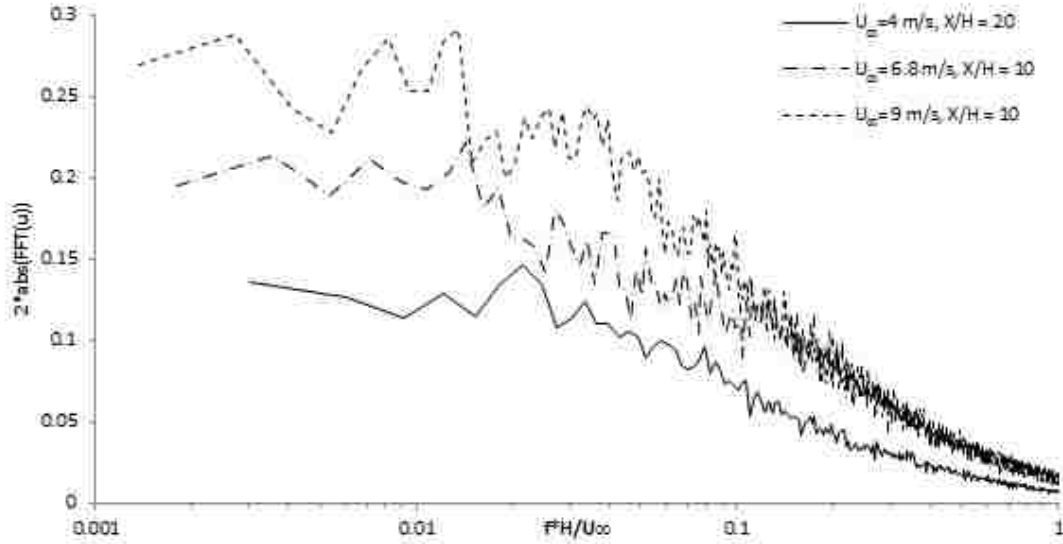


Figure 4.11 FFT of velocity fluctuation signal at  $Y/H = 1$

#### 4.3.4. Turbulence Length Scales

In studying the convection heat and mass transfer from the plate, turbulence length scales are also expected to play an important role [36-38]. In order to better visualize the range of different eddy sizes, two common scales are studied: the integral length scale, which is an indication of the large, energy-containing eddies, and the Taylor micro-scale which represents small, dissipative eddies.

The integral length scale and Taylor micro-scale at different streamwise and normal positions for smooth and ribbed walls are deduced from the Eulerian autocorrelation function between turbulence velocity fluctuations [39]:

$$R(\tau) \equiv \frac{\overline{u(t)u(t')}}{u_{rms}^2} \quad (4.5)$$

where  $\tau = t' - t$ .

If the velocity fluctuations are small compared to the flow velocity which carries the eddies, Taylor's frozen hypothesis postulates that [40]:

$$\frac{\partial}{\partial t} = -U_c \frac{\partial}{\partial x} \quad (4.6)$$

where  $U_c$  is the convection velocity or the velocity at which the flow is convected. While there is significant discussion concerning the conditions associated with the validity of Taylor's hypothesis in the turbulent boundary layer [41-43], Dennis and Nickels [41] have shown that it could be applied to a turbulent boundary layer by approximating the local mean velocity as the convection velocity instead of using the free stream value. This was adopted in the present study.

A sample autocorrelation function of the fluctuating velocity for a specific point is shown in Figure 4.12. The integral time scale is defined as the integral of this function [39]:

$$\tau_{\Lambda} = \int_0^{\infty} R(\tau) d\tau \quad (4.7)$$

Integration was truncated when  $R(\tau)$  first crossed zero. Beyond the first zero crossing, the  $\tau_{\Lambda}$  value is not physically reliable [44]. The integral length scale is an indication of the correlation distance between the velocities at two points of the flow field and could be deduced as follows [39]:

$$\Lambda = U \cdot \tau_{\Lambda} \quad (4.8)$$

The Taylor time scale ( $\tau_{\lambda}$ ) was obtained from the intersection of a parabola, fitted to the first three to five points of the correlation curve (dashed line in Figure 4.12), with the  $\tau$ -axis. Taylor length scales were then estimated from [39]:

$$\lambda = U \cdot \tau_{\lambda} \quad (4.9)$$

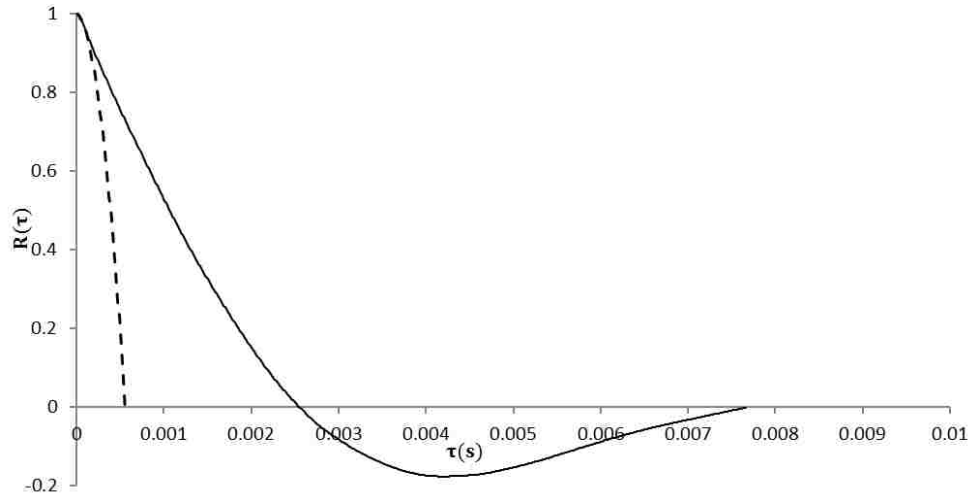


Figure 4.12 Autocorrelation coefficient for ribbed wall at  $X/H = 20$ ,  $Y/H = 2.2$  and  $U_{\infty} = 9$  m/s, the dashed line shows the parabola fitted curve to the first five points of  $R(\tau)$

Figure 4.13 shows the streamwise turbulence integral length scales at different downstream locations for smooth and ribbed walls at  $U_{\infty} = 9$  m/s. It should be mentioned that the turbulence length scale above the shear layer does not have any physical meaning since the free stream in this study is “laminar”, i.e., it has little turbulence. Therefore, the integral length scales were estimated in the normal direction until  $Tu$  reached 1%, after which they were not calculated. As for the smooth wall case,  $Tu \geq 1\%$  for just a few measurement points and hence the smooth wall was not included in these graphs. When well-defined or detectable ( $Tu \geq 1\%$ ), the average integral length scale inside the boundary layer for the smooth wall was around 0.56 cm. Except for a couple of points at

$X/H = 2, 10$  and  $20$ , the integral length scales for the ribbed wall were larger than the average integral length scale for the smooth wall. It can be seen that in spite of significant turbulence generation by the rib which might cause a reduction in eddy sizes, integral length scales are larger in the ribbed wall boundary layer than that of the smooth wall. This is likely due to the fact that large eddies are mostly confined by the geometry, or in this case by the boundary layer thickness which is larger in the ribbed wall.

The integral length scales of the ribbed wall at different downstream distances for the three free stream velocities are presented in Figure 4.14. The uncertainty in integral length for the point  $X/H = 2$  and  $Y/H = 0.3$  at  $4 \text{ m/s}$  free stream velocity is  $0.35 \text{ cm}$ , which is typical and is shown as an error bar in Figure 4.14. A general tendency of increasing integral length scale with streamwise distance can be observed in these graphs (most recognizable for  $X/H \geq 20$ ), portraying the decay of flow turbulence downstream. For  $X/H$  from  $2$  to  $20$ , a clear trend is not seen for the lowest velocity ( $U_\infty = 4 \text{ m/s}$ ) case, which might be due to the fact that flow turbulence is still being produced shortly after the rib, as corroborated by the increasing  $Tu$  in Figure 4.9.

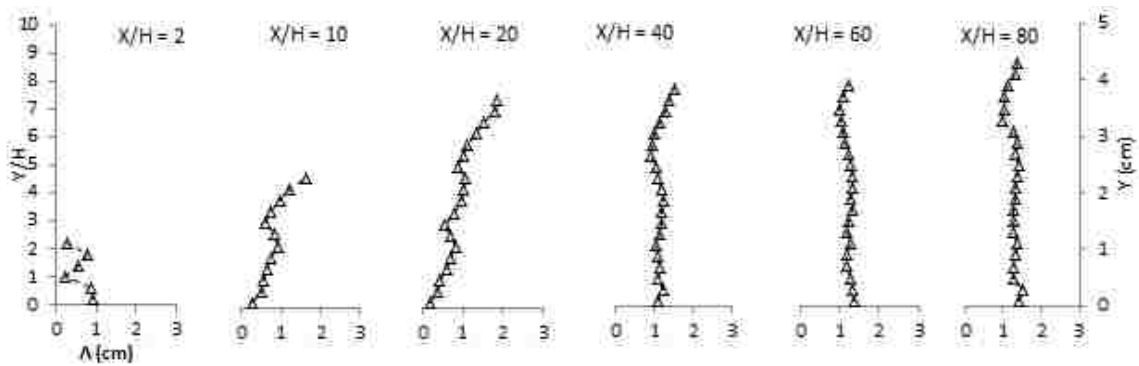


Figure 4.13 Ribbed wall integral length scale at  $U_\infty = 9 \text{ m/s}$

To have a better view of the general integral length scale trend, the averages of this parameter through the normal direction ( $Y$ ) at each streamwise position and free stream velocity were calculated and presented in Table 4.1. The streamwise increasing trend is clearly observed in this table for each velocity. Less obvious is the overall decrease in integral length scale with increasing velocity.

Figure 4.15 shows the Taylor micro-scale profile for  $U_\infty = 9 \text{ m/s}$  at different streamwise and normal locations. Typical uncertainties in Taylor micro scale are approximately  $0.08 \text{ cm}$ , shown as an error bar for the point  $X/H = 2, Y/H = 0.2$  at  $9 \text{ m/s}$  free stream velocity. For the smooth wall, Taylor micro-scales were calculated for  $X/H \geq 20$ , as at lower values of  $X/H$ , the boundary layer was still laminar and thin. As can be seen for the smooth wall, the Taylor micro-scale was larger near the solid surface ( $Y/H = 0.2$ ) and decreased with normal distance ( $Y/H = 1$ ). However, the small number of measuring points inside the smooth wall boundary layer and high level of uncertainty in the calculations make it difficult to draw a solid conclusion.

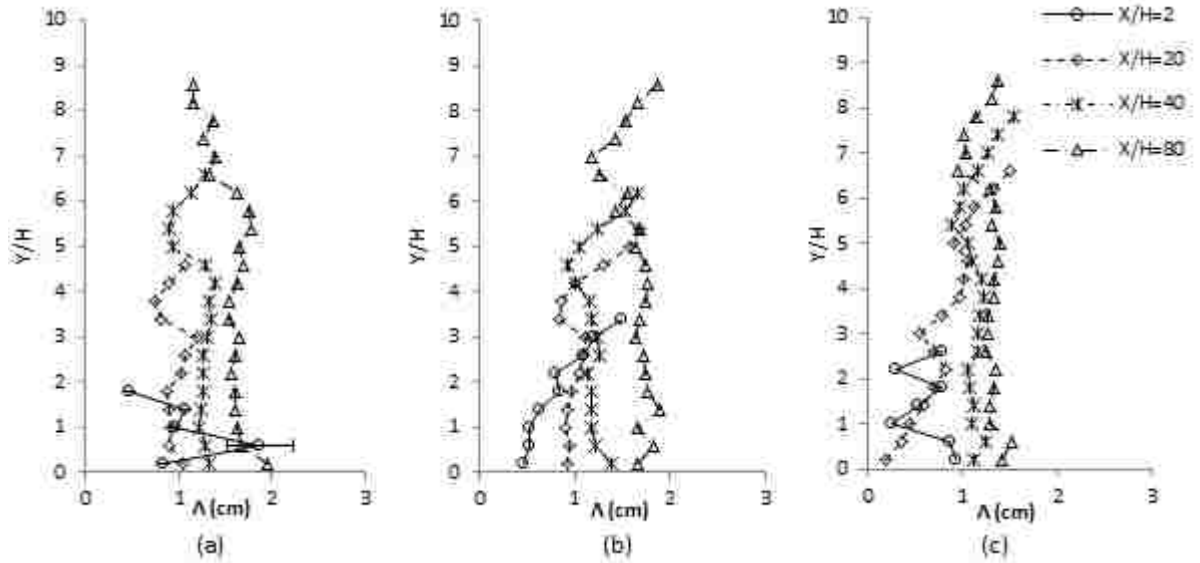


Figure 4.14 Ribbed wall Integral length scale at (a)  $U_\infty = 4$  m/s (b)  $U_\infty = 6.8$  m/s (c)  $U_\infty = 9$  m/s

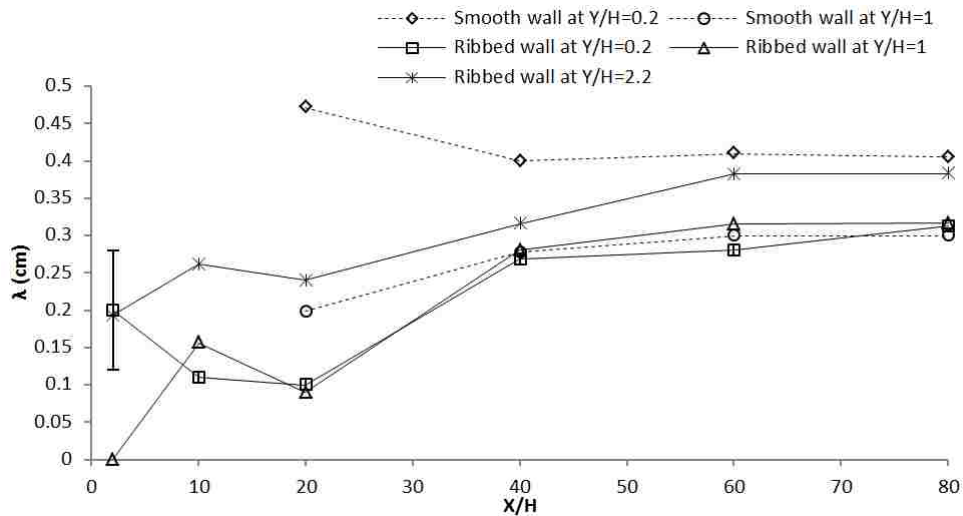


Figure 4.15 Taylor micro-scale in the boundary layer at  $U_\infty = 9$  m/s

For the ribbed wall a different trend is seen, wherein the Taylor micro-scale appears to increase from the surface to the edge of the boundary layer ( $Y/H = 2.2$ ). The increase from  $Y/H = 0.2$  to  $2.2$  corroborates with the reduction in turbulence intensity (Figure 4.9 (c)); even though the increase is of the same order as the experimental uncertainties. After  $X/H = 20$ , a general trend of increasing Taylor micro-scales with streamwise distance was observed in the ribbed wall, which seems to confirm the turbulence decay. The generally decreasing trend for  $2 \leq X/H \leq 10$  for the ribbed wall  $\lambda$  trend suggests that the turbulence was still being generated in this region. But again, it should be noted that the uncertainty in these estimates is high.

Comparing smooth and ribbed walls shows that the rib caused the Taylor micro-scale to decrease, especially next to the wall; nevertheless, the difference was no more than the experimental uncertainty. Due to the thickening of the boundary layer and higher turbulence generated near the surface of the ribbed wall as discussed earlier, small eddies were extended farther away from the surface ( $Y/H = 2.2$ ).

Table 4.1 Average integral length scale at streamwise locations of the ribbed wall

		X/H=2	X/H=10	X/H=20	X/H=40	X/H=60	X/H=80
$U_\infty = 4 \text{ m/s}$	$\Lambda_{\text{ave}} \text{ (cm)}$	1.0	1.1	1.0	1.2	1.5	1.6
	$\text{Re}_{(X+0.055)}$	$1.7 \times 10^4$	$2.7 \times 10^4$	$4.1 \times 10^4$	$6.7 \times 10^4$	$9.4 \times 10^4$	$1.2 \times 10^5$
$U_\infty = 6.8 \text{ m/s}$	$\Lambda_{\text{ave}} \text{ (cm)}$	0.8	0.9	1.1	1.3	1.6	1.7
	$\text{Re}_{(X+0.055)}$	$2.9 \times 10^4$	$4.7 \times 10^4$	$7 \times 10^4$	$1.1 \times 10^5$	$1.6 \times 10^5$	$2 \times 10^5$
$U_\infty = 9 \text{ m/s}$	$\Lambda_{\text{ave}} \text{ (cm)}$	0.6	0.8	0.9	1.1	1.2	1.3
	$\text{Re}_{(X+0.055)}$	$3.8 \times 10^4$	$6.3 \times 10^4$	$9.2 \times 10^4$	$1.5 \times 10^5$	$2.2 \times 10^5$	$2.8 \times 10^5$

#### 4.4. Conclusion

The boundary layer developing behind a surface-mounted triangular rib and a smooth wall boundary layer were experimentally investigated and compared. Time-averaged velocity profiles, turbulence intensity and length scales at three different free stream velocities (4, 6.8 and 9 m/s) and downstream distances from  $X/H = 2$  to 80 were analyzed. The velocity profile was found to be significantly affected by the rib throughout the relatively large extent of streamwise distance considered ( $X/H$  up to 80). The rib-perturbed boundary layer was observed to be 3 ~ 3.5 times thicker compared to the smooth wall boundary layer at the same free stream velocity. Also, both logarithmic and wake regions were affected by the presence of the rib. In addition, the rib significantly enhanced  $Tu$ , and this enhancement propagated beyond the boundary layer. The integral length increased inside the boundary layer in the presence of the rib, mostly due to thickening of the boundary layer while the Taylor micro-scale decreased confirming the intensification of turbulence. All of these effects: velocity profiles indicating a larger boundary layer, higher turbulence intensity, larger integral length and smaller Taylor micro-scales near the surface, are predicted to affect the convective heat transfer from the surface, compared with the smooth wall.

#### Acknowledgment

This work was made possible by the Ontario Trillium Foundation and the Natural Sciences and Engineering Research Council of Canada.

## **References**

- [1] Saha, A.K., and Acharya, S., 2005, “Unsteady RANS Simulation of Turbulent Flow and Heat Transfer in Ribbed Coolant Passages of Different Aspect Ratios,” *Int. J. Heat Mass Transfer*, 48(23-24), pp. 4704–4725.
- [2] Panigrahi, P.K., and Acharya, S., 2004, “Multi-Modal Forcing of the Turbulent Separated Shear Flow Past a Rib,” *ASME J. Fluid Eng.*, 126(1), pp. 22–31.
- [3] Bhagoria, J.L., Saini, J.S., and Solanki, S.C., 2002, “Heat Transfer Coefficient and Friction Factor Correlations for Rectangular Solar Air Heater Duct Having Transverse Wedge Shaped Rib Roughness on the Absorber Plate,” *Renew. Energy*, 25(3), pp. 341–369.
- [4] Mittal, M.K., Varun, Saini, R.P., and Singal, S.K., 2007, “Effective Efficiency of Solar Air Heaters Having Different Types of Roughness Elements on the Absorber Plate,” *Energy*, 32(5), pp. 739–745.
- [5] Chamoli, S., Thakur, N.S., and Sain, J.S., 2012, “A Review of Turbulence Promoters Used in Solar Thermal Systems,” *Renew. Sustainable Energy Rev.*, 16(5), pp. 3154–3175.
- [6] Thianpong, C., Chompookham, T., Skullong, S., and Promvong, P., 2009, “Thermal Characterization of Turbulent Flow in a Channel with Isosceles Triangular Ribs,” *Int. Comm. Heat Mass Transfer*, 36(7), pp. 712–717.
- [7] Chun, S.J., Liu, Y.Z., and Sung, H.J., 2004, “Wall Pressure Fluctuations of a Turbulent Separated and Reattaching Flow Affected by an Unsteady Wake,” *Exp. Fluids*, 37(4), pp. 531–546.
- [8] Liu, Y.Z., Kang, W., and Sung, H.J., 2005, “Assessment of the Organization of a Turbulent Separated and Reattaching Flow by Measuring Wall Pressure Fluctuations,” *Exp. Fluids*, 38(4), pp. 485–493.
- [9] Panigrahi, P.K., and Acharya, S., 2005, “Excited Turbulent Flow behind a Square Rib,” *J. Fluid Struct.*, 20 (2), pp. 235–253.
- [10] Bergeles, G., and Athanassiadis, N., 1983, “The Flow Past a Surface-Mounted Obstacle,” *ASME J. Fluid Eng.*, 105(4), pp. 461–463.
- [11] Fragos, V.P., Psychoudaki, S.P., and Malamataris, N.A., 2012, “Two-Dimensional Numerical Simulation of Vortex Shedding and Flapping Motion of Turbulent Flow around a Rib,” *Comput. Fluids*, 69, pp. 108–121.
- [12] Acharya, S., and Panigrahi, P.K., 2003, “Analysis of Large Scale Structures in Separated Shear Layers,” *Exp. Thermal Fluid Sci.*, 27(7), pp. 817–828.
- [13] Panigrahi, P.K., and Acharya, S., 1996, “Spectral Characteristics of Separated Flow behind a Surface-Mounted Square Rib,” Paper 96–1931, 27th Fluid Dynamics Conference, American Institute of Aeronautics and Astronautics (AIAA), New Orleans, LA.



- [14] Liu, Y.Z., Ke, F., and Sung, H.J., 2008, "Unsteady Separated and Reattaching Turbulent Flow over a Two-Dimensional Square Rib," *J. Fluid Struct.*, 24(3), pp. 366-381.
- [15] Kamali, R., and Binesh, A.R., 2008, "The Importance of Rib Shape Effects on the Local Heat Transfer and Flow Friction Characteristics of Square Ducts with Ribbed Internal Surfaces," *Int. Comm. Heat Mass Transfer*, 35(8), pp. 1032-40.
- [16] Patil, A.K., Saini, J.S., and Kumar, K., 2012, "A Comprehensive Review on Roughness Geometries and Investigation Techniques Used in Artificially Roughened Solar Air Heaters," *Int. J. of Renew. Energy Res.*, 2(1), pp. 1-15.
- [17] Promvong, P., and Thianpong, C., 2008, "Thermal Performance Assessment of Turbulent Channel Flows over Different Shaped Ribs," *Int. Comm. Heat Mass Transfer*, 35(10), pp. 1327-1334.
- [18] Liou, T.M., and Hwang, J.J., 1993, "Effect of Ridge Shapes on Turbulent Heat Transfer and Friction in a Rectangular Channel," *Int. J. Heat Mass Transfer*, 36(4), pp. 931-40.
- [19] Ahn, S. W., 2001, "The Effects of Roughness Types on Friction Factors and Heat Transfer in Roughened Rectangular Duct," *Int. Comm. Heat Mass Transfer*, 28(7), pp. 933-942.
- [20] Acharya, S., Dutta, S., Myrum, T.A., and Baker, R.S., 1994, "Turbulent Flow Past a Surface-Mounted Two-Dimensional Rib," *ASME J. Fluid Eng.*, 116(2), pp. 238-246.
- [21] Hwang, R. R., Chow, Y. C., and Chiang, T. P., 1999, "Numerical Predictions of Turbulent Flow over a Surface-Mounted Rib," *J. Eng. Mech.*, 125(5), pp. 497-503.
- [22] Antoniou, J., Bergeles, G., 1988, "Development of the Reattachment Flow behind Surface-Mounted Two-Dimensional Prisms," *ASME J. Fluid Eng.*, 110(2), pp. 127-133.
- [23] Acharya, S., Myrum, T.A., and Dutta, S., 1998, "Heat Transfer in Turbulent Flow Past a Surface-Mounted Two-Dimensional Rib," *ASME J. Heat Trans.*, 120(3), pp. 550-562.
- [24] Incropera, F.P., and DeWitt, D.P., 1996, *Fundamentals of Heat and Mass Transfer*, 3rd ed., John Wiley and Sons, New York, USA.
- [25] Jørgensen, F. E., 2002, "How to Measure Turbulence with Hot-Wire Anemometers - a Practical Guide," Dantec Dynamics, Skovlunde, Denmark.
- [26] Figliola, R.S., and Beasley, D.E., 2011, *Theory and Design for Mechanical Measurements*, 5th edition, John Wiley and Sons, Inc., New York, USA.
- [27] Tariq, A., Panigrahi, P.K., and Muralidhar, K., 2004, "Flow and Heat Transfer in the Wake of a Surface-Mounted Rib with a Slit," *Exp. Fluids*, 37(5), pp. 701-719.
- [28] Clauser, F.H., 1956, "Turbulent Boundary Layer," *Adv. Appl. Mech.*, 4, pp. 1-51.

- [29] Shin, J. H., and Song, S. J., 2015, "Pressure Gradient Effects on Smooth- and Rough-Surface Turbulent Boundary Layers—Part I: Favorable Pressure Gradient," *ASME J. Fluid Eng.*, 137(1), pp. 011203-1-9.
- [30] Shin, J. H., and Song, S. J., 2015, "Pressure Gradient Effects on Smooth- and Rough-Surface Turbulent Boundary Layers—Part II: Adverse Pressure Gradient," *ASME J. Fluid Eng.*, 137(1), pp. 011204-1-7.
- [31] Antonia, R. A., and Luxton, R. E., 1972, "The Response of a Turbulent Boundary Layer to a Step Change in Surface Roughness. Part 2. Rough-to-Smooth," *J. Fluid Mech.*, 53(4), pp. 737-757.
- [32] DeGraaff, D.B., and Eaton, J.K., 2000, "Reynolds-Number Scaling of the Flat-Plate Turbulent Boundary Layer," *J. Fluid Mech.*, 422, pp. 319-346.
- [33] Hancock, P. E., and Bradshaw, P., 1983, "The Effect of Free-Stream Turbulence on Turbulent Boundary Layer," *ASME J. Fluid Eng.*, 105(3), pp. 284-289.
- [34] Sucec, J., 2014, "An Integral Solution for Skin Friction in Turbulent Flow over Aerodynamically Rough Surfaces with an Arbitrary Pressure Gradient," *ASME J. Fluid Eng.*, 136(8), pp. 081103-1-8.
- [35] Saturdi, and Ching, C.Y., 1999, "Effect of a Transverse Square Groove on a Turbulent Boundary Layer," *Exper. Thermal Fluid Sci.*, 20(1), pp. 1-10.
- [36] Barrett, M. J., and Hollingsworth, D. K., 2001, "On the Calculation of Length Scales for Turbulent Heat Transfer Correlation," *J. Heat Transfer*, 123(5), pp. 878-883.
- [37] Carullo, J. S., Nasir, S., Cress, R. D., Ng, W. F., Thole, K. A., Zhang, L. J., and Moon, H. K., 2011, "The Effects of Freestream Turbulence, Turbulence Length Scale, and Exit Reynolds Number on Turbine Blade Heat Transfer in a Transonic Cascade," *J. Turbomach.*, 133(1), pp. 011030-1-11.
- [38] Sak, C., Liu, R., Ting, D.S-K., and Rankin, G.W., 2007, "The Role of Turbulence Length Scale and Turbulence Intensity on Forced Convection from a Heated Horizontal Circular Cylinder," *Exper. Thermal Fluid Sci.*, 31(4), pp. 279-289.
- [39] Hinze, J.O., 1975, *Turbulence*, 2nd ed., McGraw-Hill, New York, USA, ISBN 0-07-029037-7.
- [40] Taylor, G.I., 1938, "The Spectrum of Turbulence," *Proc. R. Soc. London, Series A*, 164, pp. 476-490.
- [41] Dennis D. J. C., and Nickels, T. B., 2008, "On the Limitations of Taylor's Hypothesis in Constructing Long Structures in a Turbulent Boundary Layer," *J. Fluid Mech.*, 614, pp. 197-206.
- [42] Lin, C.C., 1953, "On Taylor's Hypothesis and the Acceleration Terms in the Navier-Stokes Equation," *Quart. Appl. Math.*, 10(4), pp. 295-306.

[43] Lumley, J.L., 1965, "Interpretation of Time Spectra Measured In High-Intensity Shear Flows," *Phys. Fluids*, 8(6), pp. 1056–1062.

[44] Bultjes, P.J.H., 1975, "Determination of the Eulerian Longitudinal Integral Length Scale in a Turbulent Boundary Layer," *Appl. Sci. Res.*, 31(5), pp. 397-399.

## CHAPTER 5

### FLAT PLATE CONVECTION HEAT TRANSFER ENHANCEMENT VIA A SQUARE

#### RIB

##### ***5.1. Introduction***

Wall bounded roughness elements such as ribs are often employed in different industrial applications such as gas turbine blade cooling passages, heat exchangers, and solar collectors [1-6]. Boundary layer separation and reattachment over a ribbed wall creates various flow features that affect the heat transfer and friction of the surface [7]. Analyzing the flow over a ribbed wall and its effect on the heat transfer rate is complex and requires careful scrutiny [8], but is essential in designing ribbed-surface cooling systems [9].

The flow mechanism over a square rib has been extensively studied because of its complexity [2, 10-16] and potential to be applied in industry [1, 17]. At approximately  $1 \sim 2H$  before the rib (where  $H$  is the rib's height), the flow separates, sweeps past the rib and then reattaches at  $5.5 \sim 10H$  downstream [11,13,18,19]. The flow disturbance caused by rib arrays greatly increases the production of turbulent kinetic energy [20]. Other than promoting turbulence, the rib is also a vortex generator. Coherent vortices are shed from the rib edge into the wake region after the rib [11, 21]. The two identified flow features of the ribbed wall: higher turbulence energy and vorticity generation, seem to be effective in enhancing the wall heat transfer [22]. Flow and heat transfer mechanisms over the ribbed surfaces have been investigated together in some studies to understand the effect of different flow features on the surface heat transfer. Some of these studies are described in the following paragraphs.

Tariq et al. [22] investigated the flow and heat transfer of a flat plate in the wake of a surface-mounted square rib with and without a slit. They reported a detailed flow and heat transfer mechanism for a single ribbed plate. Different flow parameters and their correlation with heat transfer enhancement were studied. For a solid rib, in the area just behind the rib, the heat transfer rate was observed to be reduced. This was postulated to be due to flow recirculation in this area, preventing effective mixing. Farther downstream, due to the reduction in the vertical extent of the recirculation zone and the improved closeness of the wall to the cold fluid, the heat transfer rate increased. The heat transfer rate reached a maximum when the separated flow reattached to the wall surface and the boundary layer reinitiated. After reattachment, the development of this boundary layer led to a reduction in surface heat transfer rate. A slit in the rib with an open area less than 30% had a positive impact on the surface heat transfer enhancement and reduced the pressure penalty compared to the solid rib case. It was observed that the heat transfer enhancement correlated with the normal velocity and its temporal fluctuation.

Moon et al. [20] studied the heat transfer performance of rib-roughened rectangular cooling channels having a variety of cross-sectional rib shapes. A specific design (boot-shaped rib) showed the best heat transfer performance. It was seen that the reattachment length had a huge effect on the overall heat transfer rate, where a smaller separation zone caused a higher heat transfer rate.

Ali et al. [8] investigated the flow and heat transfer behind square and trapezoidal ribs with different angles using PIV and liquid crystal thermography (LCT) methods. Two recirculation bubbles were observed after the ribs, a large one downstream of the rib and a small secondary one in the leeward corner of the rib which disappeared at higher Reynolds numbers. For all studied rib shapes, a decreasing augmentation in Nusselt number with respect to the smooth surface was observed with increasing Reynolds number. Also, it was seen that the location of the maximum heat transfer did not match exactly with the reattachment point, based on the flow measurements.

Effect of the rib orientation on a square channel's surface heat transfer was examined experimentally by Smulsky et al. [23]. Experiments were carried out for rib orientation angles relative to the flow varying from  $50^\circ$  to  $90^\circ$  and for three values of rib height. The effect of the rib's orientation angle on the pattern of vortex formation, pressure fields and heat transfer was explored at different Reynolds numbers depending on the obstacle height. It was seen that a decrease in the angle of rib orientation relative to the flow caused the coordinates of the attachment area, pressure and heat transfer maxima to move towards the rib. Heat transfer enhancement was prompted by the reduction of the recirculation zone.

Terekhov et al. [24] experimentally studied the gas flows past a rib and past a downward step. Flow and heat transfer characteristics such as separation-flow regions, and distributions of pressures, temperatures, and heat-transfer coefficients behind the obstacles were analyzed. Also, a comparative analysis of the heat transfer enhancement by ribs and steps was performed. It was seen that ribs were more effective in enhancing the heat transfer than steps.

In addition, the effect of enhanced external turbulence on thermal and flow characteristics was studied. Enhanced external turbulence led to a reduction in separation region size and an enhancement in the local heat transfer behind the obstacles.

Kamali and Binesh [9] numerically studied the flow and heat transfer characteristics of a square duct with four different rib shapes; square, triangular, and trapezoidal with decreasing or increasing height in the flow direction. It was observed that the square rib case was the most complex case in flow analysis because there were two clear recirculation zones at both the front and back of the rib. However, the trapezoidal rib had the largest recirculation zone while the square rib had the smallest one. For the range of studied Reynolds numbers, the trapezoidal shaped rib with decreasing height in the flow direction had the highest value of heat transfer.

While many studies investigated the effect of the rib design on the flow and heat transfer, a detailed study on the impact of a single rib on the flow physics would seem to be helpful in understanding the mechanisms associated with ribbed surfaces' heat transfer enhancement. The present study investigated the flow mechanism and heat transfer over a flat plate downstream of a single square rib placed near the plate leading edge, compared to the basic flat plate case. The emphasis was toward analyzing the impact of the rib on the flow structure and its probable correlation with the surface heat transfer enhancement. To this end, heat transfer enhancement of the ribbed surface was studied at different Reynolds numbers. An attempt was made to relate the changes in different measured parameters to the heat transfer enhancement, in changing from smooth to ribbed surfaces and also with changing  $Re_H$ .

## Nomenclature

$h$	convection heat transfer coefficient ( $\text{W}/\text{m}^2\cdot\text{K}$ )	$U$	local streamwise velocity (m/s)
$H$	rib height (m)	$U_i$	instantaneous streamwise velocity (m/s)
$k$	thermal conductivity of the fluid ( $\text{W}/\text{m}\cdot\text{K}$ )	$U_\infty$	free stream velocity (m/s)
$k_{\text{PTFE}}$	thermal conductivity of the PTFE layer ( $\text{W}/\text{m}\cdot\text{K}$ )	$u_i$	Instantaneous streamwise velocity fluctuation (m/s)
$N$	number of instantaneous measurements	$u_{\text{rms}}$	root-mean-square of the streamwise velocity fluctuations (m/s)
$Nu$	Nusselt number ( $h\cdot X/k$ )	$\overline{u\bar{v}}$	Reynolds shear stress ( $\text{m}^2/\text{s}^2$ )
$Nu/Nu_0$	Nusselt enhancement with respect to the smooth surface	$V$	local normal velocity (m/s)
$Re_H$	Reynolds number based on the rib height ( $H$ )	$V_i$	instantaneous normal velocity (m/s)
$t$	PTFE layer thickness (m)	$v_i$	instantaneous normal velocity fluctuation (m/s)
$T$	time (s)	$v_{\text{rms}}$	root-mean-square of the normal velocity fluctuations (m/s)
$T_{\text{air}}$	air temperature ( $^\circ\text{C}$ )	$X$	streamwise distance from the rib (m)
$T_{\text{Al}}$	local surface temperature of the Al plate ( $^\circ\text{C}$ )	$Y$	normal distance from the plate (m)
$T_{\text{Tef},1}$	temperature of the bottom surface of the PTFE layer ( $^\circ\text{C}$ )	$Z$	distance along the width of the plate from the plate centerline (m)
$T_{\text{Tef},2}$	temperature of the top surface of the PTFE layer ( $^\circ\text{C}$ )		

## 5.2. Apparatus and Instrumentation

All experimental data for the present investigation were obtained in a wind tunnel with a 180 cm long, 76 cm high and 77 cm wide test section. The maximum free stream velocity in this wind tunnel is around 30 m/s and the background turbulence intensity is less than 0.4% when the test section is empty.

A schematic of the experimental setup used in this study is shown in Figure 5.1. The total plate dimensions were 30.5 cm wide, 65 cm long and 1 cm thick. As shown, the setup consisted of a flat aluminum (Al) plate with underlying thermocouples, over top of a thin layer of Teflon (PTFE) under which was another layer of thermocouples. Below that there was a silicone-rubber heat sheet (electrical heating layer) covered on its top by aluminum foil to better distribute the heat. This sat atop a layer of flexible ceramic insulation (93315K51, McMaster, USA). It should be noted that, whatever heat flux passes through the Teflon layer is assumed to pass through the top aluminum plate into the convective air over the plate. The thermocouple-PTFE-thermocouple sandwich acted as a heat flux sensor, embedded in the panel so that there was no disturbance to the airflow over the plate as a result of externally attached heat flux sensors. Fifty-six T-type thermocouples were

used on both sides of the PTFE layer from  $X/H = 2$  to 54 to measure the temperature difference. A close view of different layers of the set-up can be seen in Figure 5.2. The 1 mm open space on the top and bottom between the PTFE layer and the two aluminum layers, caused by the thermocouple wires, was filled with a layer of heat conductive epoxy glue (OMEGA, OB-200,  $k = 1.35 \text{ W/m-K}$ ). It was important that the thermocouple locations were aligned vertically, so that local heat fluxes could be measured. The flowing air temperature was measured by a T-type thermocouple, which was installed under the set-up on the support system to avoid being heated by the electrical heating layer.

Heat flux to the sides in the gap between the Teflon and aluminum layers was checked by some thermocouples placed 3 cm distance from the centerline, which can be seen in Figure 5.1. The temperature difference between these thermocouples and that of the centerline was small, which caused the calculated heat flux to the sides to be negligible ( $\sim 5\%$ ) compared to the total heat flux from the heater. Thus, it can be assumed that all the heat flux passing through the Teflon layer reached the aluminum layer with 95% accuracy.

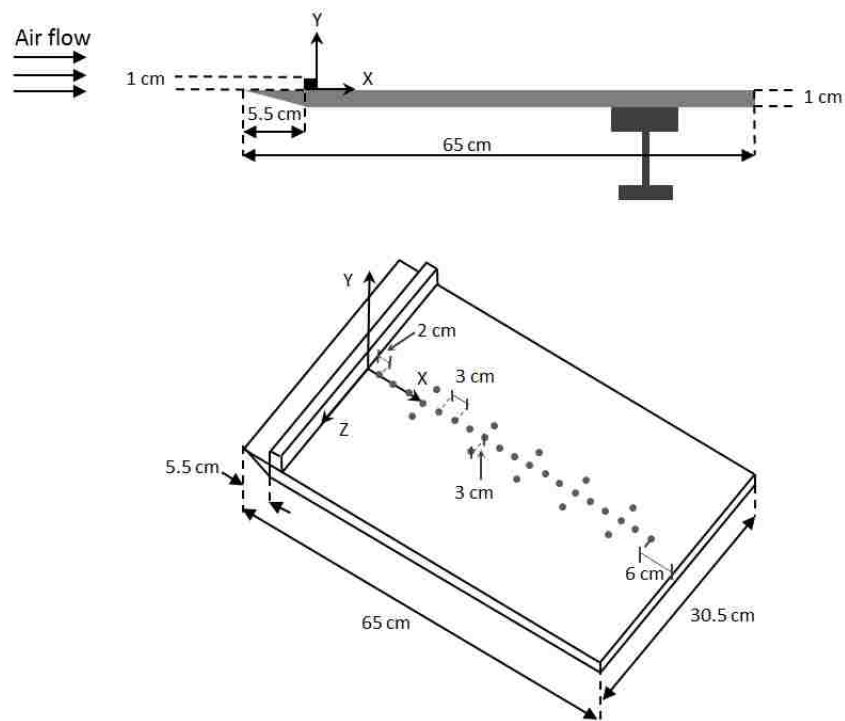


Figure 5.1 Set-up schematic

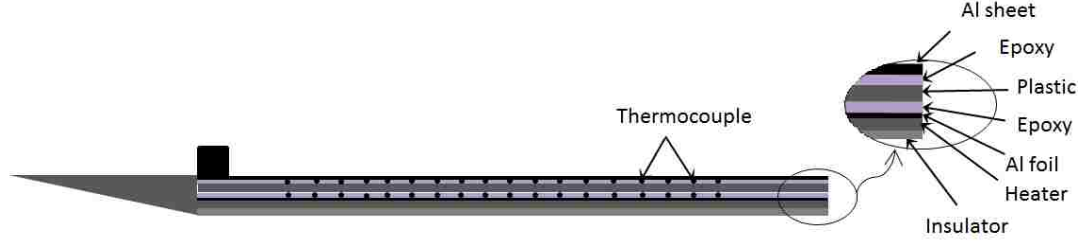


Figure 5.2 Set-up close view

X, Y and Z were the streamwise, normal to the plate and widthwise directions, respectively, with the origin located at the middle of the downstream edge of the rib. As can be seen in Figure 5.1, a  $10^\circ$  angle wedge was cut from wood and attached to the set-up leading edge in order to reduce the effect of the blunt edge. A square rib with a 1 cm dimension was placed on the set-up surface at the upstream end of the heating section ( $X = 0$ ).

The plate was placed at mid-height in the middle of the test section with the plate and support system creating a blockage of around 2% of the tunnel cross section. The velocity was varied to result in at four different Reynolds numbers based on the rib's height,  $Re_H = 1.3 \times 10^3$ ,  $2.6 \times 10^3$ ,  $5 \times 10^3$ , and  $6.3 \times 10^3$ , each tested with and without the rib. To reach a thermal steady-state condition, the heated set-up was placed in the wind tunnel for around two hours before acquiring the data. Temperatures were checked every couple of minutes until the temperature stabilized to within  $0.2^\circ\text{C}$ .

The convective heat transfer coefficient from the plate surface was calculated at each thermocouple's location from  $X/H = 2$  to 54 as follows:

$$h = \frac{k_{PTFE} \times \frac{T_{Tef,1} - T_{Tef,2}}{t}}{T_{Al} - T_{air}} \quad (5.1)$$

where  $k_{PTFE}$  is the thermal conductivity of the PTFE layer ( $0.25 \text{ W/m}\cdot\text{K}$ ) and  $t$  is its thickness (3 mm).  $T_{Tef,1}$  and  $T_{Tef,2}$  are temperatures of the bottom and top surfaces of the PTFE layer respectively. Also,  $T_{air}$  is the air temperature.  $T_{Al}$  is the local surface temperature of the Al plate, which was not measured in this experiment; but it was estimated based on the heat flux and predicted temperature difference between the PTFE's top surface and the Al top surface. At the average heat flux from the heater to the top Al plate in the experiment, 500 W, this temperature difference was calculated to be 0.7 K.

In the above calculation (Eq (5.1)), the heat transfer on the aluminum plate assumed to be solely in Y-direction, as the heat transfer was studied on the set-up center line which was far enough from the edges to avoid the edge effects. However, this assumption was checked by the side thermocouples and the temperature difference was smaller than 0.5 K (i.e. within the range of uncertainty of the thermocouples).



Streamwise and normal (X and Y) velocities at different points downstream of the rib were measured by a fiber film X-probe (type 55R51) with a Dantec streamline 55C90 constant-temperature anemometer (CTA). The probe had two Nickel wires with diameters of 70  $\mu\text{m}$  and lengths of 1.25 mm. Signals were low-passed at 30 kHz and then sampled at 80 kHz over a period of around 12.5 s, resulting in  $10^6$  data points per measurement. A 12-bit PCI-6071E National Instrument data acquisition card was used to convert the analog signal into a digital one. A computer-controlled 2-D traverse system was used to position the probe at each specified location. The computer-controlled traverse system was able to move through the widthwise direction of the test section (Z) and the direction normal to the plate (Y).

In flow studies the emphasis was placed on the region right immediately downstream of the rib, where the rib disturbance is most pronounced. Thus, velocity measurements were performed downstream of the rib at five streamwise locations;  $X/H = 2, 5, 8, 21, 30$  and at  $Z = 0$  (Figure 5.1). Measurements at each streamwise location were made from  $Y/H = 0.5$  to 5, every 0.2 cm. At  $Re_H = 1.3 \times 10^3$  and  $6.3 \times 10^3$ , tests were repeated for the ribbed and smooth plates with particular emphasis on the near-plate region ( $Y/H = 0.5$  to 1.9).

Local velocities in X and Y directions are the time average of the instantaneous velocities at that point [25]:

$$U = \frac{1}{N} \sum_{i=1}^N U_i \quad (5.2)$$

and

$$V = \frac{1}{N} \sum_{i=1}^N V_i \quad (5.3)$$

where N is the number of instantaneous measurements ( $N = 10^6$ ).

Turbulence fluctuation intensities in X and Y directions are defined as the standard deviation, or root-mean-square (rms), of the velocity fluctuations, normalized by the free stream velocity ( $U_\infty$ ) [25]:

$$u_{\text{rms}}/U_\infty = \sqrt{\sum_{i=1}^N \frac{(u_i)^2}{N}} / U_\infty \quad (5.4)$$

and

$$v_{\text{rms}}/U_\infty = \sqrt{\sum_{i=1}^N \frac{(v_i)^2}{N}} / U_\infty \quad (5.5)$$

where  $u_i$  and  $v_i$  are the streamwise and normal velocity fluctuations, which are the deviations of the instantaneous from the time-averaged velocities.

Reynolds shear stress is the cross correlation between the streamwise and normal velocity fluctuations [23]:

$$\overline{uv} = \sum_{i=1}^N \frac{u_i v_i}{N} \quad (5.6)$$

As the hot-wire probe is incapable of differentiating the flow direction this poses a challenge when qualifying the velocity in the recirculation region after the rib [22]. A method was developed in this study to modify the data measured by the hot-wire probe in the streamwise direction to partially overcome this weakness. A Matlab code was written to modify the measured streamwise velocity data during the data reduction. This methodology will be explained in detail in the “Results and Discussion” section.

A noise was detected in the hot-wire flow measurements at a couple of points; it was removed from the velocity signals.

The total uncertainty associated with each parameter consists of bias and precision uncertainties [25, 26]. Bias or systematic uncertainty of the hotwire-measured instantaneous velocities was estimated according to Jørgensen [25]. The velocity measurement bias consisted of calibration, data acquisition and data reduction uncertainties. Precision uncertainty, which concerns the repeatability of the test, was derived from Student’s t distribution method with a 95% confidence interval [26].

Bias in temperature measurements was assumed to be due just to the thermocouples (T-type thermocouple). In temperature measurements, the precision uncertainty was observed to be smaller than the bias, so the total estimated temperature uncertainty was just based on the bias of the thermocouples ( $\pm 0.5^\circ\text{C}$ ). The uncertainty in convection heat transfer coefficient ( $h$ ) was estimated to be  $9.1 \text{ (W/m}^2\text{K)}$ , from the temperature difference uncertainty ( $\pm 0.7^\circ\text{C}$ ). The Nusselt number uncertainty was estimated based on the  $h$  uncertainty and uncertainty in the streamwise location of the thermocouples. The uncertainty in positioning the thermocouples was estimated to be around  $\pm 1.2 \text{ mm}$ , consisting of the ruler and human errors. The estimated uncertainty of the Nusselt number and its enhancement ( $\text{Nu}/\text{Nu}_0$ ) were 90 and 0.2, respectively.

The uncertainty in streamwise ( $U$ ) and normal velocities ( $V$ ) and their normalized forms ( $U/U_\infty$  and  $V/U_\infty$ ) at point  $Y/H = 0.9$  in Figure 4.6 (a) ( $X/H = 2$ ) were estimated to be around  $\pm 0.2 \text{ m/s}$ ,  $\pm 0.05 \text{ m/s}$ ,  $\pm 0.03$  and  $\pm 0.008$ , respectively, mostly due to the precision uncertainty. Uncertainty in turbulent normal stresses,  $u_{\text{rms}}$  and  $v_{\text{rms}}$ , and their normalized forms,  $u_{\text{rms}}/U_\infty$  and  $v_{\text{rms}}/U_\infty$ , were also estimated to be  $\pm 0.08 \text{ m/s}$ ,  $\pm 0.03 \text{ m/s}$ ,  $\pm 0.015$  and  $\pm 0.005$ , respectively. These uncertainty values were very small compared to the symbols in the plots, so error bars were not added. The uncertainty in probe positioning in the  $Y$  direction by the traverse system was estimated to be approximately  $1.2 \text{ mm}$ .

### 5.3. Results and Discussion

The flow over the plate and the heat transfer were investigated both without and with the leading edge rib, and results are presented in this section. The surface heat transfer enhancement with respect to the smooth surface was characterized in terms of the normalized Nusselt number,

$Nu/Nu_0$ , where  $Nu_0$  corresponds to the reference case in the absence of the rib. The heat transfer measurements were performed at four different Reynolds numbers.

In order to investigate the detailed flow physics after the rib, different flow and turbulence parameters such as normalized mean velocities, and normal and shear turbulence stresses were detailed for the middle studied Reynolds numbers ( $Re_H = 2.6 \times 10^3$ ). In addition, at the lowest and highest studied Reynolds numbers, flow and turbulence parameters over the smooth and ribbed wall cases were studied and the results were compared.

### 5.3.1. Heat Transfer Results

Local, normalized Nusselt numbers are plotted against the non-dimensional streamwise distance from the rib ( $X/H$ ) in Figure 5.3. Surface heat transfer was studied at different air velocities which are presented in the form of rib's height Reynolds number ( $Re_H$ ). It is seen that the Nusselt number in the presence of the rib was consistently higher than that for the smooth plate ( $Nu/Nu_0 > 1$ ), except for the first measured point immediately downstream of the rib at  $Re_H = 5 \times 10^3$  and  $6.3 \times 10^3$ . This may be due to the significant blockage effect of the rib on the flow at higher velocities. Thus, in spite of the relatively large uncertainty in  $Nu/Nu_0$  ( $U_{Nu/Nu_0} \approx 0.2$ ), it is still can be concluded that the rib was effective in enhancing the heat transfer from the plate, as the estimated uncertainty was based on the worst case scenario.

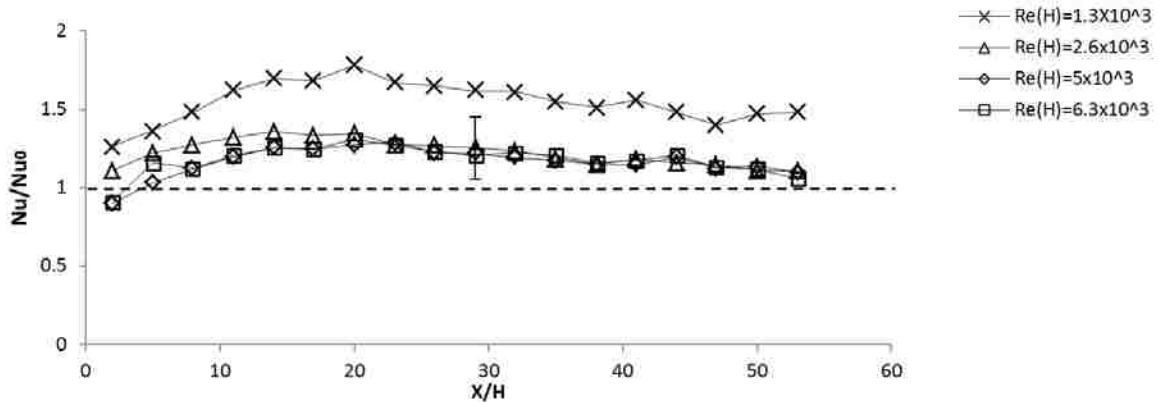


Figure 5.3 Streamwise Nusselt number enhancement at different Reynolds numbers

The variation of the local Nu augmentation can be clearly tracked in Figure 5.3. The spatial trend of the Nusselt number roughly demonstrates the flow separation, reattachment and then redevelopment of the plate boundary layer. It can be observed that immediately behind the rib, the Nusselt ratio was low, which shows the wake region where the fluid was not mixed with the prevailing flow. The Nusselt number ratio increased in the streamwise direction, peaked at around  $X/H = 10$  to  $20$  for all  $Re_H$  and subsequently decreased farther downstream. The initial increasing trend was presumably due to the reduction in the vertical extent of the recirculation zone leading to the cold bulk fluid being brought closer to the plate and the heated fluid adjacent to the surface. The maximum point in the Nu approximately indicates the reattachment of the flow after the rib

[22]. However, in the study by Ali et al. [8] the maximum heat transfer point distance was 10-12% greater than the reattachment distance as determined by PIV velocity measurements. In their study, the reattachment point was identified based on the zero horizontal velocity region, which is a generally accepted indicator of reattachment in the literature [8,11,27]. This over-prediction of the reattachment point by using the maximum heat transfer point was said to be due to the sweeping flow, which emanated from the surface immediately after the reattachment point, and which shifted the maximum heat transfer area downstream [8]. Knowing that the maximum heat transfer location does not correspond precisely with the reattachment point, the reattachment region of the flow likely occurred before  $X/H = 20$  for all of the  $Re_H$ . Figure 5.3 also shows that the reduction in Nusselt ratio after the peak point was slow.

As mentioned, for the range of studied Reynolds numbers, the rib was effective in enhancing the heat transfer rate from the surface, over a relatively long span (up to  $X/H = 54$ ). For the lowest tested  $Re_H$  of  $1.3 \times 10^3$ ,  $Nu/Nu_0$  remained high at roughly 1.5 over an extended distance after it peaked at  $X/H = 20$  with a value of around 1.7. At higher Reynolds numbers, the enhancement with respect to the un-ribbed base was much lower (no more than 1.3). Interestingly, the data corresponding to the three higher  $Re_H$  ( $2.6$ ,  $5$  and  $6.3 \times 10^3$ ) collapse onto one line, beyond  $X/H$  of 20. The collapse onto a single line appears to indicate a general fully developed turbulent heat transfer enhancement. Note that this saturation of heat transfer enhancement in the non-dimensional sense does not translate into absolute terms. In other words, the absolute heat transfer rate was always higher at a higher Reynolds number (not shown).

The notable difference between the low flow,  $Re_H = 1.3 \times 10^3$ , Nusselt augmentation and the other three Reynolds numbers specifically after  $X/H = 20$ , originates from the fact that at the low  $Re_H$ , the flow regime for the base case (over the entire smooth plate) remained laminar. At higher Reynolds numbers, the boundary layer regime over the smooth plate changed from laminar to turbulent at some distance downstream. This can be clearly seen for the case  $Re_H = 2.6 \times 10^3$ , where the  $Nu/Nu_0$  was initially higher than that of the two other high  $Re_H$  cases, but after some distance downstream ( $X/H \geq 20$ ), it reached almost the same value as the others. Since the two higher  $Re_H$  cases ( $5 \times 10^3$  and  $6.3 \times 10^3$ ) had almost the same relative Nusselt number augmentation, they were apparently turbulent from the beginning of the measurements domain for the smooth plate case. The  $Re_x$  at which the flow over the smooth plate started to become turbulent was estimated to be around  $7 \times 10^4$  which falls in the typical range of the critical  $Re$  for the flat plate ( $6 \times 10^4 \sim 3 \times 10^6$ ) according to the literature [28-30].

### **5.3.2. Flow Measurement Results**

Velocity measurements are presented in the form of the mean streamwise and normal velocities ( $U$  and  $V$ ), turbulence fluctuation intensities ( $u_{rms}$  and  $v_{rms}$ ), turbulent shear stress ( $uv$ ), and power spectra. First of all, the method developed for modifying the hot-wire data is explained. In the second and third parts, the flow and turbulence mechanism over the ribbed surface which directly affects the heat transfer mechanism was characterized at a specific  $Re_H$  ( $2.6 \times 10^3$ ) and over a large normal distance from the plate ( $0.5 \leq Y/H \leq 5$ ). Also, the effect of the rib on different flow and turbulence parameters with respect to the smooth plate case was analyzed in an attempt to understand the impact of each parameter on the heat transfer augmentation. As was observed in the previous section, the relative heat transfer augmentation was much higher at  $Re_H = 1.3 \times 10^3$

compared to other  $Re_H$  cases, while other cases showed almost the same  $Nu/Nu_0$  values. So, the low and high extremes in the Reynolds number range ( $Re_H = 1.3 \times 10^3$  and  $6.3 \times 10^3$ ) were chosen for the flow investigation in this section with specific emphasis on the near plate region ( $Y/H \leq 1.9$ ). In the last part, the energy spectra of normal velocity fluctuations for the lowest and highest  $Re_H$  at some points downstream of the rib, were analyzed to trace the vortex shedding when present.

Flow over the centerline was assumed to be 2-D. This assumption was tested by moving the hot-wire laterally from the centerline to check the velocity and turbulence parameters. The relative deviation of the side points' flow measurements from that of the centerline point was small enough (less than 8%) to consider the flow over the set-up 2-D.

### 5.3.2.1. Hot-wire Data Modification in the Recirculation Region

Generally, dual sensor probes are suitable for measuring two-dimensional flows where the total velocity vector stays within  $\pm 45^\circ$  with respect to the probe axis [25]. The hot-wire is unable to differentiate negative velocities from positive ones in the streamwise direction; that is, it is directionally insensitive. In other words, the streamwise velocity signal remains positive even when there is flow reversal.

A method was developed here to improve the data measured by the X-probe in the streamwise direction. A sample graph of instantaneous velocity ( $U_i$ ) is shown Figure 5.4 (a). The graph was truncated after 2.5 s for better visibility. A priori knowledge and other studies note that there is likely flow reversal at this point. The signal in Figure 5.4 (a) also insinuates this happening. At many instances, the velocity decreased to a near zero value and then rebounded into the positive. These are the points where the velocity signal should have crossed the time axis.

A Matlab code was written to change the flow direction when the velocity got close enough to the X axis (less than 0.05 m/s) until the next sub-threshold point. The modified signal is depicted in Figure 5.4 (b), and it appears physically sound.

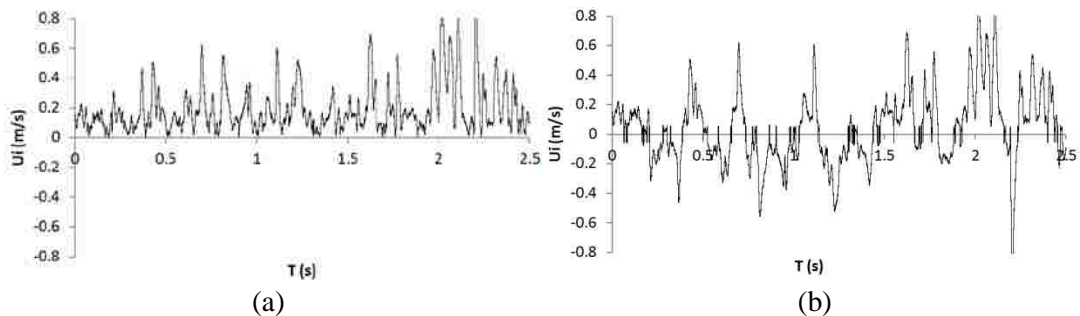


Figure 5.4 Streamwise instantaneous velocity (a) hot-wire data (b) modified hot-wire data

Also, the local velocity profiles of the modified and raw data were compared to another study in which the wake region velocity was measured by a directional sensitive method. Figure 5 compares modified and raw velocity profiles of the present study at  $Re_H = 2.6 \times 10^3$  with Liu et al. [11] velocity profiles on a square ribbed plate. Velocities were normalized by the free stream velocity.

In Liu et al. [11] the flow in the separation and reattachment regions was measured by a split-fiber film probe and the free stream velocity, rib's height and  $Re_H$  were 10 m/s, 20 mm and 13,200 respectively. Point  $X/H = 8.75$  (Figure 5.5 (a)) was taken as the reattachment point of the flow, as the velocity had almost zero value near the surface. Because of somewhat different experimental conditions in these two studies, the velocity profiles are not expected to have exactly the same values, but they should follow the same trends. It is clear that the modified velocity profiles of the present study (Figure 5.5 (b)) are closer to Liu et al.'s results than the unmodified measurements (Figure 5.5 (c)). It can be seen that negative velocities occurred in the modified version at  $X/H = 5$ , however, their magnitude appears to be less than that of Liu et al.'s. The raw data in Figure 5.5 (c) conveys that over the entire measurement domain, the  $U/U_\infty$  was never less than approximately 0.27. In short, the modified velocity profile (Figure 5.5 (b)) seems more viable, based on the literature and what is expected from the flow in the wake region.

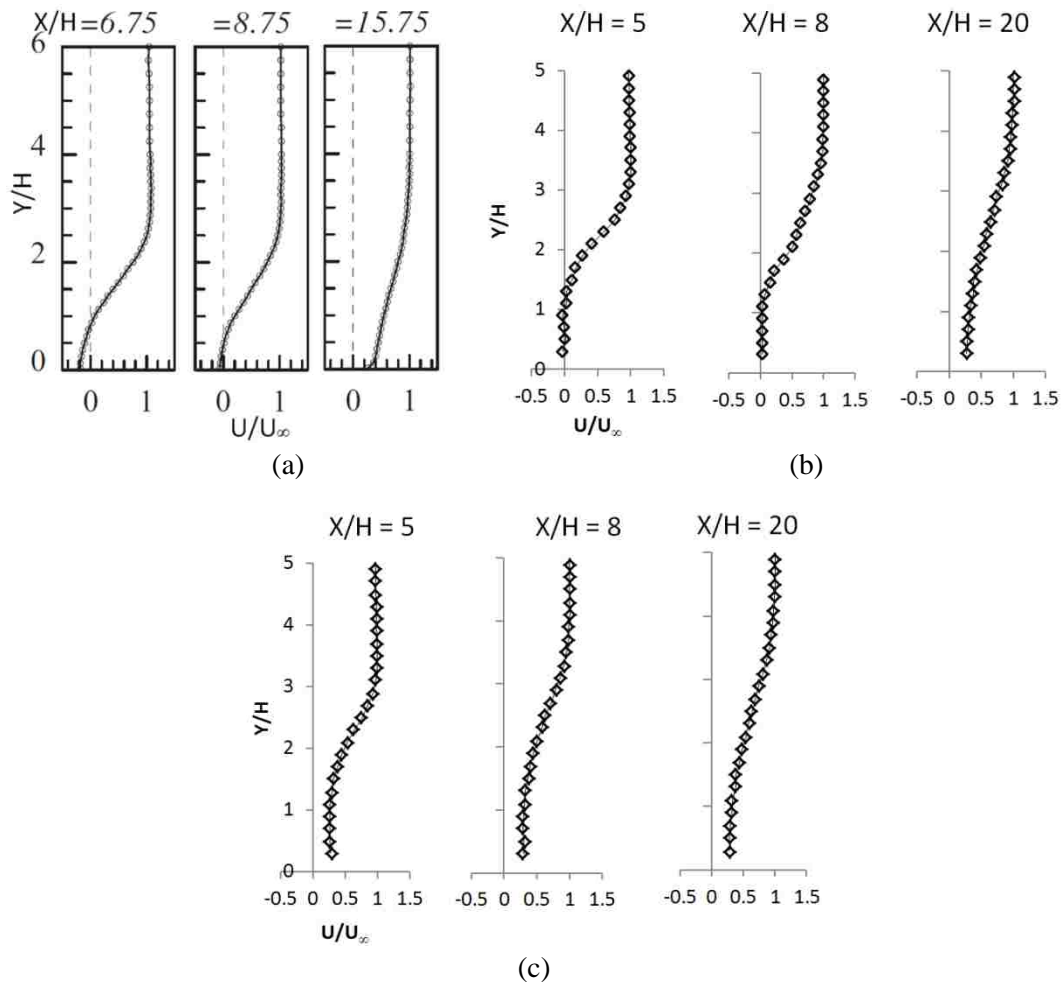


Figure 5.5 Streamwise velocity profile (a) Liu et al. [11] (b) present study's modified hot-wire data (c) present study's raw hot-wire data

### 5.3.2.2. Velocity Profiles

In the heat transfer results section, it was noted that the rib improved the convective heat transfer from the plate as the normalized Nusselt numbers ( $Nu/Nu_0$ ) were higher than unity. Furthermore, it was observed that this relative effect was higher at lower Reynolds numbers. This heat transfer enhancement was due to the effect of the rib on different flow and turbulence parameters. It is expected that an increase in the flow velocity would cause an enhancement in the heat transfer rate from the surface; however, the normal velocity ( $V$ ) was seen to be more influential in the heat transfer enhancement from a ribbed wall [22]. In this section, the effect of the rib on the flow over the surface with respect to the smooth plate case is examined. First, the overall behavior of the flow field after the rib until a large distance from the plate ( $Y/H = 5$ ) is shown in Figure 5.6. Then, ribbed and smooth plate velocities at the lowest and highest studied Reynolds numbers were studied with specific emphasis on the near-plate region ( $Y/H \leq 1.9$ ), and compared (Figures 5.7 and 5.8).

The normalized streamwise ( $U/U_\infty$ ) and normal velocity ( $V/U_\infty$ ) profiles at different streamwise locations are presented in Figure 6. In this figure, both  $U$  and  $V$  velocities were normalized by  $U_\infty$ , the free stream velocity at the corresponding  $Re_H$ . As can be seen in Figure 5.6 (a), until around  $X/H = 20$ , in the near-plate region ( $Y/H \leq 1$ ), the streamwise velocity was very low. At approximately  $Y/H = 1$  (rib's height) a change in velocity gradient in the streamwise velocity profile started, portraying the rib's edge free shear layer. This shear layer was formed and then deteriorated from  $X/H = 2$  to 32.

The reattachment point, as identified in the literature [12, 14], is the location corresponding to the zero streamwise velocity at the measurement location closest to the surface. The region between the rib and the reattachment point is the recirculation or wake region, where the streamwise velocities are likely to be negative [8,11,27]. In Figure 5.6 (a), the near-plate zero velocity point appears to be around  $X/H = 8$ . Based on the maximum heat transfer peak in Figure 5.3, the reattachment region was estimated to happen before  $X/H = 20$ , possibly at  $X/H = 14$ . Thus, the blockage of the  $U$  velocity, which is observed from  $X/H = 2$  to 8, demonstrates a wake region after the rib. The  $X/H = 20$  location is postulated to be after the reattachment point, but before the velocity profile shape had recovered from the influence of the rib's blockage. As was observed in other studies [8], the reattachment point based on the heat transfer was downstream of the reattachment based on the velocity.

Figure 5.6 (b) shows the normal velocity ( $V$ ) trend at different streamwise locations. It is noted that up to and including  $X/H = 20$  (in the wake region and shortly after the reattachment) the  $V$  velocity was negative which indicates a downward motion of the flow. The rib's edge shear layer also can be observed in these graphs. Positive  $V$  in the zone at higher  $Y/H$ , outside the wake region, indicated the subsequent upward deflection of the rib's edge free shear layer. Well after reattachment, at  $X/H = 32$ , the normal velocity had a very small positive value all along the measurement domain ( $Y/H = 0.5$  to 5). This small positive  $V$  in the free stream was assumed to be due to the air sweeping over the reattached plate shear layer [8].

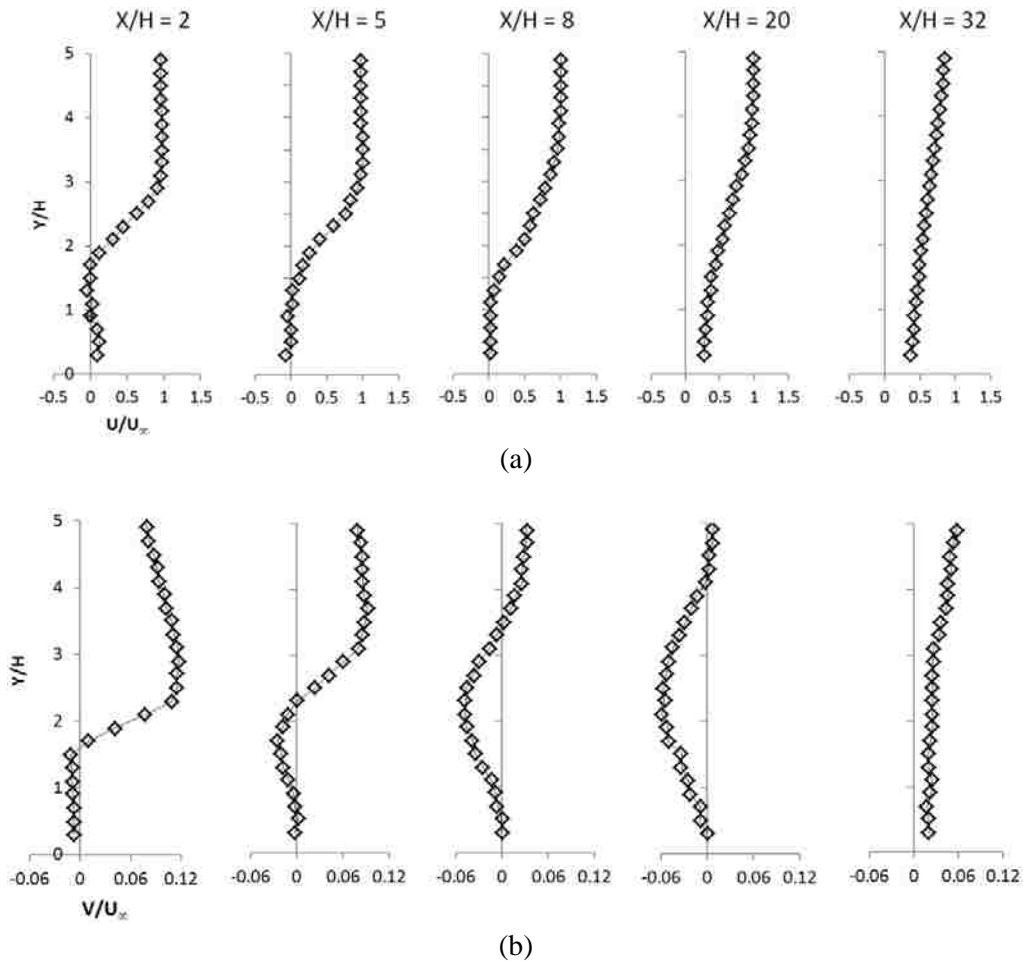


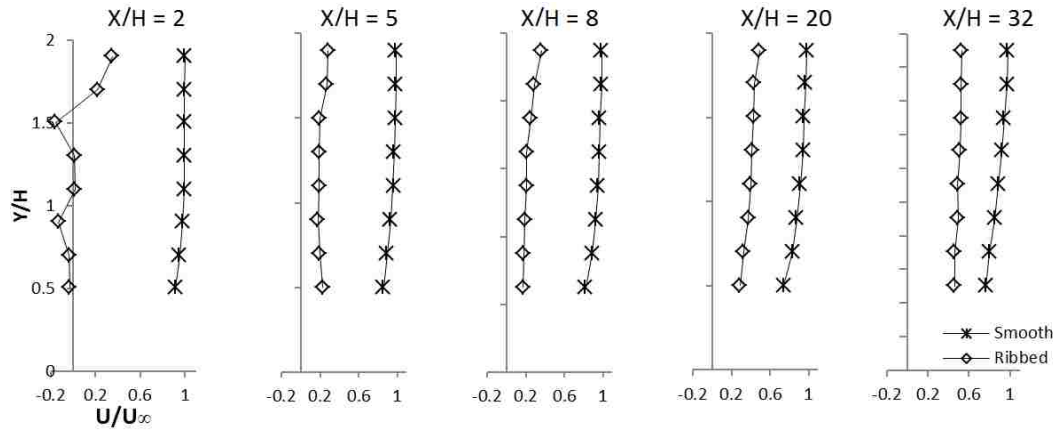
Figure 5.6 (a) Streamwise and (b) normal velocities of the flow over the ribbed plate at  $Re_H = 2.6 \times 10^3$

To analyze the effect of the rib on the flow over the surface and consequently the surface heat transfer, the ribbed and smooth plate velocities, were studied in the near-plate region ( $Y/H \leq 1.9$ ) in Figures 5.7 and 5.8. Streamwise and normal velocity profiles normalized by the free stream velocity at  $Re_H = 1.3 \times 10^3$  and  $6.3 \times 10^3$  are presented in Figures 5.7 and 5.8, respectively. The lowest and highest studied Reynolds numbers were chosen for comparison in these figures, as a big difference in heat transfer enhancement was seen between these two  $Re_H$  (Figure 5.3).

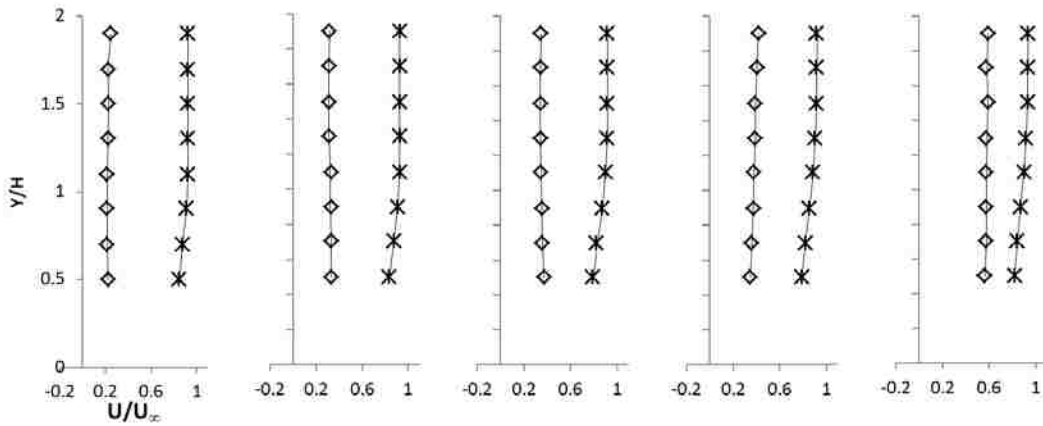
As is evident in Figure 5.7, at both  $Re_H$ , the rib blocked the flow in the streamwise direction in the near-plate region as the ribbed surface velocities were less than the smooth plate velocities. For the flow over the smooth plate, except for a couple of points, most of the measuring domain was outside of the plate's boundary layer, so the majority of the very thin developing boundary layer profile is missing here. In Figure 5.7 (a) for  $Re_H = 1.3 \times 10^3$ , until  $X/H = 2$ , the region close to the plate shows very small magnitude negative or positive values for the streamwise velocity even up to  $Y/H = 1.9$ . At  $X/H = 5$  to 32, the velocity profile shows all positive velocities near the surface, however, it seems to be still retarded from the influence of the rib's blockage. Based on this, it is highly possible



that the reattachment of the flow happened somewhere between  $X/H = 2$  and  $5$  at this  $Re_H$ . However, at  $Re_H = 6.3 \times 10^3$ , no negative streamwise velocity is witnessed in Figure 5.7 (b) even at  $X/H = 2$ . This could show again the limitation of the hot-wire for measuring the negative values which could not be properly fixed by the mentioned modification method. Also, it might indicate that the recirculation area after the rib at higher  $Re_H$  was small, which probably could not be captured in the present study measuring domain ( $0.5 \leq Y/H$  and  $2 \leq X/H$ ).



(a)



(b)

Figure 5.7 Streamwise velocity over the smooth and ribbed plate at (a)  $Re_H = 1.3 \times 10^3$  and (b)  $Re_H = 6.3 \times 10^3$

In spite of the blockage effect of the rib on the streamwise flow in the adjacent area to the plate, heat transfer showed higher results in the ribbed plate cases compared to their smooth plate counterparts (Figure 5.3). Also, comparing the low and high Reynolds number cases in Figure 5.7 shows that, the rib's blockage effect at both  $Re_H$  were almost the same but slightly higher at the lower  $Re_H$  ( $1.3 \times 10^3$ ) at some downstream distances. Recalling Figure 3 from the previous section, at this Reynolds number,  $Nu/Nu_0$  was higher compared to  $Re_H = 6.3 \times 10^3$ . This evidence indicates

that, in going from a smooth to a ribbed plate, apparently the impact of other flow and turbulence parameters on enhancing the surface heat transfer was stronger than the effect of the streamwise flow velocity. In other words, the unfavorable effect of lower streamwise velocity in the ribbed plate on the heat transfer was more than compensated by the increased flow turbulence.

Figure 5.8 presents the normal velocities over the smooth and ribbed plates, normalized by the free stream velocity, at the lowest and highest  $Re_H$ . It can be seen that the normal flow velocity over the smooth plate had very small values (close to zero). This velocity almost always increased in the presence of the rib at  $X/H < 8$ , especially with  $Y$  distance. The sign of the normal velocity was negative at almost all locations after the rib, except for  $Re_H = 6.3 \times 10^3$  at the last streamwise location ( $X/H = 32$ ), where positive  $V$  values were observed for the flow over the ribbed surface (Figure 5.6 (b)). This indicates a sweeping motion of the flow over the redeveloping boundary layer. However, at the same location for  $Re_H = 1.3 \times 10^3$ , the normal velocity over the ribbed plate had very small negative values which were very close to the smooth plate magnitudes. This suggests that at the lowest  $Re_H$  far from the rib, the velocity profiles resumed the same values as the smooth plate ones.

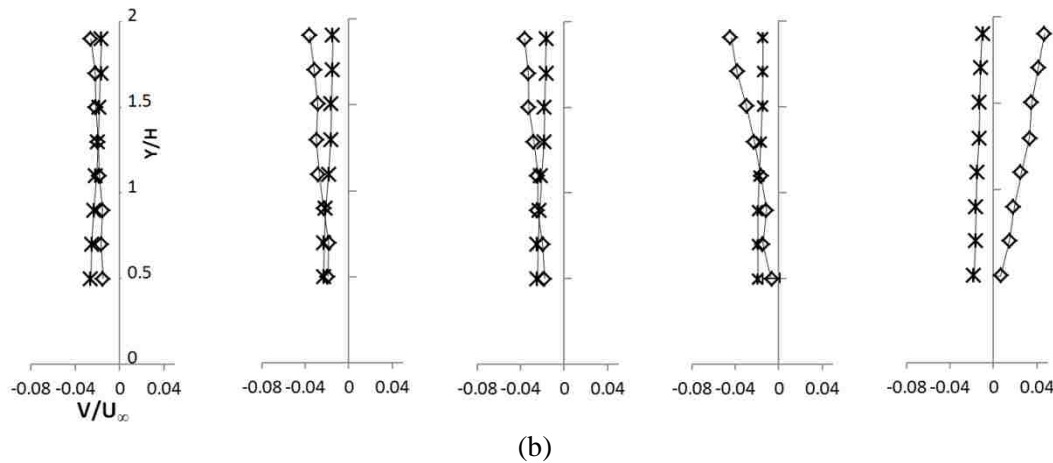
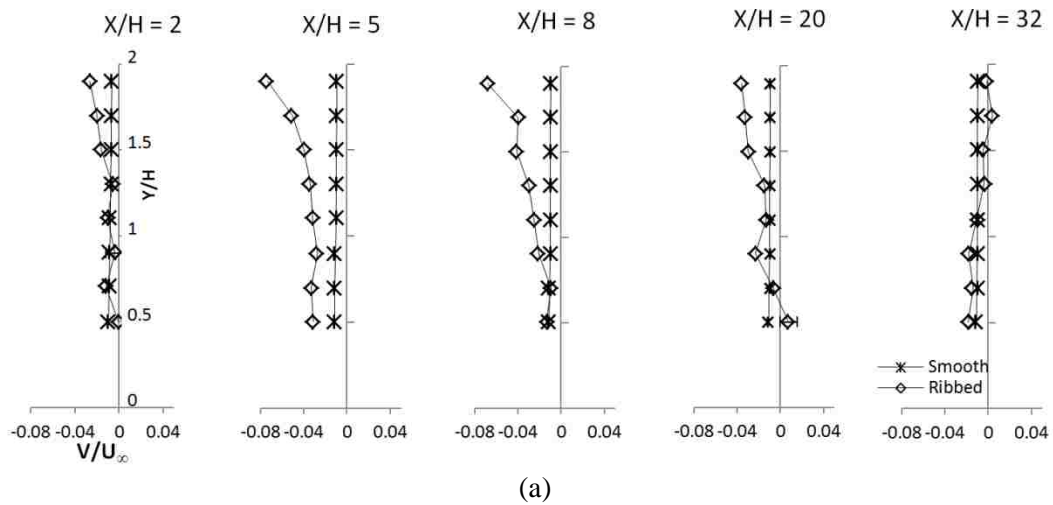


Figure 5.8 Normal velocity over the smooth and ribbed plate at (a)  $Re_H = 1.3 \times 10^3$  and (b)  $Re_H = 6.3 \times 10^3$

It is seen that the rib mostly increased the  $V$  in the flow over the surface compared to the smooth plate. Whenever the streamwise velocity was blocked by the rib, some normal velocity was created in the region behind it. However, this trend is not very conclusive, specifically for the lowest few points at some graphs where the ribbed plate values were slightly lower than that of the smooth plate. But at the same time, it should be remembered that the difference between the smooth and ribbed plates at the first few points were mostly less than the uncertainty in  $V/U_\infty$  ( $\sim 0.008$ ). Also, comparing the profiles at the two  $Re_H$ , specifically at the middle downstream distances ( $X/H = 5$ , and  $8$ ), it is noted that, apparently, the rib was more effective in increasing the normal velocity at  $Re_H = 1.3 \times 10^3$  ( $Nu/Nu_0$  was also higher at this  $Re_H$  (Figure 5.3)). More importantly, the associated physics suggest that this normal velocity created after the rib could be one of the parameters enhancing heat removal from the surface [22].

### 5.3.2.3. Turbulence Parameters

In this section, the effect of the rib on turbulence intensities ( $u_{rms}/U_\infty$  and  $v_{rms}/U_\infty$ ) and shear stress ( $\overline{uv}/U_\infty^2$ ) of the flow over the surface are presented. First, the overall profile of these parameters after the rib until a large normal distance from the plate ( $Y/H = 5$ ) were analyzed at  $Re_H = 2.6 \times 10^3$ . Then, profiles were compared at the lowest and highest  $Re_H$  for both ribbed and smooth surfaces to examine the effect of the rib on turbulence parameters at these  $Re_H$ . In the second part, the emphasis is on the area close to the plate ( $Y/H \leq 1.9$ ) in an attempt to relate these parameters to the heat transfer enhancement from the surface. It is postulated that the total turbulence generated by the rib is one of the key contributors to the heat transfer enhancement in the ribbed wall [22].

#### 5.3.2.3.1. Turbulence Intensities

Figure 5.9 illustrates the vertical profiles of the turbulence intensities in the  $X$  and  $Y$  directions plotted in terms of root mean square values ( $u_{rms}$  and  $v_{rms}$ ) normalized by the free stream velocity at  $Re_H = 2.6 \times 10^3$ . Both  $u_{rms}$  and  $v_{rms}$  had almost the same shaped profiles in the recirculation region. They increased with normal distance from the plate, reached a maximum and subsequently reduced to small values in the free stream. Comparison of these graphs with velocity profiles (Figure 5.6 (a)) shows that  $u_{rms}$  and  $v_{rms}$  peaks occurred just inside the rib's edge free shear layer. These peak points can be observed to shift away from the plate as the fluid travels downstream and the shear layer expands. Also, the depth under the rib's effect expanded, as can be seen at  $X/H = 32$ ; even at  $Y/H = 5$ , where turbulence intensities were much higher than that of the free stream value (less than 0.4%). Thus at  $X/H = 32$ , the redeveloped boundary layer after the reattachment point was extended until  $Y/H = 5$ , which caused the turbulent stresses to be higher than that of the free stream value.

Near-plate turbulence intensities in streamwise and normal directions,  $u_{rms}/U_\infty$  and  $v_{rms}/U_\infty$ , of the ribbed surface are illustrated and compared with those of the smooth plate in Figures 5.10 and 5.11 respectively. In each figure, both smooth and ribbed plate cases are shown at the lowest and highest studied  $Re_H$  ( $1.3 \times 10^3$  and  $6.3 \times 10^3$ ).

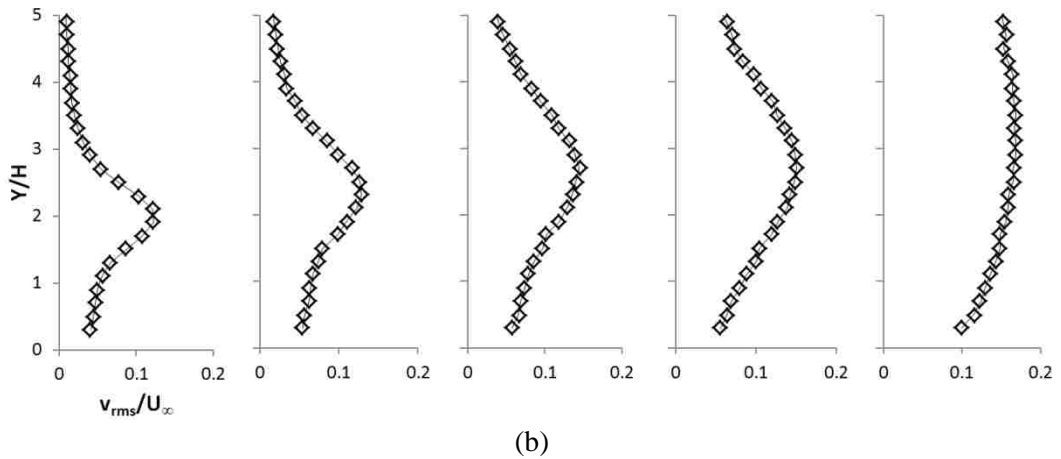
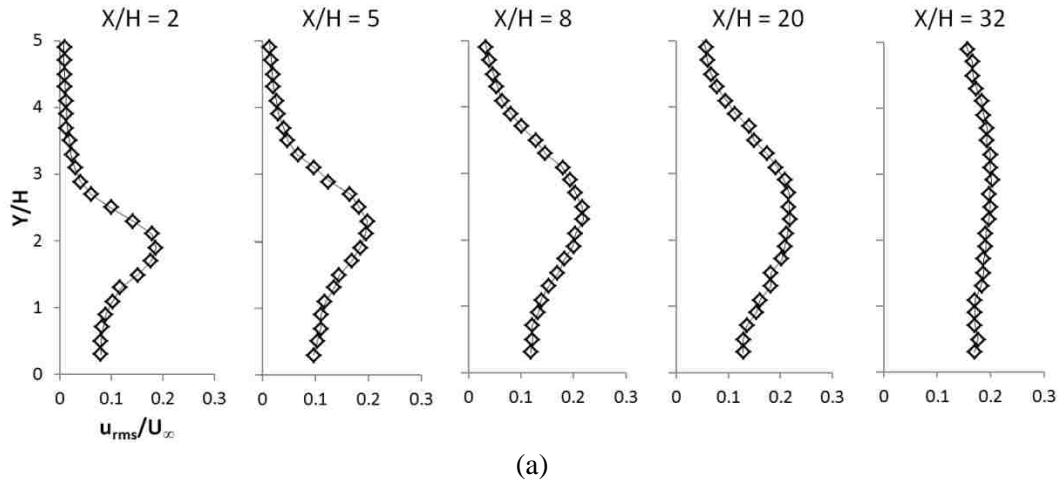


Figure 5.9 Turbulence intensities (a)  $u_{rms}/U_{\infty}$  and (b)  $v_{rms}/U_{\infty}$ , for the flow over the ribbed plate at  $Re_H = 2.6 \times 10^3$

In Figure 5.10, it is observed that the rib significantly increased turbulence intensity at all streamwise distances. For the smooth plate,  $u_{rms}/U_{\infty}$  presented a reducing trend with normal distance from adjacent to the plate ( $Y/H = 0.5$ ) to the free stream. For the ribbed plate cases,  $u_{rms}/U_{\infty}$  increased with the distance normal to the plate. As was seen in Figure 5.9 (a), where a larger normal distance over the plate ( $Y/H \leq 5$ ) was shown,  $u_{rms}$  increased in the normal direction, reached a maximum and subsequently reduced to the respective free stream value. As Figure 5.10 only shows  $Y/H \leq 1.9$ , just the first (increasing) part can be observed. At both  $Re_H$  for the smooth plate, the  $u_{rms}$  remained almost the same over the span of streamwise distance studied, however, for the ribbed plate this parameter slightly increased until  $X/H = 20$  and then decreased.

Comparison between the low and high  $Re_H$  in Figure 5.10 shows that the differences between the ribbed and smooth plate cases at some downstream distances ( $X/H = 5, 8$  and  $20$ ) were slightly higher at low  $Re_H$  ( $1.3 \times 10^3$ ). This indicates the very minor greater effect of the rib on generating relative turbulence intensity in the streamwise direction at the lower  $Re_H$  case, which arises from changing the boundary layer regime from laminar to turbulent. Also at both  $Re_H$ , the difference

between the smooth and ribbed plate cases at close locations to the surface (2~3 first points) is maximum at  $X/H = 20$ , which is more obvious at  $Re_H = 1.3 \times 10^3$ . Recalling (Figure 5.3) that the maximum Nusselt ratio enhancement was also seen to occur at around  $X/H = 20$ ; which would suggest that the heat transfer enhancement is related to the turbulent normal stress increase due to the rib.

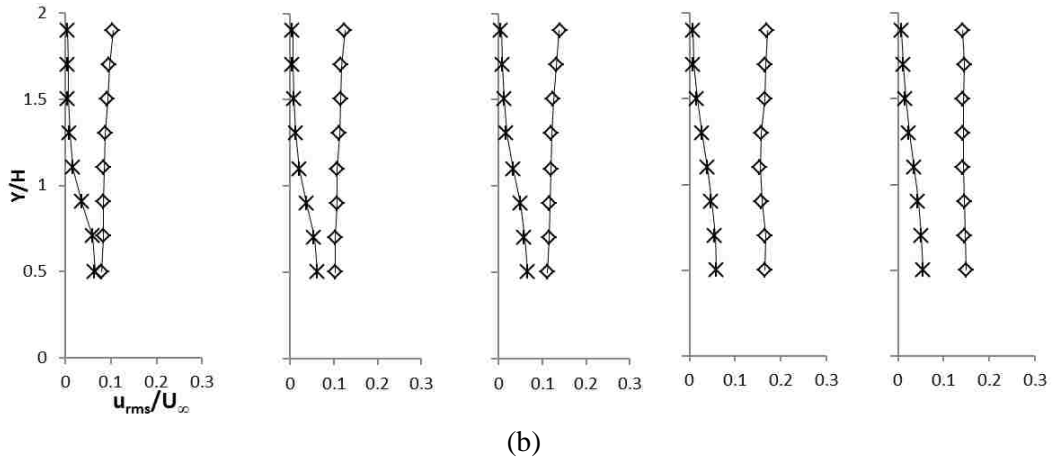
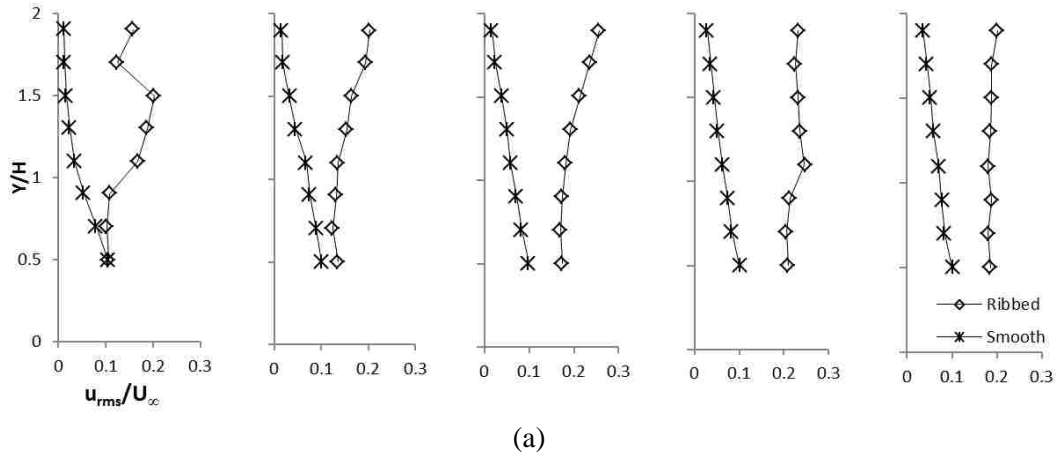


Figure 5.10 Turbulence intensity in X direction ( $u_{rms}/U_\infty$ ) at (a)  $Re_H = 1.3 \times 10^3$  and (b)  $Re_H = 6.3 \times 10^3$

Figure 5.11 illustrates that the rib also enhanced the turbulent intensity in the Y direction ( $v_{rms}$ ). Furthermore,  $v_{rms}$  exhibited the same trend as  $u_{rms}$  in Figure 5.10 for the smooth and ribbed plate cases; for the smooth plate,  $v_{rms}$  decreased in the normal direction (Y) from adjacent to the plate to the free stream (less than 0.4% at  $Y/H = 1.9$ ), whereas for the ribbed plate cases an increasing trend is observed in  $v_{rms}$  with normal distance from the plate.

Figure 5.11 also shows that  $Re_H = 1.3 \times 10^3$  presented slightly higher relative enhancements in normalized  $v_{rms}$  from smooth to ribbed plates compared to  $Re_H = 6.3 \times 10^3$ . However, this higher

enhancement is more obvious than that associated with  $u_{rms}/U_\infty$  (Figure 5.10). The considerable amount of turbulence intensity generated by the rib compared to the smooth plate, as was observed in both Figures 5.10 and 5.11, and the fact that this effect was slightly higher at the lower  $Re_H$ , all indicate the effect of the turbulence intensities ( $u_{rms}/U_\infty$  and  $v_{rms}/U_\infty$ ) on enhancing the heat transfer from the surface.

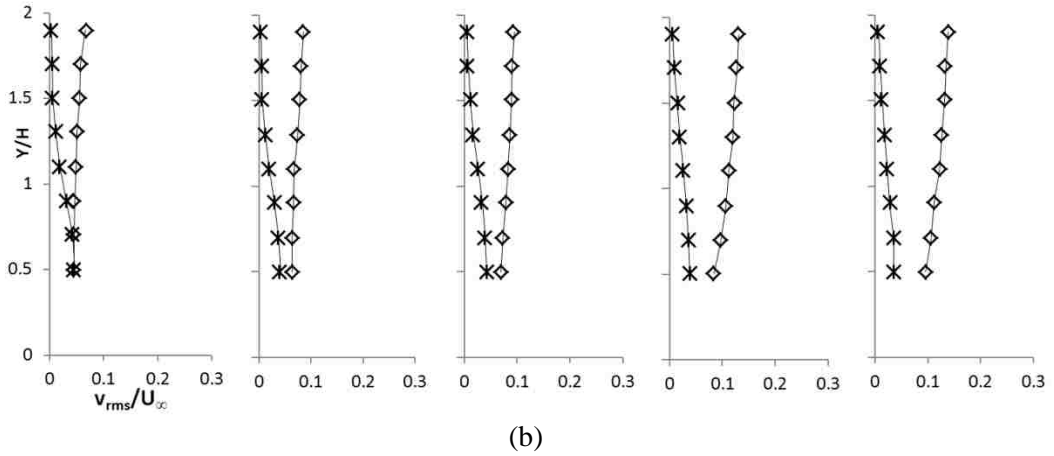
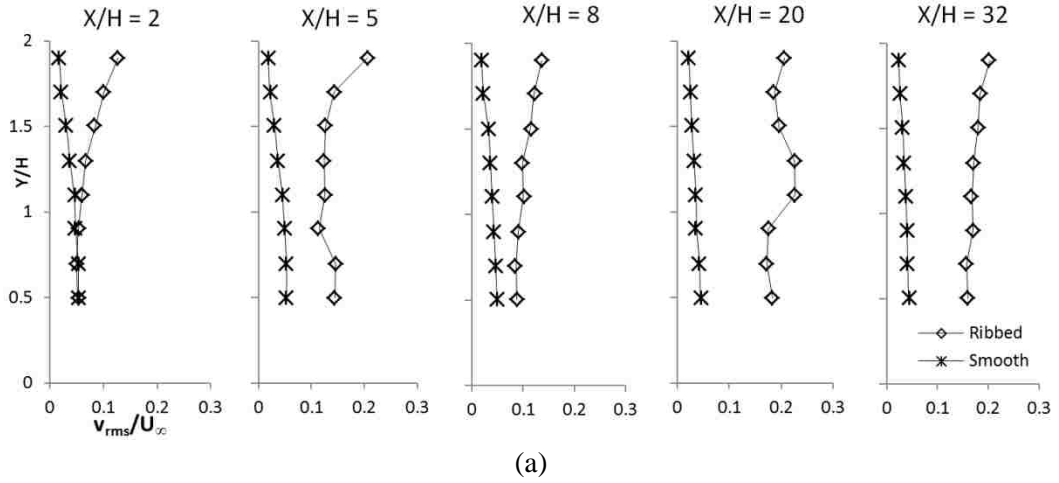


Figure 5. 11 Turbulence intensity in Y direction ( $v_{rms}/U_\infty$ ) at (a)  $Re_H=1.3 \times 10^3$  and (b)  $Re_H= 6.3 \times 10^3$

### 5.3.2.3.2. Reynolds Shear Stress

The cross correlation between the streamwise and normal velocity fluctuations, the Reynolds shear stress, is an indication of the momentum transport by the velocity fluctuations across the shear layer [22,13]. The production of this quantity is associated with the spatial gradients in the time-averaged velocity [31]. The Reynolds shear stress is presumably produced in the wall boundary layer and more so, the free shear layer from the rib's edge. Also, an increase in this parameter has been found

to increase the wall friction and heat transfer in the turbulent boundary layer compared to the laminar one [22].

The non-dimensional turbulent shear stress ( $\overline{uv}/U_\infty^2$ ) at different streamwise locations is presented in Figure 5.12. It can be seen that the profile shapes are similar to turbulence intensities' (Figures 5.9) but with negative values. The shear stress started from a small magnitude adjacent to the plate, where molecular viscosity dominates, then reached a peak at around the center of the rib's edge free shear layer, and subsequently reduced to small values in the free stream. As this parameter originated from the spatial gradient in time-averaged velocity, it had a significant magnitude inside the shear layer. The location of the peak shifted upward as the shear layer expanded downstream. At  $X/H = 32$ , the profile presents a somewhat different shape. The shear stress magnitude increased in the normal direction from  $Y/H = 0.5$  to 3 and slightly decreased to  $Y/H = 5$ . This indicates that there was a velocity gradient at  $Y/H = 5$ , which again supports the postulation that the redeveloped plate boundary layer extended beyond  $Y/H = 5$  at the farthest downstream distance.

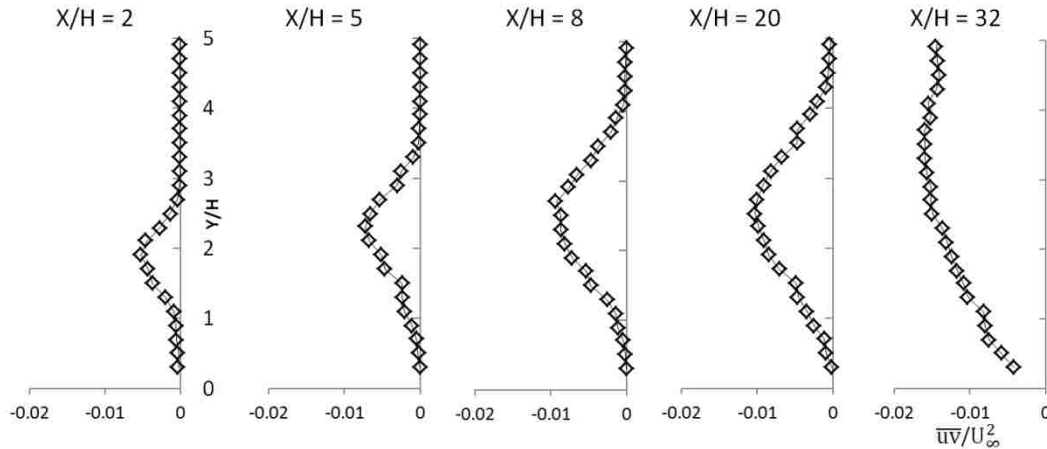


Figure 5.12 Non dimensional turbulent shear stress ( $\overline{uv}/U_\infty^2$ ) for the flow over ribbed plate at  $Re_H = 2.6 \times 10^3$

The normalized Reynolds shear stress of the flow over the ribbed and smooth plates ( $\overline{uv}$ ) with respect to the free stream velocity squared are presented in Figure 5.13.  $Re_H = 2.6 \times 10^3$  instead of the lowest  $Re_H (1.3 \times 10^3)$  was selected as the lower Reynolds number to compare with  $Re_H = 6.3 \times 10^3$  because of the high uncertainty due to small velocity magnitudes observed in  $\overline{uv}$  at the lowest free stream velocity ( $Re_H = 1.3 \times 10^3$ ). Comparing the smooth and ribbed plates, it can be seen that the rib produced some shear stress in the flow behind it, specifically at larger distances from the plate. For the smooth plate, the normalized Reynolds shear stress had very small magnitudes, which were slightly higher adjacent to the plate and decreased outside the plate boundary layer. This trend is reasonable as the production of this quantity is related to the time-averaged velocity spatial gradient [22]. In the smooth plate boundary layer,  $\overline{uv}$  was negative. However, the trend may not be observed clearly in these graphs as the magnitude is very small.

For the ribbed plate, an increase with normal distance from the plate was observed at both  $Re_H$  throughout the studied streamwise span. The overall trend of increasing shear stress magnitude ( $|\overline{uv}|$ ) with normal distance from the plate was observed in Figure 5.12, where a larger distance from the plate was shown ( $Y/H = 5$ ). It was seen (Figure 5.12) that the shear stress increased from the plate to its maximum value just inside the rib's edge shear layer and subsequently decreased to a small magnitude in the free stream.

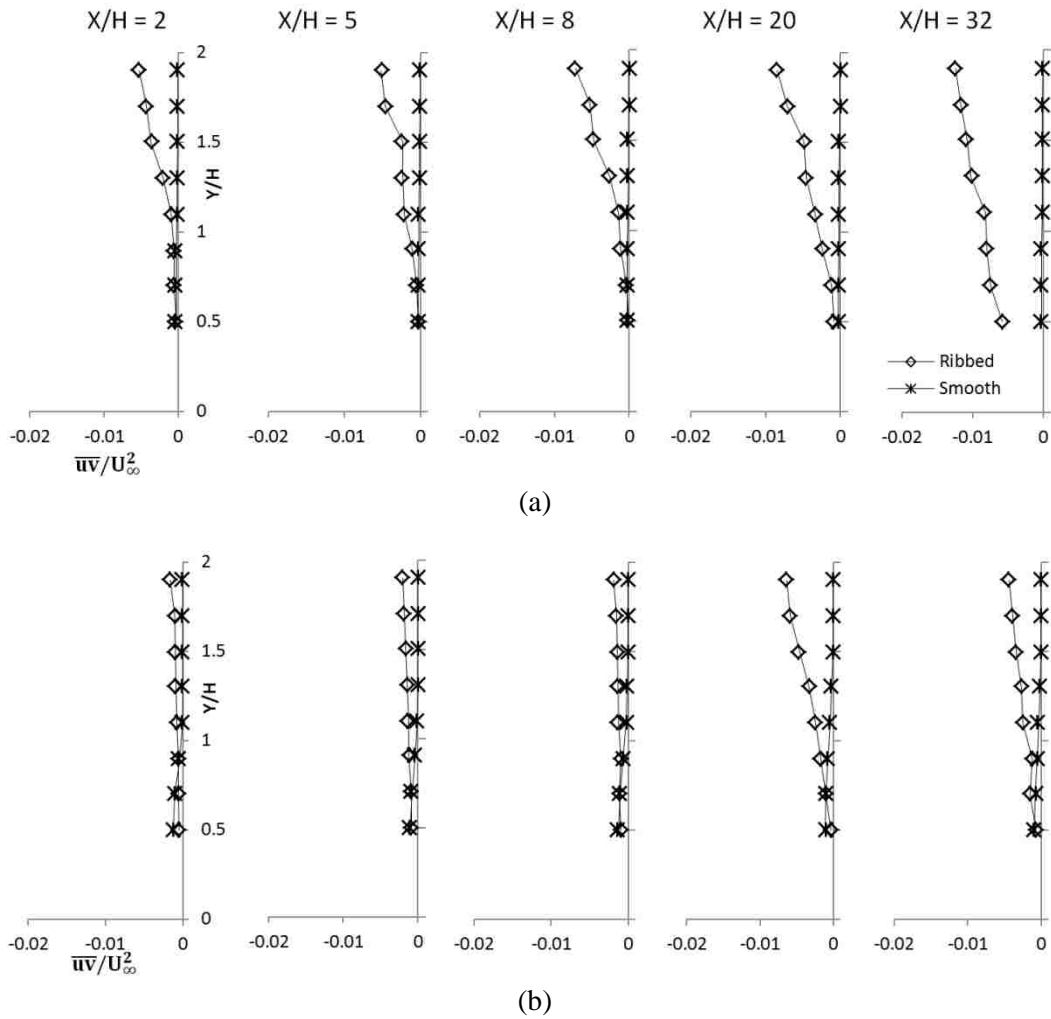


Figure 5.13 Normalized shear stress at (a)  $Re_H = 2.6 \times 10^3$  and (b)  $Re_H = 6.3 \times 10^3$

Figure 5.13 shows that at  $X/H = 2$  to  $8$ , for the first few points close to the surface, the difference between the smooth and ribbed plate is negligible. In this region, because of the higher blockage effect of the rib, specifically for the points adjacent to the plate ( $Y/H \leq 0.9$ ), the shear stresses were smaller and almost the same as the smooth plate magnitudes. While at  $X/H = 20$  and  $32$ , the difference between the smooth and ribbed plate increased for the points adjacent to the plate. This



indicates that the rib's edge free shear layer got closer and finally attached to the plate (reattachment).

Also, comparing the two  $Re_H$  cases shows that the presence of the rib was more effective in increasing the normalized shear stress at low Reynolds number ( $Re_H = 2.6 \times 10^3$ ). As can be seen,  $Re_H = 2.6 \times 10^3$  had higher relative shear stress at almost all streamwise locations compared to  $Re_H = 6.3 \times 10^3$ . This higher shear stress production in the ribbed plate, which is also higher at the lower  $Re_H$ , is likely important mechanism for the heat transfer enhancement in the ribbed surface.

#### ***5.3.2.4. Energy Spectrum***

The Fast Fourier transform was applied to the normal velocity fluctuation squared signals ( $v^2$ ), which indicate the turbulent energy spectrum in the surface normal direction. This analysis provides information about the turbulent energy distribution associated with the cascade of large to small eddies [22,32]. Also, it may contain some details about the possibility of harmonic vortex shedding from the rib's edge [11,22], which may also be effective in extracting heat from the surface [22].

Three streamwise locations;  $X/H = 5, 8$  and  $11$  with the specific emphasis on the near-plate region;  $Y/H = 0.7$ , were analyzed at the lowest and highest studied  $Re_H$  and the results are presented in Figure 5.14. Comparing the smooth and ribbed plate graphs clearly shows that the ribbed plate had a higher level of turbulence energy over the entire range of the spectrum. This again corresponds to the higher level of heat and mass transfer in the near-plate area for the ribbed plate. As can be seen for both  $Re_H$ , this difference increased from  $X/H = 5$  to  $20$ , which shows that turbulent energy was still being produced and/or injected into the boundary layer. This increasing trend was also observed in the normalized turbulence stresses in this region ( $5 \leq X/H \leq 20$ ) in Figures 5.10 and 5.11. Also, it can be observed that the higher  $Re_H$  case showed a significantly higher level of energy over the entire range of eddies compared to the lower one.

A couple of clear spectral peaks are observed in Figure 5.14 (a) for the lower  $Re_H$  case at  $Y/H = 0.7$ . These peaks are particularly clear in  $X/H = 5$  and  $20$ . The frequency of these peaks at these two locations, are 175, 360, 540, 700 and 900 Hz respectively. The corresponding Strouhal numbers based on the streamwise dimension of the rib (0.01 m) and the free stream velocity ( $U_\infty$ ) are 0.875, 1.8, 2.7, 3.5 and 4.5. These peaks are the common periodic fluctuations at these locations and seem to be the traces of the harmonic vortex shedding from the rib's edge [11,22]. For  $Re_H = 6.3 \times 10^3$ , the very high turbulence possibly destroyed and/or concealed the coherent vortices. At the lowest  $Re_H$ , the root mean squared of turbulence fluctuating velocity in normal direction ( $v_{rms}$ ) was around  $0.2 \sim 0.4$  m/s, while at  $Re_H = 6.3 \times 10^3$  it was around  $0.5 \sim 1$  m/s.

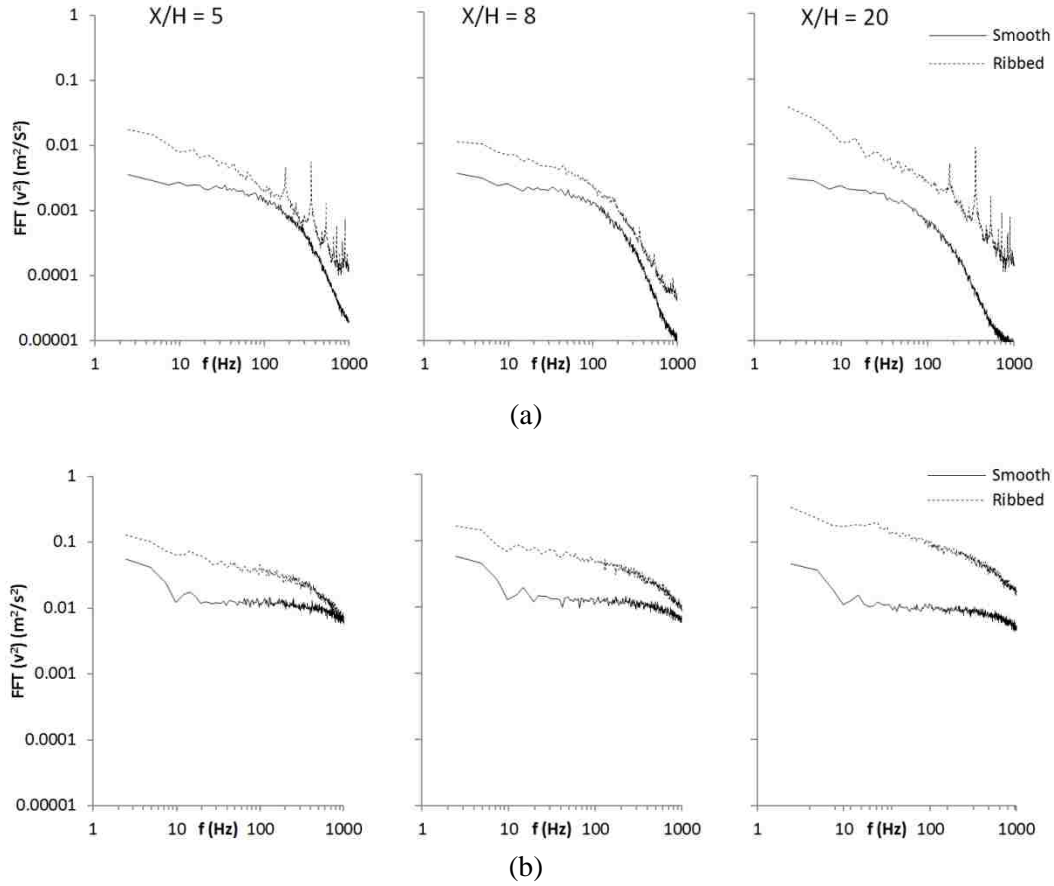


Figure 5.14 Spectra of  $v^2$  ( $m^2/s^2$ ) at  $Y/H = 0.7$  and different streamwise locations and (a)  $Re_H = 1.3 \times 10^3$  (b)  $Re_H = 6.3 \times 10^3$

#### 5.4. Conclusion

Flow and heat transfer over a surface mounted rib was investigated experimentally. Measurements were performed in a closed loop wind tunnel at four different Reynolds numbers, based on the rib's height:  $1.3 \times 10^3$ ,  $2.6 \times 10^3$ ,  $5 \times 10^3$  and  $6.3 \times 10^3$ .

Heat transfer was measured by thermocouple-semiconductor-thermocouple sandwich embedded in the panel as heat flux sensors. Heat transfer from the plate was seen to be significantly enhanced in the ribbed plate. The enhancement in heat transfer relative to the corresponding un-ribbed counterpart decreased with increasing  $Re_H$  above  $1.3 \times 10^3$ . The relative rib enhancement more or less reached the asymptotic value once the corresponding un-ribbed boundary layer became fully turbulent.

Flow and turbulence parameters were measured by an X-probe hot wire anemometer system in both streamwise and normal directions. Studying the flow and turbulence parameters behind the rib and comparing them with the smooth plate case at the highest and lowest studied  $Re_H$  revealed that the rib blocked the streamwise velocity ( $U$ ) while creating some normal velocity ( $V$ ). Also, the rib generated a significant amount of turbulence that was sustained far downstream ( $X/H$  up to 32).

Within the experimental conditions and the range of studied Reynolds numbers, the turbulence generated by the rib ( $u_{rms}$ ,  $v_{rms}$  and  $\overline{uv}$ ) turned out to be the main contributor to enhance the heat transfer. The small amount of normal velocity ( $V$ ) created in the flow after the rib was determined to be partially effective in extracting heat from the surface.

The rib is also known for generating vorticity which may also have contributed to the heat transfer augmentation, but only when the turbulence is low ( $v_{rms} = 0.2 \sim 0.4$  m/s). The energy spectra of the turbulent kinetic energy in the Y direction were studied at some points behind the rib. A couple of clear peaks were observed in the energy spectra graphs at the lowest tested  $Re_H = 1.3 \times 10^3$ , which are postulated to be the traces of the periodic vortex shedding from the rib's edge. These vortices seemed to be masked and/or destroyed by the prevailing flow turbulence at higher  $Re_H$ .

### ***Acknowledgement***

This work was made possible by the Ontario Trillium Foundation, Natural Sciences and Engineering Research Council of Canada and by Essex Energy Corporation cooperation. Furthermore, we would like to acknowledge Mr. Sai Praneeth for his help with the Matlab coding part of the project.

### ***References***

- [1] Yadav, A.S., and Bhagoria, J.L., 2.14, "A CFD based thermo-hydraulic performance analysis of an artificially roughened solar air heater having equilateral triangular sectioned rib roughness on the absorber plate," *International Journal of Heat and Mass Transfer*, 70, pp.1016–1039.
- [2] Saha, A.K., and Acharya, S., 2005, "Unsteady RANS simulation of turbulent flow and heat transfer in ribbed coolant passages of different aspect ratios, *International Journal of Heat and Mass Transfer*," 48 (23-24), pp. 4704–4725.
- [3] Panigrahi, P.K., and Acharya, S., 2004, "Multi-modal forcing of the turbulent separated shear flow past a rib," *ASME Journal of Fluid Engineering*, 126 (1), pp. 22–31.
- [4] Bhagoria, J.L., Saini, J.S., and Solanki, S.C., 2002, "Heat transfer coefficient and friction factor correlations for rectangular solar air heater duct having transverse wedge shaped rib roughness on the absorber plate," *Renewable Energy*, 25 (3), pp. 341–369.
- [5] Mittal, M.K., Varun, Saini, R.P., and Singal, S.K., 2007, "Effective efficiency of solar air heaters having different types of roughness elements on the absorber plate, *Energy*, 32 (5), pp. 739–745.
- [6] Chamoli, S., Thakur, N.S., and Sain, J.S., and 2012, "A review of turbulence promoters used in solar thermal systems," *Renewable and Sustainable Energy Reviews*, 16 (5), pp. 3154–3175.
- [7] Liu, C.H and Chung, T.N.H., 2012, "Forced convective heat transfer over ribs at various separation," *International Journal of Heat and Mass Transfer*, 55, pp. 5111–5119.
- [8] Ali, M.S., Tariq, A., and Gandhi, B.K., 2013, "Flow and heat transfer investigation behind trapezoidal rib using PIV and LCT measurements," *Experiments in Fluids*, 54, pp. 1520-1528.

- [9] Kamali, R., and Binesh, A.R., 2008, "The Importance of Rib Shape Effects on the Local Heat Transfer and Flow Friction Characteristics of Square Ducts with Ribbed Internal Surfaces," *International Communications of Heat and Mass Transfer*, 35 (8), pp. 1032-40.
- [10] Liu, Y.Z., Kang, W., and Sung, H.J., 2005, "Assessment of the organization of a turbulent separated and reattaching flow by measuring wall pressure fluctuations," *Experiments in Fluids*, 38 (4), pp. 485-493.
- [11] Liu, Y.Z., Ke, F., and Sung, H.J., 2008, "Unsteady separated and reattaching turbulent flow over a two-dimensional square rib," *Journal of Fluids and Structures*, 24 (3), pp. 366-381.
- [12] Acharaya, S., Dutta, S., Myrum, T.A., and Baker, R.S., 1994, "Turbulent flow past a surface-mounted two-dimensional rib," *ASME Journal of Fluids Engineering*, 116 (2), pp. 238-246.
- [13] Panigrahi, P.K., and Acharya, S., 2005, "Excited turbulent flow behind a square rib," *Journal of Fluids and Structures*, 20 (2), pp. 235-253.
- [14] Panigrahi, P.K., and Acharya, S., "Spectral characteristics of separated flow behind a surface-mounted square rib," *Proceedings of the 27th Fluid Dynamics Conference, American Institute of Aeronautics and Astronautics (AIAA), New Orleans, LA, 1996, Paper 96-1931*
- [15] Antoniou, J. and Bergeles, G., 1988, "Development of the reattachment flow behind surface-mounted two-dimensional prisms," *ASME Journal of Fluids Engineering*, 110 (2), pp. 127-133.
- [16] Acharya, S., Dutta, S., Myrum, T.A., and Baker, R.S., 1994, "Turbulent flow past a surface-mounted two-dimensional rib," *ASME Journal of Fluids Engineering*, 116 (2), pp. 238-246.
- [17] Murataa, A., and Mochizuki, S., 2000, "Large eddy simulation with a dynamic subgrid-scale model of turbulent heat transfer in an orthogonally rotating rectangular duct with transverse rib turbulators," *International Journal of Heat and Mass Transfer*, 43 (7), pp. 1243-1259.
- [18] Bergeles, G., and Athanassiadis, N., 1983, "The Flow Past a Surface-Mounted Obstacle," *ASME Journal of Fluids Engineering*, 105 (4), pp. 461-463.
- [19] Antoniou, J., and Bergeles, G., 1988, "Development of the reattachment flow behind surface-mounted two-dimensional prisms," *ASME Journal of Fluids Engineering*, 110 (2), pp. 127-133.
- [20] Moon, M.A., Park, M.J., and Kim, K.Y., 2014, "Evaluation of heat transfer performances of various rib shapes," *International Journal of Heat and Mass Transfer*, 71, pp. 275-284.
- [21] Cardwell, N.D., Vlachos, P.P., and Thole, K.A., 2011, "Developing and fully developed turbulent flow in ribbed channels," *Experiments in Fluids*, 50 (5), pp. 1357-1371.
- [22] Tariq, A., Panigrahi, P.K., and Muralidhar, K., 2004, "Flow and heat transfer in the wake of a surface-mounted rib with a slit," *Experiments in Fluids*, 37 (5), pp. 701-719.
- [23] Smulsky, Ya.I., Terekhov, V.I., and Yarygina, N.I., 2012, "Heat transfer in turbulent separated flow behind a rib on the surface of square channel at different orientation angles relative to flow direction," *International Journal of Heat and Mass Transfer*, 55, pp. 726-733.

- [24] Terekhov, V.I., and Yarygina, N.I., and Zhdanov, R.F., 2003, "Heat transfer in turbulent separated flows in the presence of high free-stream turbulence," *International Journal of Heat and Mass Transfer*, 46, pp. 4535–4551.
- [25] Jørgensen, F.E. 2002, "How to measure turbulence with hot-Wire anemometers - a practical guide," Dantec Dynamics, Skovlunde, Denmark.
- [26] Figliola, R.S., and Beasley, D.E., 2011, *Theory and Design for Mechanical Measurements*, 5th ed., John Wiley and Sons, Inc., New York, USA.
- [27] Panigrahi, P.K., Schroeder, A., and Kompenhans, J., 2008, "Turbulent structures and budgets behind permeable ribs," *Experimental Thermal and Fluid Science*, 32 (4), pp. 1011–1033.
- [28] Kestin, J., Maeder, P.F., and Wang, H.E., 1961, "Influence of turbulence on the transfer of heat from plates with and without a pressure gradient," *International Journal of Heat and Mass Transfer*, 3, pp. 133-154.
- [29] Junkhan, G.H., and Serovy, G.K., 1967, "Effect of free stream turbulence and pressure gradient on flat plate boundary-layer profiles and on heat transfer," *Journal of heat Transfer*, 89 (2), pp. 169-176.
- [30] Incropera, F.P., DeWitt, D.P., 1996, *Fundamentals of Heat and Mass Transfer*, 3rd ed., John Wiley and Sons, New York, USA.
- [31] Hinze, J.O., 1975, *Turbulence*, 2nd ed., McGraw-Hill, New York, USA.
- [32] Ting, D. S-K., 2016, *Basics of Engineering Turbulence*, 1st ed., Elsevier, Academic Press, New York, USA.

## CHAPTER 6

# WAVELET ANALYSIS OF PARTIAL GRID INDUCED TURBULENCE OVER A FLAT PLATE

### **6.1. Introduction**

The concept of generating nearly isotropic turbulence by a grid (perforated plate) in a wind tunnel was first introduced by Taylor in 1935 [1]. From then until now, different aspects of grid generated turbulence have been discussed extensively in many studies [2-10]. In almost all of these studies, the entire cross section of the wind tunnel was covered by the grid and not many studies were performed on a partially blocking grid. Flow and turbulence structures after a partial grid or a perforated object appear to be more complicated compared to conventional grids or solid ribs. In 1996, Judd et al., [11] performed a series of wind-tunnel experiments on the flow downstream of single and multiple porous windbreaks with a finite height and different solidities. The partial grid represented a plant canopy shelter. In their study, the experimental emphases were on the interactions of flow with the underlying plant canopy.

Using a partial grid for generating a high level of turbulence for enhancing the heat transfer rate from the downstream surface has been proposed [12]. It was observed that turbulence generated over the downstream surface was much higher than that which was generated by the grid itself. The free shear layer created at the grid's edge intensified grid turbulence. The high turbulent region generated over the surface peaked at around the grid's edge height. A partial grid, due to the higher turbulence generating potential and less flow blockage, seems to be more effective in enhancing the heat transfer from the downstream surface compared to conventional grids and solid ribs [12]. This warrants further scrutiny of the turbulent flow downstream of a partial grid. The interaction between the larger scale shearing flow over the edge of the grid and the smaller grid turbulence scale calls for wavelet analysis, which is good for revealing the transfer of the kinetic energy between scales [13].

Two main forms of the wavelet transform exist: The continuous and the discrete or orthogonal wavelet analysis. The continuous method decomposes a signal in both space and scale in a continuous manner, thus it is better suited for the analysis. This over-complete presentation of results yields to a good readability, but might result in some correlations between neighboring coefficients. Alternatively, in the discrete wavelet transform, instead of calculating wavelet coefficients at every possible scale, dyadic (power of two) scales and positions are selected. This method overcomes the neighboring coefficients correlation problem (in continuous form) and allows an orthonormal projection on a minimal number of independent (uncorrelated) modes [14,15].

The wavelet analysis has been applied in turbulent flows by Farge [14,16] and Meneveau [17] in the early 1990s. From then on, it has been utilized in a wide range of turbulence studies, a few of which are highlighted in the following paragraphs.

In 1999, Mouri et al. [18] applied an orthonormal wavelet transform on velocity signals of grid turbulence. Analyses were performed with five different wavelet families and the results were generally robust with respect to the choice of wavelet. It was seen that wavelet transform results were enhanced at the positions of the tube-like structures of vorticities. Different parameters such as the flatness factor and the scale-scale correlation of wavelet transform results were examined.

A two-dimensional continuous wavelet transform was utilized by Xu et al. [19] to study the near-wall turbulence intermittency. The intermittency level was analyzed in terms of flatness factors at different scales and different distances from the wall. Also, a specific method was proposed to decompose flow signals into intermittent and non-intermittent components.

Ruppert-Felsot et al. [15] applied wavelet tools to analyze the bursting phenomenon of a three-dimensional stretched vortex immersed in a steady laminar channel flow. The time evolution of the velocity field was measured by particle image velocimetry during several successive bursts. The orthogonal wavelet transform was utilized to split each flow realization into coherent and incoherent contributions. Also, several parameters such as the local spectrum and the local intermittency measure were proposed based on the continuous wavelet transform.

The influence of vortical structures on turbulent mixing was studied by direct numerical simulation (DNS) and wavelet-based coherent vorticity extraction by Kadoch et al. [20]. Initial conditions were taken from a direct numerical simulation database of forced homogeneous isotropic turbulence.

These previous studies indicate that the wavelet analysis shows promise in shedding light on the dynamic interaction among the cascade of turbulence scales and also the larger shearing scales. Thus, wavelet analysis is invoked in an effort to further reveal the underlying physics behind partial grid induced shearing turbulent flow over a flat plate.

### *Nomenclature*

$A_i$	approximation part of the signal at level $i$	$t$	time (s)
$a$	scale	$T_d$	time delay (s)
$b$	space	$U$	local streamwise velocity (m/s)
$D$	diagonal distance of the grid hole (cm)	$U_\infty$	free stream velocity (m/s)
$D_i$	detail part of the signal at level $i$	$u_{rms}$	root-mean-square of the streamwise velocity fluctuations (m/s)
$D(j,k)$	discrete wavelet transform of a signal $x(t)$ at level $j$ and position $k$	$uv$	Reynolds shear stress ( $m^2/s^2$ )
$f$	frequency (Hz)	$V$	local normal velocity (m/s)
$f_\Lambda$	frequency corresponding to the integral length scale (Hz)	$V_{rms}$	root-mean-square of the normal velocity fluctuations (m/s)

$f_\lambda$	frequency corresponding to the Taylor micro scale (Hz)	$W_x(a,b)$	continuous wavelet transform of a signal $x(t)$ at scale $a$ and space $b$
$f_\eta$	frequency corresponding to the Kolmogorov scale (Hz)	$X$	streamwise distance from the grid (m)
$F_a$	pseudo frequency (Hz)	$x(t)$	signal
$F_C$	center frequency of the wavelet function (Hz)	$Y$	normal distance from the plate (m)
$H$	grid height over the surface (m)	$Z$	distance along the width of the plate from the plate centerline (m)
$I(a,b)$	intermittency at scale $a$ and space $b$	$\Delta$	sampling period
$j$	level coefficient in discrete wavelet transform	$\eta$	Kolmogorov length scale (mm)
$k$	position coefficient in discrete wavelet transform	$\Lambda$	Integral length scale (mm)
$K$	Kurtosis factor	$\lambda$	Taylor micro scale (mm)
$O$	original signal	$\sigma$	standard deviation of the velocity fluctuation (m/s)
$P_{xx}$	wavelet spectrum ( $m^2/s$ )	$\psi(f)$	Fourier transform of the wavelet function
PDF	probability distribution function	$\Psi_{a,b}(t)$	wavelet function
$S$	Skewness factor		

## 6.2. Experimentation

All experimental data for the present investigation obtained in a wind tunnel with a 180 cm long, 76 cm high and 77 cm wide test section. The maximum free stream velocity in this wind tunnel is around 30 m/s and the background turbulence intensity is less than 0.4% when the test section is empty.

A schematic of the partial grid-flat plate setup used in this study is shown in Figure 6.1. The flat plate dimensions are 30.5 cm wide, 61 cm long and 1 cm thick. A  $10^\circ$  angle wedge was cut from wood and attached to the set-up leading edge to reduce the effect of the blunt edge.  $X$ ,  $Y$  and  $Z$  are the streamwise, normal to the plate and widthwise directions, respectively, with the origin located at the middle of the downstream edge of the partial grid at the horizontal flat plate surface.

To make the flow over the flat plate turbulent, a perforated plate with a diamond pattern and sharp edge was designed and placed at the leading edge of the flat plate via a support. The perforated plate was cut from an aluminum plate of 0.3 cm thickness by a computer numerical controlled machine. The outside dimensions of the perforated plate are 10 cm x 62 cm. After cutting diamond-shaped holes with a diagonal distance ( $D$ ) of 1.4 cm, the resulting solidity ratio is 0.545.



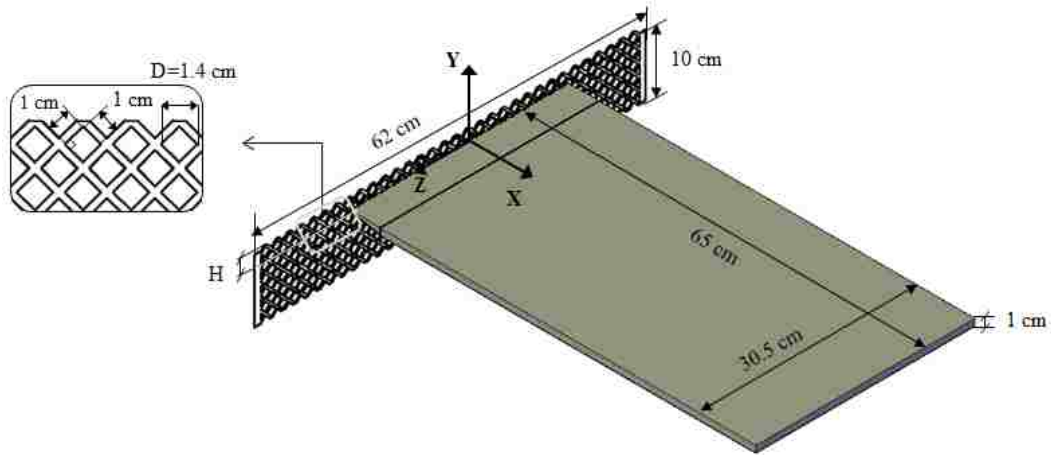


Figure 6.1 Schematic of the partial grid-flat plate setup

The plate was placed at mid-height in the middle of the test section with the plate and support system creating a blockage of around 2% of the tunnel cross section. A schematic of the setup inside the wind tunnel test section is shown in Figure 6.2.

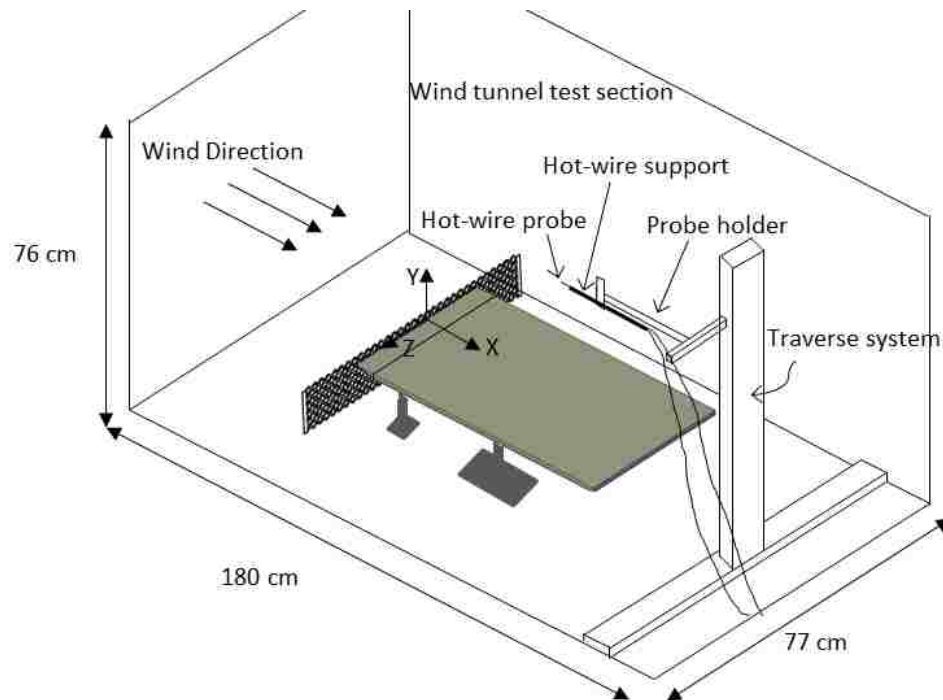


Figure 6.2 Wind tunnel test section with the experimental set-up

Streamwise and normal (X and Y) velocities at different points downstream of the rib were measured by a fiber film X-probe (type 55P61) with a Dantec streamline 55C90 constant-temperature anemometer (CTA). The probe had two Nickel wires with diameters of 70  $\mu\text{m}$  and lengths of 1.25 mm. Signals were low-passed at 30 kHz and then sampled at 40 kHz over a period of around 12.5 s, resulting in 500,000 data points per measurement. A 12-bit PCI-6071E National Instrument data acquisition card was used to convert the analog data into a digital one. A computer-controlled 2-D traverse system was used to position the probe at each specified location. The computer-controlled traverse system can move through the widthwise direction of the test section (Z) and normal direction to the plate (Y) in 2 mm steps.

### 6.2.1. Methodology

Measurements were performed at  $Z = 0$  (Figure 6.1) and at 13 points in the Y direction (from  $Y/H = 0.15$  to 2.1) at two streamwise locations ( $X/H = 8.75, 17.75$ ). H is the grid's height above the surface ( $H = 2$  cm). This particular value of H was selected based on lessons learned from the previous study [12], where the smaller H caused the higher level of turbulence near the downstream flat plate surface. As the ultimate goal of this study was to increase the level of the turbulence over the downstream surface to eventually enhance the heat transfer rate, more emphasis was put on the area close to the surface. Tests were performed at free-stream velocity of 4 m/s. The Reynolds number based on the grid hole size (D) was  $Re_D = 3.7 \times 10^3$ .

## 6.3. Wavelet Fundamentals

In this section the concept of the pertinent wavelet analysis is briefly highlighted for completeness.

### 6.3.1. Continuous Wavelet Transform

The continuous wavelet transform (CWT) is an integral transform which unfolds a field into space (1/time) and scale contributions [15]. The continuous wavelet transform of a signal  $x(t)$  is [13]:

$$W_x(a, b) = \int x(t)\psi_{a,b}(t)dt \quad (6.1)$$

where parameters a and b are the scale (frequency) and position (in time) respectively, and  $\Psi_{a,b}(t)$  is the wavelet function. The wavelet function is an oscillating function with zero mean which is well localized in both physical space and spectral space. Also, it should satisfy the admissibility condition [13]:

$$C_\Psi = \int_0^\infty \frac{\Psi(f)}{f} df < \infty \quad (6.2)$$

where  $\psi(f)$  is the Fourier transform of the wavelet function and f is the frequency.

Finding the best convolution between the signal and wavelet function is the concept of the wavelet transformation [21]. The scale parameter is related to the frequency while the position parameter is related to the time. The pseudo frequency corresponding to each scale is deduced as follows [22]:

$$F_a = \frac{F_c}{a \cdot \Delta} \quad (6.3)$$

where  $a$  is the scale,  $\Delta$  is sampling period,  $F_c$  is the center frequency of the wavelet function.

The inverse continuous wavelet transforms which gives the function  $x(t)$  is [13]:

$$x(t) = \frac{1}{C_\psi} \int_a \int_b W_x(a, b) \psi_{a,b}(t) \frac{da db}{a^2} \quad (6.4)$$

The wavelet spectrum is defined as [13]:

$$P_{xx}(a, b) = |W_x(a, b)|^2 \quad (6.5)$$

### 6.3.1.1. Intermittency Measure

The flow intermittency was quantified by a specific parameter which was proposed by Farge et al. [15]. It is defined based the spatial distribution of the local deviation from the wavelet energy spectrum at a given scale [15,16]:

$$I(a, b) = \frac{|W_x(a, b)|^2}{\int_b |W_x(a, b)|^2 db} \quad (6.6)$$

When  $I(a, b) \approx 1$ , it demonstrates that the energy is distributed evenly in the space and the flow is non-intermittent. Deviation of this parameter from unity means that the flow is intermittent and it presents an inconsistent behavior such as coherent structures [15].

### 6.3.2. Discrete (orthogonal) Wavelet Transforms

Discrete wavelet transform is defined as a sub-sample of the continuous wavelet, which decomposes the signal into discrete decomposition levels [13]:

$$D(j, k) = \sum x(t) \psi_{j,k}(t) \quad (6.7)$$

where  $j$  and  $k$  are the level and position coefficients respectively, which are dyadic sub-samples of the scale and position coefficients in the continuous wavelet analysis ( $a$  and  $b$ ) [13]:

$$a = 2^j, b = k \cdot 2^j \quad (6.8)$$

At each level, “approximations” are the high-scale, low-frequency components of the signal while “details” are low-scale, high-frequency components [23]. The inverse form of the discrete wavelet transform that gives the original function is:

$$x(t) = \sum_j \sum_k D(j, k) \psi_{j,k}(t) \quad (6.9)$$

The discrete wavelet spectrum is given by [13]:

$$P_{xx}(j, k) = |D(j, k)|^2 \quad (6.10)$$

## 6.4. Results and Discussion

The turbulence structure after a partial grid placed at the leading edge of a flat plate was explored by the wavelet transform and the results are presented in this section. In the first section, flow and turbulence intensity profiles over the surface of the flat plate were studied at two streamwise distances ( $X/H = 8.75$  and  $17.75$ ) from  $Y/H = 0.15$  to  $2.1$ . In the second part, discrete and continuous wavelet analyses are performed at four specific measuring points.

### 6.4.1. Flow under Study

To have a better insight of the flow condition after a partial grid over a flat surface, velocity, turbulence intensity and shear stress values at two different free stream distances after the grid,  $X/H = 8.75$  and  $17.75$ , were deduced from instantaneous velocity data measured by the hot-wire. Related equations and analysis can be found in Ref. [12]. Normalized velocity and turbulence profiles at these two downstream distances and from  $Y/H = 0.15$  to  $2.1$  are shown in Figure 6.3 (a) to (e). The typical uncertainties associated with each parameter was estimated based on the method explained in Ref. [12] and are shown in these graphs as error bars. The spatial ( $Y/H$ ) uncertainty is very small ( $\pm 0.02$ ) and hence, is not visible.

As can be seen in Figure 6.3 (a), the normalized streamwise velocity ( $U/U_\infty$ ) increases in the normal direction from  $Y/H = 0.15$  to  $2.1$  and approaches unity, that is, the free stream velocity. This unique thick boundary layer is created by the partial grid. The conventional boundary layer next to the surface of the flat plate is not quite visible, as the measurement point nearest to the surface is at  $Y/H = 0.5$ . These streamwise velocity profiles do not experience a drastic change in the streamwise direction from  $X/H = 8.75$  to  $17.75$ . Normal velocities ( $V/U_\infty$ ) in Figure 6.3 (b), have small negative values near the surface. This may be perceived as the prevailing “wind breaking effect” over an extended downstream span. The absolute value of the normal (to the flat plate) velocity increases in the normal direction, reaches a peak at around  $Y/H = 1.5$  and decreases subsequently. The larger negative normal velocity at the closer distance to the grid,  $X/H = 8.75$ , may be due to the significant downward motion in the recirculating region.

Both streamwise and normal turbulence intensities in Figure 6.3 (c) and (d) increase in the normal direction from the plate and peak at  $Y/H$  around  $1.5$  and subsequently decrease. They are expected to eventually reach the free stream turbulence intensity (less than  $0.04$ ). At the grid edge, a highly turbulent area is created, however the peak point does not coincide exactly with the grid edge height, it is located at the middle of the grid edge shear layer ( $Y/H \cong 1.5$ ). As expected, normalized  $u_{rms}$  and  $v_{rms}$  decrease with downstream distance from the grid which indicates decay of the turbulence kinetic energy.

Reynolds shear stress, which is a cross correlation between the streamwise and normal velocity fluctuations, at two downstream distances can be observed in Figure 6.3 (e). This parameter demonstrates the momentum transport by the velocity fluctuations across the shear layer [24, 25]. As the production of this quantity is related to the spatial gradients in the time averaged velocity, it can be produced in boundary or shear layers [26]. Furthermore, the production of this parameter seems to increase the surface heat transfer and friction [24, 25]. As can be seen in Figure 6.3 (e), this parameter presents negative values over the entire studied region. The negative sign of the uv correlation indicates the downward tendency of velocity fluctuations after the grid [27]. The

absolute value of the shear stress increased with the distance to the plate, reached a peak at the middle of the grid edge shear layer,  $Y/H \cong 1.5$ , and subsequently decreased. This peak point is corresponded to maximum turbulence intensities in Figure 6.3 (c) and (d). A general decreasing trend in the turbulence shear stress absolute value with downstream distance can be observed in this graph, which is another indication of the turbulence decay.

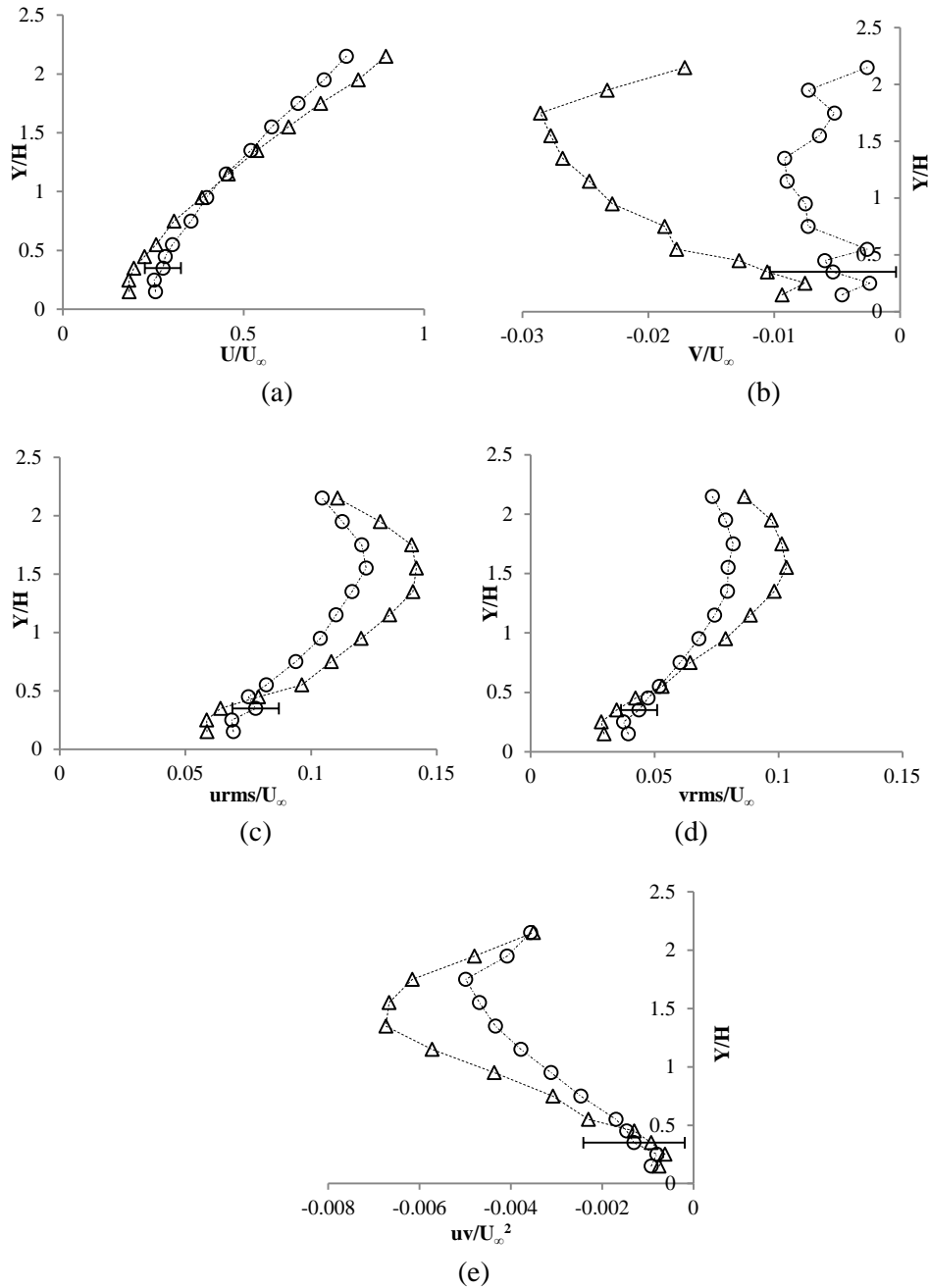


Figure 6.3 Normalized (a) streamwise (b) normal velocities (c)  $u_{rms}$  (d)  $v_{rms}$  and (e) Reynolds shear stress profiles, at different downstream distances. The triangles signify  $X/H = 8.75$  and circles  $X/H = 17.75$

### 6.4.2. Power Spectra

In order to investigate detailed flow physics after the partial grid and the trend of turbulence parameters through downstream and in the normal direction from the area behind the grid to the edge, four points were selected for wavelet analysis. These points were located at two downstream distances from the grid ( $X/H = 8.75$  and  $17.75$ ) and at the middle and just above the edge of the grid height ( $Y/H = 0.55$  and  $1.05$ ). These specific points are shown in Figure 6.4. Analyses were performed on both streamwise and normal velocity fluctuation signals,  $u$  and  $v$ .

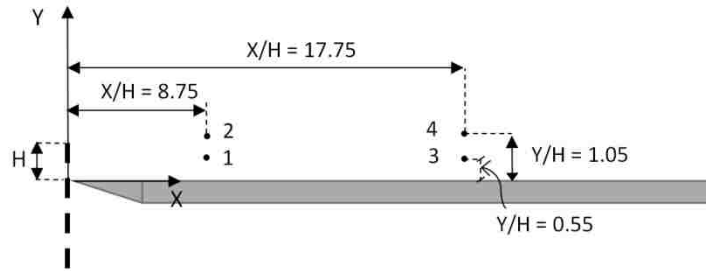


Figure 6.4 Four selected points after the grid for analysis

The Fourier power spectrum gives the distribution of the signal's time-averaged energy in the frequency domain [22]. Thus, power spectra of turbulence velocity signals are invoked to reveal information regarding the turbulence kinetic energy associated with the cascade of the large to small spectrum of eddies [27].

Power spectra of  $u$  and  $v$  signals ( $P_{uu}$  and  $P_{vv}$ ) at Points 1 to 4 are presented in Figure 6.5. The X-axis in these graphs is the frequency, which is inversely proportional to the size of the eddy motion. It can be seen that most of the energy is associated with the low-frequency, large eddies, and the amount of energy drops sharply with increasing frequency. The spectra exhibit a reduction with a slope almost of  $-5/3$  (Figure 6.5 (a)) [27]. No obvious dominant spectral peak, which could be an indication of regular vortex shedding, is observed in these graphs, except for frequencies higher than 2 kHz, where some spikes appear. The Strouhal number corresponding to the frequency at these spikes based on the grid height and free stream velocity ( $fH/U_\infty$ ) is in the range of  $8 \sim 10$ . This is much larger than the typical Strouhal number associated with the vortex shedding in the flow after obstacles reported in the literature ( $0.03 \sim 0.19$ ) [24,28]. Thus, high-frequency spikes are presumably due to the existence of some noise in the measured signals. The highly unorganized, turbulent flow downstream of the multi-hole partial grid probably disintegrated or hindered the formation of regular vortices. Comparing  $u$  and  $v$  signals in both figures reveals that the energy of the signal in the dominant flow direction is higher than that of the normal direction, especially at the lower frequencies.

Moving in the normal direction to the plate ( $Y$ ) from Point 1 to 2 (Figure 6.5 (a) to (b)) and 3 to 4 (Figure 6.5 (c) to (d)), a slight increase (the area underneath the line) in the magnitude of both  $u$  and  $v$  power spectra in all ranges of frequencies can be seen. This shows a rise in the flow turbulence energy from the middle height to the edge of the grid. Also, moving downstream from Point 1 to 3

and 2 to 4, a slight reduction can be observed in  $P_{uu}$  and  $P_{vv}$ , which is an indication of turbulence energy decay in both streamwise and normal directions.

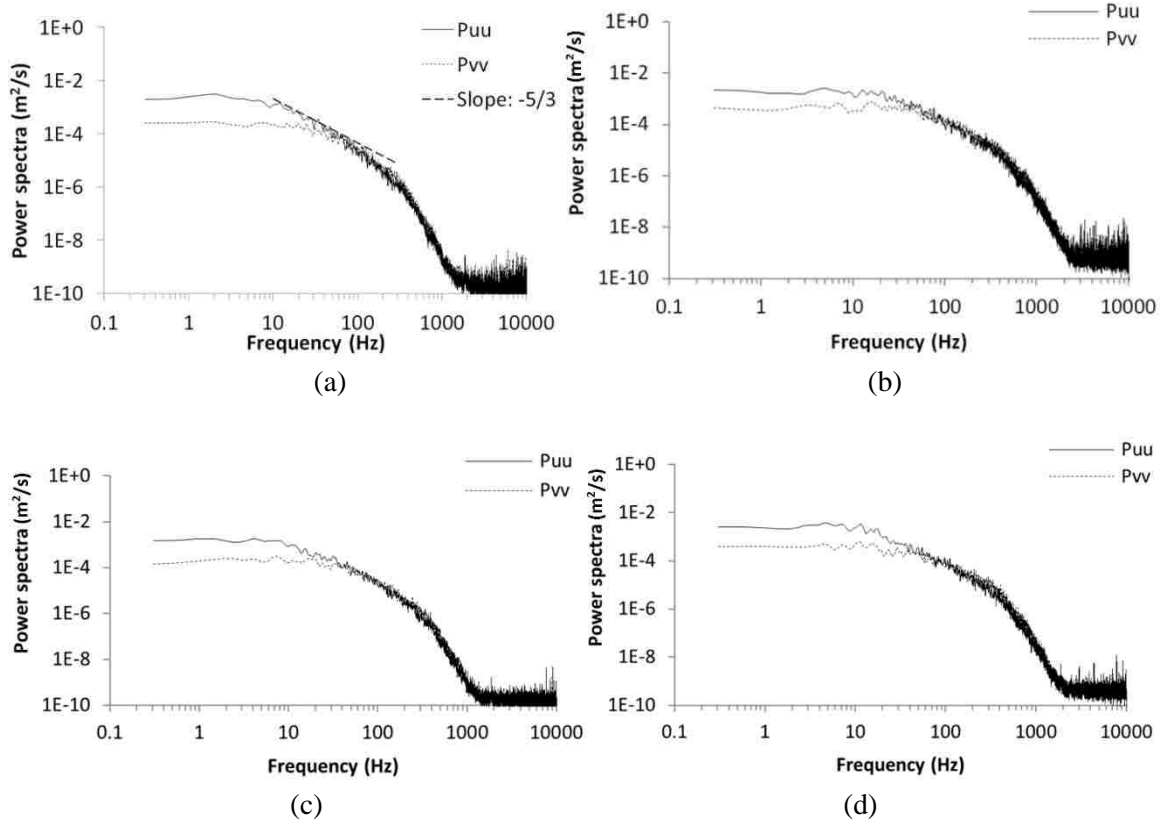


Figure 6.5 Power spectra of  $u$  and  $v$  signals ( $P_{uu}$  and  $P_{vv}$ ) at points: (a) 1 ( $X/H = 8.75$ ,  $Y/H = 0.55$ ), (b) 2 ( $X/H = 8.75$ ,  $Y/H = 1.05$ ), (c) 3 ( $X/H = 17.75$ ,  $Y/H = 0.55$ ) and (d) 4 ( $X/H = 17.75$ ,  $Y/H = 1.05$ )

To have a better view of the frequency range in the turbulence energy cascade, Integral ( $\Lambda$ ), Taylor ( $\lambda$ ) and Kolmogorov ( $\eta$ ) length scales and their corresponding frequencies in the streamwise direction were estimated at these four specific points and are shown in Table 6.1. The Integral scale represents large eddies in the turbulence energy cascade, while the Taylor and Kolmogorov scales signify the average small and smallest eddies respectively [27]. Methods for estimating these turbulence scales are discussed in detail elsewhere [12].

A turbulence energy cascade starts from the large scales, where energy is harvested from the mean flow to successively smaller scales, Taylor and Kolmogorov, where the kinetic energy is dissipated by the viscosity [27]. As can be seen in Table 6.1, at each point the lowest frequency corresponds to largest eddies (integral length scale) while the highest frequency belongs to the smallest eddies (Kolmogorov scale), as was assumed based on Taylor's Frozen hypothesis [26].

Table 6.1 Turbulence scales (length and frequency) at Points 1 to 4

Point	$\Lambda$ (mm) $f_{\Lambda}$ (Hz)	$\lambda$ (mm) $f_{\lambda}$ (Hz)	$\eta$ (mm) $f_{\eta}$ (Hz)
1 (X/H = 8.75, Y/H = 0.55)	17.6 62	5.1 225	0.2 1347
2 (X/H = 8.75, Y/H = 1.05)	15.7 168	6.2 425	0.1 4165
3 (X/H = 17.75, Y/H = 0.55)	20.1 67.5	5.2 244	0.2 1407
4 (X/H = 17.75, Y/H = 1.05)	23.3 104	7.1 348	0.2 2930

From points at the middle height of the grid (Points 1 (X/H = 8.75, Y/H = 0.55) and 3 (X/H = 17.75, Y/H = 0.55)) to the edge of the grid (Points 2 (X/H = 8.75, Y/H = 1.05) and 4 (X/H = 17.75, Y/H = 1.05)) the frequencies in all ranges of eddies increase, which demonstrates an overall rise in the turbulence energy. This is in agreement with results shown in Figure 6.5. Moving downstream, from Point 1 to 3 and 2 to 4, frequencies decrease and length scales increase, which is an indication of the turbulence energy decay.

The highest frequency in Table 6.1 is 4165 Hz which belongs to the Kolmogorov scale at Point 2. As the turbulence cascade for all of the four studied points ends at this high limit, signal components at frequencies higher than 5 kHz are not going to be discussed in the following sections.

### 6.4.3. Wavelet analysis

Finding the best convolution between the signal and the wavelet function, sometimes called the “mother wavelet,” is a key objective in the wavelet analysis [21]. The mother wavelet has a zero mean value, so it is able to derive variations of the signal [18]. Several wavelet functions exist which can be selected for a given application depending on the flow physics. However, there is no standard procedure for choosing the mother wavelet, but an accepted approach is to use the one with a shape similar to the signal’s shape. Nevertheless, different wavelet functions can be applied to the signal and results could be compared to evaluate the best one for a specific application [22].

In this study, to choose the best wavelet function and validate the wavelet analysis, results from the discrete wavelet transform at different levels were compared using the filtered original signal in the same frequency ranges. The filtered signal was verified to have almost the same amplitude and trend as the original signal. A couple of digital filters (low pass and band pass) were designed based on frequency ranges corresponding to discrete wavelet transform levels (Table 6.2). However, it should be kept in mind that digital filters may also have some side effects on the signal, first and foremost, they introduce a delay in the signal.



Several wavelet functions commonly utilized in turbulence studies were applied on the signals and the results were compared with the filtered signals. Figure 6. 6 shows part of the comparison of signal  $u$  (m/s) at Point 1 ( $X/H = 8.75$ ,  $Y/H = 0.55$ ). In this figure, the filtered signal (Figure 6.6 (a)) and discrete wavelet analysis results by some of the wavelet functions; “Discrete Meyer (dmey)” function (Figure 6.6 (b)), “Haar” (Figure 6.6 (c)) and “Debouche (db10)” (Figure 6.6 (d)) at some specific frequency ranges are shown. The time delay ( $T_d$ , around 0.125 s in this case) caused the filtered signals to slightly lag behind that of discrete wavelet transforms. Mother wavelet, “dmey” and “db10” comparable results with the filtered signal. However, at higher frequency ranges (1.25 ~ 2.5 kHz) the output results from “dmey” seem to be closer to the filtered signal, as “db10” illustrates larger spikes. As can be seen, “Haar” presents a very different trend and amplitude compared to the filtered signal, especially at higher frequencies. Based on these results, “dmey” was selected as the base wavelet function for both discrete and continuous wavelet analyses.

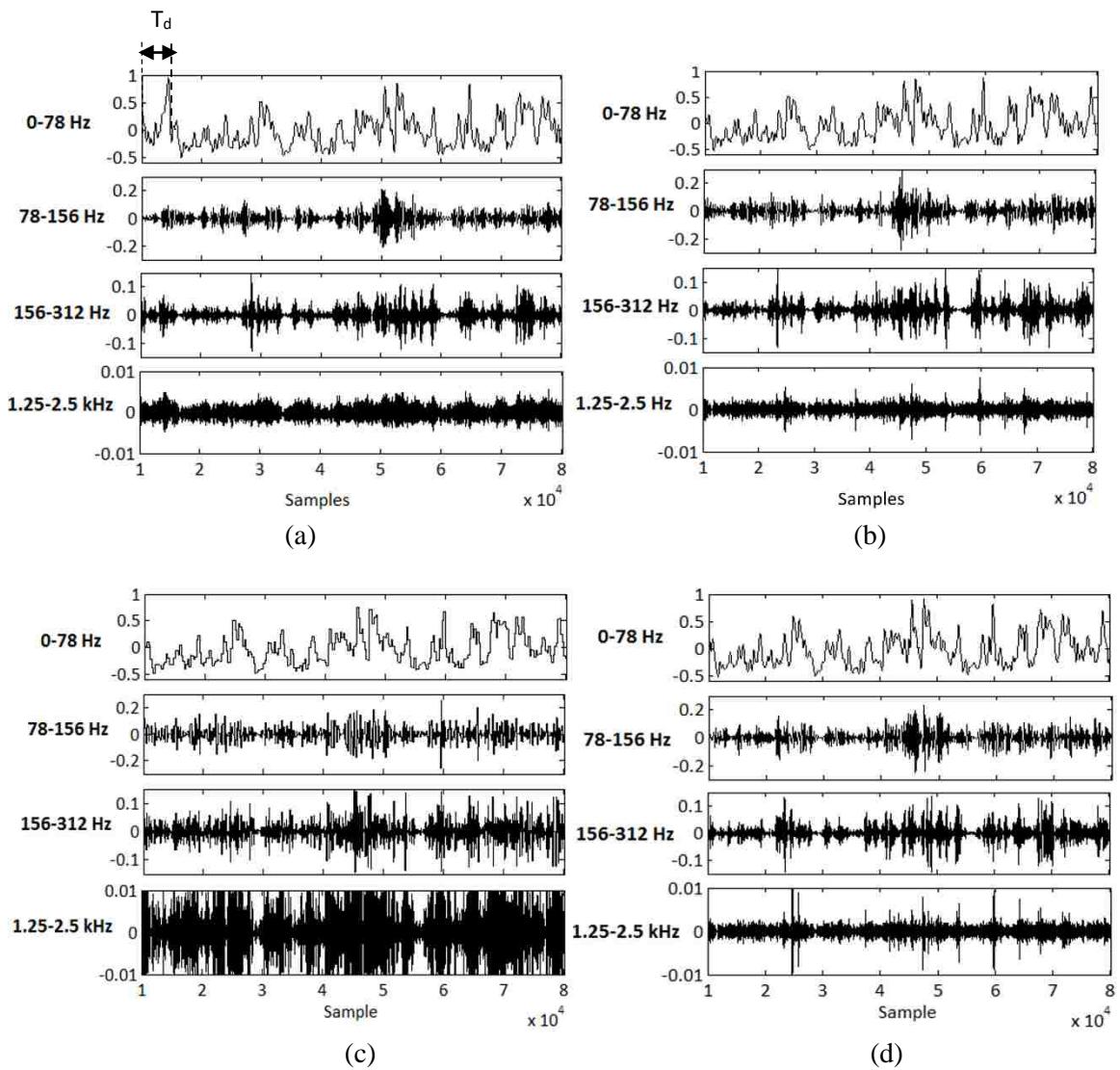


Figure 6.6 Comparison between the filtered signal (a), and wavelet transforms with different functions: (b) dmey (c) Haar (d) db10 performed on the  $u$  signal at Point 1 ( $X/H = 8.75$ ,  $Y/H = 0.55$ )

### 6.4.3.1. Discrete wavelet analysis

Discrete wavelet analysis disintegrates a signal in a magnitude-time domain at different frequency ranges. Streamwise and normal velocity fluctuation signals,  $u$  and  $v$ , at the four mentioned points (Figure 6.4) were decomposed into 8 levels by the discrete wavelet method. The “dmey” function was utilized in the analyses as the base function. Different frequency ranges corresponding to each level of the analysis are shown in Table 6.2. At each level, the signal is decomposed into the low-frequency part (Approximation) and the high-frequency part (Detail).

Table 6.2 Discrete wavelet transform levels and frequencies

Approximation	Frequency (Hz)	Detail	Frequency (Hz)
A1	0 ~ 10000	D1	10000 ~ 20000
A2	0 ~ 5000	D2	5000 ~ 10000
A3	0 ~ 2500	D3	2500 ~ 5000
A4	0 ~ 1250	D4	1250 ~ 2500
A5	0 ~ 625	D5	625 ~ 1250
A6	0 ~ 312.5	D6	312.5~625
A7	0 ~ 156.2	D7	156.2 ~ 312.5
A8	0 ~ 78.1	D8	78.1 ~ 156.2

Signals ( $u$  and  $v$ ) and their decompositions (A8 to D3) are shown in Figures 6.7 to 6.10. The analysis was performed on signals for a 6 s duration. However, for better visibility, just 2 s are shown in these graphs. The signal’s component at the lowest frequency range (0 ~ 78.1 Hz) or the approximation part of the signal at level 8 (A8) includes the lower frequency fluctuations of the signal where most of the kinetic energy (KE) of the signal resides. Thus, its trend is similar to the overall trend of the signal. At higher frequency ranges, the plots illustrate the detail part of the signal.

An overall decreasing trend in signal decomposition amplitudes with increasing frequency, from A8 to D3, can be observed in all of these graphs (except for some specific levels which are assumed to be due to some noises in the signal and will be discussed later in this section). This is in agreement with Figure 6.5, where turbulence energy decreased continuously with increasing frequency from large to small eddies. As mentioned before, most of the fluctuating energy is associated with large-scale motions while most of the vorticity is associated with small-scale motions [18]. Thus, this continuous decreasing trend in the amplitude of signal components with increasing frequency could be another indication that no regular vortices were present at these points.

Figure 6.7 presents velocity fluctuation signals ( $u$  and  $v$ ) and their decompositions at different levels at Point 1 ( $X/H = 8.75$  and  $Y/H = 0.55$ ). A continuous decreasing trend in signals' component amplitudes, from A8 to D4, is observed in both  $u$  and  $v$ . From D4 to D3, a slight increase in amplitude is seen. This small rise is likely due to some noises in the signal at higher frequencies, as seen before in the power spectra (Figure 6.5). Comparing  $u$  and  $v$  graphs and their components in this figure reveals that amplitudes of signal  $u$  and its approximation level component (A8) are greater than that of  $v$ . This indicates that in the prevailing flow direction, the velocity fluctuation magnitude is greater than those in the other directions. Comparing  $u_{rms}/U_\infty$  and  $v_{rms}/U_\infty$  (Figure 6.3 (a) and (d)) also confirms this observation.

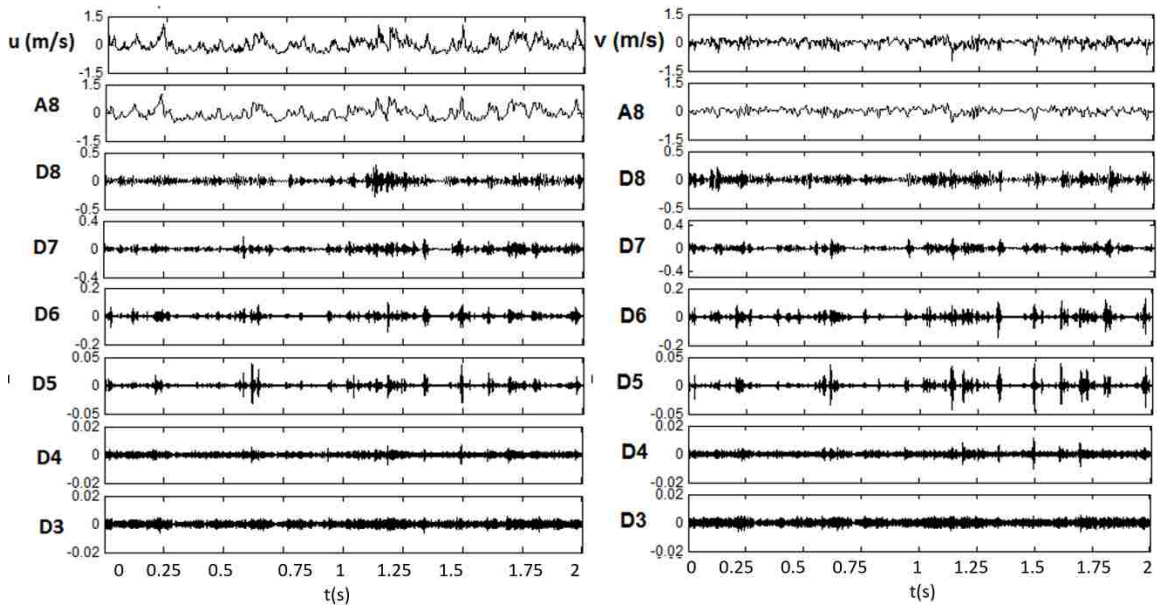


Figure 6.7 Discrete wavelet analysis of  $u$  (m/s) and  $v$  (m/s) signals at  $X/H = 8.75$  and  $Y/H = 0.55$

Figure 6.8 illustrates  $u$  and  $v$  signals and their decompositions at Point 2 which was located at around the edge of the grid height ( $X/H = 8.75$  and  $Y/H = 1.05$ ). Compared to Point 1, the signal amplitude at all levels (frequency ranges) is significantly larger. This reveals that the turbulence energy level in both streamwise and normal directions increases from Point 1 (at the mid height of the grid) to Point 2 (near the edge of the grid). This is in agreement with turbulence intensity and shear stress trends in the previous section (Figure 6.3 (c), (d) and (e)). Comparison between  $u$  and  $v$  shows that the amplitude of  $u$  and its approximation component (A8) are slightly larger than that of  $v$ . On the other hand, in detail levels (higher frequency ranges), components of  $v$  show larger spikes.

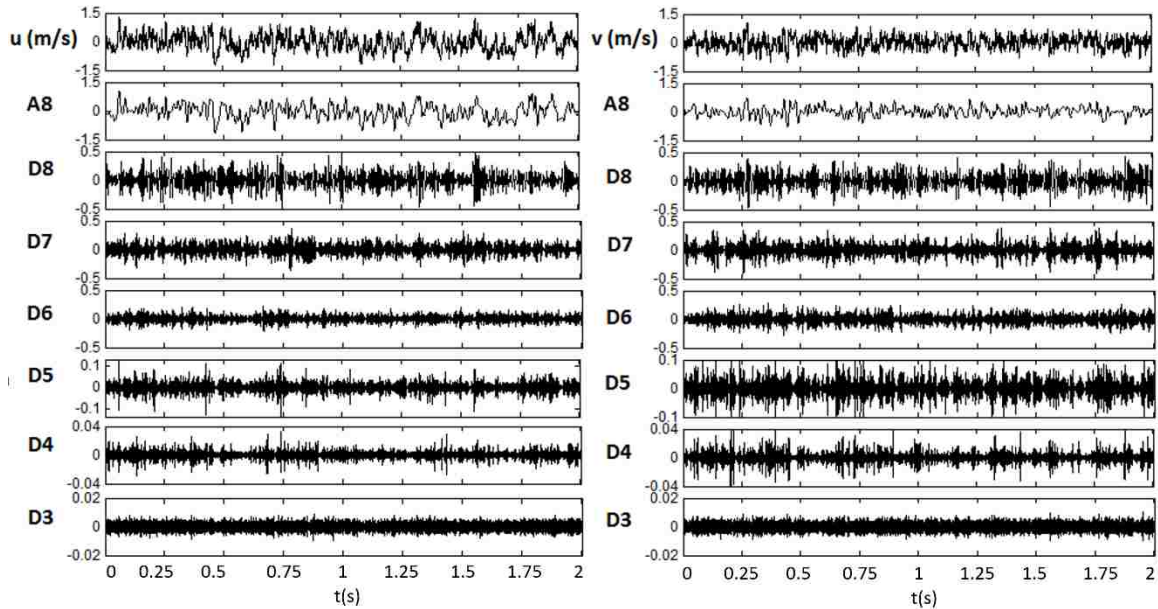


Figure 6.8 Discrete wavelet analysis of  $u$  (m/s) and  $v$  (m/s) signals at  $X/H = 8.75$  and  $Y/H = 1.05$

Figure 6.9 presents discrete wavelet analysis results at Point 3 ( $X/H = 17.75$  and  $Y/H = 0.55$ ). The higher  $u$  amplitude compared to that of the  $v$  signal is seen here again. While at higher frequency ranges, specifically D8, D6 and D5,  $v$  decompositions have larger amplitudes. Compared to Point 1, which is located at the same height but closer distance to the grid ( $X/H = 8.75$ ), both  $u$  and  $v$  signals and their decompositions have considerably smaller amplitudes, confirming the downstream decay of the turbulence energy at all ranges of scales. This is in agreement with Figure 6.3 (c), (d) and (e), where a reduction was observed in turbulence intensities and shear stress in the downstream direction.

Figure 6.10 shows results for Point 4 which is at the same downstream distance as Point 3 ( $X/H = 17.75$ ) but near the grid edge in the vertical direction ( $Y/H = 1.05$ ). Compared to Point 3, there is a significant rise in both  $u$  and  $v$  signals and their components. This indicates that some turbulence energy is generated at around the grid edge in all scales. However, this energy is lower than that of Point 2, which was located at the same level but closer to the grid, that is, the turbulence has decayed to some extent by the time it reaches Point 4. In spite of the smaller amplitude of signal  $v$  compared to  $u$ , its components in detail levels, specifically at D6 and D5 levels have larger spikes.

What was seen in all of these figures (Figure 6.7 to 6.10), at detail levels D8~D3, is that some spikes appear in the signal, which are not observed at approximation level A8, where the signal shows a smoother trend. This could be an indication of the higher intermittency of the signal at higher frequencies. The intermittency of each signal's components at different frequency ranges was analyzed in terms of the flatness factor (Figure 6.11) and also quantified by calculating the local intermittency parameter in the continuous wavelet analysis (Figures 6.16 and 6.17).

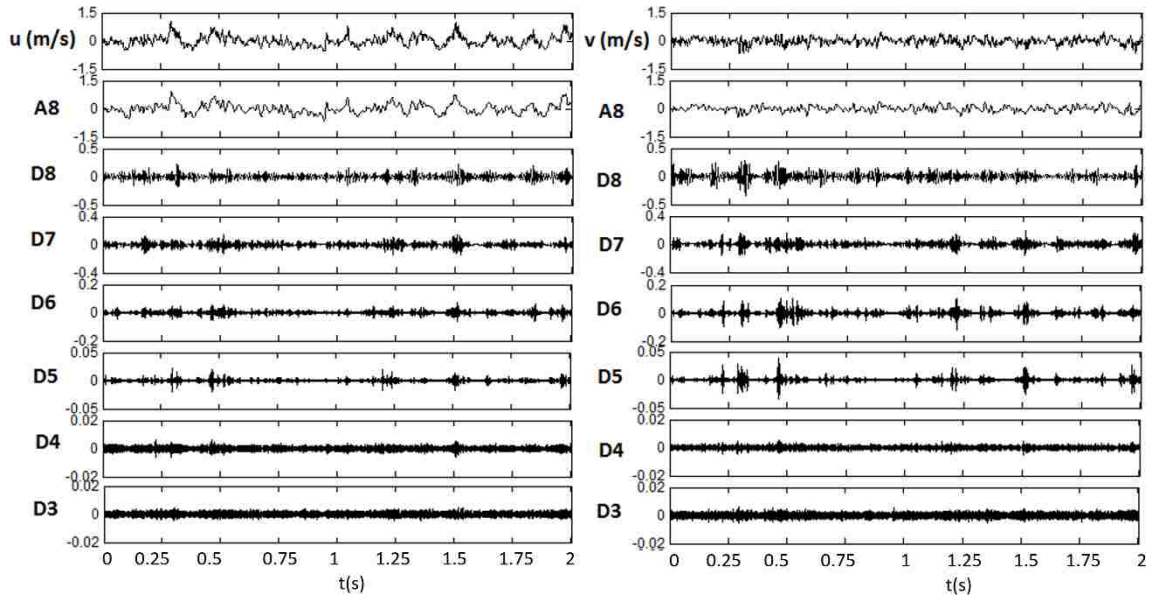


Figure 6.9 Discrete wavelet analysis of  $u$  (m/s) and  $v$  (m/s) signals at  $X/H = 17.75$  and  $Y/H = 0.55$

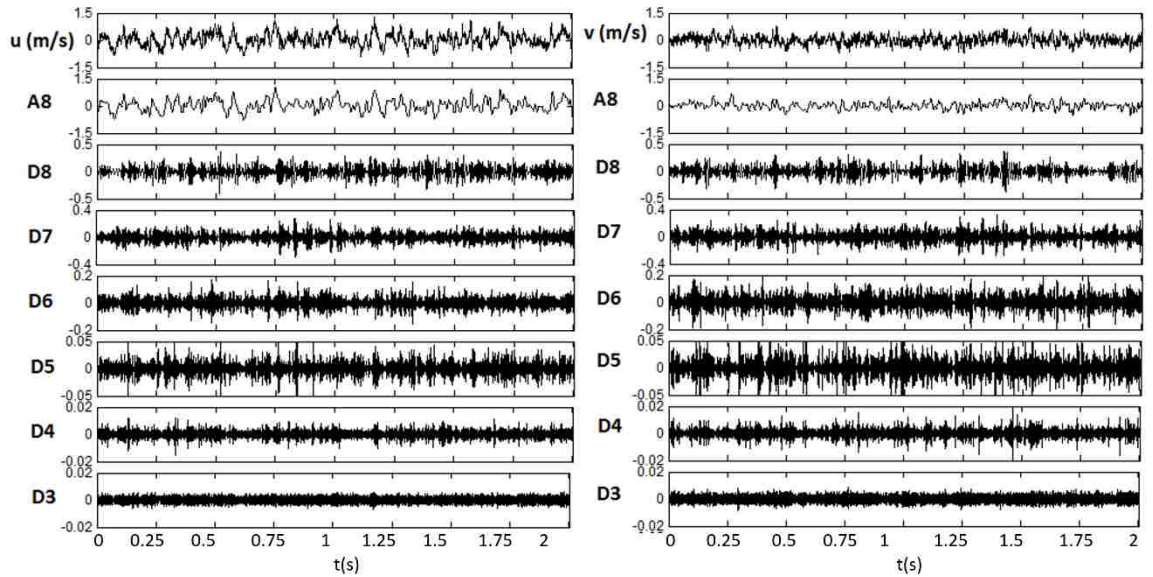


Figure 6.10 Discrete wavelet analysis of  $u$  (m/s) and  $v$  (m/s) signals at  $X/H = 17.75$  and  $Y/H = 1.05$

#### 6.4.3.1.1. Skewness and Flatness Factors

The random behavior of turbulent flows can be described by several statistical factors. Two of these factors are skewness and flatness (kurtosis), which signify the shape of the probability distribution function [27]. Both parameters are discussed in this section.

The third central moment of the signal ( $\overline{u^3}$  or  $\overline{v^3}$ ) indicates the amount of skewness in the probability distribution of the signal. This measure of the lack of symmetry is commonly expressed in a normalized form called the skewness factor [27]:

$$S \equiv (\overline{u^3} \text{ or } \overline{v^3})/(\sigma^3) \quad (6.10)$$

The smaller value of  $S$ , the more symmetrical the probability distribution of the signal. A perfect, symmetrically distributed signal gives  $S = 0$ .

Returning to  $u$  and  $v$  signals and their decompositions in Figures 6.7 to 6.10, it can be observed that at Points 1 ( $X/H = 8.75$ ,  $Y/H = 0.55$ ) and 3 ( $X/H = 17.75$ ,  $Y/H = 0.55$ ) (Figures 6.7 and 6.9),  $u$  is positively while  $v$  is negatively skewed. The positively skewed signal indicates that most of the time the fluctuating velocity is concentrated below the mean value (zero), while it fluctuates much farther, though only sparsely, to the extreme values above the mean (zero) [27]. Part of the positive skewness of the streamwise velocity fluctuation ( $u$ ) signal could be due to the hot-wire limitation in measuring the velocities when the velocity vector is outside the  $\pm 45^\circ$  window with respect to the probe axis [29]. Skewness of signals and their components are quantified in Figure 6.11, which shows the skewness of  $u$  and  $v$  signals and their decompositions at Points 1 to 4. In this figure, the X-axis shows the level of the signal's component. Frequency ranges corresponding to each decomposition level are shown again in Table 6.3. The symbol "O" means the original  $u$  or  $v$  signal. Different turbulence length scales ( $\Lambda$ ,  $\lambda$  and  $\eta$ ) estimated at these measuring points (Table 6.1), are also shown on different levels based on their corresponding frequency ranges.

Figures 6.11 (a) and (c) show that the skewness factor for both  $u$  and  $v$  signals (O) and their approximation level components (A8), at Points 1 ( $X/H = 8.75$ ,  $Y/H = 0.55$ ) and 3 ( $X/H = 17.75$ ,  $Y/H = 0.55$ ), which are located at the middle height of the grid, deviate from zero. The sign of  $S$  in these graphs indicates the direction of the largest velocity fluctuations, while the magnitude of  $S$  depicts the degree of asymmetry in the distribution of velocity fluctuations [12]. These results confirm that at Points 1 and 3 the streamwise velocity fluctuations ( $u$ ) tend to be positive, while the normal velocity fluctuations ( $v$ ) tend to be negative. The integral length scale ( $\Lambda$ ) at these two points coincides with A8. As can be seen, at turbulence length scales smaller than  $\Lambda$  (higher frequency ranges),  $S$  decreases to almost zero, except for D3 and D4 levels at Point 1. This reveals that at smaller turbulence scales (higher frequency ranges) the signal is more symmetrical around its mean value compared to large scales. The significant rise in  $S$  value at D3 and D4 levels compared to lower levels at Point 1 is presumably due to noise at higher frequency ranges, as mentioned earlier.

Figures 6.11 (a) and (c) also depicts that the  $S$  values for both  $u$  and  $v$  signals are higher at Point 1, which is located at a closer downstream distance to the grid compared to Point 3 ( $X/H = 17.75$ ,  $Y/H = 0.55$ ). This shows the larger effect of the grid on the velocity fluctuation deflection at a closer downstream distance.

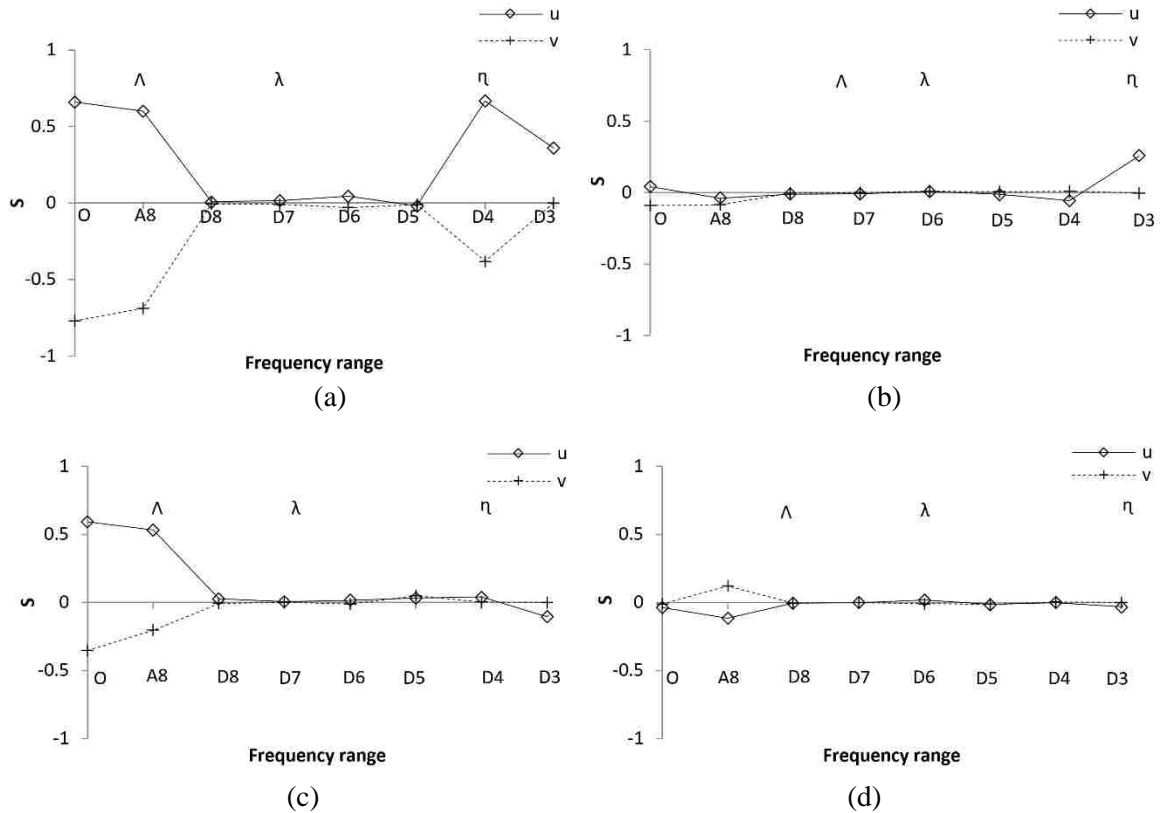


Figure 6.11 Skewness factor at (a) point 1 ( $X/H = 8.75$ ,  $Y/H = 0.55$ ), (b) point 2 ( $X/H = 8.75$ ,  $Y/H = 1.05$ ), (c) point 3 ( $X/H = 17.75$ ,  $Y/H = 0.55$ ) and (d) point 4 ( $X/H = 17.75$ ,  $Y/H = 1.05$ )

Table 6.3 Frequency range corresponding to each discrete wavelet decomposition level

O	A8 (Hz)	D8 (Hz)	D7 (Hz)	D6 (Hz)	D5 (Hz)	D4 (kHz)	D3 (kHz)
Signal	0~78.1	78.1~156.2	156.2~312.5	312.5~625	625~1250	1.25~2.5	2.5~ 5

At Points 2 and 4 (Figure 6.11 (b) and (d)), which are located in line with the edge of the grid,  $S$  factors of both  $u$  and  $v$  signals are smaller (close to zero) compared to points at the middle height of the grid (Points 1 and 3). At all frequency ranges,  $S$  is almost zero, with a small deviation observed at D3 for Point 2 ( $X/H = 8.75$ ,  $Y/H = 1.05$ ) and A8 for Point 4 ( $X/H = 17.75$ ,  $Y/H = 1.05$ ). This indicates that the corresponding signals and their components are almost symmetrical at these two measuring points.

Thus as can be seen, the fluctuating velocity signals ( $u$  and  $v$ ) at height  $Y/H = 0.55$  (Points 1 and 3) are more asymmetrical compared to those at  $Y/H = 1.05$  (Points 2 and 4). This shows that other than the average downward flow direction (positive  $U$  and negative  $V$ , Figures 6.3 (a) and (b)) at these streamwise locations, closer to the wall the flow fluctuations tend to be more downward (to the wall). However, the fluctuation magnitudes (turbulence intensities,  $u_{rms}$  and  $v_{rms}$ ) at the grid

height level (Points 2 and 4) are higher than that at the mid height level (Points 1 and 3) (Figures 6.3 (c) and (d)). This might be due the reattachment of the flow to the surface, which causes more downward tendency at closer distances to the wall.

The probability distribution function (PDF) curves of  $u$  and  $v$  signals at Points 1 and 3 are portrayed in Figure 6.12 (a). As expected, this figure depicts that the PDF curves for signals  $u_1$  and  $u_3$  with positive skewness factors (Figure 6.11) have longer tails in the positive  $X$  ( $u$  or  $v$ ) direction. This indicates that the signal has extreme fluctuations in the positive direction, while, it spends more time (the area under the PDF curve) in the negative direction [27]. But as can be seen, this trend is reversed for  $v_1$  and  $v_3$  signals which are negatively skewed. To make this discussion clearer, signals  $u_1$  and  $v_1$  are depicted in Figure 6.12 (b) for  $10^5$  data points (samples). As can be seen, signal  $u_1$  has some extreme values in the positive direction, while for  $v_1$  this is reversed.

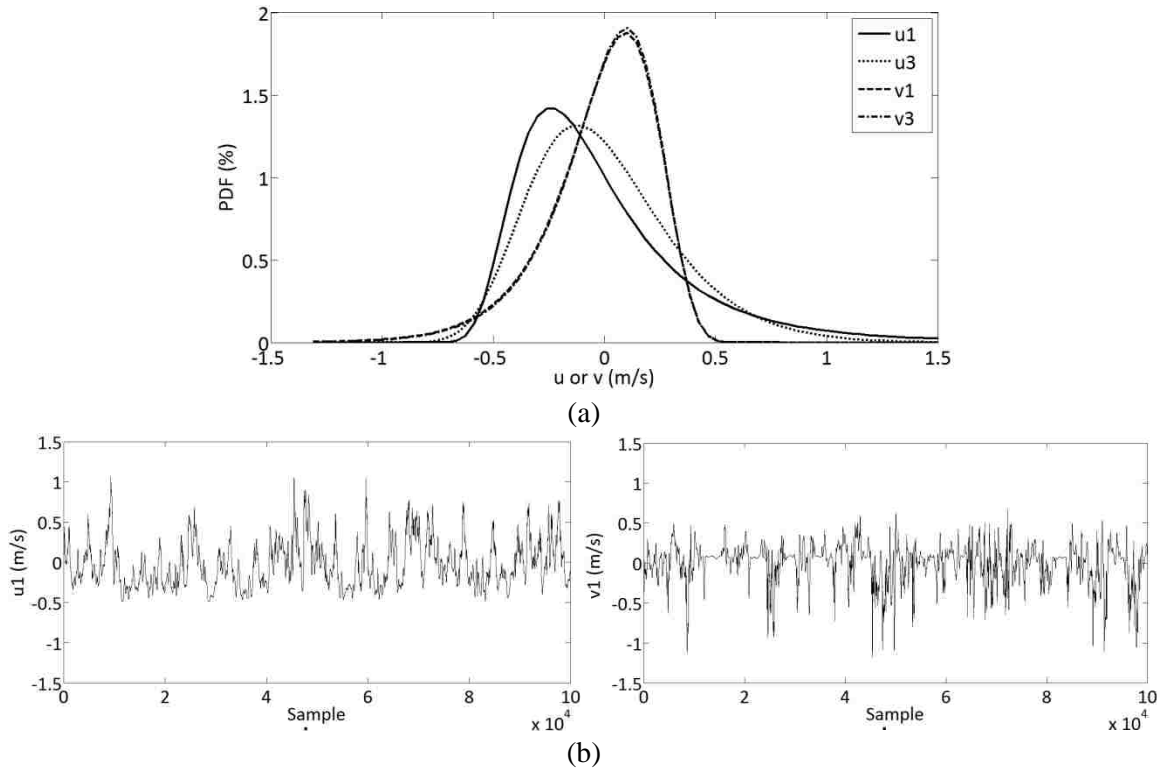


Figure 6.12 (a) PDF curves of  $u$  and  $v$  signals at Points 1 ( $u_1$  and  $v_1$  at  $X/H = 8.75$ ,  $Y/H = 0.55$ ) and 3 ( $u_3$  and  $v_3$  at  $X/H = 17.75$ ,  $Y/H = 0.55$ ) (b) fluctuating velocities at Point 1 ( $u_1$  and  $v_1$ )

The normalized fourth central moment of the signal gives the flatness factor or kurtosis ( $K$ ) [27]:

$$K \equiv (\overline{u^4 \text{ or } v^4}) / (\sigma^4) \quad (6.11)$$

This parameter shows the peakedness or flatness of the probability distribution function (PDF). A flatness factor of 3 means that the distribution is Gaussian. The larger the  $K$ , the flatter and wider



the two tails and narrower the peak in the PDF curve. Narrow and peaked PDF curves (larger  $K$ ) correspond to a higher level of intermittency of that parameter [18,27].

Flatness factors ( $K$ ) of  $u$  and  $v$  signals and their components at Points 1 to 4 are shown in Figure 6.13. All original signals ( $u$  and  $v$ ) have flatness factors around 3. As can be seen in this figure,  $K$  increases with frequency and reaches a peak value at D4 or D5 or increases constantly until D3 for all for measured points. Part of the very large  $K$  values at D5 to D3 are postulated to be artificial and due to previously-mentioned noises at these high frequencies. The large deviation of this parameter from the value of 3 indicates a narrower peak of the PDF curve, which can be seen in Figure 6.14. Different turbulence scales are shown in Figure 6.13. At large scales ( $\Lambda$  and larger)  $K$  is almost equal to the Gaussian value of 3, as the scale decreases below the integral length scale ( $\Lambda$ ),  $K$  starts to increase. This indicates the higher level of intermittency in the signal at higher frequency ranges or smaller scales, which was also observed in other studies [18]. Also, as can be seen at Points 1 and 3, the deviation of  $K$  factor from the value 3 (specifically at larger frequency ranges, not D3) is larger than that of Points 2 and 4. This indicates that at the grid middle height level the velocity fluctuation signal is more intermittent compared to the edge grid level points. As was discussed in skewness section, this might be due to the effect of the flow reattachment to the surface or the presence of a narrow recirculation region which causes higher intermittency in the velocity fluctuation signals at the closer distances to the wall.

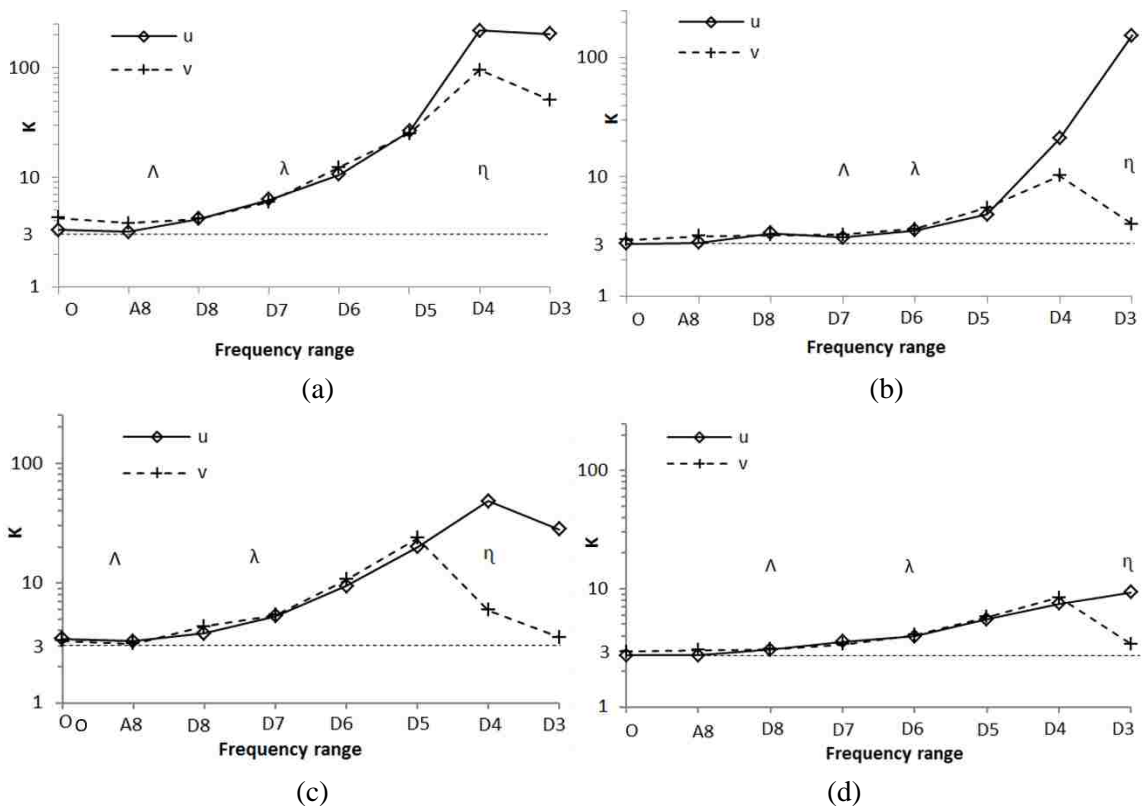


Figure 6.13 Flatness factor at (a) point 1 ( $X/H = 8.75$ ,  $Y/H = 0.55$ ), (b) point 2 ( $X/H = 8.75$ ,  $Y/H = 1.05$ ), (c) point 3 ( $X/H = 17.75$ ,  $Y/H = 0.55$ ) and (d) point 4 ( $X/H = 17.75$ ,  $Y/H = 1.05$ )

Figure 6.14 illustrates PDF curves of  $u$  and  $v$  signals and their decompositions at Point 1 ( $X/H = 8.75$ ,  $Y/H = 0.55$ ) to clarify the relation between the  $K$  value and the PDF curve shape. The original  $u$  signals' PDF curve coincides with that of their largest frequency range components, A8 (0 ~ 78 Hz). For better visibility, only frequency ranges until D5 are shown and Y axis maximum is set at PDF = 30%.

By increasing the frequency range from A8 to D5, the PDF curve becomes 'peakier' (concentrated around zero) and its two tails, diminishing and flatter. Also, as was observed in Figure 6.13, going from A8 to D5, the  $K$  factor deviates progressively more from three. The sign of skewness factors in these graphs (long tail of PDF curves to the right or left) may not be easily recognized here.

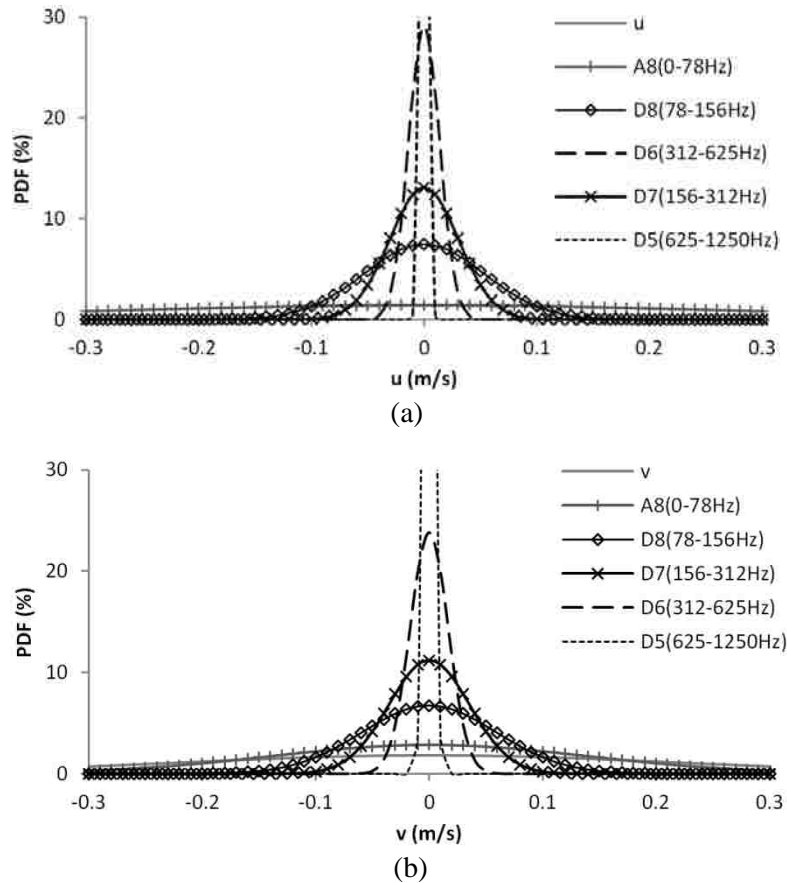


Figure 6.14 PDF curves of (1)  $u$  and (2)  $v$  signals at the point 1 ( $X/H = 8.75$ ,  $Y/H = 0.55$ )

#### 6.4.3.2. Continuous wavelet analysis

The continuous wavelet transform presents a continuous decomposition of the signal in both scale and space. While, in the discrete form some information might be missing due to its dyadic nature [14,15], no information on the turbulence signal analyses is missed in the continuous wavelet analysis.

Continuous wavelet analysis was applied on streamwise and normal velocity fluctuation signals ( $u$  and  $v$ ) utilizing the same wavelet function as the discrete wavelet analysis ('dmey') and the results are presented in Figures 6.15 and 6.16. In these figures, the energy distribution of signals over time and frequency can be seen at Points 1 to 4 in a continuous fashion. X, Y and Z axes in these plots illustrate time, frequency and wavelet coefficient (energy), respectively. In these graphs any slice parallel to the time-energy plane shows the signal's energy fluctuation as a function of the time. While, a slice parallel to the frequency-energy plane illustrates the signal's instantaneous spectral energy distribution [13]. The signal was studied for a 6 s duration but only 2 s is shown here to enhance the visibility. Frequencies were calculated from the corresponding scales based on Equation (6.3). The low scale continuous wavelet coefficients represent the fine-scale features (high frequency components), while the high scale continuous wavelet coefficients depict the coarse-scale features in the input signal (low frequency components).

As can be observed, the continuous wavelet method results in a relatively smooth pattern with energy level increasing with decreasing frequency. The signal's energy belongs mainly to the range of frequencies  $0 \sim 132$  Hz at Points 1 ( $X/H = 8.75$ ,  $Y/H = 0.55$ ) and 3 ( $X/H = 17.75$ ,  $Y/H = 0.55$ ) and  $0 \sim 265$  Hz at Points 2 ( $X/H = 8.75$ ,  $Y/H = 1.05$ ) and 4 ( $X/H = 17.75$ ,  $Y/H = 1.05$ ). A series of high energy events (peaks) in these ranges of frequencies is also observed, which does not seem to have any systematic trend. However, at a specific point they happen at almost the same time and frequency range for both  $u$  and  $v$  signals. For instance, at Point 1 (Figure 6.15 (a) and (b)) at around 0.1, 1 and 1.2 s and frequency range  $0 \sim 132$  Hz, some clear peaks are observed in both the  $u$  and  $v$  graphs. These events may not be visible in the power spectra graphs (Figure 6.5) as they are being averaged out over the entire time series. These observations may be an indication of the presence of coherent vortical structures; this will be discussed further in the intermittency analysis (next section).

In Figure 6.15, the energy level of both  $u$  and  $v$  signals significantly increases from the two points at the middle height of the grid (Points 1 and 3) to the two points around the edge of the grid (Points 2 and 4) in all ranges of frequencies. This confirms that the turbulent energy is mainly created around the edge of the grid. Also, moving downstream from Point 1 to 3 and Point 2 to 4, there is a notable reduction in the turbulent energy at any specific distance from the surface. The same trends were seen in the discrete wavelet analysis results (Figures 6.7 to 6.10) and power spectra (Figure 6.5). This indicates that the turbulence energy generated at the edge of the grid extended a far downstream (up to and beyond  $X/H = 17.75$ ), albeit degradation due to turbulence decay.

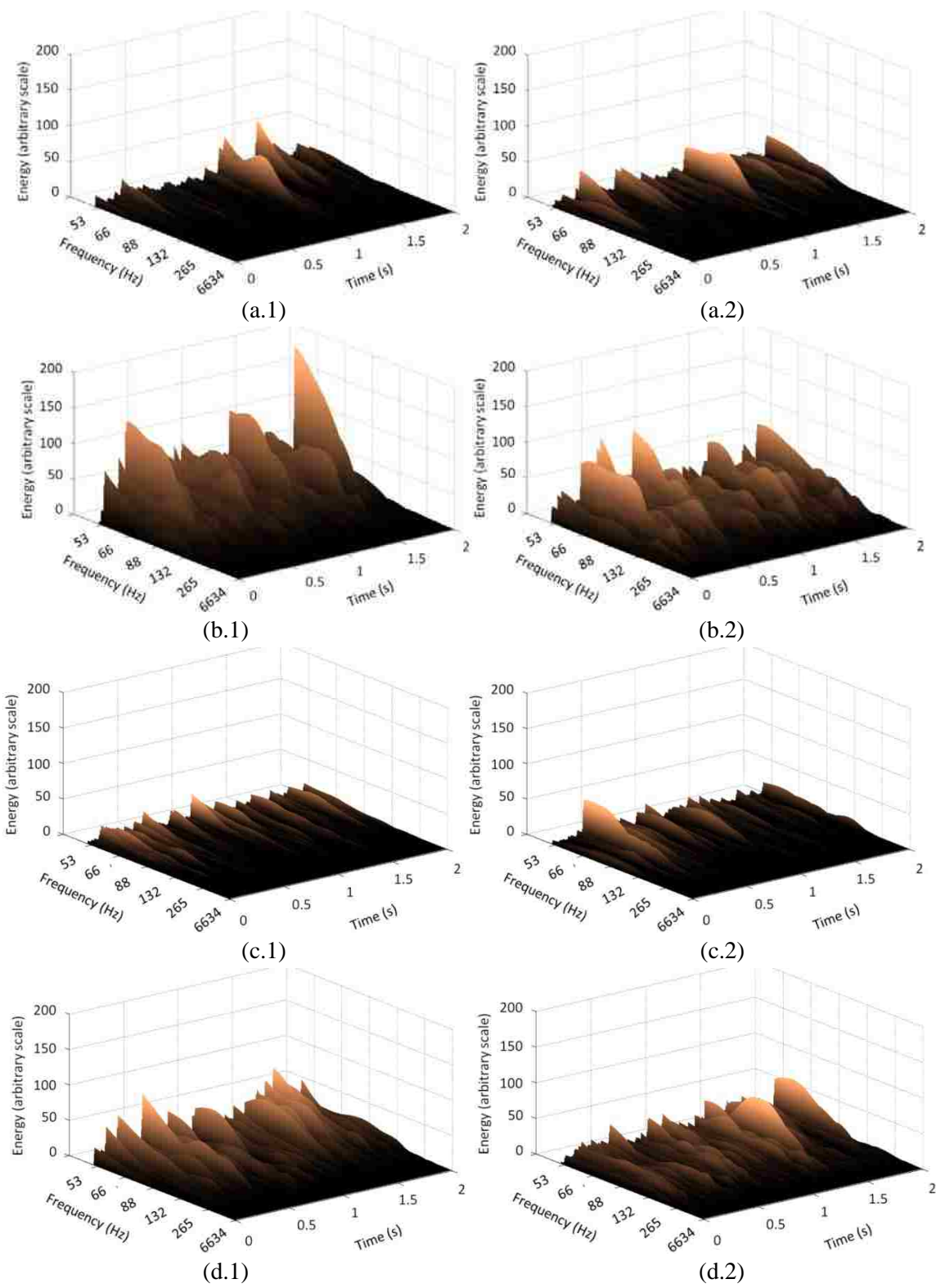


Figure 6.15 Continuous wavelet transform of  $u$  and  $v$  signals at (a.1, a.2) Point 1 ( $X/H = 8.75$ ,  $Y/H = 0.55$ ), (b.1, b.2) Point 2 ( $X/H = 8.75$ ,  $Y/H = 1.05$ ), (c.1, c.2) Point 3 ( $X/H = 17.75$ ,  $Y/H = 0.55$ ) and (d.1, d.2) Point 4 ( $X/H = 17.75$ ,  $Y/H = 1.05$ )

#### 6.4.3.2.1. Intermittency analysis

The local intermittency measures ( $I$ ) based on continuous wavelet analysis results for both  $u$  and  $v$  signals were computed according to Equation (6.6) and presented in Figure 6.16 in a space-scale fashion. Graphs are shown until the intermittency factor equal to 100. This parameter demonstrates the spatial distribution of the local deviation from the time-averaged wavelet energy spectra at a given scale. Deviation of this parameter from unity quantifies the level of the flow intermittency. When  $I \approx 1$  at each frequency (scale), the energy is distributed evenly in the time axis and the flow is non-intermittent [15].

It can be observed that the intermittency is larger at the highest frequency range (6634 Hz) and decreases as it goes to lower frequencies. It is supposed that part of the very high intermittency values at the frequency range of 6634 Hz are due to the presence of some noises in the signals. At some specific times (for instance at  $t \sim 1$  s in Figure 6.17 (a.1) and (a.2)) the intermittency increases again at around 66 Hz. This phenomenon was also seen in the flatness factor graphs where  $K$  increased from large to small turbulence scales, which is associated to a rise in the intermittency level.

As was mentioned, in the frequency range of  $0 \sim 132$  Hz some peaks are observed in these graphs. Taking a look back to Figure 6.15, it can be seen that these peaks coincide with peaks in the signals' energy in continuous wavelet transforms. For example, in Figures 6.17 (a.1) and (a.2) for both  $u$  and  $v$  signals at  $t \sim 1$  s and around 66 Hz ( $0 \sim 132$  Hz), a peak in the intermittency factor can be seen, this was also observed in Figure 6.15 (a.1) at the same time and frequency. This indicates that in regions where the turbulence energy is higher, the intermittency is moderately high. These observations seem to suggest some coherent structures or regular vortices, particularly at Point 1. The corresponding Strouhal number based on the partial grid height (0.02 m) and the free stream velocity ( $U_\infty$ ) is 0.33. This is close to the typical Strouhal number associated with the vortex shedding in the flow after obstacles reported in the literature ( $0.03 \sim 0.19$ ) [24,28]. It worth noting that, different obstacles utilized in the mentioned literature (square rib with slit in Ref. [24] and square rib in Ref. [28]) from that of the current study (partial grid) could be responsible for the moderate variation in the value of the Strouhal number.

Moreover, at both downstream distances, the level of the intermittency shows a reduction specifically at smaller scales (higher frequencies) from points at the mid height (Points 1 and 3) to points at the edge of the grid (Points 2 and 4). This was also observed in Figure 6.13, where  $K$  factors showed higher values at Points 1 and 3. As was discussed, this phenomenon is plausibly due to the reattachment of the flow over the surface or the very thin wake (recirculation) vortex over the surface, causing high flow intermittency in this region.

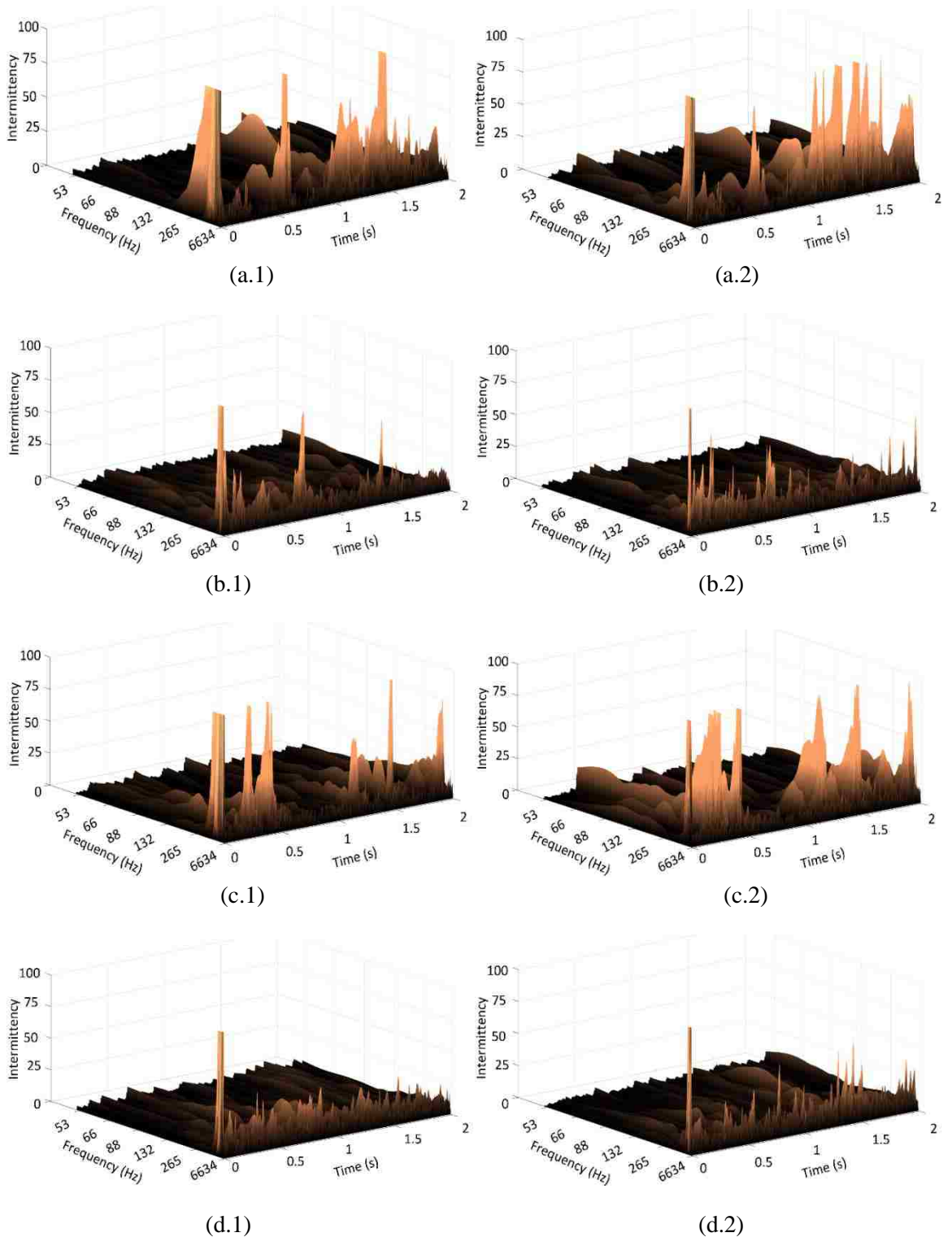


Figure 6.16 Local intermittency factor of (a.1) u (a.2) v signals at Point 1 ( $X/H = 8.75$ ,  $Y/H = 0.55$ ), (b.1) u and (b.2) v signals at Point 2 ( $X/H = 8.75$ ,  $Y/H = 1.05$ ), (c.1) u and (c.2) v signals at Point 3 ( $X/H = 17.75$ ,  $Y/H = 0.55$ ) and (d.1) u and (d.2) v signals at Point 4 ( $X/H = 17.75$ ,  $Y/H = 1.05$ )

## **6.5. Conclusion**

Flow and turbulence structures over a flat plate downstream of a finite height grid were investigated. Four specific points after the grid were selected to be analyzed by the wavelet analysis in order to elucidate the detailed turbulence structures after the partial grid; two points at each of two downstream distances ( $X/H = 8.75$  and  $17.75$ ) corresponding to the middle height and the height of the edge of the grid ( $Y/H = 0.55$  and  $1.05$ ). Velocity fluctuation signals ( $u$  and  $v$ ) at these four points were analyzed by discrete and continuous wavelet analyses.

In the turbulence energy cascade from large to small scales, besides the continuous reduction in the energy level which was observed in the power spectra and in both discrete and continuous wavelets, some spikes were also captured in the continuous transforms. These peaks which occurred at the lower frequency range ( $0 \sim 132$  Hz) at some specific times (especially at  $X/H = 8.75$  and  $Y/H = 0.55$ ) were probably traces of coherent vortical structures created by the partial grid. Also, analyzing the higher moments (skewness and flatness factors) of velocity fluctuation signals and their components and the continuous intermittency factor revealed that, in general, the intermittency and symmetry in the signals increased from large to small turbulence scales.

Going from points at the mid height of the grid to the edge, turbulence energy was enhanced over the entire range of scales. Also, mid-height points were seen to have more intermittent and asymmetrical turbulence velocity signals than edge points. This is apparently due to the reattachment of the flow to the surface or the near boundary recirculation region which causes the velocity fluctuation signals at closer points to the surface more intermittent and asymmetrical.

## **Acknowledgements**

This work was made possible by the Ontario Trillium Foundation and the Natural Sciences and Engineering Research Council of Canada.

## **References**

- [1] Taylor, G.I., 1935, "Statistical theory of turbulence," Proc R Soc London Series A Math and Phys Sci., 151, pp.421–478.
- [2] Batchelor, G.K., 1948, "Energy decay and self-preserving correlation functions in isotropic turbulence," Quart. Appl. Math, 6, pp. 97-116.
- [3] Batchelor, G.K, and Townsend, A.A., 1948, "Decay of isotropic turbulence in the initial period," Proc. R. Soc. London A., 193, pp. 539-558.
- [4] Grant, H.L, and Nisbet, I.C.T., 1957, "The inhomogeneity of grid turbulence," J. Fluid Mech., 2(3), pp. 263-272.
- [5] Murzyn, F., and Be'lorgey, M., 2005, "Experimental investigation of the grid-generated turbulence features in a free surface flow," Exper. Thermal Fluid Sci., 29(8), pp. 925–935.
- [6] Liu, R, Ting, D.S.-K, and Checkel, M.D., 2007, "Constant Reynolds number turbulence downstream of an orificed perforated plate," Exper. Thermal Fluid Sci., 31(8), pp. 897–908.

- [7] Yao, H.D., and He, G.W., 2009, “A kinematic subgrid scale model for large-eddy simulation of turbulence-generated sound,” *J. Turbul.*, 10(19), pp. 1–14.
- [8] Goodfrienda, L., Chowa, F.K., Vanellab, M., and Balaras, E., 2013, “Large-eddy simulation of decaying isotropic turbulence across a grid refinement interface using explicit filtering and reconstruction,” *J. Turbul.*, 14(12), pp. 58–76.
- [9] Hearst, R.J., and Lavoie, P., 2014, “Scale-by-scale energy budget in fractal element grid-generated turbulence,” *J. Turbul.*, 15(8), pp. 540–554.
- [10] Thormann, A., and Meneveau, C., 2015, “Decaying turbulence in the presence of a shearless uniform kinetic energy gradient,” *J. Turbul.*, 16(5), pp. 442-459.
- [11] Judd, M., Raupach, J.M.R., and Finnigan, J.J., 1996, “A wind tunnel study of turbulent flow around single and multiple windbreaks, Part I: Velocity Fields,” *Bound-Layer Meteor.*, 80, pp. 127-165.
- [12] Fouladi, F., Henshaw, P., and Ting, D.S.-K., 2015 “Turbulent flow over a flat plate downstream of a finite height perforated plate,” *J. Fluids Eng-T. ASME.*, 137(2), pp. 021203-1-12.
- [13] Indrusiak, M.L.S., and Möller, S.V., 2004, “Wavelet analysis of experimental turbulence time series,” *IV Escola de Primavera de Transicao e Turbulencia*, PortoAlerge, Bresilera.
- [14] Farge, M., 1992, “Wavelet transforms and their applications to turbulence,” *Annu. Rev. Fluid Mech.*, 24, pp. 395–457.
- [15] Ruppert-Felsot, J., Farge, M., and Petitjeans, P., 2009, “Wavelet tools to study intermittency: application to vortex bursting,” *J. Fluids Mech.*, 636, pp. 427-453.
- [16] Farge, M., Guezennec, Y., Ho CM, and Meneveau, C., 1990, “Continuous wavelet analysis of coherent structures,” *Proceedings of the 1990 Summer Program*, In Stanford University, Studying Turbulence Using Numerical Simulation Databases, 3, pp. 331–348.
- [17] Meneveau, C., 1991, “Analysis of turbulence in the orthonormal wavelet representation,” *J. Fluid Mech.*, 232, pp. 469-520.
- [18] Mouri, H., Kubotani, H., Fujitani, T., Nino, H., and Takaoka, M., 1999, “Wavelet analyses of velocities in laboratory isotropic turbulence,” *J. Fluid Mech.*, 389, pp. 229-254.
- [19] Xu, C.X., Li, L., Cui, G.-X., and Zhang, Z.-S., 2006, “Multi-scale analysis of near-wall turbulence intermittency,” *J. Turbul.*, 7(25), pp. 1–15.
- [20] Kadoch, B., Iyer K, Donzis D, Schneider, K., Farge, M., and Yeung, P.K., 2011, “On the role of vortical structures for turbulent mixing using direct numerical simulation and wavelet-based coherent vorticity extraction,” *J. Turbul.*, 12(9), pp. 1–17.
- [21] Kellnerova, R., Kukacka, L., Jurcakova K, Uruba, V., and Janour, Z., 2011, “Comparison of wavelet analysis with velocity derivatives for detection of shear layer and vortices inside a turbulent boundary layer,” *J. Phys: Conference series*, 318(6), 1-10.



- [22] Indrusiak, M.L.S., and Möller, S.V., 2011, "Wavelet analysis of unsteady flows: Application on the determination of the Strouhal number of the transient wake behind a single cylinder," *Exp. Therm. Fluid Sci.*, 35, pp. 319–327.
- [23] Luo, G.Y., Osypiw, D., and Irle, M., 2003, "On-Line Vibration Analysis with Fast Continuous Wavelet Algorithm for Condition Monitoring of Bearing," *J. Vib. Control*, 9(8), pp.931-947.
- [24] Tariq, A., Panigrahi, P.K., and Muralidhar, K., 2004, "Flow and heat transfer in the wake of a surface-mounted rib with a slit," *Exp. Fluids.*, 37(5), pp. 701–719.
- [25] Fouladi, F., Henshaw, P., and Ting, D.S.-K, 2017, "Flat plate convection heat transfer enhancement via a square rib," *Int. J. Heat Mass Tran.*, 104, pp. 1202-1216.
- [26] Hinze, J.O., 1975, *Turbulence*. 2nd ed., McGraw-Hill, New York, USA.
- [27] Ting, D.S.-K., 2016, "Basics of engineering turbulence," 1st ed., Elsevier, Academic Press, New York, USA.
- [28] Liu, Y.Z., Ke, F., and Sung, H.J., 2008, "Unsteady separated and reattaching turbulent flow over a two-dimensional square rib," *J. Fluid Struct.*, 24 (3), pp. 366-381.
- [29] Jørgensen, F.E., 2002, "How to measure turbulence with hot-Wire anemometers - a practical guide", Dantec Dynamics, Skovlunde, Denmark.

## CHAPTER 7

### FLAT PLATE HEAT CONVECTION ENHANCEMENT BY A DISCRETE TRANSVERSE RIB

#### ***7.1. Introduction***

Utilizing wall-bounded roughness elements such as ribs is a common method for enhancing the surface heat transfer rate in different industries [1-4]. Flow separation and reattachment over the surface after a transverse rib promotes turbulence over the downstream surface [5]. This separation and reattachment mechanism, along with some vortices originated from the rib, were found to augment the flow mixing and convection heat transfer rate from the downstream surface [5-7]. However, it should be kept in mind that ribs also cause a pressure drop in the flow which would increase pump energy in forced flows [8].

Creating gaps inside the rib generates jet flows which can break the secondary flow (wake vortex) into smaller pieces and thus, generating a higher level of turbulence downstream. This allows the secondary flow to mix with the main flow through the gap and accelerates and energizes the retarded boundary layer flow along the surface, increasing the heat transfer rate [9]. Some studies on discrete ribs' thermo-hydraulic performance are discussed below.

The flow characteristics and heat transfer of a multiple discrete V-ribbed wall were studied by Kumar et al. [9]. It was realized that due to the interaction of the secondary stream flowing through the discrete ribs and the main stream, these ribs showed a higher level of heat transfer enhancement compared to continuous ones. However, the friction factor was also higher for the wall with discrete ribs.

Han and Zhang [10] studied the influence of different discrete rib orientations on the heat transfer and pressure drop in a square duct. The 60-degree V-shape broken rib led to the highest heat transfer enhancement, while the transverse broken rib presented the largest pressure drop.

Liou et al. [11] performed a comparison on detached and attached ribs in a duct. The detached rib was seen to have a higher heat transfer rate as it had the advantage of eliminating the hot spot behind the rib.

Tariq et al. [12] investigated the flow and heat transfer in the wake of a surface-mounted square rib with and without a horizontal slit with different open area ratios from 10% to 50%. Different flow parameters and their correlation with heat transfer enhancement were studied. It was seen that the flow through the slit altered the flow structure inside the reattaching shear layer after the rib. A slit in the rib with an open area less than 30% had a positive impact on both the surface heat transfer enhancement and pressure penalty compared to the solid rib case. It was also seen that the secondary flow through the slit affected the unsteadiness of the recirculation bubble, which influenced the heat transfer in the pre-reattachment region. The heat transfer enhancement correlated with the normal velocity and its temporal fluctuation.

Liou et al. [5] performed detailed investigations on the heat transfer and fluid flow in a square duct with 12 different shaped vortex generators. The local Nusselt number was measured by utilizing liquid crystal thermography. Flow patterns were measured by a Laser-Doppler Velocimeter. The 45-degree V-shape pointing upstream and the delta winglet pointing upstream vortex generators provided the highest Nusselt number augmentation. The direction and strength of the secondary flows were found to be the most effective parameters for heat transfer enhancement. It was seen that the downwash region of the secondary flow (the normal velocity into the surface) was associated with the highest enhancement of the Nusselt number; this was followed by the convective mean velocity (the mean velocity across the surface) and turbulence kinetic energy.

Singh et al. [13] experimentally studied the heat and fluid flow characteristics in a rectangular duct which was roughened with multiple discrete V-shaped ribs. Different ranges of relative gap width and relative gap position of ribs at various Reynolds numbers were investigated. For the investigated range of parameters, the maximum Nusselt number and friction factor enhancement for the roughened duct were found to be 3.04 and 3.11 times that for the smooth duct, respectively. Nusselt number and friction factor correlations in terms of Re and rib parameters were developed.

Karwa [14] experimentally investigated the heat transfer and friction in a rectangular duct which had a roughened wall with multiple rows of transverse, inclined, V-continuous and V-discrete patterns of ribs. The V-pattern was examined at two configurations: pointing upstream (V-up) and pointing downstream (V-down). It was seen that the V-down discrete arrangement had the highest heat transfer among all patterns.

Gill et al. [15] presented an experimental study on the heat transfer and friction factor of a rectangular duct which was roughened by broken arc-shaped ribs combined with staggered rib pieces which were positioned behind the main rib. The effect of different opening (gap) sizes of the rib on Nusselt number and friction factor were studied. Also, results were compared to a smooth wall and continuous roughened wall. The highest Nusselt number enhancement compared to that of the smooth duct occurred when the relative gap width was equal to the rib height.

Normally, multiple rows of ribs are applied on a surface as most of the ribbed wall applications are limited to ducts or heat exchangers, where inside walls can be continuously roughened without any major interference with the device performance. The present study, on the other hand, aims at enhancing heat convection from a photovoltaic (PV) panel. It is impractical to have multiple rows of ribs as they can interfere with the solar radiation absorption. Thus, the effect of a single row of discrete rectangular ribs at the leading edge of a plate was investigated. Also, the effect of the gap in the rib on the flow and turbulence structures was studied.

### ***Nomenclature***

abs ( $V/U_\infty$ )	absolute value of the normalized local velocity in the Y direction	uw	turbulence shear stress in XZ plane ( $m^2/s^2$ )
h	convective heat transfer coefficient ( $W/m^2.K$ )	U	local time averaged streamwise velocity (m/s)
H	rib height over the surface (cm)	$U/U_\infty$	normalized streamwise velocity
k	thermal conductivity of the air ( $W/m.K$ )	$U_\infty$	free stream velocity (m/s)

L	plate length (cm)	$V_{rms}$	root-mean-square of the normal velocity fluctuations (m/s)
L1	rib tooth width (cm)	$\tau_{vw}$	turbulence shear stress in YZ plane ( $m^2/s^2$ )
L2	rib gap width (cm)	V	local time averaged normal velocity (m/s)
Nu	Nusselt number of the ribbed plate ( $h.X/k$ )	$W_{rms}$	root-mean-square of the cross stream velocity fluctuations (m/s)
$Nu_0$	Nusselt number of the smooth plate (no rib)	W	local time averaged cross stream velocity (m/s)
$Nu/Nu_0$	heat transfer enhancement of the ribbed plate with respect to the smooth plate	$W/U_\infty$	normalized cross stream velocity
$R^2$	coefficient of determination	X	streamwise distance from the rib (cm)
Rib 1-1	discrete rib with 1 cm tooth and 1 cm gap width	$X/H$	normalized distance from the rib based on the rib height
Rib 1-0.5	discrete rib with 1 cm tooth and 0.5 cm gap width	$X/L$	normalized distance from the rib based on the plate length
Rib 0.5-0.5	discrete rib with 0.5 cm tooth and 0.5 cm gap width	Y	normal distance from the plate (cm)
Rib 0.5-1	discrete rib with 0.5 cm tooth and 1 cm gap width	$Y/H$	normalized distance from the plate based on the rib height
Rib F-0	full rib (no gap)	Z	distance along the width of the plate from the plate centerline (cm)
$u_{rms}$	root-mean-square of the streamwise velocity fluctuations (m/s)	$\Delta T$	temperature difference ( $^{\circ}C$ )
$\tau_{uv}$	turbulence shear stress in XY plane ( $m^2/s^2$ )		

## 7.2. Experimentation

All experimental data for the present investigation were obtained in a wind tunnel with a 180 cm long, 76 cm high and 77 cm wide test section. The maximum free stream velocity in this wind tunnel is around 30 m/s and the background turbulence intensity is less than 0.4% when the test section is empty.

Detailed schematics of the experimental set-up used in this study are shown in Figures 7.1 and 7.2. The total plate dimensions were 30.5 cm wide, 65 cm long and 1 cm thick. The set-up consists of an electrical heater with an insulator layer underneath and an aluminum foil on the top to distribute the heat evenly. A plastic sheet with pairs of thermocouples above and below it is located on the top of the Al foil, acting as an internal heat flux sensor. Thus there was no disturbance to the airflow over the plate as would be caused by externally attached heat flux sensors. The gap which is created because of the presence of thermocouples and wires was filled with heat conductive epoxy glue. The top surface of the set-up was covered by an aluminum plate. A close-up view of the different layers of the set-up is inserted in Figure 7.1. A more detailed version of the set-up description can be found in Ref. [16].

The thermocouple-PTFE-thermocouple sandwich measures the conduction heat transfer through the plastic sheet. It is assumed that whatever heat flux passes through the plastic layer passes through the top aluminum plate into the convective air over the plate.

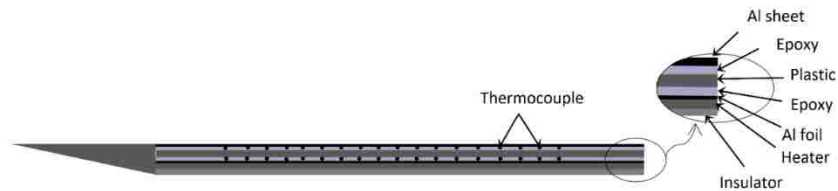


Figure 7.1 Set-up layers' close view

X, Y and Z were the streamwise, normal to the plate and widthwise directions, respectively, with the origin located at the middle of the rib. As can be seen in Figures 7.1 and 7.2, a  $10^\circ$  angle wedge was cut from wood and attached to the set-up leading edge in order to reduce the effect of the blunt edge. Ribs were placed at the leading edge of the set-up ( $X = 0$ ).

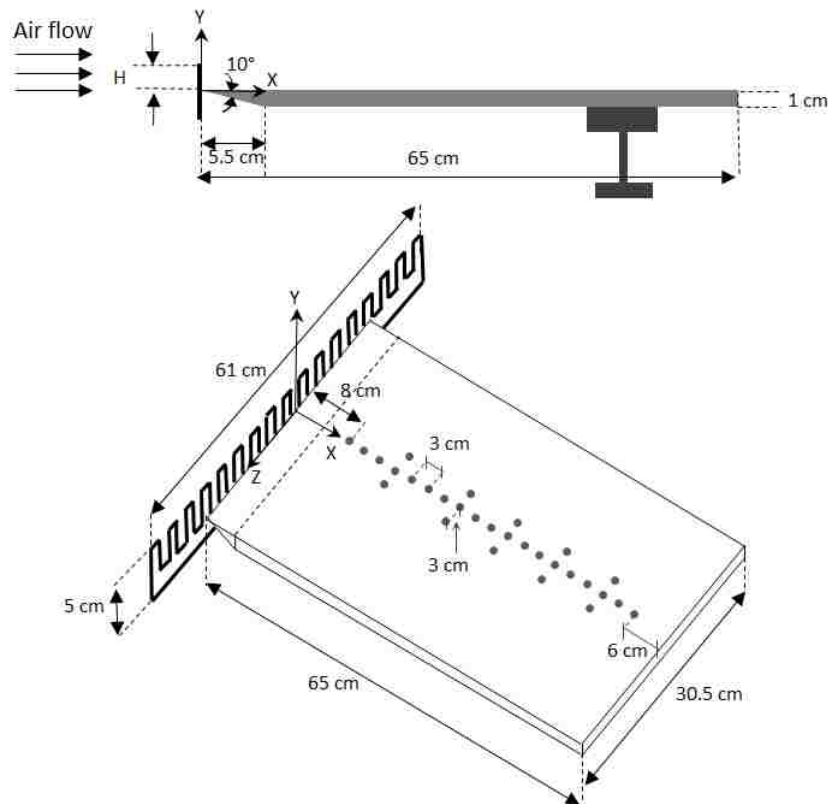


Figure 7.2 Set-up schematic

Four different broken ribs and one full rib were designed for these experiments (Figure 7.3). Ribs were cut from an aluminum plate with 3 mm thickness by a computer numerical controlled machine. As can be seen, the rib design is identifiable by two numbers; the first is the tooth width (L1), and the second is the gap width (L2). “Rib F-0” represents the full rib. In later graphs one more number is added to each rib’s identification number, which signifies the value of H above the plate surface. All ribs had an outside dimension of 5 cm by 61 cm.

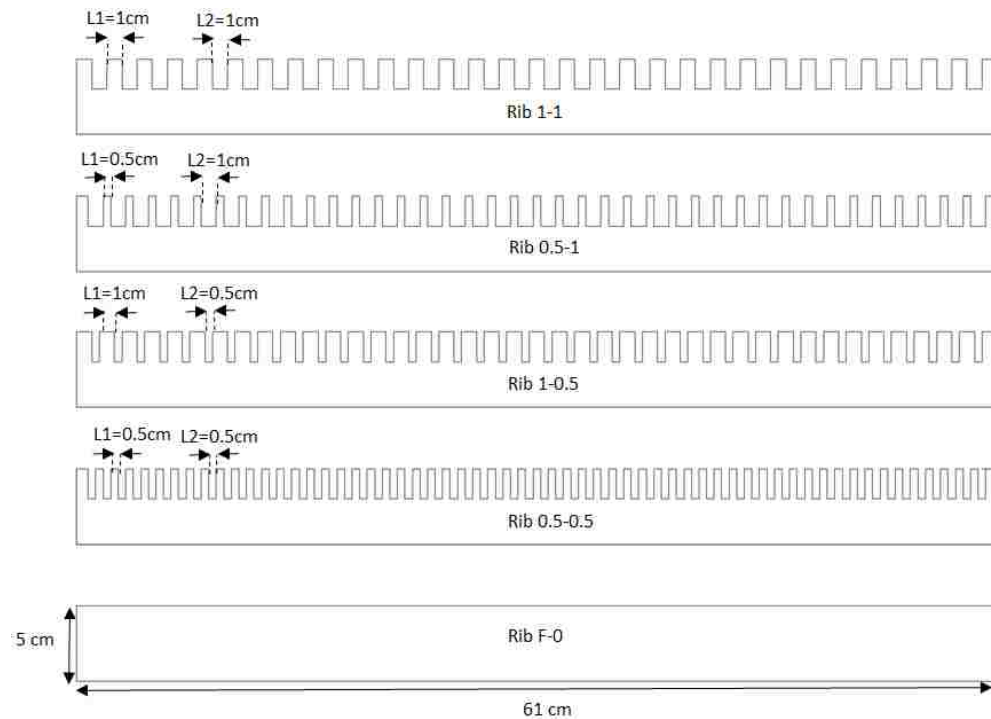


Figure 7.3 The five different tested ribs, Rib L1-L2, L1 signifies the tooth width and L2 the gap width, Rib F-0 signifies the full rib

The set-up was placed at mid-height of the test section with the plate and support system creating a blockage of around 2% of the tunnel cross section. Two different free stream velocities ( $U_\infty = 4$  and 10 m/s) and three different rib heights ( $H = 0.5, 1$  and 2 cm) were tested. The heat transfer test procedure and convection heat transfer coefficient calculating method were previously explained in detail [16].

Streamwise, normal and cross stream (X, Y and Z) velocities at different points downstream of the rib were measured by a gold-plated tri-axial probe (type 55P95) with a Dantec streamline 91C10 constant-temperature anemometer (CTA). Gold-plated probes have 5  $\mu\text{m}$  diameter and 3 mm long platinum-plated tungsten wire sensors. The wire ends are copper- and gold-plated to a thickness of 15 to 20  $\mu\text{m}$ , leaving an active sensor, 1.25 mm, in the middle of the wire. Signals were low-passed at 30 kHz and then sampled at 80 kHz over a period of around 12.5 s, resulting in  $10^6$  data points per measurement. A 12-bit PCI-6071E National Instrument data acquisition card was used to

convert the analog signal into a digital one. A computer-controlled 2-D traverse system was used to position the probe at each specified location. The traverse system was able to move through the cross stream direction of the test section ( $Z$ ) and the direction normal to the plate ( $Y$ ).

One free stream velocity ( $U_\infty = 4$  m/s) and rib's height ( $H = 1$  cm) were chosen for the velocity measurements. Measurements were conducted at five different streamwise locations downstream of the rib;  $X/L = 0.15, 0.3, 0.45, 0.6, 0.75$  and at  $Z = 0$  (Figure 7.1), where  $L$  is the set-up length (65 cm). Measurements at the first streamwise location were made from  $Y/H = 0.5$  to 10 and at other ones from  $Y/H = 0.5$  to 2.4 (particular emphasis was on the near-plate region), every 0.2 cm, where  $H = 1$  cm. Local velocities ( $U, V$  and  $W$ ) and turbulence intensities ( $u_{rms}, v_{rms}$  and  $w_{rms}$ ) were deduced in  $X, Y$  and  $Z$  directions and the calculation procedures can be found in Ref. [16].

### **7.3. Results and Discussion**

Heat transfer and flow measurements results are analyzed in this section. Heat transfer along the set-up's center line after five different ribs (Figure 7.3) are presented in the first part. Two different free stream velocities and three different rib's heights were studied in this part. In the second part, three ribs which showed the best or worst thermal performances in the first part are selected for the flow analysis. Flow and turbulence measurements are performed at  $U_\infty = 4$  m/s,  $H = 1$  cm and five different downstream distances.

#### **7.3.1. Heat transfer results**

Heat transfer augmentation at different streamwise locations ( $X/L = 0.12$  to 0.82) was quantified by normalizing the Nusselt number ( $Nu$ ) based on the smooth surface Nusselt number ( $Nu_0$ ). Results are presented at two different velocities ( $U_\infty = 4$  and 10 m/s) and three rib heights ( $H = 0.5, 1$  and 2 cm) in Figures 4 to 6. Each rib with its specific height ( $H$ ) is identified by a symbol (Rib #-#) in these graphs, where the third number identifies the rib height over the plate surface. The first and second numbers in these symbols demonstrate the tooth and the gap widths of the rib, respectively. For example, Rib 1-0.5-1 corresponds to the rib with a 1 cm tooth, 0.5 cm gap and 1 cm height.

Heat transfer parameter uncertainties are estimated from the temperature difference and thermocouple location uncertainties. Thermocouples are calibrated at three different environmental temperatures and the total uncertainty in temperature difference ( $\Delta T$ ) measurements is estimated to be around  $\pm 0.2^\circ\text{C}$ . The uncertainty in positioning the thermocouples is approximately  $\pm 1.2$  mm, consisting of the ruler and human errors. The total uncertainty in the Nusselt number enhancement ( $Nu/Nu_0$ ) is about 0.1 which is shown by an error bar in this graph.

Figures 7.4 (a) and (b) compare the heat transfer enhancement after the five different ribs at 4 m/s and 10 m/s free stream velocities, respectively. Graphs (a.1 or b.1), (a.2 or b.2) and (a.3 or b.3) in these figures correspond to rib heights ( $H$ ) of 0.5, 1 and 2 cm, respectively. An interesting observation in all of these graphs is that the  $Nu/Nu_0$  is higher than 1 at nearly all points, which indicates the effectiveness of ribs (either full or discrete) at all studied heights and velocities. The few exceptions are associated with higher  $H$  and at locations shortly behind the rib, where non-negligible local velocity retardation occurs, and near the end of the flat plate, presumably under the influence of a wake effect.

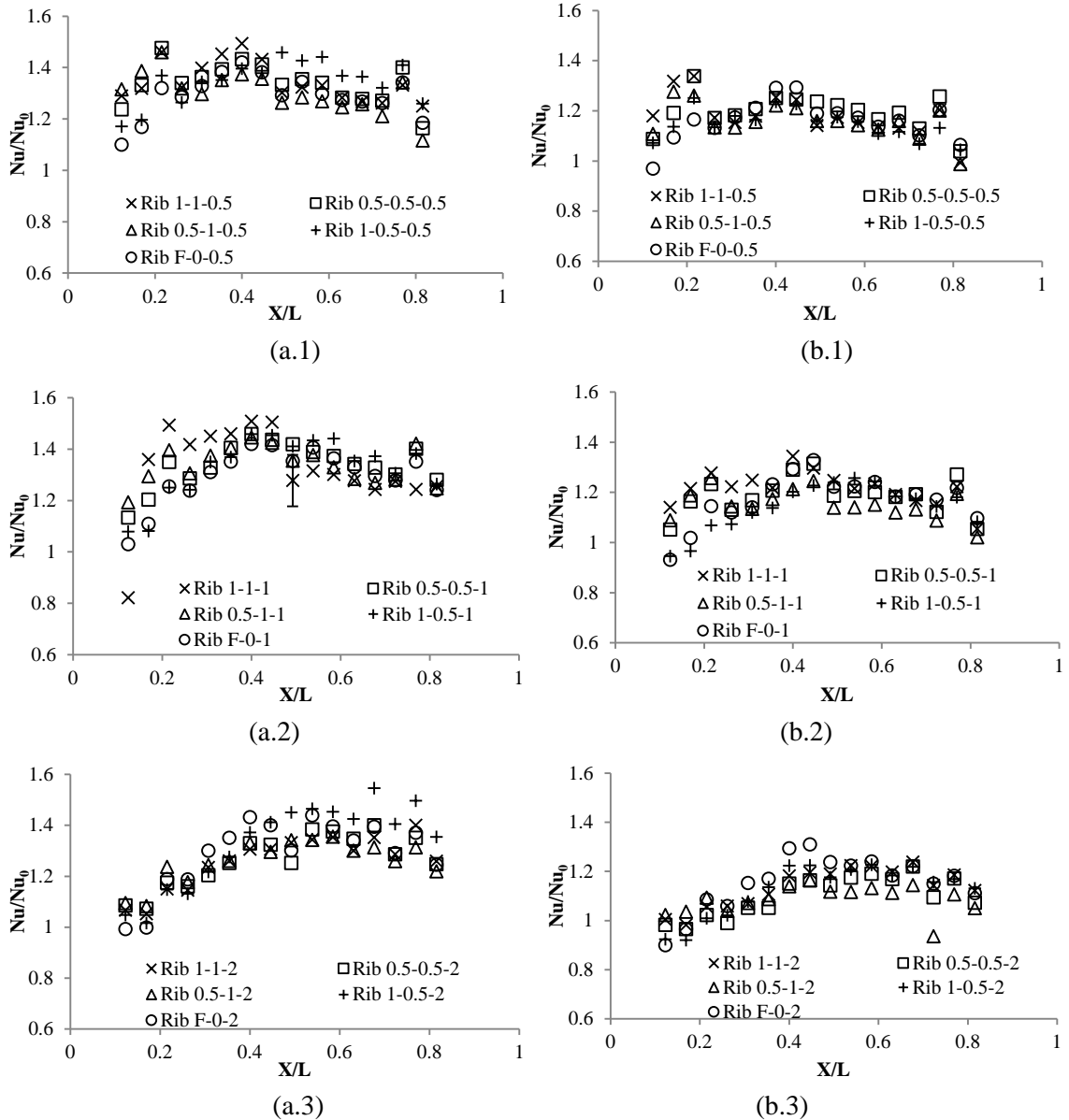


Figure 7.4 Heat transfer enhancement at (a)  $U_\infty = 4$  m/s and: (a.1)  $H = 0.5$  cm, (a.2)  $H = 1$  cm and (a.3)  $H = 2$  cm and (b)  $U_\infty = 10$  m/s and: (b.1)  $H = 0.5$  cm, (b.2)  $H = 1$  cm, (b.3)  $H = 2$  cm

As can be seen in Figure 7.4,  $Nu/Nu_0$  had an increasing-decreasing trend in almost all cases, except for Figure 7.4 (a.3) where the reducing trend is not seen clearly after the plate midpoint. This increasing-decreasing trend can be explained as follows; the lower  $Nu/Nu_0$  immediately downstream of the rib was due to the wake region which prevented effective flow mixing. Farther downstream, the secondary flow brought the cooler free stream flow in contact with the downstream surface and enhanced the heat transfer rate. The heat transfer rate reached a maximum at a point around the flow reattachment to the wall surface and after that, the boundary layer reinitiated. However, the graphs do not peak at the same point, which indicates that the reattachment



of the flow to the surface occurred at different downstream distances. After reattachment, the development of the boundary layer lead to a gradually increasing reduction in the surface heat transfer rate [12,16].

It is difficult to compare different ribs' thermal performances and make a general conclusion as the rank of  $Nu/Nu_0$  is not constant. As can be seen, sequences generally switch at around the middle of the plate ( $X/L = 0.5$ ). For instance, the rib which showed the highest Nusselt number enhancement in the first half, had the lowest one at larger downstream distances. Thus, for clarity, the first and second halves of the set-up or graphs ( $0 \leq X/L \leq 0.5$  and  $0.5 \leq X/L \leq 1$ ) are discussed separately.

In the first half of the set-up, at both free stream velocities (Figure 7.4 (a) and (b)) and all rib heights, Rib 1-1 often showed the highest heat transfer enhancement. While, the full rib and sometimes Rib 1-0.5 showed the lowest Nusselt number enhancement. However, this generalization does not include all downstream locations in the first half of the set-up, especially for  $H = 2$  cm (Figures 7.4 (a.3) and (b.3)). In the second half of the plate, Rib 1-0.5 and sometimes the full rib and Rib 0.5-0.5 had the best, and Rib 1-1 and Rib 0.5-1 had the worst thermal performances. Thus, it can be seen that from the first to the second half of the set-up the sequence of the rib thermal performances was almost reversed. But, it should be mentioned that, most of the time, differences between ribs' performances are lower than the estimated uncertainty in  $Nu/Nu_0$ , which makes it difficult to arrive at a solid conclusion.

Comparing the full rib with discrete ones shows that creating gaps along the rib, was effective regarding the heat transfer enhancement at closer downstream distances to the rib. While at larger distances, as can be seen in Figure 7.4, discrete ribs did not always have higher Nusselt number augmentations compared to the full rib.

Figure 7.5 (a) and (b) compares the Nusselt number enhancement of ribs with the same tooth width and different gap sizes at  $U_\infty = 4$  m/s and  $H = 1$  cm; with Rib 1-1-1 and Rib 1-0.5-1 in Figure 7.5 (a) and Rib 0.5-0.5-1 and Rib 0.5-1-1 in Figure 7.5 (b). To smooth the data, window averaging was done on every two adjacent points. Thus, the  $Nu/Nu_0$  and also  $X/L$  values of every two adjacent data points were averaged and results are plotted in this figure. It can be seen in Figure 7.5 (a) that Rib 1-1-1 with the larger gap had a higher Nusselt number enhancement in the first half of the plate, while Rib 1-0.5-1 showed better performance in the latter half. The same conclusion is valid, though less obvious, for ribs with narrower teeth (Rib 0.5-0.5-1 and Rib 0.5-1-1). Thus, it can be concluded that closer to the rib, the larger opening ratio seems to act better, while at larger downstream distances, the smaller one is more effective regarding the heat transfer enhancement from the surface.

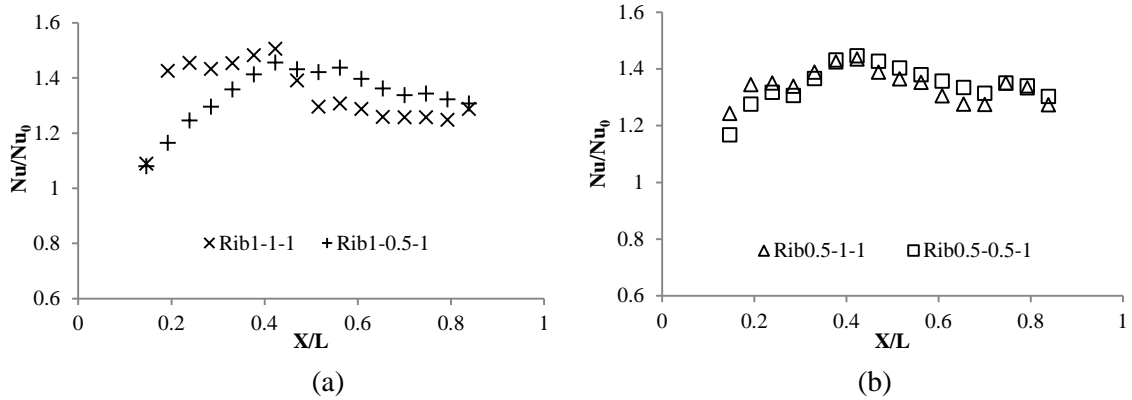


Figure 7.5 Heat transfer enhancement at  $U_\infty = 4$  m/s and  $H = 1$  cm (a) ribs 1-1-1 and 1-0.5-1 (b) ribs 0.5-0.5-1 and 0.5-1-1

Figure 7.6 (a) to (d) compares the Nusselt number enhancement at different rib heights and free stream velocities for each rib separately. A clear trend which is seen in all of these graphs is a reduction in  $Nu/Nu_0$  with increasing free stream velocity from 4 to 10 m/s at each rib's height. This originates from the fact that at the lower free stream velocity, the flow regime changed from laminar in the base case (smooth wall) to turbulent for the ribbed wall. While, at the higher air velocity (10 m/s), the boundary layer regime is turbulent for both cases (smooth and ribbed case) at almost all downstream locations, so the relative Nusselt number enhancement was less. In other words, the base  $Nu_0$  values at the higher free stream velocity were larger, masking the corresponding  $Nu$  numbers when the heat transfer enhancement is expressed in  $Nu/Nu_0$ .

Furthermore, comparing the Nusselt number enhancement at different heights shows that the smaller rib height (0.5 cm) had higher Nusselt number augmentations at smaller downstream distances, while moving to larger downstream distances, the larger rib heights (2 cm) were more effective. This indicates that the effect of a smaller rib decreased and almost faded away after a certain downstream distance. Conversely, a rib at a larger height caused a higher flow blockage immediately downstream of the rib, but its effect on the flow (including flow disturbances) lasted for a longer downstream distance.

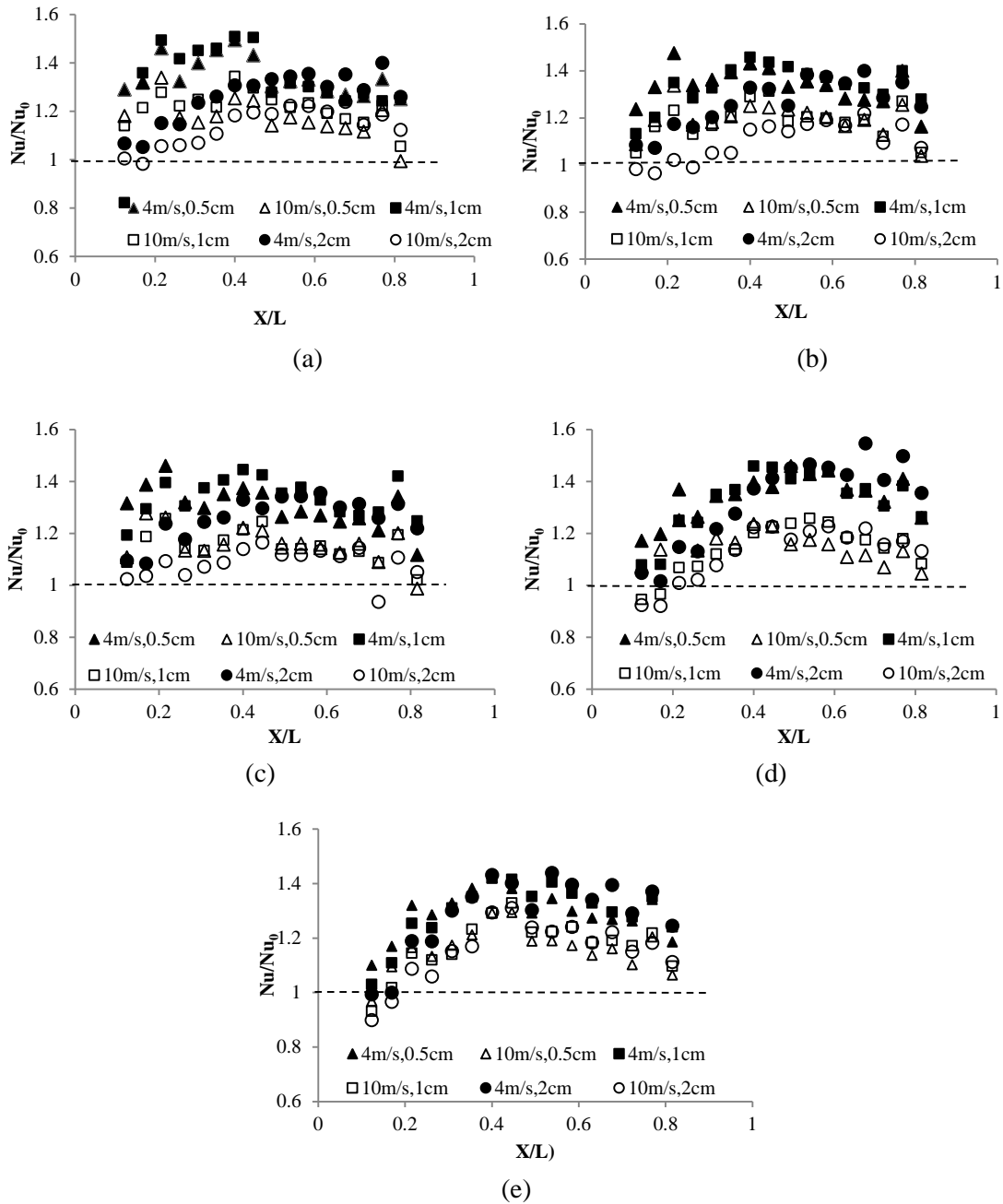


Figure 7.6 Heat transfer enhancement comparison for different grids at two different rib's heights and free stream velocities (a) Rib 1-1 (b) Rib 0.5-0.5 (c) Rib 0.5-1 (d) Rib 1-0.5 and (e) Rib F-0

### 7.3.2. Time-averaged flow field results

#### 7.3.2.1. Velocity

Flow characteristics over the surface dictate the heat transfer mechanism. In this section, the flow and turbulence features and their probable effects on the surface heat transfer enhancement are discussed. Rib 1-1-1, Rib 1-0.5-1 and Rib F-0-1 were selected to be investigated as they usually

had the highest or lowest relative heat transfer enhancement in the first or second half of the plate. Also, the effect of gaps in the rib on the flow mechanism was analyzed by comparing the full rib flow parameters to that of discrete ribs. One free stream velocity and one rib's height ( $U_\infty = 4 \text{ m/s}$ ,  $H = 1 \text{ cm}$ ) were selected for the fluid mechanics experiments and analysis. The instantaneous velocity was measured in all three (X, Y and Z) directions (Figure 7.3) at five streamwise locations downstream of the rib ( $X/L = 0.15$  to  $0.75$ ). U, V and W notations in these graphs correspond to the mean velocity in X, Y and Z directions (Figure 7.2), respectively. All velocities and turbulence parameters were non-dimensionalized by the free seam velocity ( $U_\infty$ ). Normalized velocity, turbulence intensity and shear stress profiles for Rib F-0-1, Rib 1-1-1 and Rib 1-0.5-1 are presented in Figures 7.7 to 7.17. At the first downstream distance ( $X/L = 0.15$ ), measurements were performed until a large normal distance to the plate ( $Y/H = 10$ ) to form a full profile of different parameters. At other downstream distances, measurements were performed until  $Y/H = 4.5$ , to focus on the phenomena closer to the flat plate.

Total uncertainty in measured velocities consists of bias and precision but is mostly due to the precision uncertainty [16]. The estimated uncertainty in normalized streamwise ( $U/U_\infty$ ), normal ( $V/U_\infty$ ) and cross stream velocities ( $W/U_\infty$ ) at point  $X/L = 0.75$  and  $Y/H = 0.9$  are around  $\pm 0.05$ ,  $\pm 0.03$ ,  $\pm 0.01$ , respectively. The uncertainty in turbulence intensities,  $u_{\text{rms}}/U_\infty$ ,  $v_{\text{rms}}/U_\infty$  and  $w_{\text{rms}}/U_\infty$  are estimated to be  $\pm 0.01$ . The uncertainty in shear stresses,  $uv/U_\infty$ ,  $vw/U_\infty$  and  $uw/U_\infty$ , are around  $\pm 0.0012$ ,  $\pm 0.002$  and  $\pm 0.0005$ , respectively. These uncertainties are shown by error bars in the last of each set of graphs, but their values are small and may not be visible.

Figure 7.7 illustrates streamwise velocity ( $U/U_\infty$ ) profiles after Rib F-0-1, Rib 1-1-1 and Rib 1-0.5-1. The full profile of the streamwise velocity after these ribs is observed at  $X/L = 0.15$ . As can be observed after all of these ribs,  $U/U_\infty$  illustrates almost the same trend; from  $Y/H = 0.5$  to  $2$ , it had small values, while at around  $Y/H = 2$ , it started to increase and the rib's edge shear layer appeared, and at  $Y/H \cong 4.5$  it reached the free stream value ( $U/U_\infty \cong 1$ ). It is worth noting that the free shear layer was a little bit higher than the rib's edge level upstream.

As it was mentioned before, the flow over the rib is characterized by the separation and reattachment to the downstream surface. The reattachment point, as identified in the literature, is the location corresponding to the zero streamwise velocity at the measurement location closest to the surface [17,18]. The region between the rib and the reattachment point is the recirculation or wake region, where the streamwise velocities are likely to be negative [19-21]. However for all of these ribs at  $X/L = 0.15$ , U had small positive values over the surface until  $Y/H \cong 2.5$ . It is presumed that part of this positive U may come from the hot-wire's weakness in detecting negative streamwise velocities, as discussed in Ref. [16]. Nevertheless, the profile shape at this downstream distance is very similar to the streamwise velocity profile shape in the recirculation area [16-18].

At downstream distances,  $X/L$ , from  $0.3$  to  $0.75$  ( $X/H = 9.75$  to  $48.75$ ), velocity profiles are shown until  $Y/H = 4.5$ . These profiles are different from that at  $X/L = 0.15$  as the shear layer was thicker and had merged with the emerging surface boundary layer. But, for Rib F-0-1 and Rib 1-0.5-1 at  $X/L = 0.3$ , the profile shapes still show significant flow blockage, while that of Rib 1-1-1 more or less has no inflection point. This indicates that the separated flow reached the surface and the boundary layer was trying to reinitiate from the surface. In all of these graphs, Rib 1-1-1 had the

highest streamwise velocity, which indicates the lower flow blockage effect of this rib, except for  $X/L = 0.75$ , where all ribs had almost the same velocity values. At  $X/L = 0.75$  ( $X/H = 48.75$ ), for all three ribs the flow was fully reattached to the surface and the turbulent flow boundary layer had developed.

The streamwise velocity for Rib 1-1-1 at  $X/L = 0.3$  to  $0.6$  had larger values compared to the other two ribs. While at  $X/L = 0.15$  ( $X/H = 9.75$ ), where apparently all three ribs were still in the recirculation area, and at  $X/L = 0.75$  ( $X/H = 48.75$ ), where separated flows completely reattached to the surface, all three ribs show almost the same values.

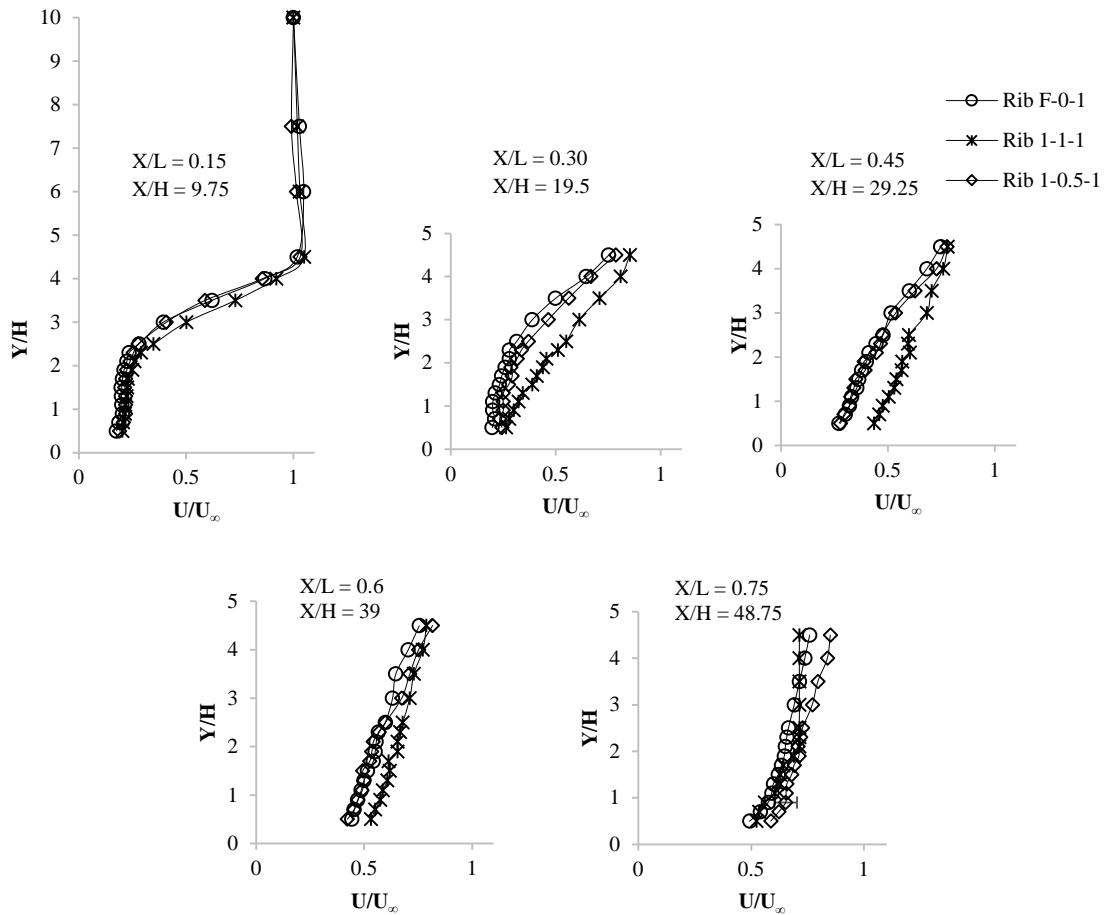


Figure 7.7 Rib F-0-1, Rib 1-1-1 and Rib 1-0.5-1 streamwise velocity profiles ( $U/U_\infty$ ) at different downstream distances

Figure 7.8 illustrates the normalized normal velocities ( $V/U_\infty$ ) after Rib F-0-1 and Rib 1-1-1 and Rib 1-0.5-1 at 5 different downstream distances. The overall trend of the normal velocity can be observed at  $X/L = 0.15$ . Velocities started from very small values close to the surface, which were mostly negative, and reached a negative and then a positive peak point at around  $Y/H = 3$  and  $4.5$ ,

respectively. At  $Y/H$  more than 4.5, it almost decreased to the free stream value. However, at other downstream distances, this trend is not clear, as profiles are presented until  $Y/H = 4.5$ . At  $X/L = 0.75$  ( $X/H = 48.75$ ), normal velocities after all of these three ribs had a very small positive values all over the surface until  $Y/H = 4.5$ . This shows that the boundary layer had redeveloped over the surface with a slightly outward flow direction.

Very small  $V$  values near the surface at  $X/L = 0.15$  ( $X/H = 9.75$ ) for these ribs, along with the streamwise velocity profile shapes (Figure 7), reveal that at this location the flow was still in the wake region. This continued until  $X/L = 0.3$  and  $0.45$  for Rib 1-0.5-1 and Rib F-0-1.

For Rib F-0-1 until  $Y/H \sim 4.5$ , the  $V$  velocity was very small, which is yet another indication of the stronger flow blockage compared to the discrete ribs. Thus, it can be seen that gaps in the rib created some normal velocity (specifically in Rib 1-1-1 with its larger gap ratio). Negative velocity means that the flow stream was toward the surface, while positive shows that the flow was moving outward (upward). This negative normal velocity was also reported in the literature in the flow behind a rib [16,20]. Small positive  $V$  values after Rib 1-0.5-1 at larger normal distances ( $2.5 < Y/H$ ) from the surface may have been due to the smaller gap width, which created a stronger jet flow through gaps and caused the flow to move in an upward direction from the surface.

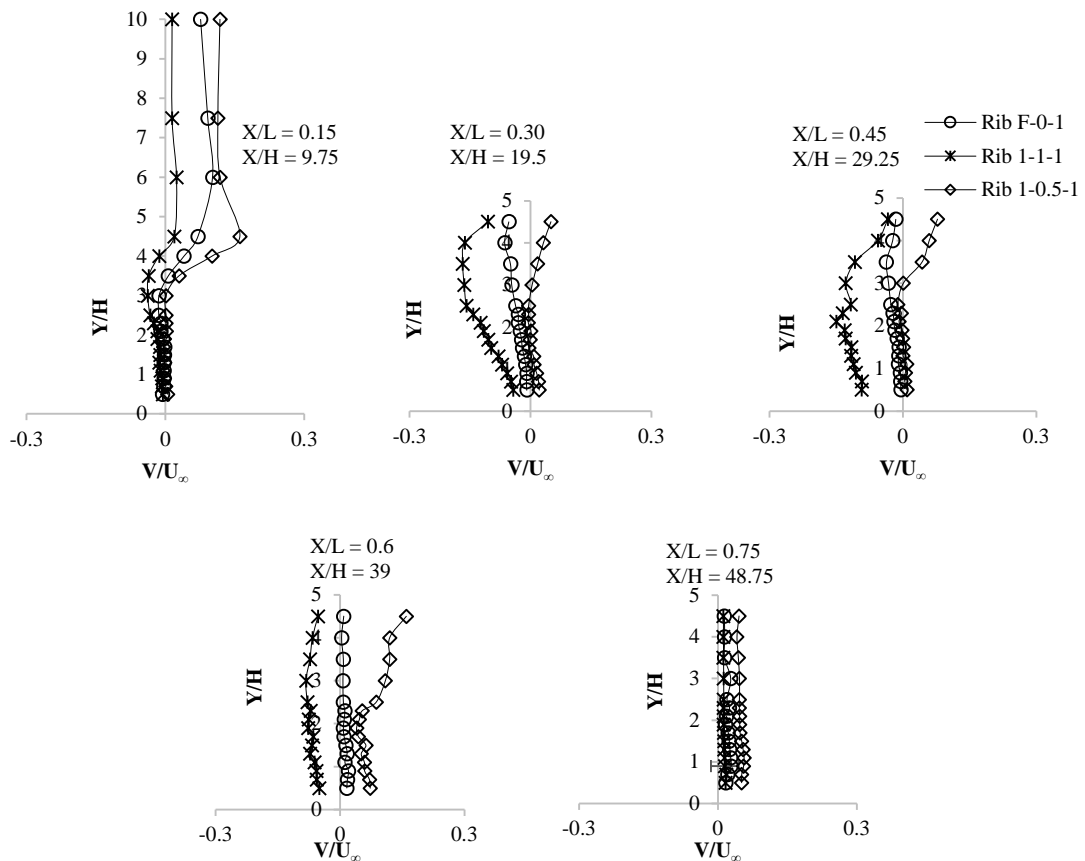


Figure 7.8 Rib F-0-1, Rib 1-1-1 and Rib 1-0.5-1 normal velocity profiles ( $V/U_\infty$ ) at different downstream distances

Cross stream velocities after the ribs are presented in Figure 7.9. As portrayed in this figure at  $X/L = 0.15$  ( $X/H = 9.75$ ), cross stream velocities started from small values near the surface (almost negative), reached a negative peak point at around  $Y/H = 3.5$ , then decreased to the free stream velocity. After Rib F-0, the cross stream velocity was very small over the entire plate, while for discrete ribs it had larger magnitudes, though fluctuated from positive to negative at different downstream distances. This is expected as the gaps in the rib converted some streamwise flow energy into cross stream flow. The negative or positive sign of the cross stream velocity at each point indicates whether the flow was to the right or left side of the plate.

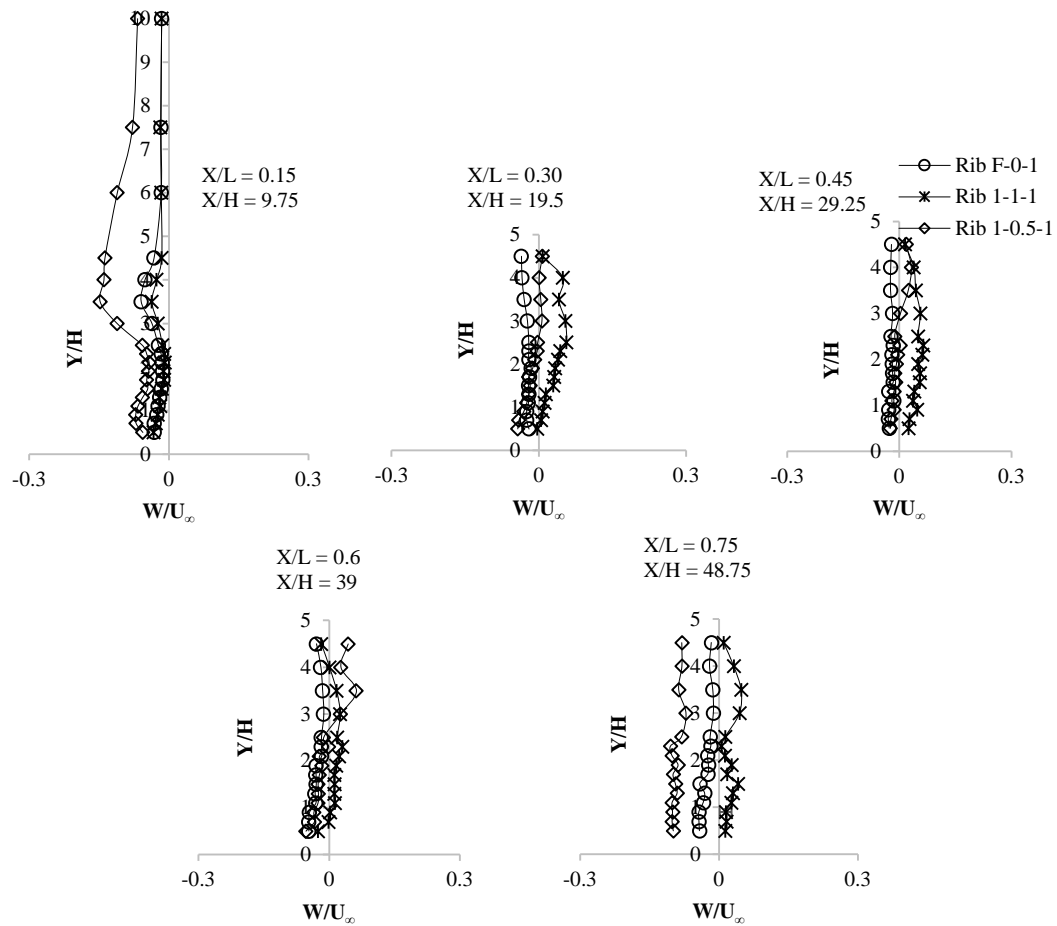


Figure 7.9 Rib F-0-1, Rib 1-1-1 and Rib 1-0.5-1 cross stream velocity profiles ( $W/U_\infty$ ) at different downstream distances

The flow structure is detectable from the velocity ( $U$ ,  $V$  and  $W$ ) profile shapes and values, especially  $U$ . Higher velocity values for Rib 1-1-1 at  $X/L = 0.3$  and  $0.45$  ( $X/H = 19.5$  and  $29.25$ ), reveals that the flow blockage after this rib was less than the others and the flow was probably reattached to the surface within this span of the plate. Also, flow profiles after Rib F-0-1 and Rib 1-0.5-1 until  $X/L = 0.45$  ( $X/H = 29.25$ ) show that the flow still was not fully reattached to the

surface. The higher heat transfer rate enhancement of Rib 1-1-1 until  $X/L = 0.45$  ( $X/H = 29.25$ ) might be due to the shorter reattachment length and higher velocity values compared to the other ribs. On the other hand, for Rib F-0-1 and Rib 1-0.5-1, the flow reattachment occurred after this downstream distance which caused a rise in the surface heat transfer enhancement.

To have a clearer view of the flow pattern over the surface, estimates of the velocity vectors and schematics of the flow direction in the XY plane after different ribs are presented in Figure 7.10. The approximate reattachment region is illustrated by thick arrows in this figure. The downward-upward motion of the flow seen after these ribs (more clearly after Rib 1-1-1), illustrates the reattachment and then reflection of the flow over the surface. As depicted, the reattachment point after Rib 1-1-1 happened at a smaller downstream distance compared to Rib 1-0.5-1 and Rib F-0-1. This shows that the larger gap size (gap ratio of 1) reduced the flow reattachment length, or weakened the organized flow structure. This could be an effective way to enhance the heat transfer rate of a surface and will be discussed further.

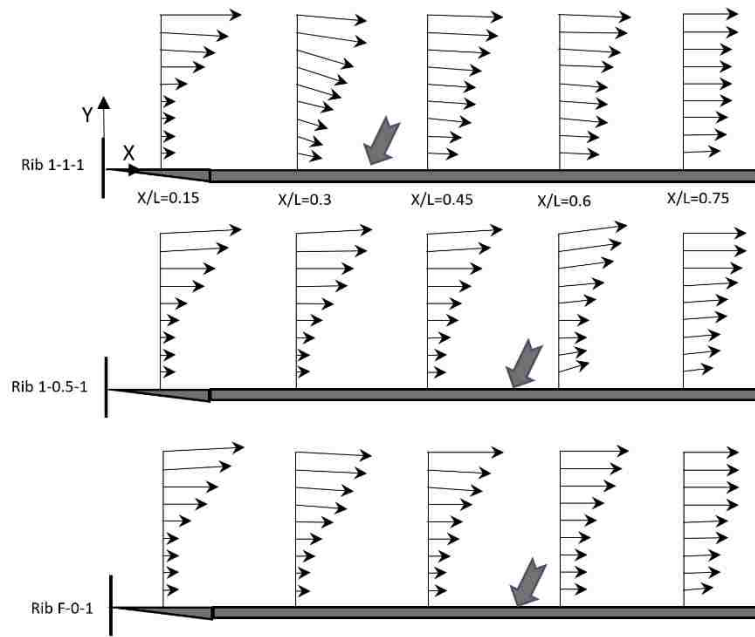


Figure 7.10 Time-averaged overall flow profile in the XY plane after the rib

### 7.3.2.2. Turbulence Intensity and Shear Stress

Turbulence fluctuations ( $u_{rms}$ ,  $v_{rms}$  and  $w_{rms}$ ) and shear stresses ( $uv$ ,  $vw$  and  $uw$ ) are responsible for exchanging momentum between the turbulence and the mean flow. Thus, they correspond to flow mixing and high heat transfer rates [8,22]. These turbulence fluctuating stresses, in their normalized form, are discussed in this section.

The profile of normalized fluctuating normal stresses ( $u_{rms}/U_\infty$ ,  $v_{rms}/U_\infty$  and  $w_{rms}/U_\infty$ ), which are called turbulence intensity, in streamwise, normal and cross stream directions are depicted in



Figures 7.11, 7.12 and 7.13, respectively. The overall trend of turbulence intensities in different directions is the same; it increased in the normal direction from the surface to reach a peak at around  $Y/H = 3 \sim 3.5$  and then decreased to the free stream turbulence intensity (less than 0.04). Comparing Figure 7.11 with Figures 7.12 and 7.13 reveals that, the turbulence intensity in the prevailing flow direction ( $u_{rms}/U_\infty$ ) was higher than those in the two other directions.

Comparing full and discrete ribs in Figure 7.12 indicates that discrete ribs created more turbulence in the streamwise direction at all downstream locations. However, Rib 1-1-1 until  $X/L = 0.45$  ( $X/H = 29.25$ ) had the highest turbulence intensity, while after that Rib 1-0.5-1 had the highest (at  $X/L = 0.6$ , Rib 1-0.5-1 had a slightly larger value compared to the other ribs). Thus, it is observed that the larger gap width was more effective in generating turbulence intensities at closer downstream distances to the rib, while the rib with the smaller gap width acted better at longer downstream distances. This presumably was due to the flow reattachment after Rib 1-1-1 which happened at  $X/L < 0.6$ , while for Rib 1-0.5-1, it occurred at a larger downstream distance. The flow blockage effect can also be observed in the turbulence intensity profile at  $X/L = 0.15$  ( $X/H = 9.75$ ), which was very small from  $Y/H = 0.5$  to around 2. While at  $X/L = 0.3$  ( $X/H = 19.5$ ), the turbulence intensity was, on average, higher, starting from closer to the surface ( $Y/H = 0.5$ ).

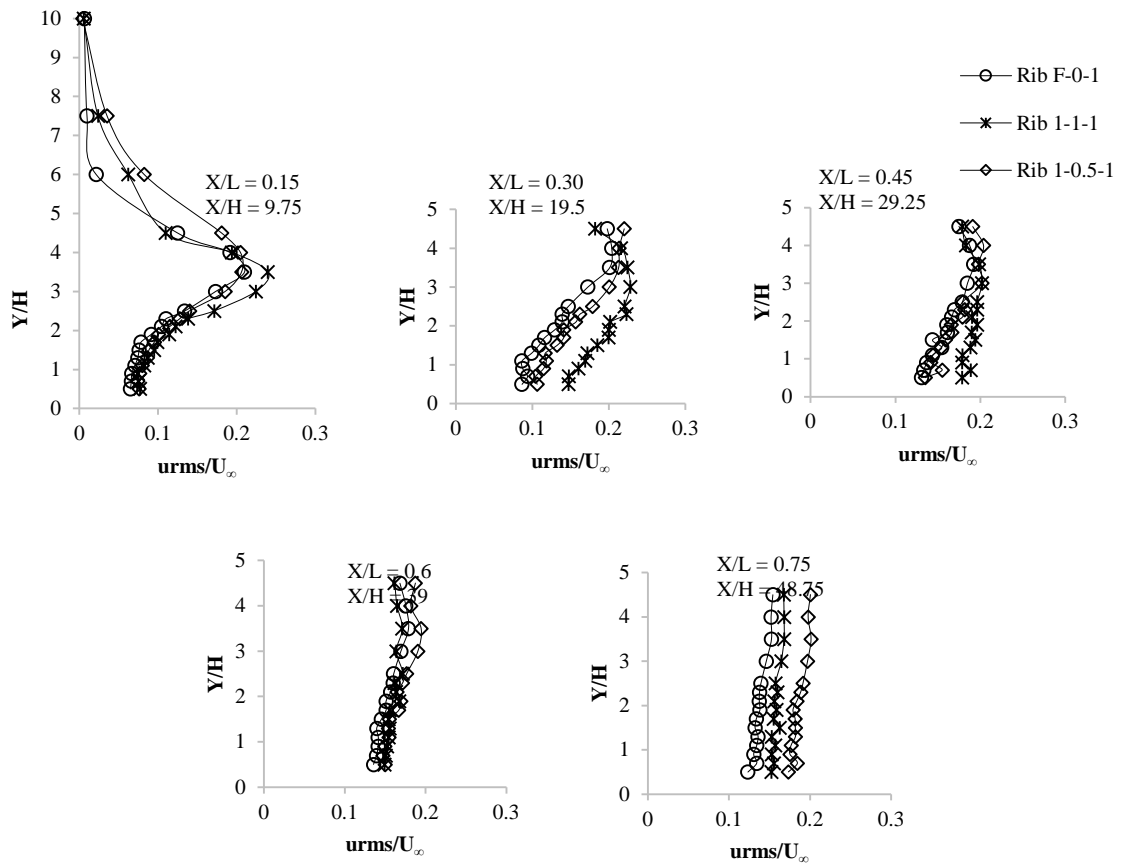


Figure 7.11 Streamwise turbulence intensity profiles ( $u_{rms}/U_\infty$ ) of Rib F-0-1, Rib 1-1-1 and Rib 1-0.5-1 at different downstream distances

Turbulence intensity profiles in the normal direction ( $v_{rms}/U_\infty$ ) are illustrated in Figure 7.12. The full profile shape at  $X/L = 0.15$  is very similar to the  $u_{rms}/U_\infty$  in Figure 7.11. At larger downstream distances ( $X/L > 0.15$ ), the increasing trend started from the closest points to the surface in the normal direction. However, a couple of first points for Rib F-0-1 and Rib 1-0.5-1 at  $X/L = 0.3$  do not fit into this pattern, which may show that the flow after these ribs at this location was still in the wake region. Taking a look back at  $u_{rms}$  profiles, it is clear that a higher level of turbulence was generated by discrete ribs compared to the full rib (Rib F-0-1). Also, until  $X/L = 0.6$  ( $X/H = 39$ ), Rib 1-1-1 had the largest values, while after that, Rib 1-0.5-1 had the largest value (at  $X/L = 0.6$ , slightly larger than that of the other two ribs).

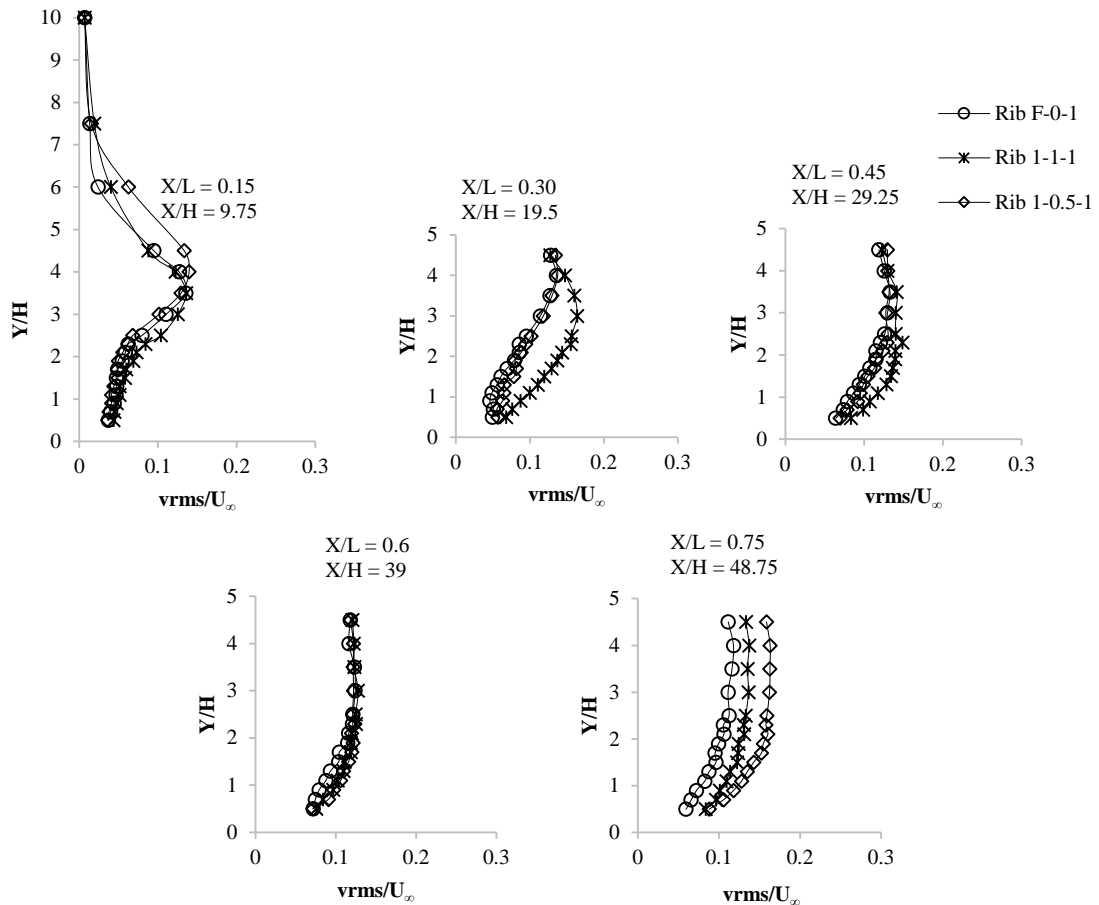


Figure 7.12 Normal turbulence intensity profiles ( $v_{rms}/U_\infty$ ) of Rib F-0-1, Rib 1-1-1 and Rib 1-0.5-1 at different downstream distances

Cross stream turbulence intensities at different downstream distances can be seen in Figure 7.13. Trends are largely the same as  $u_{rms}$  and  $v_{rms}$ . At almost all downstream distances Rib 1-1-1 had the largest value.

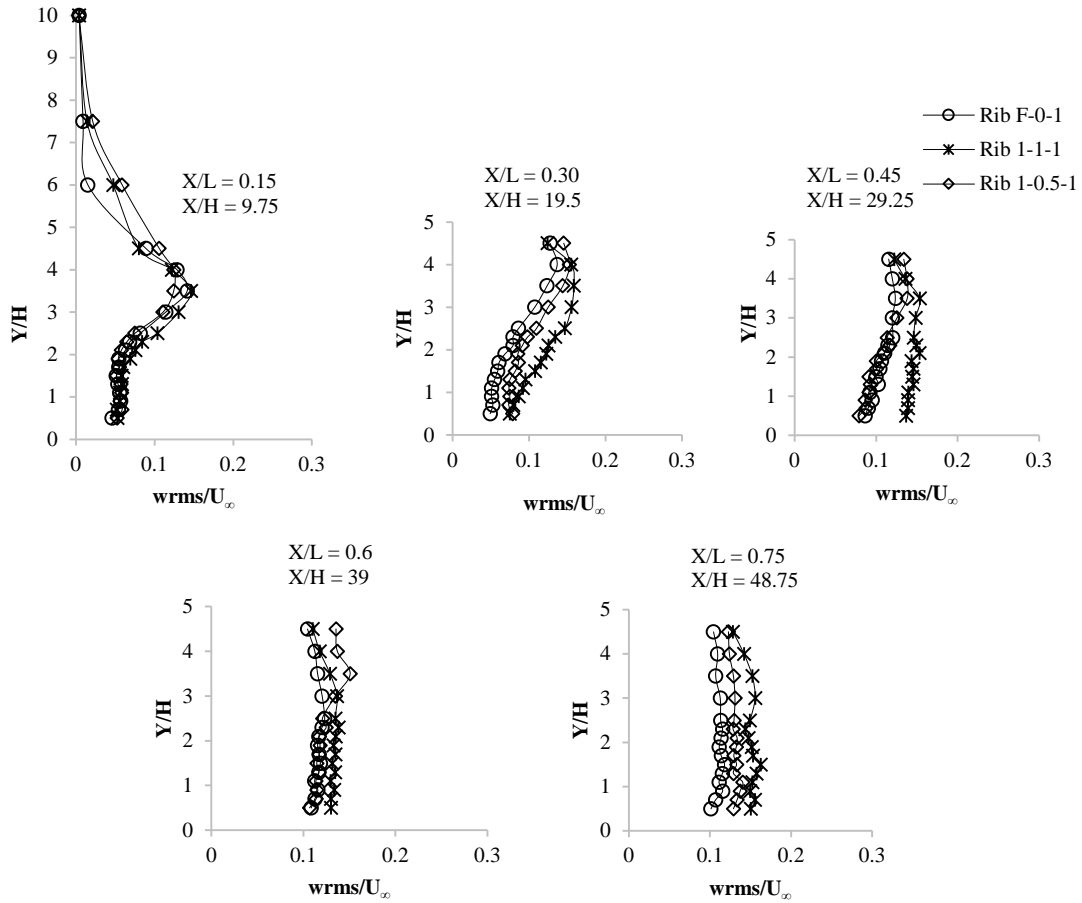


Figure 7.13 Cross stream turbulence intensity profiles ( $w_{rms}/U_\infty$ ) for Rib F-0-1, Rib 1-1-1 and Rib 1-0.5-1 at different downstream distances

Studying turbulence intensity profiles in all three directions (Figures 7.11-13), reveals that discrete ribs generated a higher level of turbulence compared to the full rib. The gaps of ribs tended to reduce the flow blockage as the main flow mixed with the secondary flow and created a higher level of turbulence behind the rib. The rib with the larger gap ratio created higher turbulence intensity immediately downstream of the rib, while at larger downstream distances, the rib with the smaller gap ratio had higher turbulence intensity. This presumably is because the smaller gap creates higher flow blockage right behind the rib and flow reattaches to the surface at a larger distance. Also, these small gaps generate stronger jet flows which projected farther downstream.

Normalized shear stress profiles in XY, XZ and YZ planes:  $uv/U_\infty^2$ ,  $uw/U_\infty^2$  and  $vw/U_\infty^2$ , are presented in Figures 7.14 to 7.16, respectively. As depicted in these figures, the shear stress in the XY plane ( $uv$ ) was much higher than the other two.

As shown in Figure 7.14, at all downstream distances,  $uv$  was negative for all ribs over the entire surface. The profile can be seen at  $X/L = 0.15$  ( $X/H = 9.75$ ); it had very small values near the surface until  $Y/H \cong 2$ , started to increase in magnitude and reached a (negative) peak at  $Y/H = 3.5$ ,

then decreased to very small values at the free stream. However, at larger downstream distances the increasing trend in the Y direction started closer to the plate. This shows that, at closer distances due to the higher flow blockage near the surface, there was a lower level of turbulent shear stress in this (XY) plane. At almost all downstream distances, Rib 1-1-1 had a higher  $uv$  value compared to the two other ribs.

As portrayed in Figure 7.15,  $uw$  more or less had the same profile shape as  $uv$ . Comparing different rib's profiles shows that at  $X/L = 0.15$  ( $X/H = 9.75$ ), Rib 1-0.5-1 had significantly larger values compared to two other ribs, while at larger downstream distances all ribs had almost the same value or Rib 1-1-1 had a slightly larger value.

Comparing  $uw$  after these ribs at different downstream distances does not reveal a specific trend. At  $X/L = 0.15$  ( $X/H = 9.75$ ), Rib 1-0.5-1 had the highest while at  $X/L = 0.3$  and  $0.6$  ( $X/H = 19.5$  and  $29.25$ ), Rib 1-1-1 had the highest values among the ribs. For Rib F-0-1,  $uw$  always had small values, specifically at a larger downstream distances. So, it can be concluded that creating opening areas in the rib would increase shear stresses.

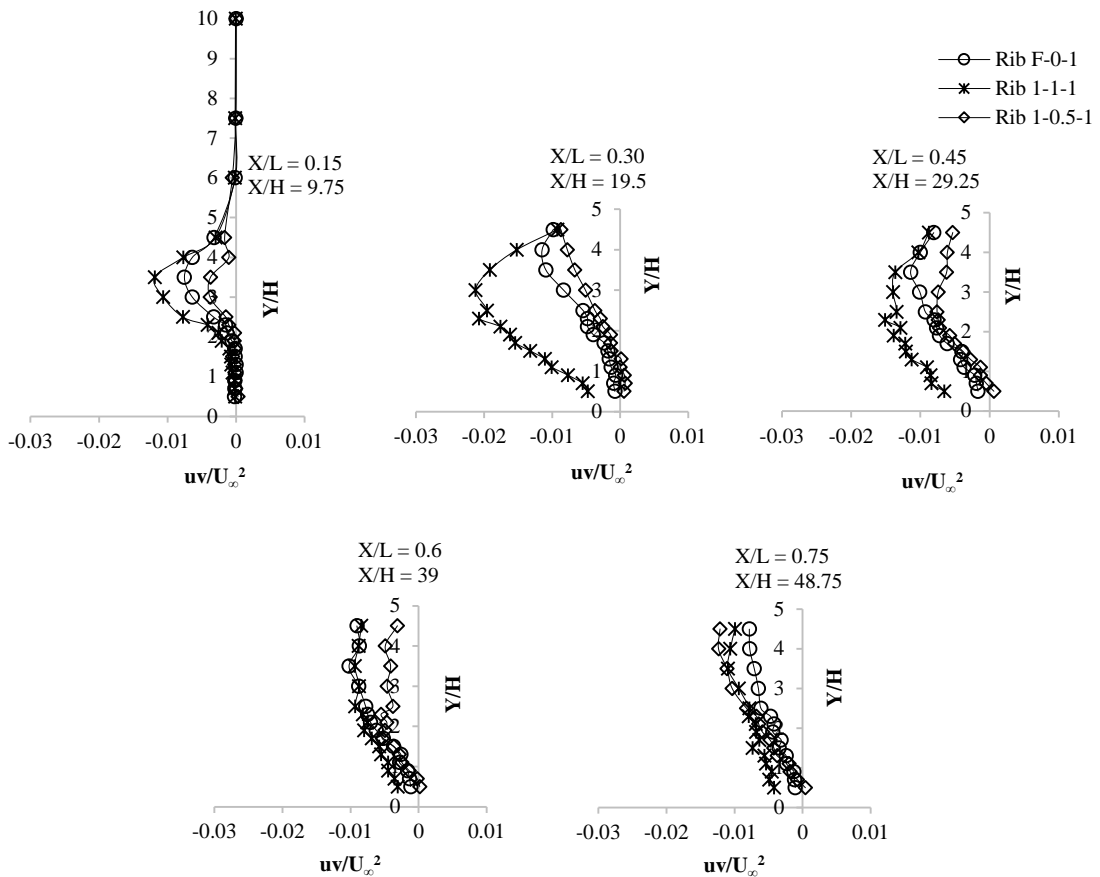


Figure 7.14 Shear stress profiles ( $uv/U_\infty^2$ ) for Rib F-0-1, Rib 1-1-1 and Rib 1-0.5-1 at different downstream distances

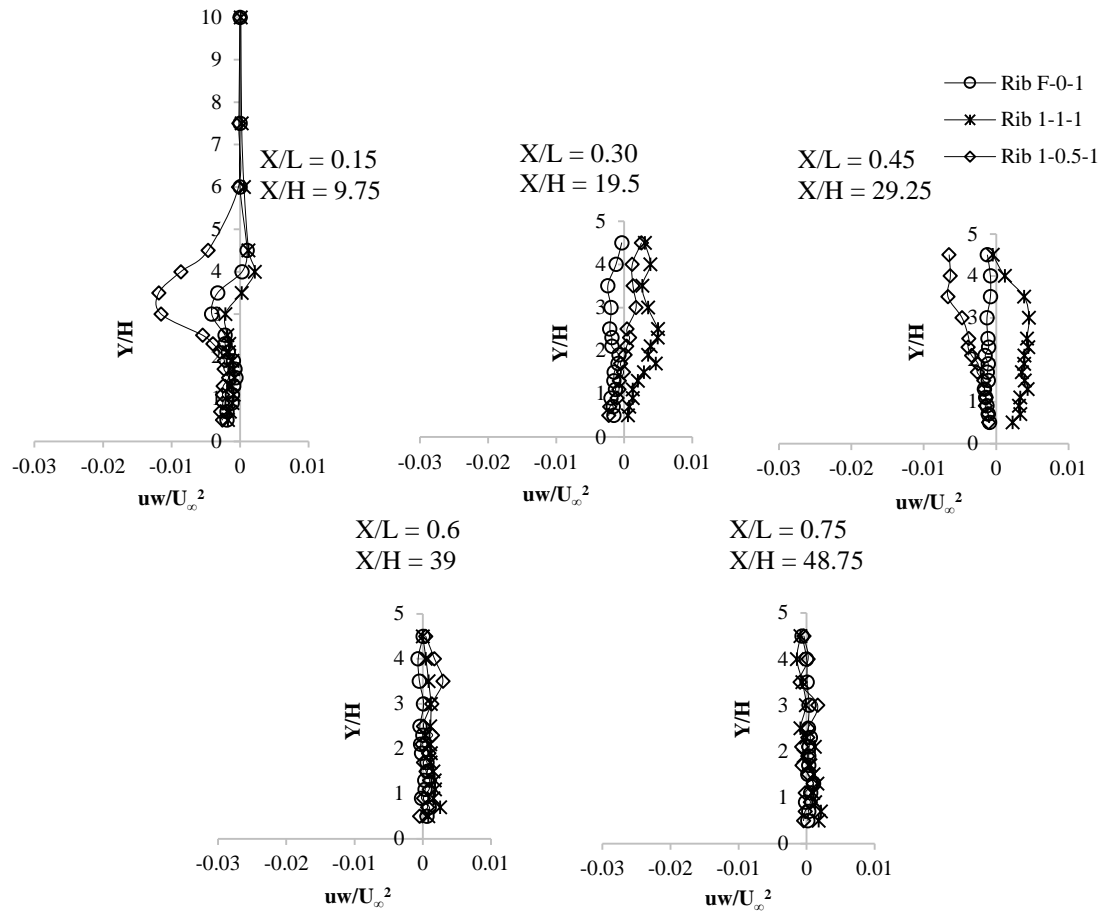


Figure 7.15 Shear stress profiles ( $uw/U_\infty^2$ ) of Rib F-0-1, Rib 1-1-1 and Rib 1-0.5-1 at different downstream distances

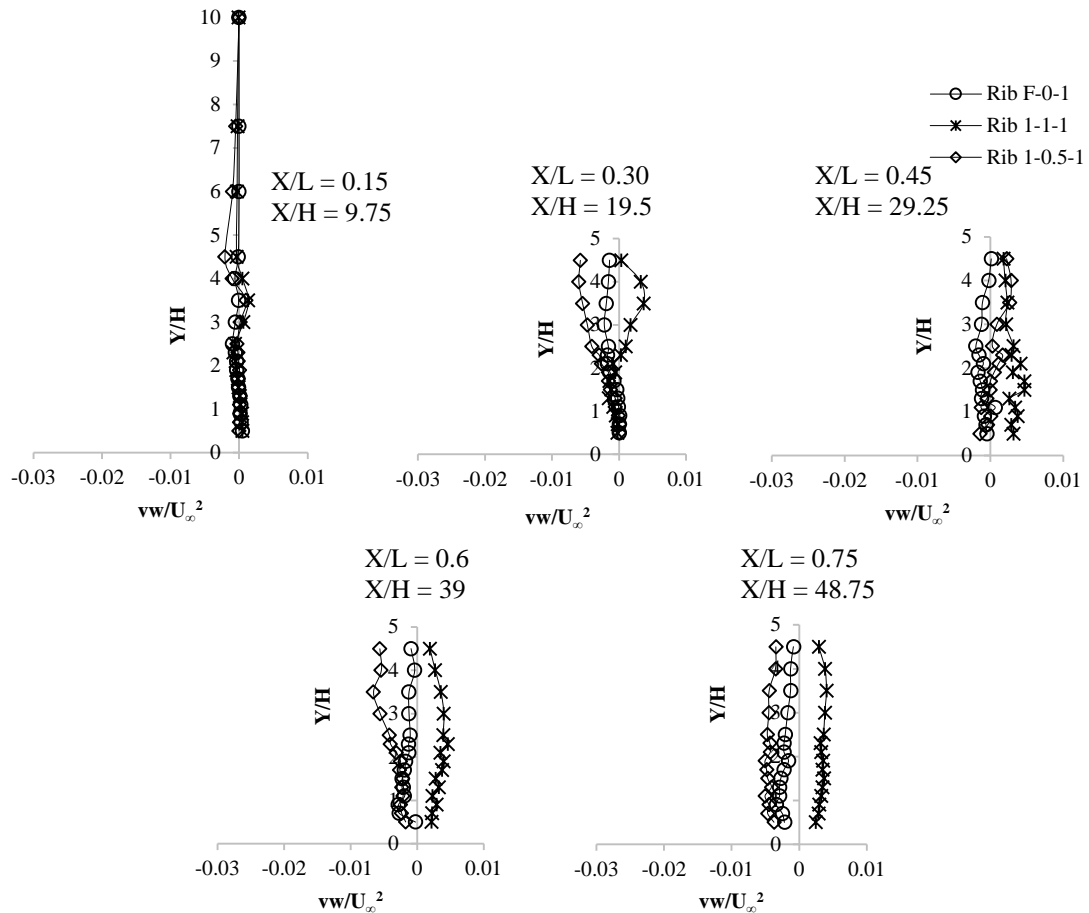


Figure 7.16 Shear stress profiles ( $vw/U_\infty^2$ ) of Rib F-0-1, Rib 1-1-1 and Rib 1-0.5-1 at different downstream distances

Shear stress profiles in the YZ plane ( $vw$ ) can be observed in Figure 7.16. At  $X/L = 0.15$  ( $X/H = 9.75$ ), all ribs had very small  $vw$  values. In addition, for Rib F-0-1,  $vw$  was small at all studied downstream distances. Rib 1-1-1 had positive values except for  $X/L = 0.3$  ( $X/H = 19.5$ ), while, Rib 1-0.5-1 always had negative values.

Relating heat transfer trends to the physics of the flow is not straightforward, as many flow parameters are involved in defining the heat transfer trend of the surface. As was discussed previously, based on estimated flow patterns after these ribs (Figures 7.10), Rib 1-1-1 had a smaller reattachment length compared to Rib F-0-1 and Rib 1-0.5-1. According to the literature, the heat transfer rate increases after flow reattachment to the surface [12,16,19]. Thus, higher heat transfer enhancement at closer downstream distances to Rib 1-1-1, could have been partly due to the shorter reattachment length after this rib. While the larger reattachment length for Rib 1-0.5-1 and Rib F-0-1 postponed the high heat transfer region farther downstream. This difference in the flow structure after these different ribs caused some variations in the flow and turbulence parameter values, some of which were exemplified through higher turbulence stresses just discussed (Figures 7.14 and 7.15). The following section tries to identify the most dominant flow dynamic factors in

determining the behavior of the heat transfer augmentation of the surface. Figures 7.17-7.19 compare the streamwise  $Nu/Nu_0$  distribution after Rib 1-1-1, Rib 1-0.5-1 and Rib F-0-1 at  $U_\infty = 4$  m/s with that of flow parameters. Values in the  $Nu/Nu_0$  graphs are the average of two adjacent data points. The flow parameter values in these graphs are the average of the values at the first three measured points ( $Y/H = 0.5, 0.7$  and  $0.9$ ) at each downstream distance.

Figure 7.17 presents the streamwise distribution of the Nusselt number enhancement and normalized velocities in the X, Y and Z directions for Rib 1-1-1, Rib 1-0.5-1 and Rib F-0-1. In the first half of the plate (up to  $X/L \cong 0.45$ ), the Nusselt number enhancement after rib 1-1-1 (larger gap) was significantly higher than that of the other two ribs. Somewhere along the midpoint of the plate,  $Nu/Nu_0$  associated with this rib decreased to values smaller than that of Rib 1-0.5-1 (smaller gap width) and the full rib (no gap).

The streamwise velocity near the surface after all these ribs had a general increasing trend with downstream distance, as the flow recovered from the blockage of the rib. The very early  $U/U_\infty$  recovery, sort of conformed to the increasing  $Nu/Nu_0$  trend, but not the later (and somewhat lesser) recovery. For example, at  $X/L = 0.6$ , in spite of the larger streamwise velocity value, Rib 1-1-1 had a slightly smaller Nusselt number augmentation compared to the other two ribs. Thus, heat transfer is not entirely dependent on the streamwise velocity.

The streamwise distribution of the normal velocity ( $V/U_\infty$ ) does not show a similar trend for all ribs. For Rib 1-1-1 an obvious increasing-decreasing trend is observed in velocity absolute values, which agrees with the  $Nu/Nu_0$  streamwise trend. Also, until  $X/L = 0.45$ , Rib 1-1-1 had the largest absolute value of  $V$ , while at  $X/L = 0.6$  and  $0.75$ , Rib 1-0.5-1 showed larger (at  $X/L = 0.6$  slightly larger) values than the two other ones. Knowing that Rib 1-1-1 had the highest Nusselt number enhancement until  $X/L = 0.45$ , and at larger downstream distances Rib 1-0.5-1 illustrated the highest value, suggests that the normal velocity could be a more influential factor on the heat transfer of the plate, which may counter the streamwise velocity effect. Physically this makes sense as the normal velocity brings the cooler flow to, or sweeps away the hot flow from, the surface.

The streamwise distribution of cross stream velocities ( $W/U_\infty$ ) again does not present a similar trend for all ribs. The magnitude had an increasing-decreasing trend for Rib 1-1-1 and a decreasing-increasing trend for Rib F-0-1. Also, the rank of ribs' absolute values at different downstream points does not agree with the order of the  $Nu/Nu_0$ . Apparently, the cross stream velocity had the weakest correlation with  $Nu$ . This shows that moving any bulk heated fluid in the transverse direction does not promote the heat transfer.

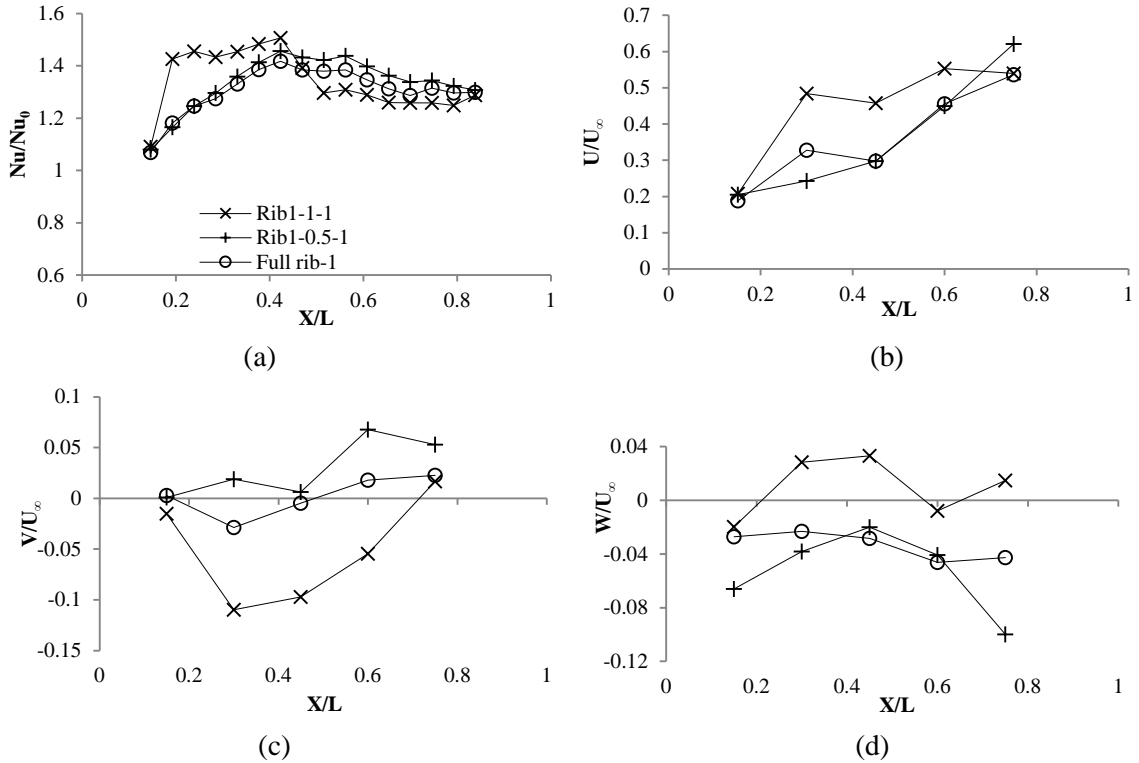


Figure 7.17 The streamwise distribution of (a)  $Nu/Nu_0$  versus (b)  $U/U_\infty$  (c)  $V/U_\infty$  (d)  $W/U_\infty$  for Rib1-1-1, Rib 1-0.5-1 and Rib F-0-1

For  $u_{rms}$  and  $v_{rms}$  (Figure 7.18), a general increasing-decreasing trend with streamwise direction is observed. Also, Rib 1-1-1 had the highest turbulence intensity until  $X/L = 0.45$ , which decreased to the values close to that of Rib 1-0.5-1 at  $X/L = 0.6$ , and beyond which it was second after Rib 1-0.5-1. For  $w_{rms}$ , there is a trend of steady increase with downstream distance and the value for Rib 1-1-1 is always the largest one among the three ribs. From these observations it can be concluded that  $u_{rms}$  and  $v_{rms}$  correlations with  $Nu/Nu_0$  seem to be stronger compared to  $w_{rms}$ . At  $X/L = 0.6$ , in spite of almost the same or even higher turbulence intensity for Rib 1-1-1, it had the lowest Nusselt number enhancement. The larger positive  $V$  value at this point for Rib 1-0.5-1 (Figure 7.18) might overcome the lower turbulence intensity effect.

Streamwise trends of  $Nu/Nu_0$  and turbulence shear stresses are shown in Figure 7.19. Among all shear stresses profiles, the  $uv/U_\infty^2$  magnitude seems to follow an increasing-decreasing trend (which can be clearly seen for Rib 1-1-1 case). However, the sequence of ribs shear stress values do not seem to correlate well with that of the  $Nu/Nu_0$ , as Rib 1-1-1 has the highest value at all downstream distances.



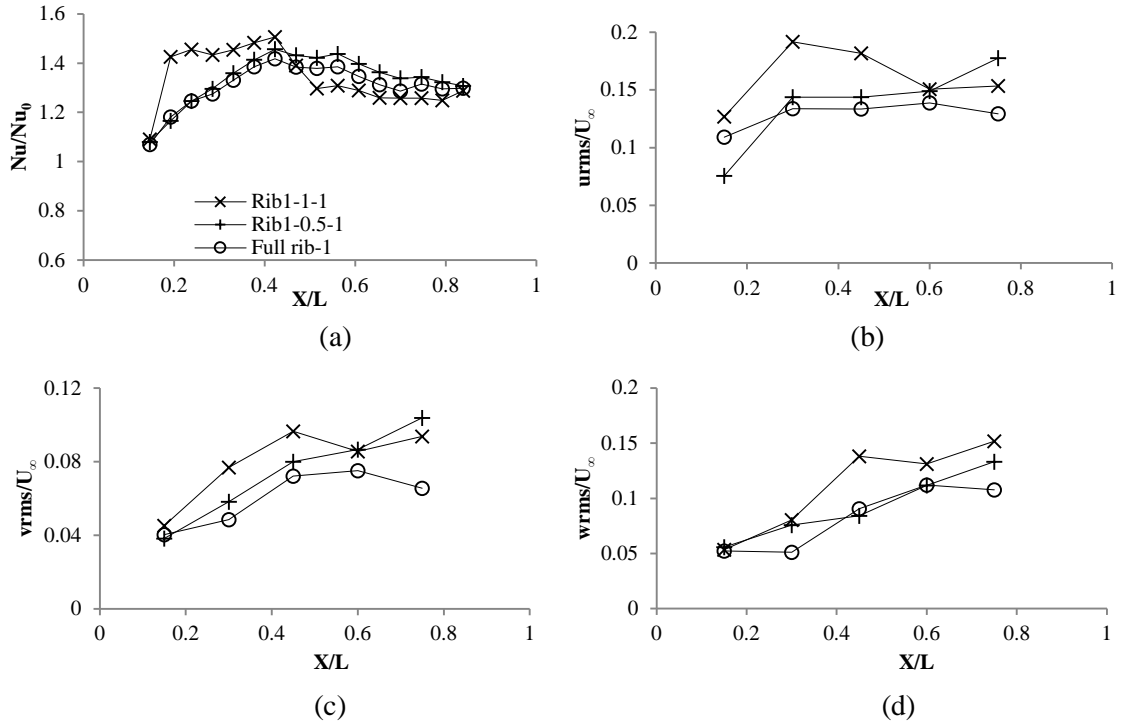


Figure 7.18 The streamwise distribution of (a)  $Nu/Nu_0$  versus (b)  $u_{rms}/U_\infty$  (b)  $v_{rms}/U_\infty$  (c)  $w_{rms}/U_\infty$  for Rib 1-1-1, Rib 1-0.5-1 and Rib F-0-1

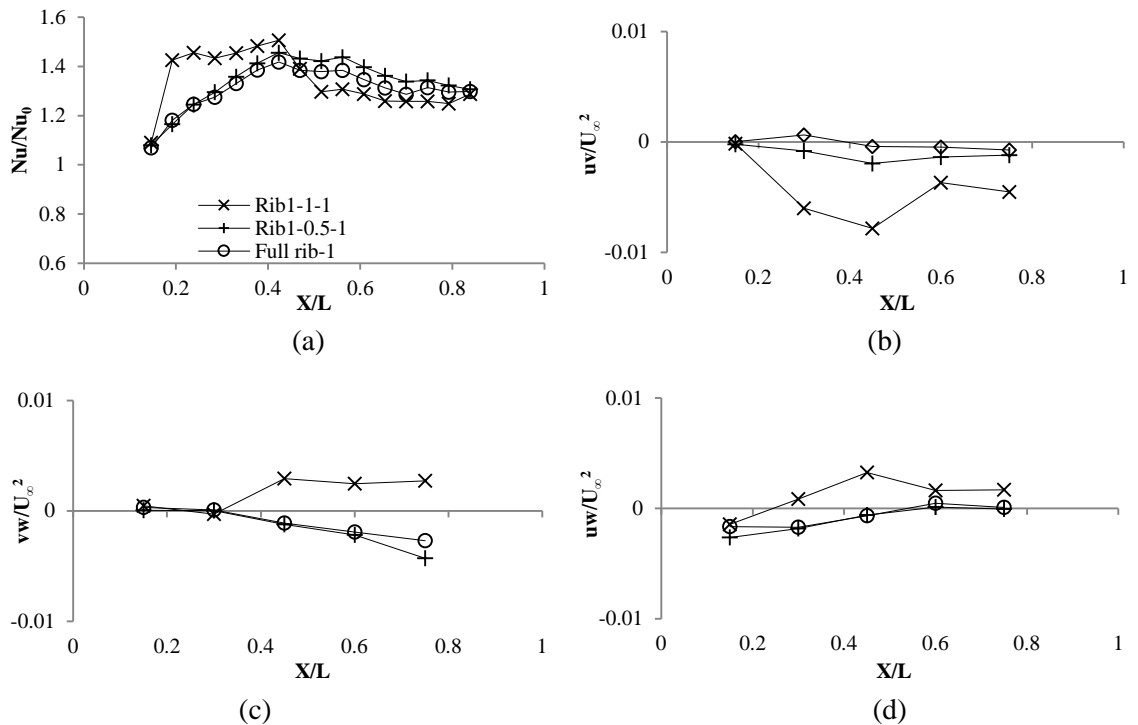


Figure 7.19 The streamwise distribution of (a)  $Nu/Nu_0$  versus (b)  $uv/U_\infty^2$  (b)  $vw/U_\infty^2$  (c)  $uw/U_\infty^2$  for Rib 1-1-1, Rib 1-0.5-1 and Rib F-0-1

To compare the relative significance of the various turbulent flow parameters with the Nusselt number enhancement,  $Nu/Nu_0$  versus the most influential of the studied flow parameters are depicted in Figure 7.20. From the presented and discussed results,  $Nu/Nu_0$  was plotted against  $u_{rms}/U_\infty$ ,  $v_{rms}/U_\infty$ ,  $abs(V/U_\infty)$  and  $U/U_\infty$ . Amidst the scatter of the data points, we see the slope corresponding to  $v_{rms}/U_\infty$  is the highest at around 4.1, then  $u_{rms}/U_\infty$  at 3.2,  $abs(V/U_\infty)$  at 1.9 and  $U/U_\infty$  at 0.5. The corresponding coefficients of determination ( $R^2$ ), which indicate the goodness of the linear fit, are relatively far from the ideal value of unity. As depicted in Figure 7.20,  $R^2$  for  $u_{rms}/U_\infty$ ,  $v_{rms}/U_\infty$ ,  $abs(V/U_\infty)$  and  $U/U_\infty$  are 0.55, 0.49, 0.29 and 0.28, respectively. These low  $R^2$  values are presumably mostly due to our inability to vary any one of the studied parameters independently at one time. In other words, any significant variation of a parameter occurred with some coupled change in other parameters. Nonetheless, these results confirm with the extensive observation and discussion on the detailed flow physics that have been presented.

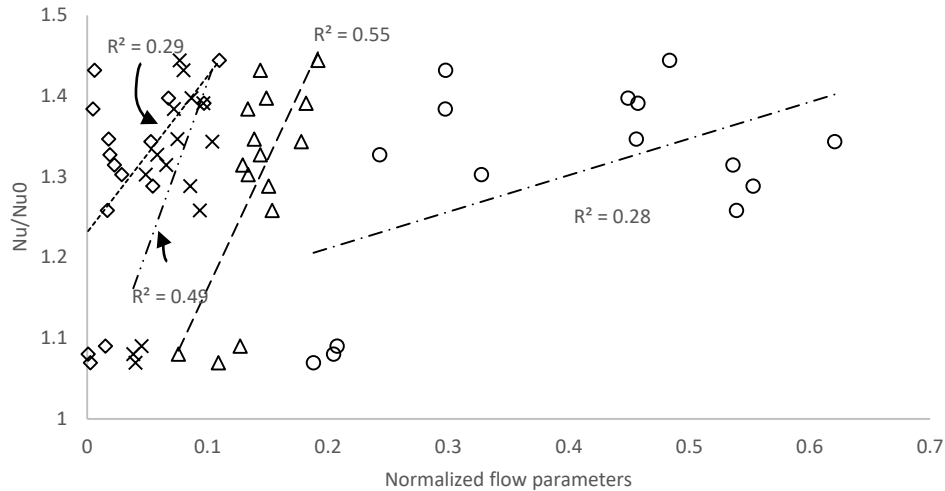


Figure 7.20  $Nu/Nu_0$  correlation with different flow and turbulence parameters; triangles correspond to  $u_{rms}/U_\infty$ , x's to  $v_{rms}/U_\infty$ , diamonds to  $abs(V/U_\infty)$  and circles to  $U/U_\infty$

#### 7.4. Conclusion

An experimental study was performed to investigate the heat transfer enhancement and flow characteristics over a surface downstream of full and discrete ribs with different gap ratios. Convective heat transfer from the surface was studied for different ribs (one full rib and four discrete ribs), free stream velocities and rib heights. Ribs with larger gap ratios were observed to be more effective at enhancing the heat transfer augmentation at closer distances to the rib, while at larger downstream distances from the rib, discrete ribs with smaller gap ratios were more effective. Also, comparing the full rib's heat transfer performance with that of discrete ribs revealed that, creating a gap in the rib was effective in enhancing the heat transfer rate at closer distances to the rib, but not necessarily at larger downstream distances.

To analyze the flow structure after ribs and identify possible reasons behind heat transfer enhancement trends, flow over the surface at several downstream distances from the rib was measured and analyzed. Three different ribs, one full rib and two discrete ribs with different gap ratios were selected for fluid mechanics measurements. It was seen that the gap in the rib enhanced the turbulence intensity and shear stresses. At the same time, gaps decreased the flow blockage so that streamwise, normal and cross stream velocities over the surface immediately after the rib increased. All these effects enhanced the heat transfer rate in discrete ribs compared to the full rib, specifically at closer downstream distances to the rib. Also, it was observed that the larger gap width caused the flow to reattach to the surface at a shorter downstream distance from the rib, which affected the heat transfer enhancement trend. Comparing different flow parameters' streamwise trends with that of  $Nu/Nu_0$ , shows that turbulence intensities in the streamwise and normal directions seem to be most correlated with heat transfer augmentation. Nonetheless, streamwise and normal mean velocities ( $U$  and  $V$ ) also play some role.

### ***Acknowledgment***

This work was made possible by the Ontario Trillium Foundation, the Natural Sciences and Engineering Research Council of Canada and the Essex Energy Corporation.

### ***References***

- [1] Saha, A.K., and Acharya, S., 2007, "Turbulent Heat Transfer in Ribbed Coolant Passages of Different Aspect Ratios: Parametric Effects," *ASME Journal of Heat Transfer*, 129, pp. 449-463.
- [2] Kiml, R., Mochizuki, S., and Murata, A., 2001, "Effects of Rib Arrangements on Heat Transfer and Flow Behavior in a Rectangular Rib-Roughened Passage: Application to Cooling of Gas Turbine Blade Trailing Edge," *ASME Journal of Heat Transfer*, 123, pp. 675-681.
- [3] Kang, C., and Yang, K-S., 2016, Characterization of Turbulent Heat Transfer in Ribbed Pipe Flow," *ASME Journal of Heat Transfer*, 138, pp. 041901-1-9.
- [4] Xie, G., Liu, J., Zhang, W., Lorenzini, G., and Biserni, C., 2014, "Numerical Prediction of Turbulent Flow and Heat Transfer Enhancement in a Square Passage with Various Truncated Ribs on One Wall," *ASME Journal of Heat Transfer*, 136, pp. 011902-1-11.
- [5] Liou, T-M., Chen, C.-C., and Tsai, T-W., 2000, "Heat Transfer and Fluid Flow in a Square Duct with 12 Different Shaped Vortex Generators," *ASME Journal of Heat Transfer*, 122, pp. 327-335.
- [6] Kumar, A., and Kim, M-H., 2015, "Effect of Roughness Width Ratios in Discrete Multi V-rib with Staggered Rib Roughness on Overall Thermal Performance of Solar Air Channel," *Solar Energy*, 119, pp. 399-414.
- [7] Kumar, A., and Kim, M-H., 2014," Numerical Optimization of Solar Air Heaters Having Different Types of Roughness Shapes on the Heated Plate-Technical Note," *Energy*, 72, pp. 731-738.
- [8] Tang, X-Y., and Zhu, D-S., 2013," Flow Structure and Heat Transfer in a Narrow Rectangular Channel with Different Discrete Rib Arrays," *Chemical Engineering and Processing*, 69, pp. 1- 14.

- [9] Kumar, A., Saini, R.P., and Saini, J.S., 2013, "Development of Correlations for Nusselt Number and Friction Factor for Solar Air Heater with Roughened Duct having Multi V-shaped with Gap Rib as Artificial Roughness," *Renewable Energy*, 58, pp. 151-163.
- [10] Han, J.C., and Zhang, Y.M., 1992, "High Performance Heat Transfer Ducts with Parallel, Broken and V-shaped Broken Ribs," *International Journal of Heat and Mass Transfer*, 35, pp. 513–523.
- [11] [Liou](#), T.-M., [Wang](#), W.-B., and [Chang](#), Y.-J., 1995, "Holographic Interferometry Study of Spatially Periodic Heat Transfer in a Channel with Ribs Detached from One Wall," *ASME Journal of Heat Transfer*, 117(1), pp. 32-39.
- [12] Tariq, A., Panigrahi, P.K., and Muralidhar, K., 2004, "Flow and Heat Transfer in the Wake of a Surface-Mounted Rib with a Slit," *Experiments in Fluids*, 37, pp. 701–719.
- [13] Singh, S., Chander, S., and Saini, J.S., 2011, "Heat Transfer and Friction Factor Correlations of Solar Air Heater Ducts Artificially Roughened with Discrete V-down Ribs," *Energy*, 36, pp. 5053-5064.
- [14] Karwa, R., 2003, "Experimental Studies of Augmented Heat Transfer and Friction in Asymmetrically Heated Rectangular Ducts with Ribs on the Heated Wall in Transverse, Inclined, V-continuous and V-discrete Pattern," *International Communication of Heat and Mass Transfer*, 30(2), pp. 241-250.
- [15] Gill, R.S., Hans, V.S., and Saini, J.S., 2015, "Heat Transfer and Friction Characteristics of Solar Air Heater Duct Roughened by Broken Arc Shaped Ribs Combined with Staggered Rib Piece," *International Journal of Engineering Research & Technology (IJERT)*, 4 (11), pp. 604-610.
- [16] Fouladi, F., Henshaw, P., Ting, D. S-K., and S. Ray, 2017, "Flat Plate Convection Heat Transfer Enhancement via a Square Rib," [International Journal of Heat and Mass Transfer](#), 104, pp. 1202–1216.
- [17] Acharaya, S., Dutta, S., Myrum, T.A., and Baker, R.S., 1994, "Turbulent Flow Past a Surface-Mounted Two-dimensional Rib," *ASME Journal of Fluids Engineering*, 116 (2), pp. 238–246.
- [18] Panigrahi, P.K. and Acharya, S., 1996, "Spectral characteristics of separated flow behind a surface-mounted square rib," *Proc. of the 27th Fluid Dynamics Conference*, American Institute of Aeronautics and Astronautics (AIAA), New Orleans, LA, Paper 96–1931.
- [19] Ali, M.S., Tariq, A., and Gandhi, B.K., 2013, "Flow and Heat Transfer Investigation Behind Trapezoidal Rib Using PIV and LCT Measurements," *Experiments in Fluids* 54, pp. 1520-1528.
- [20] Liu, Y.Z., Ke, F., and Sung, H.J., 2008, "Unsteady Separated and Reattaching Turbulent Flow Over a Two-dimensional Square Rib," *Journal of Fluids and Structures*, 24(3), pp. 366-381.
- [21] Panigrahi, P.K., Schroeder, A., and Kompenhans, J., 2008, "Turbulent Structures and Budgets Behind Permeable Ribs," *Experimental Thermal and Fluid Science*, 32 (4), pp. 1011–1033.

[22] Ting, D. S-K., 2016, *Basics of Engineering Turbulence*, 1st ed., Elsevier, Academic Press, New York, ISBN: 978-0-12-803970-0.

## CHAPTER 8

### CONCLUSION

The conclusions of different parts of the present research were discussed extensively in chapters 2 to 7. In this chapter, the overall conclusions and the main contribution of this study are reviewed and suggestions for future research are also included.

The ultimate intention in this research work is to increase the heat transfer rate from a PV panel to promote its performance. PV panels suffer from low efficiency, and increasing the solar cell temperature degrades their performance [1]. One method which is used in different industrial applications is to disturb the air flow over the surface by applying some objects (such as ribs) to augment the mixing rate and ultimately the convective heat transfer rate [2-6]. In working towards this goal, understanding the flow and turbulence physics over a surface after an object at its leading edge and determining the most effective flow parameters on the flat plate convective heat transfer rate were also pursued in this study. Objects such as full and discrete ribs and partial grids were placed at the leading edge of a surrogate PV panel and flow and turbulence structures are investigated in this research. For two of these objects (square rib and discrete ribs) the effect of the combination of different flow parameters on the heat transfer was studied.

#### *Nomenclature*

abs ( $V/U_\infty$ )	absolute value of the normalized local velocity in the Y direction	Rib F-0	full rectangular rib (no gap)
$Gr/Re^2$	Richardson number	$u_{rms}$	root-mean-square of the streamwise velocity fluctuations (m/s)
H	rib height over the surface (cm)	U	local time averaged streamwise velocity (m/s)
k	thermal conductivity of the air (W/m.K)	$U_\infty$	free stream velocity (m/s)
Nu	Nusselt number of the ribbed plate ( $h.X/k$ )	$v_{rms}$	root-mean-square of the normal velocity fluctuations (m/s)
$Nu_0$	Nusselt number of the smooth plate (no rib)	V	local time averaged normal velocity (m/s)
$Nu/Nu_0$	heat transfer enhancement of the ribbed plate with respect to the smooth plate	X	streamwise distance from the rib (cm)
Rib 1-1	discrete rib with 1 cm tooth and 1 cm gap width	Y	normal distance from the plate (cm)
Rib 1-0.5	discrete rib with 1 cm tooth and 0.5 cm gap width		

#### *8.1. Concluding Remarks*

To perform an overall study on the effect of all studied objects at the leading edge of a surface on the heat transfer enhancement, the Nusselt enhancement results of these objects at velocity ( $U_\infty = 4$  m/s) and rib's height ( $H = 1$ cm) were compiled in one graph (Figure 8.1). Heat transfer enhancement results of the square rib, rectangular full and discrete ribs, and partial grid from Chapters 5, 7 and Appendix. A, respectively, are presented in one graph in this figure. The height

$H = 1$  cm was selected for comparisons here as the heat transfer test on the partial grid at different heights (Appendix. A,  $H = 1, 2$  and  $3$  cm) showed that the best thermal performance happened at the lowest tested height ( $H = 1$  cm) and the square rib tested in Chapter 5 had the fixed height of  $1$  cm. Also, the free stream velocity  $U_\infty = 4$  m/s was selected as it was mutual in experiments on different objects. As can be seen, until  $X/H \cong 11$ , a square rib and after that until  $X/H \cong 30$ , a discrete rectangular rib with  $1$  cm tooth and  $1$  cm gap width (Rib 1-1) shows the best heat transfer rate enhancement. At larger downstream distances, the discrete rectangular rib with  $1$  cm tooth and  $0.5$  cm gap width (Rib1-0.5) seems to have highest Nusselt enhancement. The partial grid illustrates the lowest thermal performance at almost all downstream distances.

Also, the Richardson number ( $Gr/Re^2$ ) was calculated to evaluate the importance of the natural convection mechanism in the total convection heat transfer from the plate [7]. The Grashof number was calculated based on the horizontal plate characteristic length (area/perimeter) and the average plate temperature with Rib 1-1-1 at the leading edge and at  $U_\infty = 4$  m/s. The Reynolds number was calculated based on two characteristic lengths; plate half-length and rib height. For both Reynolds numbers,  $Gr/Re^2$  was much smaller than  $0.1$  ( $2.7 \times 10^{-2}$  and  $2.7 \times 10^{-5}$ ) which indicates that the contribution of natural convection at this free stream velocity is negligible [7], and this contribution would be even less at higher velocities.

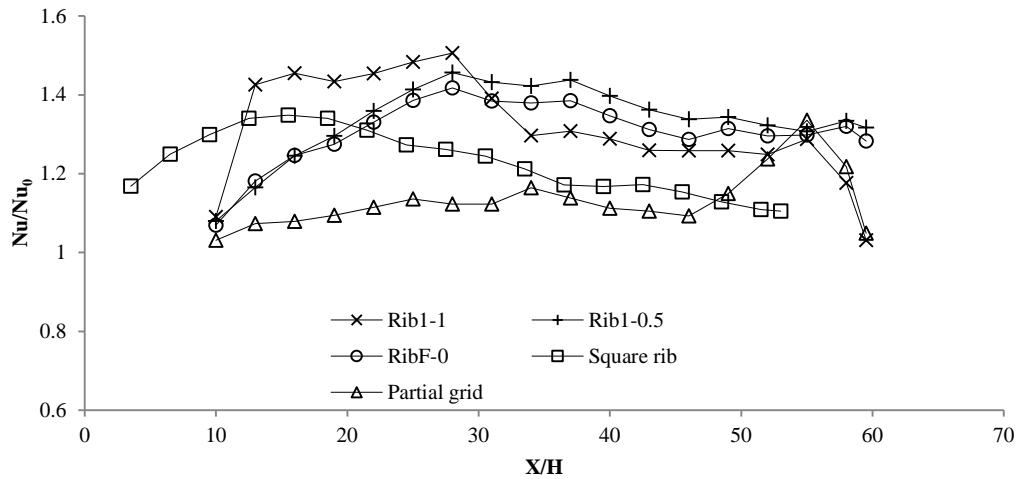


Figure 8.1 Comparing heat transfer enhancements of the surface after different objects at the leading edge at  $U_\infty = 4$  m/s and  $H = 1$  cm

Furthermore, to derive a general conclusion on probable effects of the flow structure on Nusselt enhancement trends, flow parameters after these objects must be considered. Velocity and turbulence intensity profiles over the surface in the streamwise ( $X$ ) and normal ( $Y$ ) directions at two different downstream distances from the object ( $X/H \approx 9$  and  $20$ ) are compared (Figure 8.2 (a) and (b)). These two approximate downstream distances were selected as they were the location fluid mechanics measurements after these objects. It has to be mentioned that, for the partial grid,

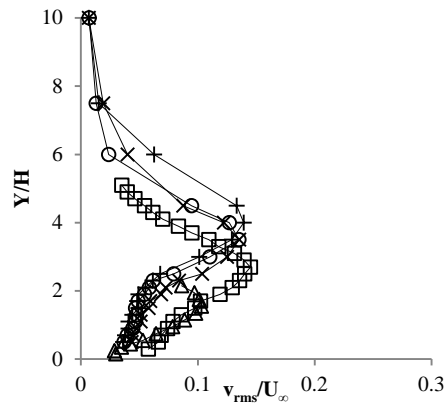
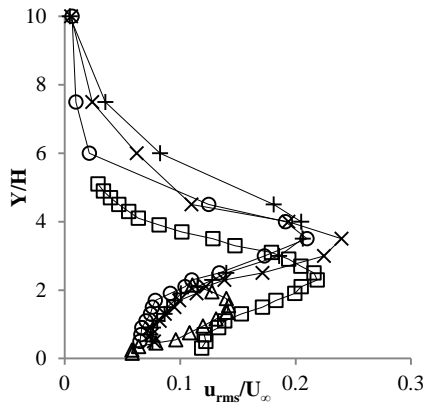
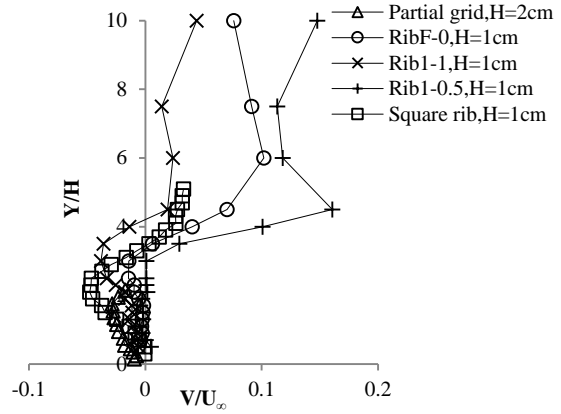
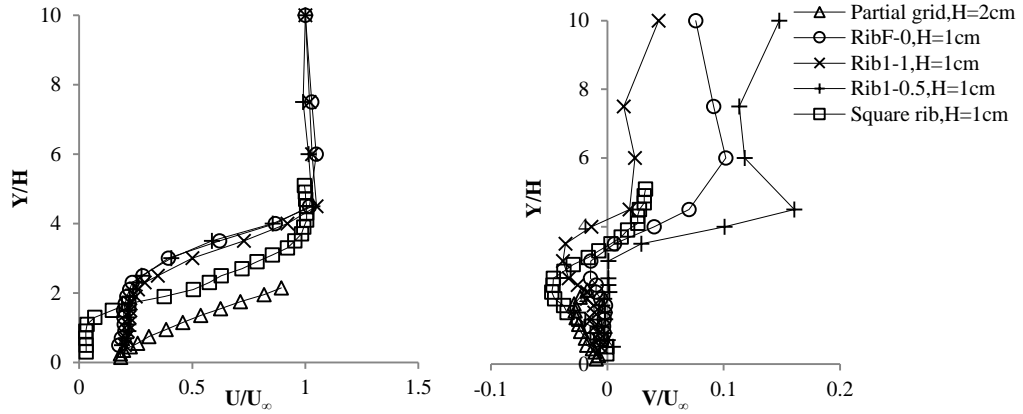
flow mechanics results just at a grid height of 2 cm were measured (Appendix.A). However, all distances in the X and Y directions in these graphs are normalized by the objects heights ( $H = 1$  cm in full and discrete ribs and 2 cm in partial grid).

The streamwise velocity profile shapes after these objects at  $X/H \approx 9$  (Figure 8.2 (a)) reveals that the partial grid, even with its higher height, created less flow blockage compared to other objects. However, at points closest to the surface, the partial grid U velocity was almost the same as that of the full and discrete ribs. For the square rib at the points close to the surface, due to the hot-wire data modifications (Chapter 5), lower streamwise velocity values were observed compared to that of the other objects. But an obvious observation in this graph is the difference between the profile shapes after the partial grid and other objects. From previous Chapters (5 and 7) and the literature [7-9], the streamwise velocity profile in the recirculation region behind the rib has a specific shape. The velocity is very small and almost constant in the normal direction to the surface (Y) until a specific height, and then starts to increase, as can be seen in square, rectangular and discrete rib profiles in Figure 8.2 (a). For the partial grid, the profile shape does not show the same trend as the velocity increased after the first point over the surface. Apparently, the recirculation or wake region behind the partial grid was smaller than that for other objects and at this downstream distance ( $X/H \approx 9$ ) the flow had reattached completely to the surface and the boundary layer started to reinitiate from the surface. It seems like jet flows through the grid holes broke the wake vortex into smaller pieces or completely destroyed it.

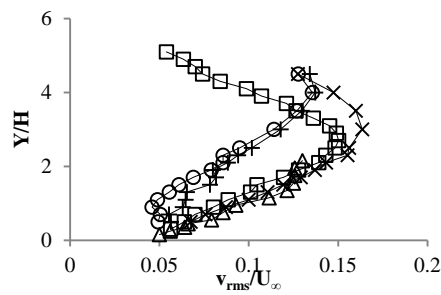
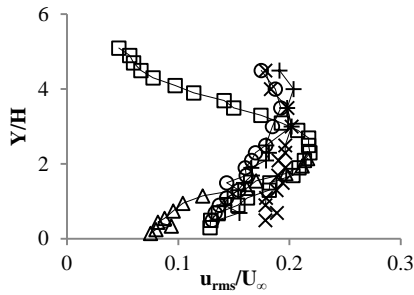
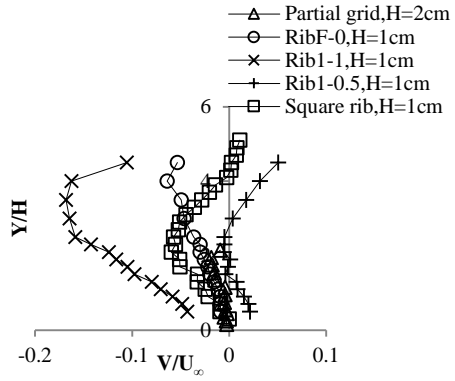
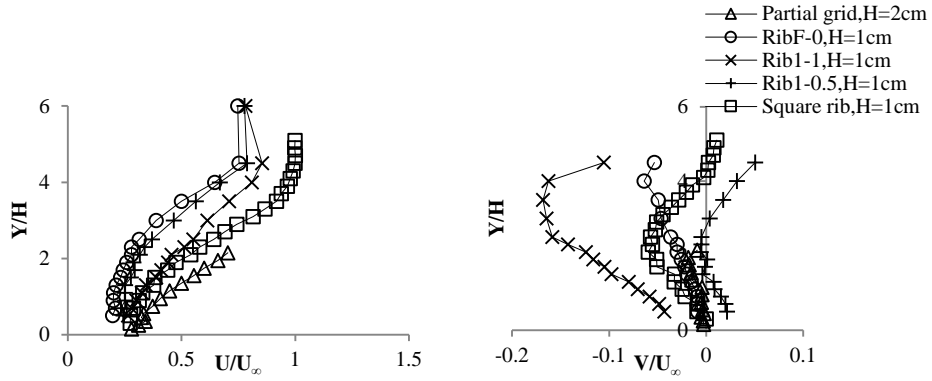
Normal velocity, at this specific downstream distance, had almost same values close to the surface after all of the objects. However, at higher distances from the surface ( $Y/H > 1.5$ ), V presented different values after different objects, but still illustrated almost similar trends.

Turbulence intensity profiles after these objects are also shown at  $X/H \approx 9$  in this figure. As can be seen, the square rib showed the highest turbulence intensity in both streamwise and normal directions, especially for points closest to the surface. Considering that the square is the most effective Nusselt enhancement device in Figure 8.1 at  $X/H \approx 9$ , may again confirm the outcomes in Chapters 5 and 7 that turbulence intensities in streamwise and normal directions are important factors in heat transfer enhancement.





(a)



(b)

Figure 8.2 Flow velocity and turbulence intensity profiles in streamwise direction at  $U_\infty = 4 \text{ m/s}$  and (a)  $X/H \approx 9$  (b)  $X/H \approx 20$

At the larger downstream distance ( $X/H \approx 20$ , Figure 8.2 (b)), streamwise velocity profiles again show that the partial grid had the least flow blockage, which is not as obvious as the case at  $X/H \approx 9$ . Also, profile shapes for the full rectangular rib and Rib 1-0.5 show that apparently the flow was not completely reattached to the surface (as discussed extensively in Chapter 7). While for other objects (Rib 1-1, square rib and partial grid), streamwise profile shapes show that flow was already or was closed to being reattached to the surface.

The normal velocity profiles have the same trend but different values at this downstream distance. Normal velocities after discrete Rib 1-1 were significantly larger in magnitude compared to that of other objects, which indicates closeness to the flow reattachment points after this object.

The  $u_{\text{rms}}$  graph at this specific downstream distance shows that Rib 1-1 created more streamwise turbulence at the closest distances to the surface, while the partial grid had smaller values compared to other objects. This might be again due to the fact that the flow separation and reattachment, which is readily distinguishable after a rectangular or square rib, generated a higher level of turbulence compared to the partial grid for which the wake vortex was smaller or non-existent. For turbulence intensity in the Y direction ( $v_{\text{rms}}$ ) all profiles show almost the same values at the closest distances to the rib, while the profile shapes for the full rib and Rib 1-0.5 may again indicate that flow reattachment to the surface had not yet occurred.

Referring to Figure 8.1, it can be observed that the discrete Rib 1-1 had larger Nusselt enhancement compared to other objects at this downstream distance ( $X/H = 20$ ). The reason based on flow results at this specific downstream distance, may be the larger normal velocity and turbulence intensity values for Rib 1-1, due to the flow reattachment at this location. At larger downstream distances ( $X/H > 30$ ), the Nusselt enhancement for Rib 1-0.5 and Rib F-0 exceeded that of Rib 1-1 and other objects. As was discussed in Chapter 7, the greater heat transfer was due to the flow reattachment after Rib 1-0.5 and Rib F-0 which happened in this further downstream area and the higher turbulence intensity and normal velocity (specifically for Rib 1-0.5) created by these ribs.

Finally, it may be concluded that the flow structure over a surface downstream of an object (flow separation-reattachment behaviour), which is detectable by several flow parameters, has a tremendous effect on the heat transfer enhancement. Also, among flow parameters, normal velocity and turbulence intensities are most effective parameters to enhance the heat transfer.

Furthermore, as the ultimate goal of the present study is enhancing the efficiency of a PV panel, the effect of the discrete rib (Rib 1-1) on a surrogate PV panel is investigated. The studied heated flat plate in chapter 2 is considered as the surrogate PV panel. The set-up top surface temperature reduction caused by the rib is calculated to be in the range of  $2.7 \sim 4.7$  °C. The average enhancement in the PV panel efficiency which is calculated (by Equation 2.2) at this temperature difference is 0.23%. This enhancement in the efficiency at the studied day in Chapter 2 (April 13<sup>th</sup>) with an average irradiance of  $550 \text{ kW/m}^2$  and  $2000 \text{ m}^2$  total area of PV panels leads to 2.5 kW of power output augmentation. Thus, it can be seen that, this simple-designed passive method can lead to a noticeable enhancement in harvesting the solar energy by a PV farm.

## **8.2. Future Work Recommendations**

This study attempted to correlate some flow and turbulence parameters to the convective heat transfer enhancement of air flowing over a flat plate. More detailed turbulence parameters such as intermittency, small and large eddies, symmetry and etc. could be considered in this investigation to establish a more comprehensive conclusion on the effect of flow and turbulence structures on the flat plate convective heat transfer.

As PV panels in general are mounted tilted to the horizon. Wind normally moves horizontal to the ground, so it is not very likely that the free stream wind will flow parallel to the panel, although panels flush to inclined roofs may experience deflected flow parallel to the roof. It seems logical that the effect of the turbulence enhancer will have its greatest effect when the air flow is parallel to the panel and minimal effect when the air flow is perpendicular to the panel. However, the effectiveness of the studied objects at different wind incident angles should be investigated.

A parametrical study can be performed on the geometry of the rectangular discrete rib to find the optimum one in terms of maximizing heat transfer enhancement for a long downstream distance over the surface. Flow and turbulence structures would need to be studied in detail.

Different vortex generators instead of ribs can be applied at the leading edge of a heated flat plate's. The heat transfer enhancement and the flow physics should be studied and compared with transverse ribs.

## **References**

- [1] Spectrolab, Inc., Sylmar, C.A., 1977, "Photovoltaic Systems Concept Study: Final Report," (ALO-2748-12) U.S. Dept. of Energy, Division of Solar Energy, Springfield, VA.
- [2] Yadav, A.S., Bhagoria, J.L., 2014, "A CFD Based Thermo-hydraulic Performance Analysis of an Artificially Roughened Solar Air Heater Having Equilateral Triangular Sectioned Rib Roughness on the Absorber Plate," *International Journal of Heat and Mass Transfer*, 70, 1016–1039.
- [3] Mittal, M.K., Varun, Saini, R.P., Singal, S.K., 2007, "Effective Efficiency of Solar Air Heaters Having Different Types of Roughness Elements on the Absorber Plate," *Energy*, 32 (5), 739–745.
- [4] Greig, D., Siddiqui, K., Karava, P., 2012, "An Experimental Investigation of the Flow Structure Over a Corrugated Waveform in a Transpired Air Collector," *International Journal of Heat and Fluid Flow*, 38, 133–144.
- [5] Chamoli, S., Thakur, N.S., Sain, J.S., 2012, "A Review of Turbulence Promoters Used in Solar Thermal Systems," *Renewable and Sustainable Energy Reviews*, 16 (5), 3154–3175.
- [6] Bhagoria, J.L., Saini, J.S., Solanki, S.C., 2002, "Heat Transfer Coefficient and Friction Factor Correlations for Rectangular Solar Air Heater Duct Having Transverse Wedge Shaped Rib Roughness on the Absorber Plate," *Renewable Energy*, 25 (3), 341–369.
- [7] Y.A. Cengel, 2003, *Heat Transfer*, 2nd ed., McGraw-Hill, New York, ISBN: 0-07-245893-3.

## APPENDICES

### Appendix A. Heat transfer enhancement and flow measurements of a heated flat plate after a partial grid with different heights

Heat transfer of the set-up which is explained in chapters 4-7 after the diamond shape partial grid is tested at different free stream velocities and grid's heights. The set-up and grid schematic are shown here again (Figure A.1).

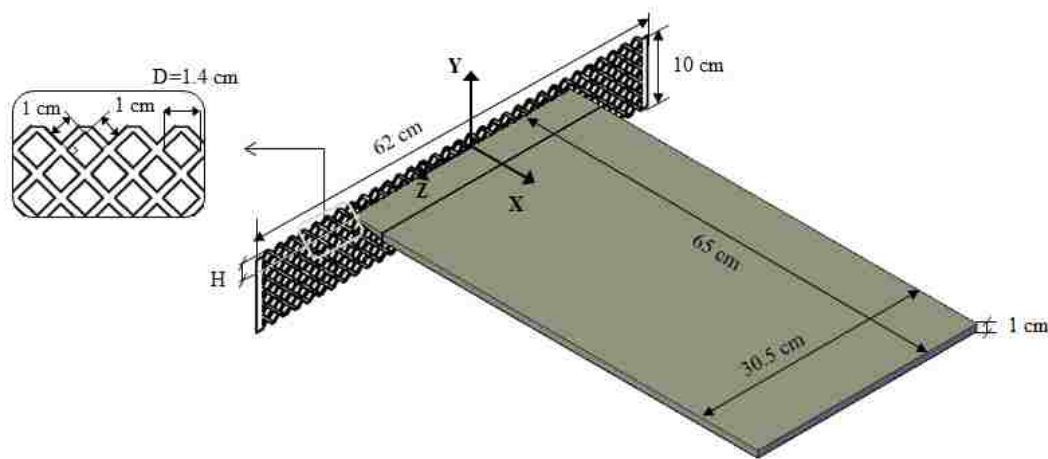


Figure A.1 Schematic of the experimental setup and the partial grid

As the smaller grid's height seems to be more effective in increasing the turbulence intensity and less flow blockage (see chapter 3 results), three different grids' heights ( $H = 1, 2$  and  $3$  cm) are chosen to be tested for the heat transfer part. Figure A.2 illustrates the heat transfer enhancement from the set-up at  $U_\infty = 4, 7.5$  and  $10$  m/s. As can be seen from  $H = 3$  cm to  $1$  cm, the Nusselt enhancement improves at all free stream velocities. This is supposed to be due to the lower flow blockage after the grid with lower height and also creating higher level of turbulence near the downstream surface. However, this grid seems to be just effective in terms of heat transfer augmentation at lower velocity where the based case flow over the surface at that velocity is laminar.

At  $H = 1$  cm, grid seems more like a discrete rib rather than a grid, thus in chapter 7 discrete ribs with different gap widths and heights are investigated.

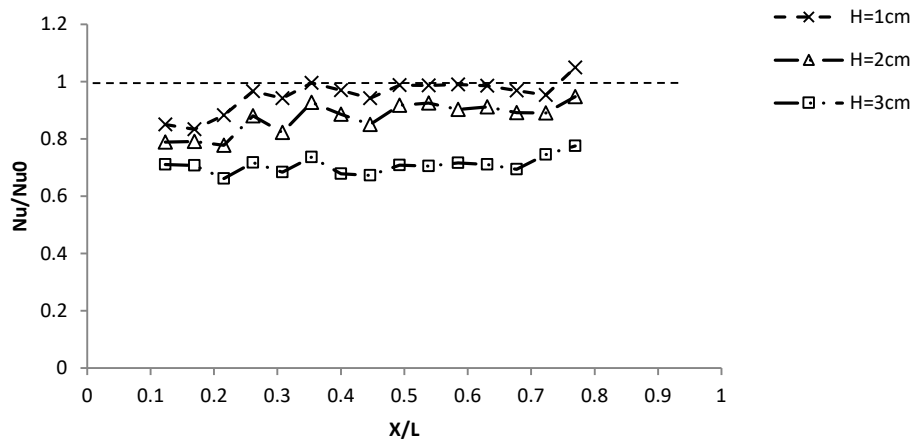
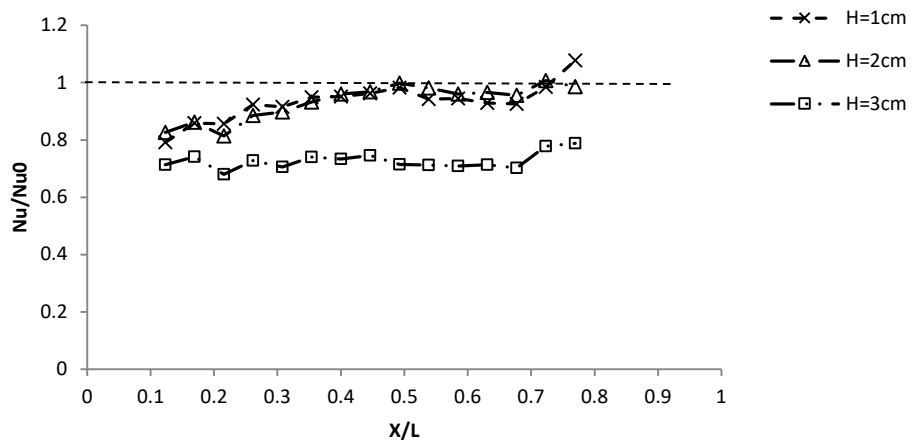
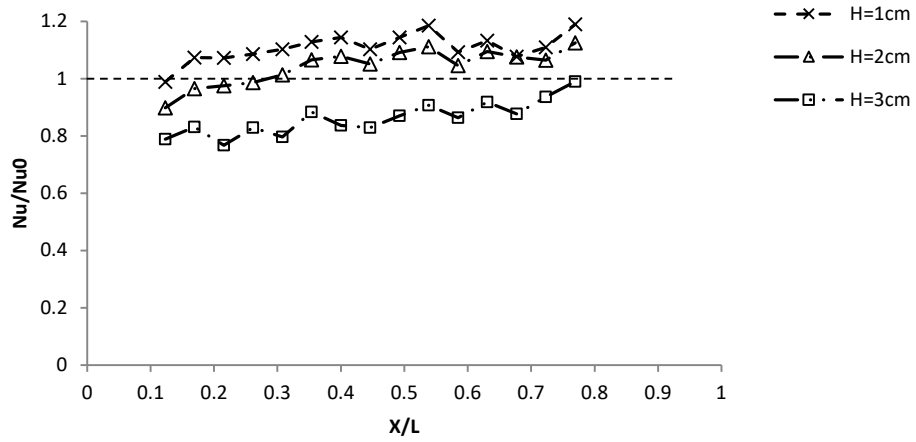


Figure A.2 Heat transfer enhancement after the partial grid with different heights and free stream velocities (a)  $U_\infty = 4$  m/s (b)  $U_\infty = 7.5$  m/s (c)  $U_\infty = 10$  m/s

Figure A. 3 presents the flow measurements result over the surface after the partial grid at height 2 cm,  $U_\infty = 4$  m/s and 5 different downstream locations ( $X/H = 4.25$  to 20).

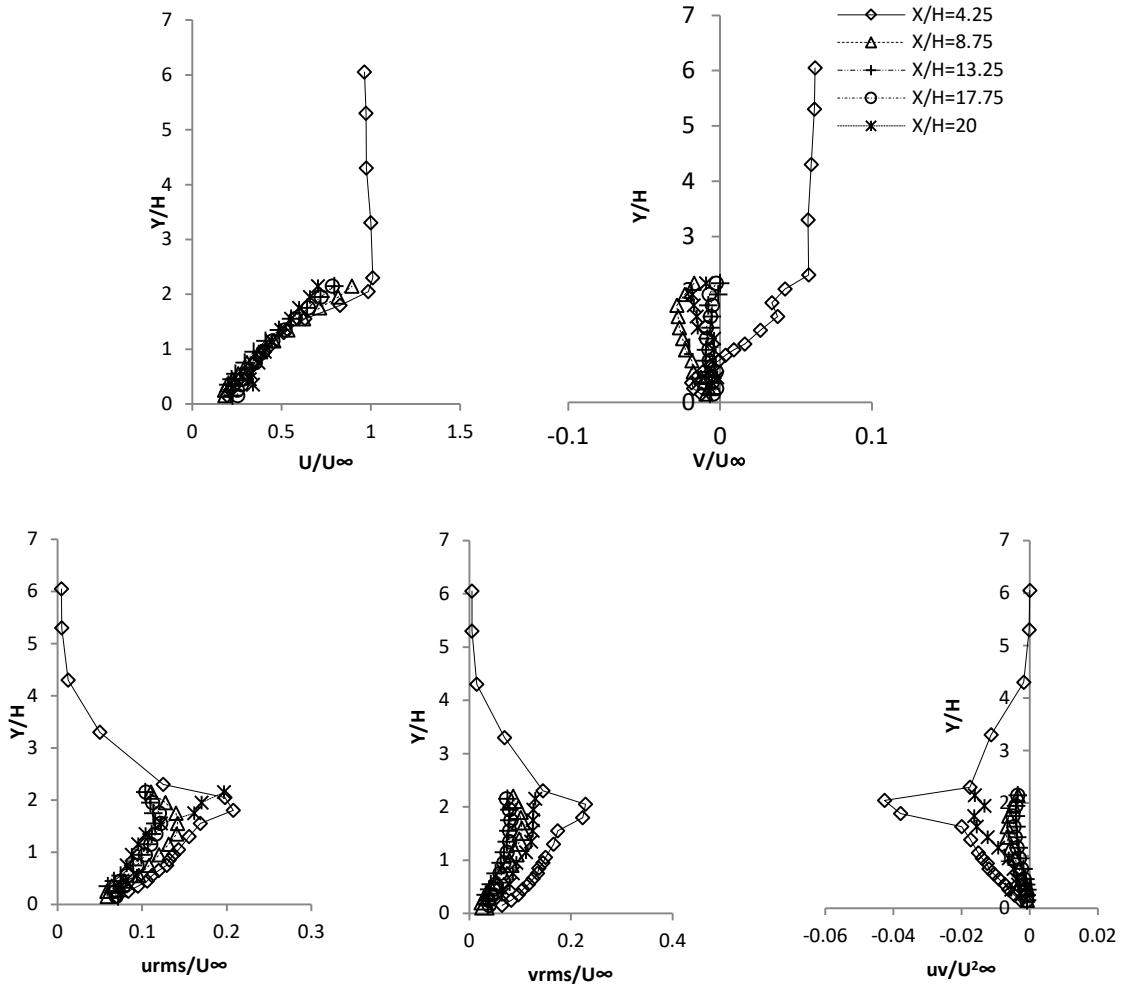


Figure A.3 Flow turbulence parameters after the partial grid with  $H = 2$  cm and  $U_\infty = 4$  m/s

A grid with different pattern has been also investigated. As depicted in Figure A.4, the oval-shaped grid with two different hole sizes was tested. The hole length in the small grid is 1.5 cm, while in the large one, it is 3 cm.

Figure A.5 depicts the heat transfer enhancement after these grids at three different heights ( $H = 0.5, 1.5$  and  $2.5$  cm) and  $7.5$  m/s free stream velocity. Apparently, the small grid is more effective in enhancing the heat transfer rate from the surface. Also as can be seen, from smaller to larger heights, the heat transfer enhancement decreases.

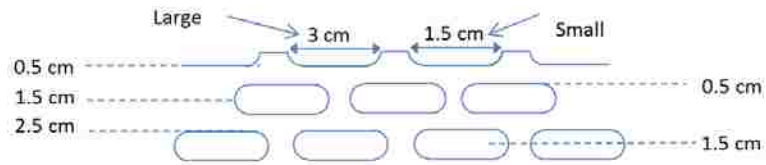


Figure A.4 Oval-shaped grid with two different small and large dimensions

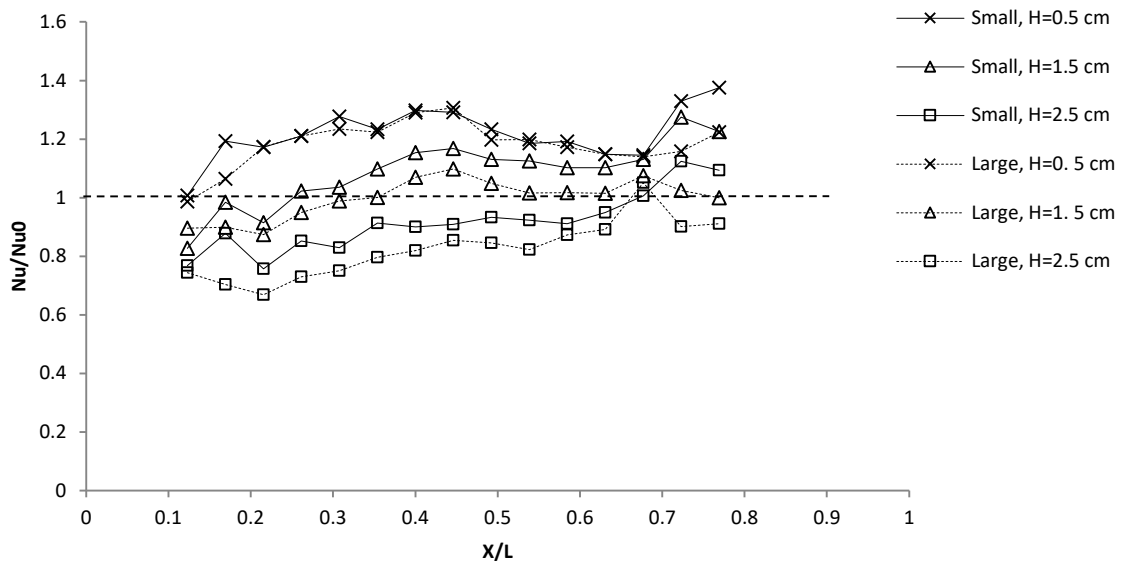


Figure A.5 Heat transfer enhancement after the oval-shaped partial grid with two different hole lengths (small = 1.5 cm and Large = 3 cm) and different heights at  $U_{\infty} = 7.5$  m/s

## Appendix B. Uncertainty Analysis

Some details of uncertainty analysis are explained below.

### **B.1. Velocity Measurements Uncertainty**

The uncertainty in velocity measurements consists of bias and precision uncertainties.

**Bias or systematic uncertainty** in instantaneous velocity ( $U_i$ ) measured by hotwire was estimated based on the information provided by Dantec Company [1] as follows (the uncertainty a parameter is labeled “ $U_{\text{parameter}}$ ”):

**-Calibrator uncertainty:**

$$U_{U_i \text{Calibration}} \cong 1\% U_i \quad (\text{B.1})$$

**-Data acquisition uncertainty:**  $\frac{1}{2}$  of the resolution of the A/D board.

The A/D board used in this work is 12-bit, which leads to a resolution of  $2^{12}$ . As the maximum output voltage is 10 volts, the total uncertainty of the output voltage can be written as:

$$U_{E_i} = \pm \left(\frac{1}{2}\right) \times 10 \times 2^{-12} = 0.0012 \text{ V} \quad (\text{B.2})$$

$E_i$  is the measured voltage by the hotwire.

The uncertainty of digitalized hot-wire output would be:

$$U_{U_i \text{Acquisition}} = U_{E_i} \times \frac{\partial U_i}{\partial E_i} = 0.0012 \times (C_1 + 2C_2 E_i + 3C_3 E_i^2 + 4C_4 E_i^3) \quad (\text{B.3})$$

**-Data reduction uncertainty** is due to curve fitting and calculation truncation. The linearization relative standard uncertainty of the input data in a hot-wire anemometer is around 0.5% [1]. The uncertainty of the post processing of the data by MATLAB code is assumed to be negligible.

$$U_{U_i, \text{Data reduction}} \cong U_{U_i, \text{linearization}} \cong 0.5\% U_i \quad (\text{B.4})$$

So, the estimated systematic uncertainty (bias) for the instantaneous velocity ( $U_i$ ) is:

$$U_{U_i} = \sqrt{0.000125 U_i^2 + [0.0012 \times (C_1 + 2C_2 E_i + 3C_3 E_i^2 + 4C_4 E_i^3)]^2} \quad (\text{B.5})$$

Mean local velocity ( $U$ ) [1]:



$$U = \frac{1}{N} \sum_{i=1}^N U_i \quad (\text{B.6})$$

where N is the number of samples.

Bias for the mean local velocity (U) [1]:

$$\begin{aligned} U_U &= \sqrt{\sum_{i=1}^N \left( \frac{\partial U}{\partial U_i} \times U_{U_i} \right)^2} = \sqrt{\sum_{i=1}^N \left( \frac{1}{N} \times U_{U_i} \right)^2} = \sqrt{\frac{1}{N^2} \times \sum_{i=1}^N (U_{U_i})^2} \\ &= \frac{1}{N} \times \sqrt{\sum_{i=1}^N (U_{U_i})^2} \end{aligned} \quad (\text{B.7})$$

A MATLAB code was written for calculating the systematic uncertainty at each point. The estimated systematic uncertainty (bias) in U for the 4m/s free stream velocity was  $10^{-4}$  m/s, which is a very small value.

Uncertainties related to experimental conditions and other effects such as human error are included in the precision error, which concerns the repeatability of the test. The experiment for some specific points was repeated and the precision uncertainty was estimated from Student's t distribution method with a 95% confidence interval [2].

The total uncertainty in velocity (U) and normalized velocity ( $U/U_\infty$ ) at point  $Y/H = 0.6$  in Figure B.1 (a) (4 m/s free stream velocity and  $X/H = 2$ ) were estimated to be around  $\pm 0.33$  m/s and  $\pm 0.02$ , mostly due to the precision uncertainty.

The uncertainty in the probe positioning is associated with the traverse system and the ruler that was used to place the hotwire at the measuring points. The traverse system resolution was very small and negligible ( $\sim 10^{-3}$  mm) and the ruler resolution was 1 mm. On the other hand, the major error involved is the human error which was estimated to be around 1 mm. So, the total uncertainty in probe positioning was estimated to be:

$$U_Y = \pm \sqrt{\left(\frac{10^{-3}}{2}\right)^2 + (0.5)^2 + (1)^2} = \pm 1.2 \text{ mm} \quad (\text{B.8})$$

This value was assumed to be the uncertainty in the boundary layer thickness as well. Boundary layer value was obtained by crossing the straight line of  $U/U_\infty = 0.99$  through the velocity profile curve, not based on the data points. Because the uncertainty value was very small compared to the symbols in the velocity graphs in the manuscript, error bars were not added. In the figure below, the uncertainty in  $U/U_\infty$  and  $\delta$  parameters can be observed clearly as error bars for the  $U_\infty = 9\text{m/s}$  case.

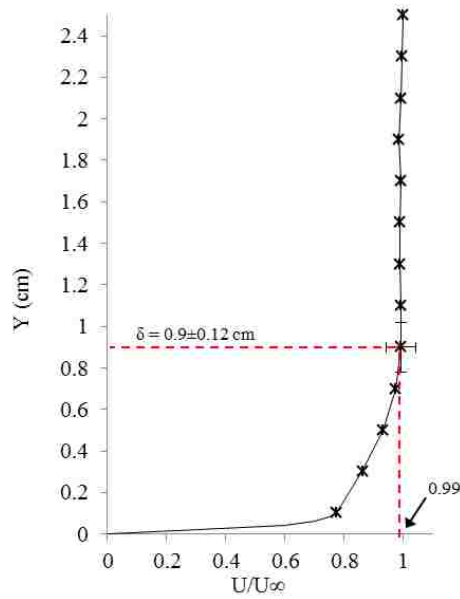


Figure B.1 Uncertainty in  $U/U_\infty$  and boundary layer thickness

### ***B.2. Heat Transfer Parameters Uncertainty***

As mentioned in the paper the total uncertainty in temperature was assumed to be just due to the thermocouples' bias (T-type thermocouple) as the precision uncertainty was observed to be much smaller than the bias. So, the total temperature measurement uncertainty was estimated to be around  $\pm 0.5K$ , which was the thermocouples' bias. Thus, the uncertainty in temperature difference was estimated to be:

$$U_{\Delta T} = \pm \sqrt{2 \times U_T^2} = \pm 0.7 K \quad (\text{B.9})$$

Uncertainty in the Nusselt number was calculated from the uncertainty in temperature difference ( $\pm 0.7K$ ) and streamwise location of the thermocouples. Furthermore, thermocouples were calibrated in three different environmental temperatures and the uncertainty in the temperature difference ( $U_{\Delta T}$ ) was estimated to be ( $\pm 0.2K$ ). The uncertainty in other heat transfer parameters is estimated from this uncertainty instead of the factory reported bias uncertainty in the temperature which is measured by thermocouples.

The uncertainty in the probe positioning is associated with the traverse system and the ruler that was used to place the hotwire at the measuring points. The traverse system resolution was very small and negligible ( $\sim 10^{-3}$  mm) and the ruler resolution was 1 mm. On the other hand, the major error involved is the human error which was estimated to be around 1 mm. So, the total uncertainty in probe positioning was estimated to be:

$$U_X = \pm \sqrt{\left(\frac{10^{-3}}{2}\right)^2 + (0.5)^2 + (1)^2} = \pm 1.2 \text{ mm} \quad (\text{B.10})$$

Uncertainty in heat transfer coefficient ( $U_h$ ):

$$h = \frac{k_{PTFE} \times \frac{T_{Tef,1} - T_{Tef,2}}{t}}{T_{Al} - T_{air}} = \frac{k_{PTFE} \times \frac{\Delta T_{Tef}}{t}}{\Delta T_{Al-air}} \quad (\text{B.11})$$

$$U_h = \sqrt{\left(\frac{\partial h}{\partial \Delta T_{Tef}} \times U_{\Delta T}\right)^2 + \left(\frac{\partial h}{\partial \Delta T_{Al-air}} \times U_{\Delta T}\right)^2} \quad (\text{B.12})$$

At almost high  $\Delta T_{Tef}$  ( $\Delta T_{Tef} = 6.7\text{K}$ ),  $\Delta T_{Al-air}$  is equal to 10.2K and the convection heat transfer coefficient and its uncertainty were estimated to be:

$$h = 54.7 \text{ (W/m}^2\text{K)} \quad (\text{B.13})$$

$$U_h = 2 \text{ (W/m}^2\text{K)} \quad (\text{B.14})$$

$$Nu = h \cdot X / k_{air} \quad (\text{B.15})$$

$$U_{Nu} = \sqrt{\left(\frac{\partial Nu}{\partial h} \times U_h\right)^2 + \left(\frac{\partial Nu}{\partial X} \times U_X\right)^2} = 21 \quad (\text{B.16})$$

$$U_{Nu/Nu_0} = \sqrt{\left(\frac{\partial Nu/Nu_0}{\partial Nu} \times U_{Nu}\right)^2 + \left(\frac{\partial Nu/Nu_0}{\partial Nu_0} \times U_{Nu_0}\right)^2} = 0.1 \quad (\text{B.17})$$

### References

[1] Jørgensen, F. E., 2002, "How to Measure Turbulence with Hot-Wire Anemometers - a Practical Guide," Dantec Dynamics, Skovlunde, Denmark

[2] Figliola, R.S. and Beasley, D.E., 2011, Theory and Design for Mechanical Measurements, 5th edition, John Wiley and Sons, Inc., New York, USA

## Appendix C. Air Flow Quality in the Wind Tunnel

To test the flow quality in the wind tunnel, the flow velocity was measured in an empty test section. Measurements were performed in a rectangular domain in the middle cross sectional area of the test section with 1000 measuring points at  $U_\infty \cong 7.8$  m/s. Figure C.1 demonstrates the results. The distance of the measurement domain from the side walls was 1.5 cm, and 0.5 cm and 1 cm from the bottom and top walls, respectively. The boundary layer thickness of the test section's walls was measured to be 2 ~ 2.5 cm. For the area outside the boundary layers, the velocity varied in the range of  $\pm 0.2$  m/s and turbulence intensity was measured to be from 0.18% to 0.38%.

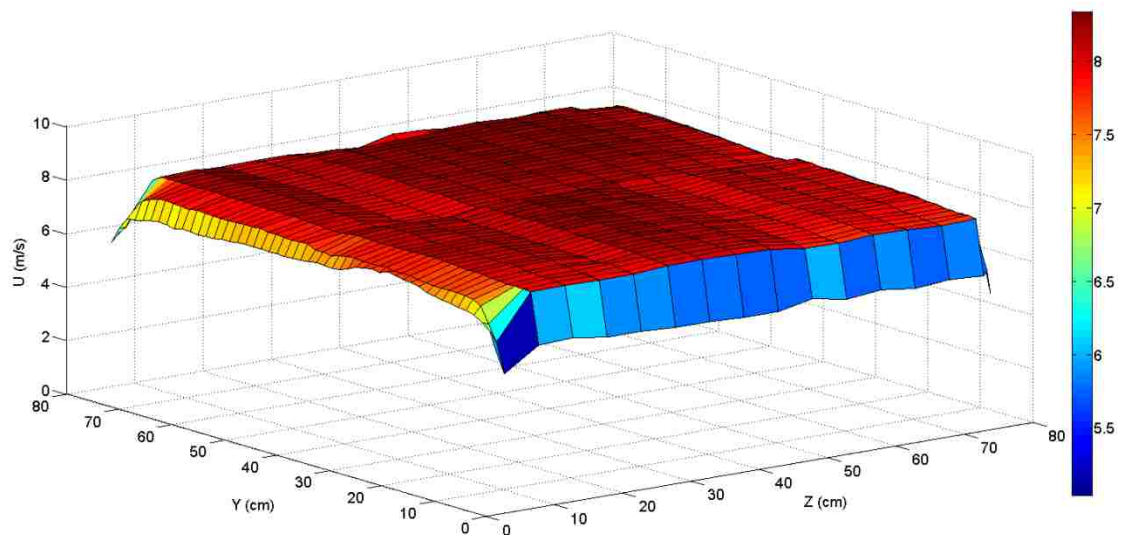


Figure C.1 Flow measurement in an empty wind tunnel test section

## Appendix D. Turbulent Flow behind a Partially Blocking Grid

### *D.1. Introduction*

Grid-generated turbulence has been the subject of numerous investigations for over seventy years. Generating a nearly-isotropic turbulence using a perforated plate in a wind tunnel was first introduced by Taylor in 1935 [1]. At a short distance from the grid, the turbulence is neither homogeneous, nor isotropic. It becomes homogeneous in the lateral direction and quasi isotropic after some distance downstream of the grid [2]. This region is the initial developing region which has been determined to range from  $10 \sim 15 D$  [2] to  $20 D$  [3]. However, it has been pointed out by many researchers [4-9] that, even at larger distances, grid-generated turbulence can deviate from an isotropic and homogenous state and the amount of this deviation varies from study to study. After this stage there are the initial and final decay regions where the turbulent kinetic energy decays downstream [3, 10, 11].

Conventional grid-generated turbulence has been discussed extensively in recent years. Murzyn and Be'lorgey [12] experimentally investigated the time and length scales of grid-generated turbulence occurring in a flume with a free surface flow. In Liu et al.'s study [13], homogeneous, nearly isotropic turbulence was experimentally produced using an orificed, perforated plate in a wind tunnel. Llor [14] studied the decay of homogeneous isotropic turbulence theoretically. Liberzon et al. [15] investigated the turbulent dissipation rate in a decaying grid turbulent flow using particle image velocimetry and laser Doppler velocimetry. George [16] reviewed the experimental, theoretical and numerical studies for the asymptotic effect of initial and upstream conditions on turbulence. Horender [17] discussed the turbulent flow downstream of a large-solidity (96%) perforated plate at 1m/s bulk velocity.

Except for one study [18], in all of these previous grid turbulence studies, the perforated plate covered the whole cross section of the wind tunnel. In Judd et al.'s study [18] a wind-tunnel experiment was conducted on the flow around a single or multiple porous windbreak of finite height that was sheltering a model plant canopy with a lower height. In their work, the experimental emphases were on the interactions of flow with the underlying plant canopy [18]. A grid partially blocking the middle of a larger wind tunnel, however, has not been investigated. The somewhat symmetrical flow over and under (and around the two sides of) a partial grid is of fundamental interest. Furthermore, it provides a baseline assessment of the turbulent flow over a flat plate downstream of a partial grid. The intention is that the grid will enhance the heat transfer from the flat plate.

### *D.2. Apparatus and Instrumentation*

The experiment was conducted in a closed loop wind tunnel with a 180 cm long test section (76 cm high and 77 cm wide). The maximum free stream velocity in the wind tunnel may be as high as 30 m/s when the test section is empty. The background turbulence level of the wind tunnel was measured to be less than 0.4%.

Figure D.1 presents an isometric view of the grid which was hung in the middle of the wind tunnel test section. The X, Y and Z directions are stream-wise, vertical and cross-flow, respectively, with

the base point located at the center of the perforated plate. The perforated plate was cut from an aluminum sheet of 0.3 cm thickness by a computer numerical controlled machine. The outside dimensions of the perforated plate were 10 cm x 62 cm. After cutting diamond-shaped holes with a diagonal distance (D) of 1.4 cm, the resulting solidity was 0.545.

The velocity at different points downstream of the perforated plate was measured using a 1-D boundary layer hot-wire probe (type 55P15) as part of a Dantec streamline 55C90 constant-temperature anemometer (CTA). The probe has a platinum-plated tungsten wire with a diameter of 5  $\mu\text{m}$  and a length of 1.25 mm. Signals were low-passed at 30 kHz and then sampled at 80 kHz over a period of approximately 25 s, resulting in  $2 \times 10^6$  data points per measurement. A 12-bit PCI-6071E National Instrument data acquisition card was used to convert the analog signals into digital data. A computer-controlled 2-D traverse system was used to position the probe at the specified location (Figure D.1). The traverse system can move crosswise (Z) in the test section and vertically (Y) with a 3.2 mm (0.125 inch) resolution.

Measurements were performed at 75 points in the Y direction from  $Y = -18.5$  to 18.5 cm ( $Y/D = -13.2$  to 13.2; every 0.5 cm) at  $Z = 0$  (Figure D.1) and repeated at three streamwise locations ( $X/D = 10, 20$  and 30). Tests were performed at 6 m/s free stream velocity.

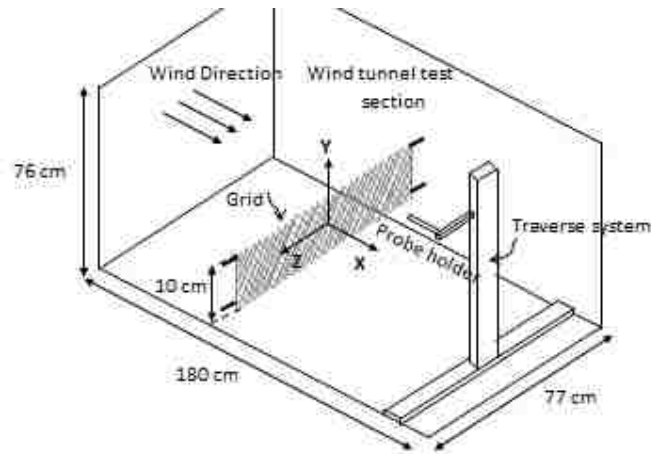


Figure D.1 Test section isometric

### ***D.3. Results and Discussion***

#### ***D.3.1. Velocity Profiles***

The overall flow behavior behind the grid can be detected from the streamwise velocity profiles. Figure D.2 shows the velocity profiles after a perforated plate at three different downstream distances. As can be seen, the perforated plate caused the flow to be retarded such that the velocity downstream of the grid was approximately one half the free stream value as expected due to the blockage effect of a 54% solidity ratio grid. This significant reduction in the flow velocity magnitude may not be a desirable outcome if our purpose is to enhance convection heat transfer of

a flat plate perpendicular to the grid. Nonetheless, the mean velocity reduction should be considered along with other heat transfer alteration parameters which were affected, such as the turbulence intensity and length scale. Two shear layers at the edges of the perforated plate ( $Y \approx \pm 5$  cm) can be distinguished in these profiles. At  $X/D = 10$ , it can be seen that the velocity had its minimum value ( $\sim 3.3$  m/s) at  $Y = 0$ , increased slowly to almost constant values from  $Y = \pm 2.5$  to  $Y = \pm 5$  cm, and then the shear layers started at  $Y \approx \pm 5$  cm. At  $X/D = 20$  and  $30$  for the area behind the grid ( $-5 \text{ cm} \leq Y \leq 5 \text{ cm}$ ), the profile has smoother curvature but still has its minimum at  $Y = 0$ . The vertical growth of the shear layers with downstream distance can also be observed in these graphs. As can be seen, the shear layer started from the edges of the grid ( $Y \approx \pm 5$  cm) and extended to  $Y \approx \pm 7.5, 9.5$  and  $10.5$  cm in  $X/D = 10, 20$  and  $30$ , respectively.

The total uncertainty associated with each parameter consists of bias and precision uncertainties [19, 20]. Bias or systematic uncertainty of the hotwire-measured instantaneous velocities has been estimated according to Ref. [19]. Precision uncertainty, which concerns the repeatability of the test, has been derived from Student's  $t$  distribution method with a 95% confidence interval [20]. As a result, the uncertainty in velocity ( $U$ ) at point  $X/D = 10, Y = 0$  in Figure D.2 is estimated to be around  $\pm 0.3$  m/s, mostly due to the precision uncertainty.

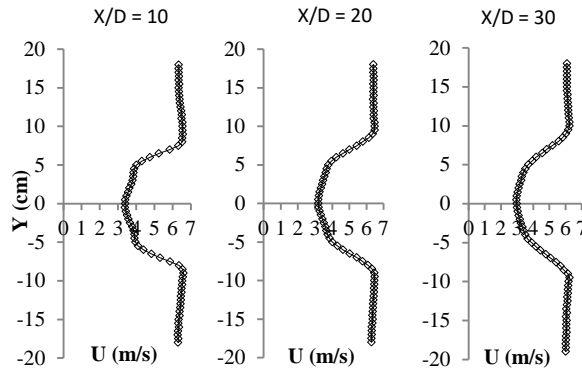


Figure D.2 Velocity profiles after grid

### D.3.2. Turbulence Intensity

Other than flow velocity, turbulence intensity is known to play an important role in convection heat transfer. It is defined as the normalized standard deviation, or root-mean-square (rms), of the velocity fluctuations [19]:

$$Tu = \frac{u'}{U_\infty} \quad (D.1)$$

where  $U_\infty$  is the free stream velocity; and  $u'$  is calculated from [19]:

$$u' = \sqrt{\sum_{i=1}^N \frac{(u - U)^2}{N - 1}} \quad (\text{D.2})$$

where  $u$  is the instantaneous velocity,  $U$  is the time-averaged velocity and  $N$  is the sampling size ( $2 \times 10^6$ ).

Figure D.3 illustrates the turbulence intensity profile after the grid at the same three downstream distances. As is seen,  $Tu$  had almost a constant value in the area behind the grid,  $-5 \text{ cm} \leq Y \leq 5 \text{ cm}$ . At the level of the grid edges ( $Y = \pm 5 \text{ cm}$ ),  $Tu$  increased drastically to a peak value and then decreased with almost the same slope to the free stream turbulence intensity ( $\sim 0.4\%$ ). By comparing these plots to the velocity profiles (Figure D.2), it can be seen that the turbulence intensity increase happened at the beginning of the perforated plate edge's shear layer ( $Y = \pm 5 \text{ cm}$ ), as it extended outward from  $Y = 5$ , reached a peak at  $Y$  around  $6.5 \sim 7.5 \text{ cm}$ , and approached the free stream's  $Tu$  at the farthest edge of the boundary layer. This illustrates significant turbulence generation around the edge of the perforated plate.  $Tu$  for the mid-grid area decayed from 4.5% to 2.5% to 1.6% at  $X/D = 10, 20$  and  $30$ , respectively. This appears similar to the normal decay of grid turbulence [21]. The corresponding peak  $Tu$  in the shear layers decreased from roughly 9% to 7.5% to 6.3%. The uncertainty in  $Tu$  for the point  $X/D = 10, Y = 0$  is around  $\pm 0.7\%$   $Tu$ .

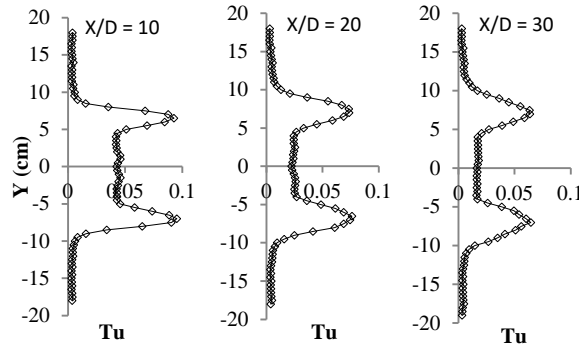


Figure D.3 Turbulence intensity profiles after grid

As was observed, the level of  $Tu$  resulting from the shear flow around the edge of the grid was much higher than that behind the grid itself. Also, it seems that this higher level of disturbances lasted quite far downstream. Thus, a low height perforated plate at the leading edge of a surface can generate a high degree of disturbance near the surface and may be very effective for enhancing the heat transfer.

### D.3.3. Turbulence Length Scales

Other than the fluctuation intensity, it is known that the turbulent length scales could also be effective parameters influencing momentum and heat transport [22,23]. The most relevant turbulence scales for any application are not obvious. As a first step, one large and one small



turbulent length scales were estimated. It is a common practice to pick the integral length scale to represent the large scale and the Taylor micro-scale to represent the smaller, dissipative eddies. For the detailed calculation procedure of the integral length scale and the Taylor micro-scale, see Ref. [24].

Figure D.4 presents the integral length scale profile at different downstream distances. Since the values of length scales,  $\Lambda$ , above the shear layer were ill-defined due to very low turbulence in the free stream, graphs are truncated beyond  $Y = \pm 8, 10.5$  and  $11.5$  cm for  $X/D = 10, 20$  and  $30$ , respectively. As can be seen, the integral length scale has a peak at  $Y = 0$  and decreased vertically upward and downward to a constant value at  $Y \cong \pm 1, 2$  and  $3$  cm for  $X/D = 10, 20$  and  $30$ , respectively, and remained at this value until reaching the outer edges of the shear layers. Within the shear layer where the velocity gradient is highest (see Figure D.2), the turbulence generation is at its maximum. Consequently,  $\Lambda$  is smallest and it increases as we move away (upward/downward) from this maximum shear regime. The general trend of increasing  $\Lambda$  with downstream distance confirms the decay of grid turbulence [4]. The unusually large increase in  $\Lambda$  around  $Y = 0$  seems to be resulted in part by the expanding wake behind the grid, allowing the “domain confined” larger length to expand, in addition to normal decay and negligible turbulence production because the local velocity gradient is nil. The uncertainty in integral length scale value is estimated to be around 0.3 cm.

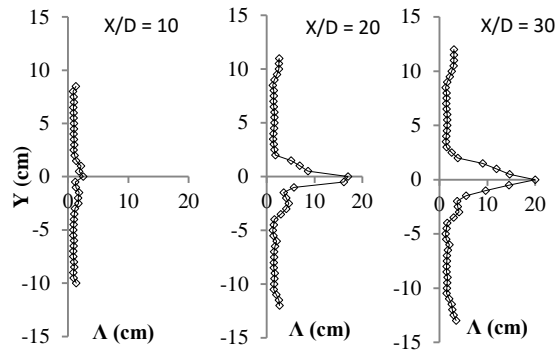


Figure D.4 Integral length scale profiles after grid

Taylor micro-scales at some specific points for different free stream distances were calculated and are shown in Figure D.5. Again, it can be seen that the graphs have a peak value at  $Y = 0$  cm but the difference between this value and the other points is not nearly as significant as that associated with the integral length. The peak values at  $Y = 0$  cm, were 0.55 cm, 0.74 cm and 0.85 cm at  $X/D = 10, 20$  and  $30$ , respectively, showing a general trend of increasing Taylor micro-scales with streamwise distance, which demonstrates the decaying trend of turbulence moving downstream.

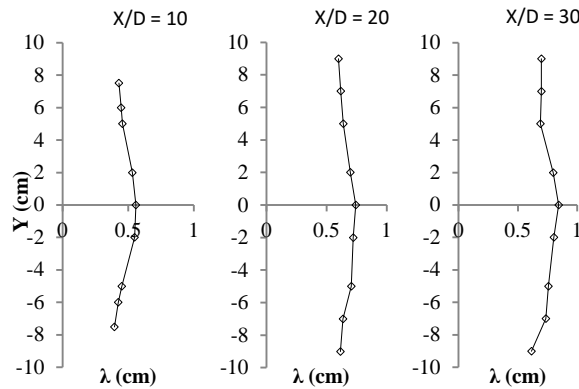


Figure D.5 Taylor micro-scale profiles after grid

#### ***D.4. Conclusions***

The flow downstream of a perforated plate (grid) partially blocking the middle of a wind tunnel test section has been studied to provide baseline data for enhancing the convection heat transfer via partial grid turbulence. The 54% solidity ratio grid retarded the flow to approximately 50% of its free stream value. The velocity profiles showed two shear layers at the grid edges. Significantly higher turbulence intensity and lower integral length and Taylor micro-scales distinguished the grid edges compared to the area behind the grid. These observations at the grid edge shear layers indicate great potential for furthering convection heat transfer enhancement well beyond grid turbulence

#### ***Acknowledgments***

This work was made possible by the Ontario Trillium Foundation and the Natural Sciences and Engineering Research Council of Canada.

#### ***References***

- [1] Taylor, G.I. 1935, "Statistical theory of turbulence," *Proc. R. Soc. London, Series A, Math. and Phys. Sci.*, 151, pp. 421–478
- [2] Hinze, J.O. 1975, *Turbulence*, 2nd edition, McGraw-Hill, New York, USA, ISBN 0-07-029037-7
- [3] Batchelor, G.K., and Townsend, A.A. 1948, "Decay of isotropic turbulence in the initial period," *Proc. R. Soc. London A.*, 193, pp. 539-558
- [4] Grant, H. L., and Nisbet, I.C.T. 1957, "The inhomogeneity of grid turbulence," *J. Fluid Mech.*, 2(3), pp. 263-272
- [5] Grant, H.L. 1958, "The large eddies of turbulent motion," *J. Fluid Mech.*, 4(2), pp. 149-190
- [6] Uberoi, M.S. 1963, "Energy transfer in isotropic turbulence," *Phys. Fluids*, 6(8), pp. 1048-1056
- [7] Uberoi, M.S., and Wallis, S. 1966, "Small axisymmetric contraction of grid turbulence," *J. Fluid Mech.*, 24(3), pp. 539-543

- [8] Comte-Bellot, G., and Corrsin, S. 1966, "The use of a contraction to improve the isotropy of grid-generated turbulence," *J. Fluid Mech.*, 25(4), pp. 657-682
- [9] Van Atta, C.W., and Chen, R. 1968, "Correlation measurements in grid turbulence using digital harmonic analysis," *J. Fluid Mech.*, 34(3), pp. 497-515
- [10] Batchelor, G.K. 1948, "Energy decay and self-preserving correlation functions in isotropic turbulence," *Quart. Appl. Math.*, 6, pp. 97-116
- [11] Batchelor, G.K., and Townsend, A.A. 1948, "Decay of isotropic turbulence in the final period," *Proc. R. Soc. London A.*, 194, pp. 527-543
- [12] Murzyn, F., and Bełorgey, M. 2005, "Experimental investigation of the grid-generated turbulence features in a free surface flow," *Exper. Thermal Fluid Sci.*, 29(8), pp. 925-935
- [13] Liu, R., Ting, D.S-K., and Checkel, M.D. 2007, "Constant Reynolds number turbulence downstream of an orificed perforated plate," *Exper. Thermal Fluid Sci.*, 31(8), pp. 897-908
- [14] Llor, A. 2011, "Langevin equation of big structure dynamics in turbulence: Landau's invariant in the decay of homogeneous isotropic turbulence," *Euro. J. Mechanics B/Fluids*, 30(5) pp. 480-504
- [15] Liberzon, A., Gurka, R., Sarathi, P., and Kopp, G.A. 2012, "Estimate of turbulent dissipation in a decaying grid turbulent flow," *Exper. Thermal Fluid Sci.*, 39, pp. 71-78
- [16] George, W.K. 2012, "Asymptotic effect of initial and upstream conditions on turbulence," *ASME J. Fluid Eng.*, 134(6), pp. 061203-1-27
- [17] Horender, S. 2013, "Turbulent flow downstream of a large solidity perforated plate: near-field characteristics of interacting jets," *Fluid Dyn. Res.*, 45(2), pp. 025501-1-22
- [18] Judd, M., Raupach, J.M.R., and Finnigan, J.J. 1996, "A wind tunnel study of turbulent flow around single and multiple windbreaks, Part I: Velocity Fields," *Boundary-Layer Meteorology*, 80, pp. 127-165
- [19] Jørgensen, F. E. 2002, "How to measure turbulence with hot-wire anemometers - a practical guide," Dantec Dynamics
- [20] Figliola, R.S., and Beasley, D.E. 2011, *Theory and Design for Mechanical Measurements*, 5th edition, John Wiley and Sons, Inc., New York, USA
- [21] Patten, N., Griffin, P., and Young, T.M. 2013, "Effects of freestream turbulence on the characteristics in the boundary layer near the transition onset location," *ASME J. Fluid Eng.*, 135(7), pp. 071203-1-9
- [22] Carullo, J. S., Nasir, S., Cress, R. D., Ng, W. F., Thole, K. A., Zhang, L. J., and Moon, H. K. 2011, "The effects of freestream turbulence, turbulence length scale, and exit Reynolds number on turbine blade heat transfer in a transonic cascade," *J. Turbomach.*, 133(1), pp. 011030-1-11

[23] Sak, C., Liu, R., Ting, D.S-K., and Rankin, G.W. 2007 “The role of turbulence length scale and turbulence intensity on forced convection from a heated horizontal circular cylinder,” *Exper. Thermal Fluid Sci.*, 31, pp. 279-289

[24] Fouladi, F., Henshaw, P., Ting, D. S.-K., 2015, “Turbulent flow over a flat plate downstream of a finite height perforated plate,” *ASME J. Fluid Eng.*, 137, 021203-1-12

## Appendix E. Wavelet Analysis OF Finite Height Grid Turbulence over a Flat Plate

### ***E.1. Introduction***

PV panels are one of the most promising renewable energy generation systems. However, a major problem of these systems is their low efficiency: 13-22% of the incident energy is converted into electricity, the balance being converted into heat [1]. The heat added to the PV panels leads to an increase in the PV cell temperature which has a negative effect on the system efficiency [2]. Several studies investigated the passive and active cooling of PV panels. In most of these studies the effect of wind velocity on the heat transfer coefficient has been investigated and attempts were made to find an appropriate relation for convection heat transfer as a function of the wind velocity [3-7] In these outdoor studies, however, the individual effects of the various turbulence characteristics of natural wind on the convective heat transfer were lumped together under turbulence intensity and not systematically sorted out [3]. On the other hand, various turbulence parameters have been proven to have great influences on the heat transfer rate from surfaces [8, 9].

Passive PV cooling can, in theory, be augmented by mounting a perforated plate (grid) upstream of the PV module. Flow after the grid would be turbulent, which is supposed to enhance the heat transfer from the flat plate. Flow-induced turbulence has been studied experimentally since the 1930s. Taylor [10] was the first one who reported generating nearly-isotropic turbulence using a perforated plate in a wind tunnel; Batchelor [11], Batchelor and Townsend [12, 13] and Hinze [14] also studied post-grid turbulence and the decay of the turbulent energy. In recent years, grid turbulence has been investigated in several studies [15-18].

In almost all of the mentioned studies, the grid covered the total cross section of the wind tunnel. In this study, the grid has a finite height to simulate a more likely situation for PV panels. The partial grid at the leading edge of the plate may cause a secondary flow or intermittent vortex shedding which would be useful in scouring a swath of warmed-up fluid out of the downstream boundary layer.

Fourier and wavelet transforms are two useful tools to show the details of sizes and decay of eddies in this study. The corresponding fluctuation distribution will assist in better fundamental understanding of the influence of the grid's edge on an otherwise conventional grid turbulence study.

### ***E.2. Wavelet Fundamentals***

In recent years, the wavelet transform has been used in a wide variety of applications in the study of non-linear and intermittent phenomena, where Fourier spectral analysis is not suitable. The Fourier spectrum represents the energy distribution of the signal in the frequency domain and is estimated over the entire time interval. On the other hand, wavelet analysis decomposes a time series over a time frequency space, thus providing power distribution visualization along time and frequency, yielding an enhancement over Fourier analysis [19]. In 1992, Farge [20] used wavelet analysis for coherent structures in turbulent flows. After that, it has been utilized in a wide range of turbulence studies, a few of which are mentioned here. In 1999, Mouri et al. [21] performed wavelet analyses on velocities in laboratory isotropic turbulence.

### E.3. Experimental Methodology

The experiment was conducted in a closed loop wind tunnel with a 180 cm long test section (76 cm high and 77 cm wide). The maximum free stream velocity in the wind tunnel may be as high as 30 m/s when the test section is empty. The background turbulence level of the wind tunnel was measured to be less than 0.4%.

The experimental setup consists of a flat plate with a vertical perforated plate (grid) mounted normal to the flow, at the leading edge of the flat plate. Figure E.1 presents an isometric view of the flat plate and perforated plate. The X, Y and Z directions are stream-wise, normal to the flat plate (vertical) and cross-flow, respectively, with the base point located at the center of the leading edge of the flat plate. The perforated plate was cut from an aluminum plate of 0.3 cm thickness by a computer numerical controlled machine. The outside dimensions of the perforated plate were 16 cm x 62 cm. After cutting diamond-shaped holes with a diagonal distance (D) of 1.4 cm, the resulting solidity was 0.545.

The flat plate is a 1.5 mm thick aluminum plate with dimensions of 33.5 cm (width) x 52.5 cm (length) laminated on a 0.2 cm layer of carbon fiber over a 2 cm layer of wood, bringing the total thickness to 3.7 cm. A wooden wedge with a 21° bevel was attached to the main wood piece to reduce the effect of the blunt leading edge. The flat plate was placed at half height and in the middle of the test section. Figure 2 shows the test section and setup isometric.

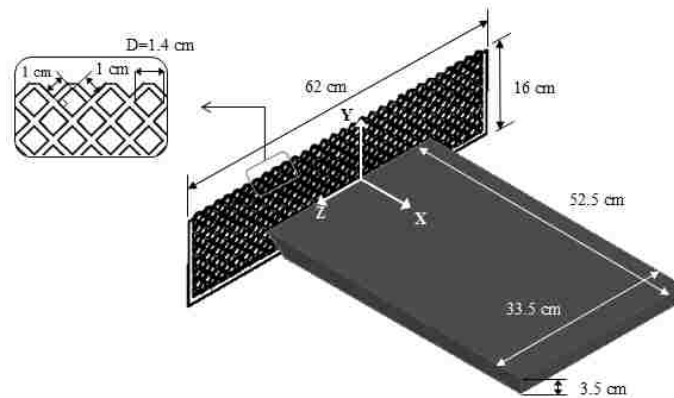


Figure E.1 Flat plate and perforated plate isometric

The velocity at different points downstream of the perforated plate was measured using a 1-D boundary layer hot-wire probe (type 55P15) as part of a Dantec streamline 55C90 constant-temperature anemometer (CTA). The probe has a platinum-plated tungsten wire with a diameter of 5  $\mu\text{m}$  and a length of 1.25 mm. Signals were sampled at 20 kHz over a period of around 6.5 s, resulting in 130,000 data points per measurement. A 12-bit PCI-6071E National Instrument data acquisition card was used to convert the analog signals into digital data. A computer-controlled 2-D traverse system was used to position the probe at the specified location (Figure E.2). The traverse

system can move through the crosswise direction of the test section (Z) and in the normal direction to the plate (Y) with a 3.2 mm (0.125 inch) resolution.

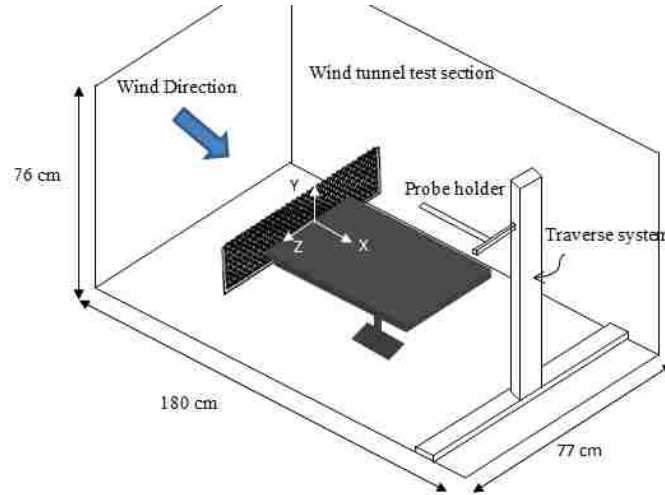


Figure E.2 Test section isometric

Measurements were performed at 50 points in the Y direction at  $Z = 0$  (Figure E.1) and repeated at three streamwise locations ( $X/D = 10, 20$  and  $30$ ). Tests were performed at 4.5 m/s free stream velocity, resulting in a Reynolds number at the end of the flat plate ( $Re_L$ ) of  $1.5 \times 10^5$ , which indicates that the flow over an ideal smooth flat plate would be laminar [23].

### ***E.3.1. Turbulence Velocity***

Local velocity is the time average of the instantaneous velocities at that point [24]:

$$U = \frac{1}{N} \sum_{i=1}^N U_i \quad (\text{E.1})$$

where  $N$  is the number of instantaneous measurements ( $N = 10^6$ ).

Velocity fluctuation is defined as:

$$u_i = U_i - U \quad (\text{E.2})$$

where  $U$  is the local velocity and  $U_i$  is the instantaneous velocity.

The intensity of the velocity fluctuations is typically quantified in terms of the turbulence intensity:

$$Tu = \frac{u_i}{U_\infty} \quad (\text{E.3})$$

### ***E.3.2. Fourier transform***

The Fourier transform of a function  $x(t)$  is [19]:

$$x(f) = \frac{1}{2\pi} \sum_0^T x(t)e^{-ift} \quad (\text{E.4})$$

where  $t$  and  $f$  are time and frequency, respectively. The Fourier spectrum, which is defined as follows, demonstrates the distribution of the energy of the signal in the frequency domain and is estimated over the entire area:

$$P_{xx}(f) = |x(f)|^2 \quad (\text{E.5})$$

where  $f$  is the frequency.

### ***E.4. Wavelet transform***

Continuous wavelet transform of a function  $x(t)$  is:

$$W_x(a, b) = \int x(t)\psi_{a,b}(t)dt \quad (\text{E.6})$$

where the parameters  $a$  and  $b$  are scale and position respectively, and  $\psi_{a,b}(t)$  is the wavelet function [19]. The scale parameter is related to the frequency while the position parameter is related to the time.

The wavelet spectrum is defined as:

$$P_{xx}(a, b) = |W_x(a, b)|^2 \quad (\text{E.7})$$

The wavelet spectrum gives the energy which is related to each time and frequency [19].

The discrete wavelet transform, which is defined as a sub-sample of the continuous wavelet, decomposes the signal into decomposition levels [25]:

$$D(j, k) = \sum x(t) \psi_{j,k}(t) \quad (\text{E.8})$$

where  $j$  and  $k$  are the level and position coefficient, which are dyadic sub-samples of  $a$  and  $b$  in continuous wavelet analysis [25]:

$$a = 2^j, b = k \cdot 2^j \quad (\text{E.9})$$

At each level the approximations are the high-scale, low frequency components of the signal while the details are the low-scale, high frequency components [26].

The discrete wavelet spectrum is given by [27]:



$$P_{xx}(j, k) = |D(j, k)|^2 \quad (\text{E.10})$$

The pseudo frequency corresponding to each decomposition level is calculated as follows [27]:

$$F_a = \frac{F_c}{a \cdot \Delta} \quad (\text{E.11})$$

where  $a$  is the scale,  $\Delta$  is sampling period,  $F_c$  is the center frequency of wavelet.

Different wavelet functions have been applied to the turbulence velocity signals. The Daubechies Basis Wavelet (db7) function was chosen to be used since it presented the trend of the signal more clearly than other wavelet functions and it has been proven to be appropriate for application in a variety of turbulence studies [19, 21]. Analysis was performed on the velocity fluctuation signal of four different points behind the grid:  $X/D = 10$  and  $20$ ,  $Y = 5.7$  cm and  $10.7$  cm. Continuous wavelet analysis has been performed from scale 0 to 512 which corresponds to the frequency range 13846 to 27.05 Hz. Discrete wavelet transform was performed to level 9. The range of the frequencies for the approximation and detail levels of the discrete wavelet analysis which are calculated from Eq. (11) can be seen in Table 1:

Table. E.1. Frequency range of different levels of discrete wavelet analysis  
Approximation Frequency (Hz) Detail Frequency (Hz)

Approximation	Frequency (Hz)	Detail	Frequency (Hz)
A1	0 ~ 6923	D1	6923 ~ 13846
A2	0 ~ 3461.5	D2	3461.5 ~ 6923
A3	0 ~ 1730.7	D3	1730.7 ~ 3461.5
A4	0 ~ 865.4	D4	865.4 ~ 1730.7
A5	0 ~ 432.7	D5	432.7 ~ 865.4
A6	0 ~ 216.3	D6	216.3 ~ 432.7
A7	0 ~ 108.2	D7	108.2 ~ 216.3
A8	0 ~ 54.1	D8	54.1 ~ 108.2

A9	0 ~ 27.05	D9	27.05 ~ 54.1
----	-----------	----	--------------

## E.5. Results and Discussion

### E.5.1. Velocity Profile

Velocity profiles of the flow after the perforated plate at three downstream distances are shown in Figure E.3. As can be seen, flow after the perforated plate experiences two boundary layers: one at the flat plate surface and the other one at the upper edge of the grid ( $Y = 10.7$  cm). These two boundary layers grow as the flow progresses downstream. The uncertainty associated with each parameter is shown as error bars for a single point in the graphs (Figures E.3 (a) and E.4 (a)). This is the total uncertainty which consists of bias and precision uncertainties [28]. As shown in Figure E.3 (a), the uncertainty in velocity at point  $Y=9.2$  cm (4.5 m/s free stream velocity and  $X/D=10$ ) is calculated to be roughly  $\pm 0.3$  m/s, which is mainly because of the precision uncertainty. In addition, the hot-wire position uncertainty in the normal direction ( $Y$ ) is estimated to be around 2 mm.

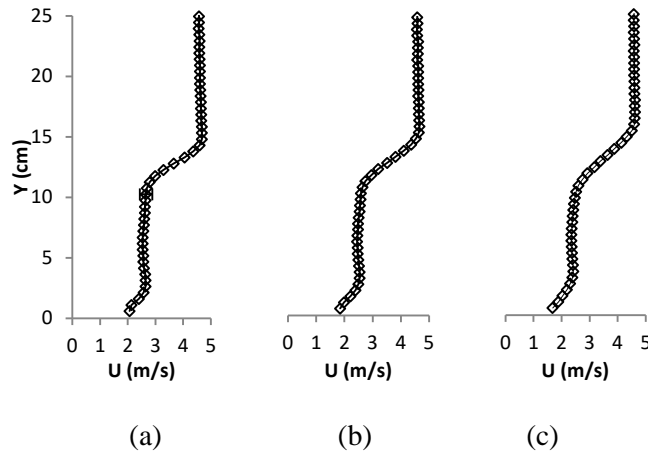


Figure E.3 Velocity Profile at 4.5 m/s free stream velocity for: (a)  $X/D = 10$ , (b)  $X/D = 20$ , and (c)  $X/D = 30$

### E.5.2. Turbulence Intensity

Figure E.4 demonstrates the turbulence intensity profile at three different downstream distances. As can be seen, turbulence intensity is higher near the wall surface (around 5%) and decreases to an almost constant value in front of the grid. At the edge of the grid suddenly it increases to a high value (around 10%) and then drops to the free stream turbulence intensity which is less than 4%. It can be observed that, for the area behind the grid (until 11 cm), turbulence intensity behaves just like conventional (full height) grid turbulence and decreases with downstream distance, which demonstrates the decay of the turbulence. But downstream of the edge of the grid the same trend is not observed. Two points ( $Y = 5.7$  and  $10.7$  cm) at two downstream distances ( $X/D = 10$  and  $30$ )

were chosen to study the effect of the grid's edge and also the downstream distance on the turbulence. As can be seen Figure 4 at the level of  $Y = 5.7$  cm,  $Tu$  for  $X/D = 10$  is 3.3% and for  $X/D = 30$ , it is around 1.7%. At the level  $Y = 10.7$  cm at  $X/D = 10$ ,  $Tu$  is 3.8% and downstream increases very slightly to a value of 3.9%. Thus, the points at the height of the edge of the grid do not experience a decay of turbulent kinetic energy. Also, from  $Y = 5.7$  to  $Y = 1.7$  cm,  $Tu$  increases at both free stream distances, but more significantly for  $X/D = 30$ . The relative uncertainty for a specific point ( $Y = 7.2$  cm) is shown in Figure E.4 ( $X/D = 10$ ), which is around  $\pm 0.7\%$ .

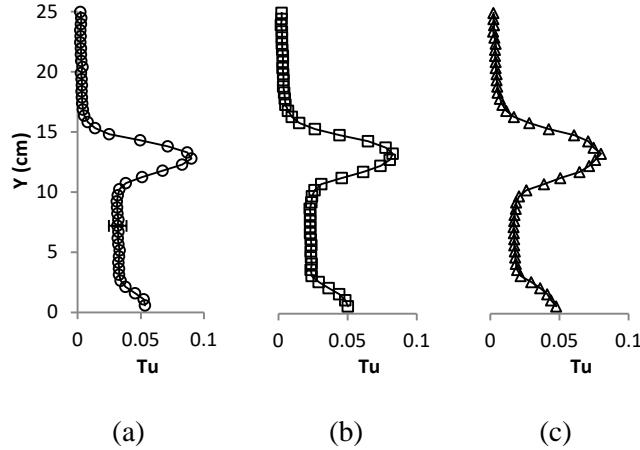


Figure E.4 Turbulence intensity at 4.5 m/s free stream velocity, the circles signify  $X/D = 10$  cm, the squares  $X/D = 20$  cm, and the triangles  $X/D = 30$  cm

### E.5.3. Fourier Transform

Figure E.5 shows the results of Fast Fourier Transform (FFT) analysis of the fluctuation velocities at  $X/D = 10$  at points  $Y = 5.7$  and  $10.7$  cm. The energy of the fluctuation signal at low frequency is high and it decreases as the frequency increases. This indicates that large eddies possess most of the energy of the turbulence. Also it can be observed that the energy of the signal is higher at  $Y = 10.7$  cm than  $Y = 5.7$  cm at almost all frequency ranges. This indicates that turbulence is higher at the edge of the grid than behind the grid. The same result can be seen in  $Tu$  (Figure 4) for  $X/D = 10$ , where the turbulence intensity at the point  $Y = 10.7$  cm is slightly higher than at  $Y = 5.7$  cm.

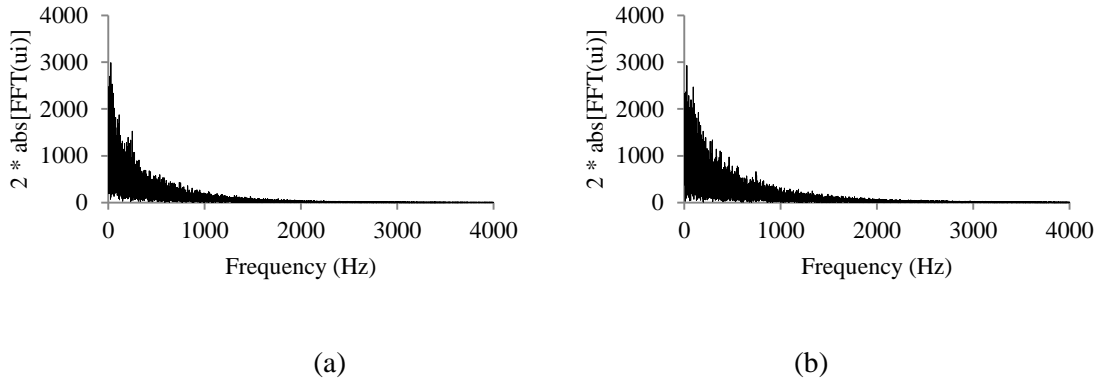


Figure E.5 Fourier transform for the points  $X/D = 10$  (a)  $Y = 5.7$  cm (b)  $Y = 10.7$  cm

Figure E.6 presents the fast Fourier transform for  $X/D = 30$  and points  $Y = 5.7$  and  $10.7$  cm. Again, it can be observed that the energy of the signal at all ranges of the frequencies (eddies) is higher at  $Y = 10.7$  cm, but the difference is more significant for these two points. Comparing Figures E.5 and E.6 shows that point  $X/D = 30$ ,  $Y = 5.7$  cm possesses the lowest level of the energy among these points, which can also be seen in turbulence intensity graph (Figure E.4). Also, at the level  $Y = 5.7$  cm from  $X/D = 10$  to  $30$ , it is observed that the signal's energy in all frequency ranges decreases, which indicates the decay of the turbulence. In Figure E.6 (a) it is also seen that above  $2500$  Hz, the energy of the signal is almost zero. This may suggest that that even the very small eddies are dissipated at this point. At level  $Y = 10.7$  cm, Figure E.6 (b) does not show the same trend at all frequencies: at very low frequencies (less than  $100$  Hz, very large eddies) the energy increases from  $X/D = 10$  to  $30$ , and above this frequency, it decreases slightly downstream. So, decay of the turbulence at the level of the grid's height happens only for eddies with frequencies higher than  $100$  Hz.

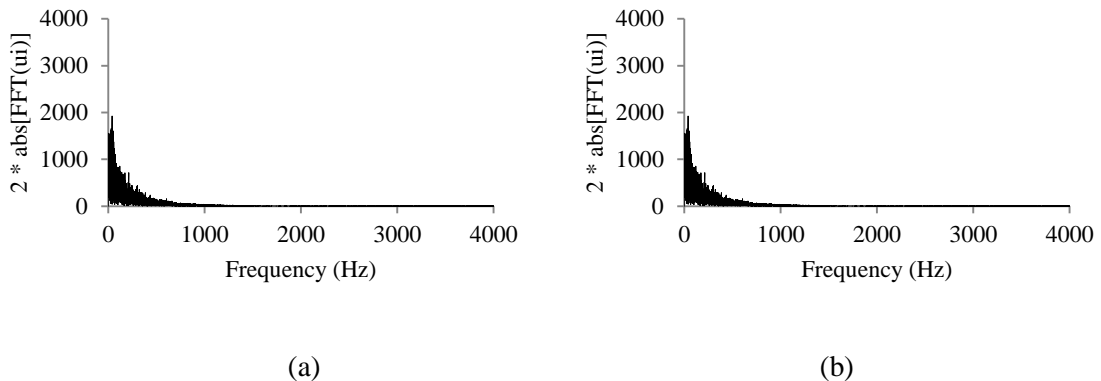
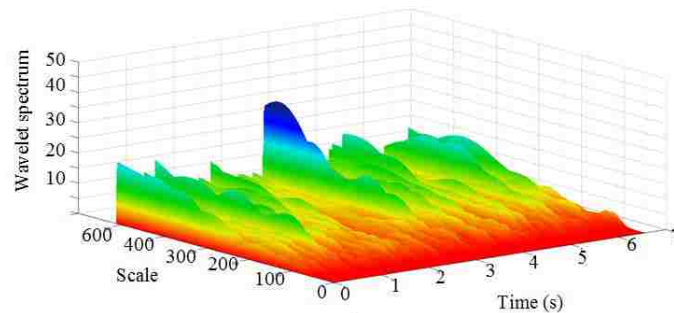


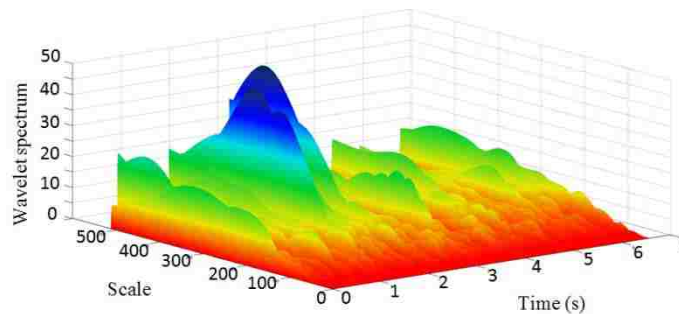
Figure E.6 Fourier transform for the points  $X/D = 30$  (a)  $Y = 5.7$  cm (b)  $Y = 10.7$  cm

#### ***E.5.4. Wavelet Analysis***

Figure E.7 presents the continuous wavelet spectra for  $X/D = 10$  and points  $Y = 5.7$  and  $Y = 10.7$  cm computed according to Equation (E.4) over time and frequency (scale). In these graphs, the frequency range of  $13846 \sim 54.1$  Hz corresponds to the scales  $0 \sim 512$ . It can be seen that for the ranges of very high frequencies (low scales) the level of activity is very low and as the frequency decreases the energy of the signal increases. Comparing these two graphs (Figures E.7 (a) and (b)) shows that at point  $Y = 10.7$  cm (edge of the grid), the signal indicates a little bit higher level of energy than at point  $Y = 5.7$  cm, which appears more significant for scales higher than 200 (very low frequencies:  $0 \sim 70$  Hz). At this range of frequencies, more peaks that have higher values can be observed. This shows that at the edge of the grid, eddies contain more kinetic energy. One other interesting observation from these two graphs is for both of these signals at low frequencies (high scales) the signal shows an intermittent, almost regular, behavior. This suggests that the distribution of the small eddies is more periodic than that of the large eddies.



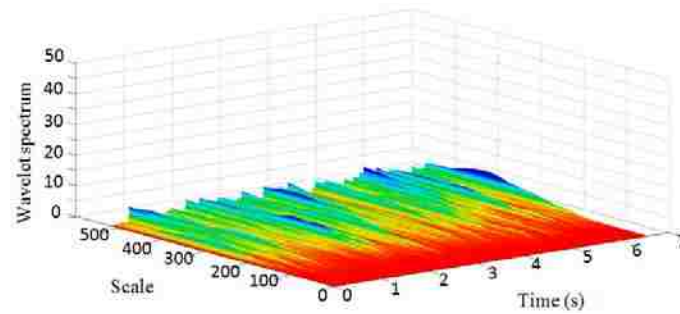
(a)



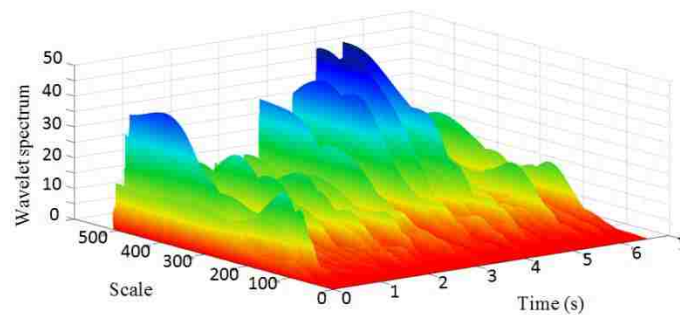
(b)

Figure E.7 Continues wavelet analysis for points  $X/D = 10$  and: (a)  $Y = 5.7$  cm (b)  $Y = 10.7$  cm, Frequency range:  $13746 - 27.05$  Hz

Figure E.8 presents the continuous wavelet spectra for  $X/D = 30$  and points  $Y = 5.7$  and  $Y = 10.7$  cm. Again it can be seen that at lower frequencies both signals contain more energy and have intermittent peaks. From  $Y = 5.7$  to  $10.7$  cm the level of the energy increases drastically at all of the frequency ranges.



(a)



(b)

Figure E.8 Continues wavelet analysis for point  $X/D = 30$  and: (a)  $Y = 5.7$  cm (b)  $Y = 10.7$  cm, Frequency range: 13746-27.05 Hz

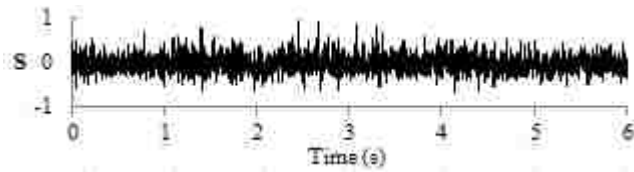
To see what does happen to the turbulence energy in a stream-wise direction, Figures E.7 (a) and E.8 (a) were compared and Figures E.7 (b) and E.8 (b) were compared. At level  $Y = 5.7$  cm for all frequency ranges, a significant decrease in energy level can be observed moving downstream from  $X/D = 10$  to  $30$ . The same result was seen in the Fourier transform analysis. For height  $Y = 10.7$  cm, the energy level seems to increase from  $X/D = 10$  to  $30$  at scales more than 100 (frequencies lower than 137 Hz).  $X/D = 30$  demonstrates more and higher peaks. Below this scale, the trend in the signal's energy is not clear.

Discrete wavelet transform has also been performed on these four points. Figure E.9 presents the results for the point  $Y = 10.7$  cm at  $X/D = 10$ , for 9 levels (with arbitrary scales). Figure E.9 (a) shows the original signal for the 6 s duration, while E.9 (b) and (c) present the approximation and detail levels of the discrete wavelet analysis respectively. The frequency ranges corresponding to each level have been shown in Table E.1. At each level the approximation covers the low part and

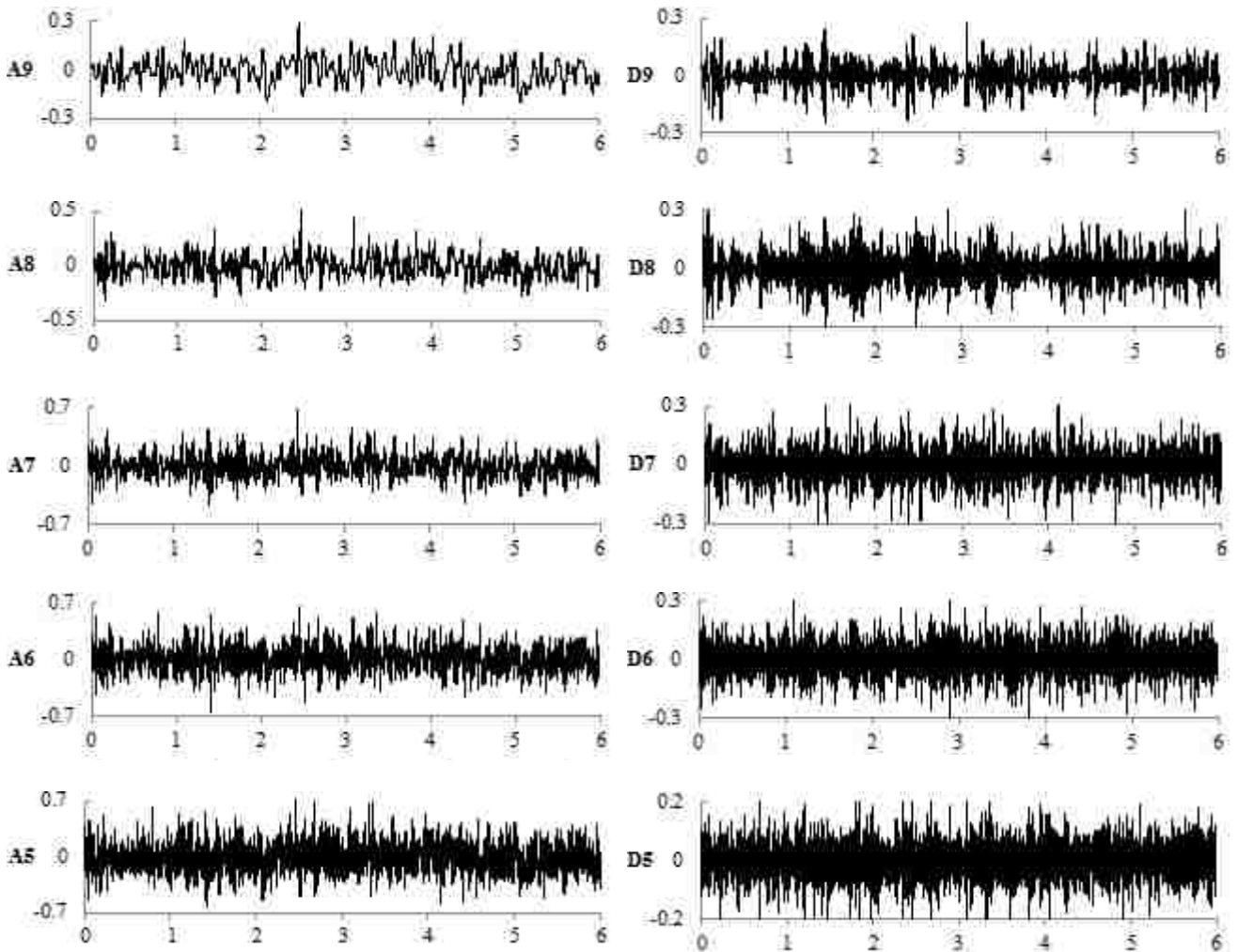
the detail covers the high part in the range of frequency. As observed, Figure E.9 (b) approximation level 1 (A1), with a frequency range of 0 to 6923 Hz, is very close to the original signal. While approximation level 9 (A9, 0 ~ 27.05 Hz) has fewer fluctuations and represents more clearly the overall trend of the signal.

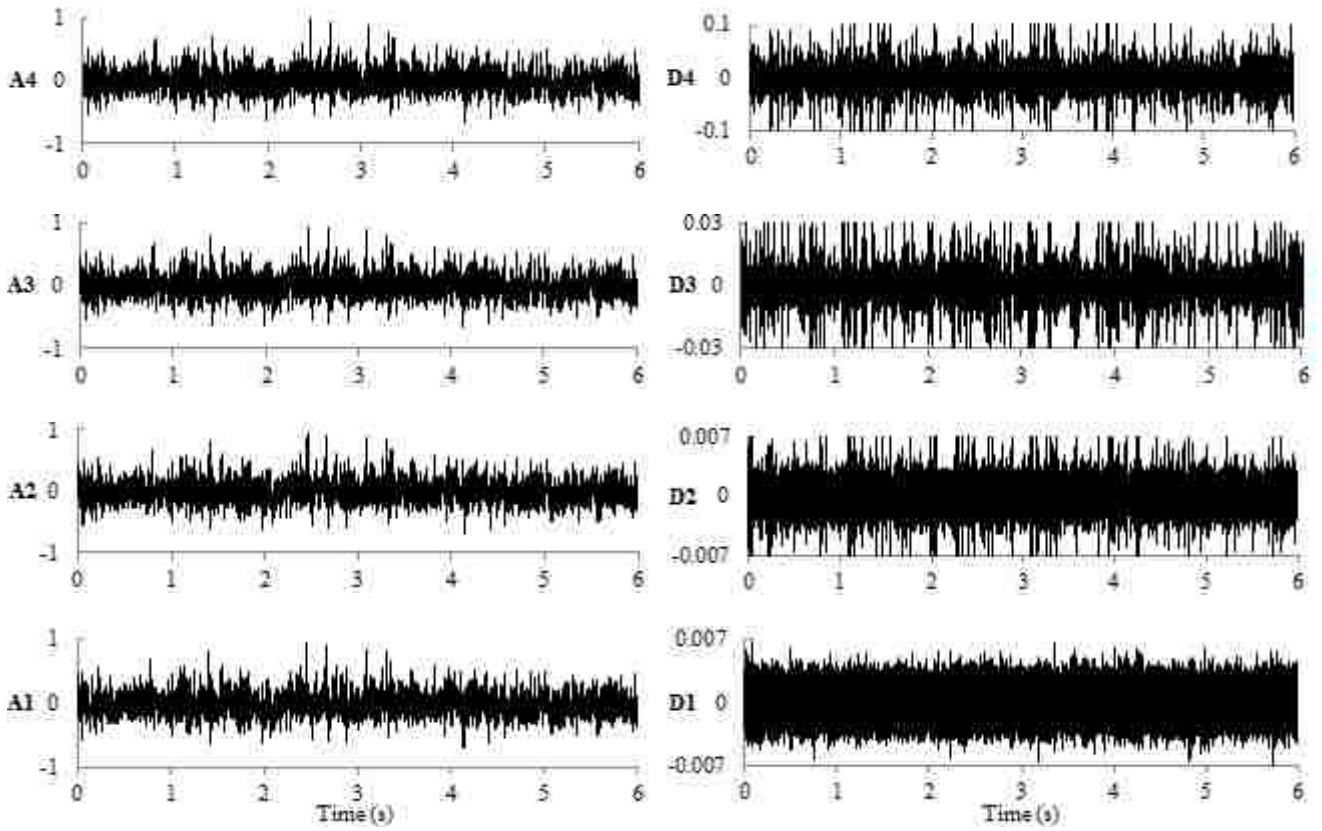
For details (Figure E.9 (c)), it can be seen that going from D1 (frequency 6923 ~ 13846 Hz) to D9 (frequency 27.05 ~ 54.1 Hz), the signal appears to fluctuate less.

The original signal may be reconstructed from D1 to 9 and A1 (Figure E.10).



(a)

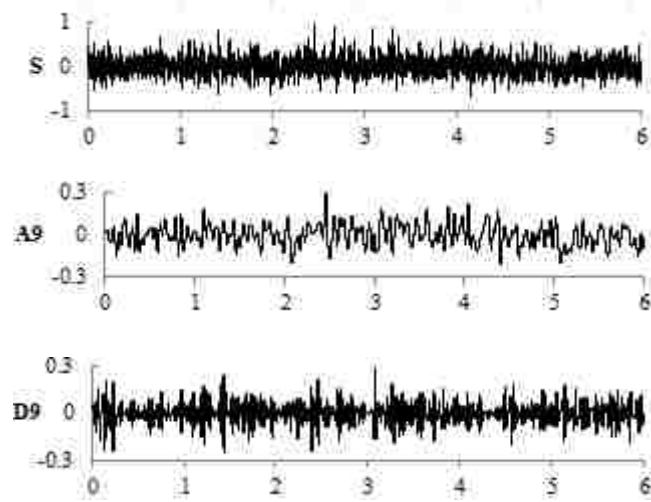




(b)

(c)

Figure E.9 Discrete wavelet analysis for point  $X/D = 10$  and  $Y = 5.7$  cm (a) original signal (b) approximation levels (A1-A9) (c) detail levels (D1-D9)





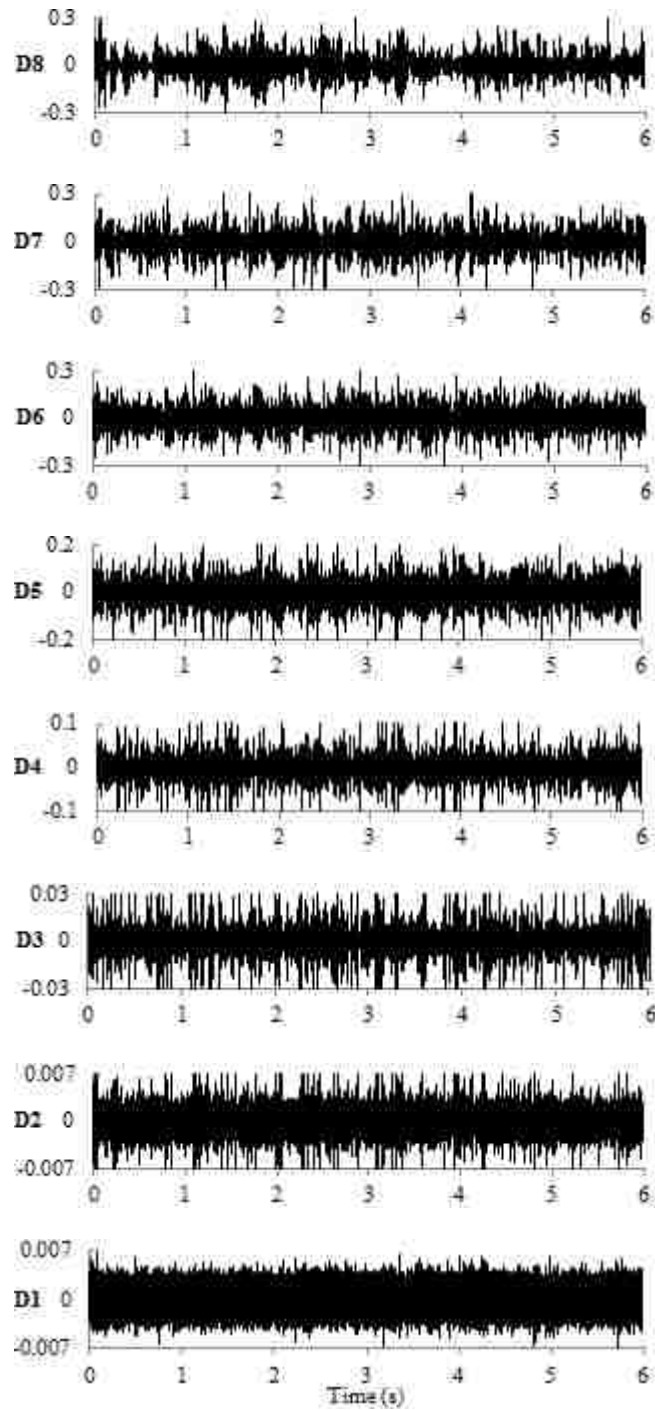


Figure E.10 Signal reconstruction

### ***E.6. Conclusions***

An experimental wind-tunnel study was performed on a flat plate, to which a vertical, finite height, perforated plate was mounted perpendicular to the airflow at the flat plate leading edge. Before the heat transfer is explored, the detail of the flow downstream of a finite height perforated plate for an

isothermal case was studied. Four points at two different levels and two downstream distances were chosen to study the effect of the edge of, and distance from, the grid. Fourier and wavelet transforms were applied to the velocity data collected at two downstream distances and two heights (four points) to analyze the turbulence. Results from both transform analyses indicated that for the points which are located at the level of the grid's height, the energy is higher than points which are behind the grid (i.e. in the flow shadow of the grid). Behind the grid ( $Y = 5.7$  cm) the turbulence energy decreased going downstream from  $X/D = 10$  to  $30$ . This shows the decay of the turbulence in this region. However, values at the height of the edge of the grid ( $Y = 10.7$  cm) did not exhibit the same trend. For frequencies less than around  $100$  Hz it was seen that the energy of the signal increased, while for higher frequencies it decreased slightly. This trend was clearest in the Fourier analysis. This suggests that at the edge of the grid, the decay of the energy while moving downstream is insignificantly for eddies with frequencies higher than  $100$  Hz (small eddies), while the energy of the larger eddies increase. These results may be used to design a perforated grid which enhances the heat loss from the surface of a PV module heated by the sun.

### ***Acknowledgements***

This work was made possible by the Ontario Trillium Foundation and the Natural Sciences and Engineering Research Council of Canada.

### ***References***

- [1] Touni, J.K. and Tripanagnostopoulos, Y., 2007, "Air-cooled PV/T solar collectors with low cost performance improvements", *Solar Energy*, 181 (4), pp. 498-511.
- [2] Kalogirou, S., 2009, "Solar Energy Engineering: Process and Systems", Burlington, MA: Elsevier Inc.
- [3] Kumar, S., Sharma, V.B., Kandpal, T.C. and Mullick, S.C., 1997, "Wind induced heat losses from outer cover of solar collectors", *Renewable Energy*, 10(4), pp. 613–616.
- [4] Francey, J.L.A. and Papaioannou, J., 1985, "Wind-related heat losses of a flat-plate collector", *Solar Energy*, 35(1), pp. 15–19.
- [5] Kumar, S. and Mullick, S.C., 2010, "Wind heat transfer coefficient in solar collectors in outdoor conditions", *Solar Energy*, 84(6), pp. 956–963.
- [6] Sharples, S. and Charlesworth, P.S., 1998, "Full scale measurement of wind induced convective heat transfer from a roof mounted flat plate solar collector", *Solar Energy*, 62(2), pp. 69–77.
- [7] Sartori, S., 2006, "Convection coefficient equations for forced air flow over flat surfaces", *Solar Energy* 80, pp. 1063–1071.
- [8] Blair, M. F., 1983, "Influence of Free-Stream Turbulence on Turbulent Boundary Layer Heat Transfer and Mean Profile Development, Part I—Experimental Data", *J. Heat Transfer*, 105(1), pp. 33-40.

- [9] Barrett, M. J., and Hollingsworth, D. K., 2001, "On the calculation of length scales for turbulent heat transfer correlation", *J. Heat Transfer*, 123(5), pp. 878-883.
- [10] Taylor, G.I., 1935, "Statistical theory of turbulence", *Proc. R. Soc. London, Series A, Math. and Phys. Sci.*, 151, pp. 421-478.
- [11] Batchelor, G.K., 1948, "Energy decay and self-preserving correlation functions in isotropic turbulence", *Quart. Appl. Math.*, 6, pp. 97-116.
- [12] Batchelor, G.K., and Townsend, A.A., 1948, "Decay of isotropic turbulence in the initial period", *Proc. R. Soc. London A.*, 193, pp. 539-558.
- [13] Batchelor, G.K., and Townsend, A.A., 1948, "Decay of isotropic turbulence in the final period", *Proc. R. Soc. London A.*, 194, pp. 527-543.
- [14] Hinze, J.O., 1975, *Turbulence*, 2nd edition, McGraw-Hill, New York, USA, ISBN 0-07-029037-7.
- [15] Murzyn, F., and Bełorgey, M., 2005, "Experimental investigation of the grid-generated turbulence features in a free surface flow", *Exper. Thermal Fluid Sci.*, 29(8), pp. 925-935.
- [16] Llor, A., 2011, "Langevin equation of big structure dynamics in turbulence: Landau's invariant in the decay of homogeneous isotropic turbulence", *Euro. J. Mechanics B/Fluids*, 30(5) pp. 480-504.
- [17] Liberzon, A., Gurka, R., Sarathi, P., and Kopp, G.A., 2012, "Estimate of turbulent dissipation in a decaying grid turbulent flow", *Exper. Thermal Fluid Sci.*, 39, pp. 71-78.
- [18] George, W.K., 2012, "Asymptotic effect of initial and upstream conditions on turbulence", *J. Fluids Engin.*, 134(6), pp. 061203-1-27.
- [19] Indrusiak, M. L. S. and Möller, S. V., 2004, *Wavelet analysis of experimental turbulence time series*, IV Escola de Primavera de Transicao e Turbulencia, PortoAlerge, Bresilera.
- [20] Farge, M., 1992, "Wavelet transforms and their applications to turbulence", *Annu. Rev. Fluid Mech.*, 24, 395-457.
- [21] Mouri, H., Kubotani, H., Fujitani, T., Niino, H., and Takaoka, M., 1999, "Wavelet analyses of velocities in laboratory isotropic turbulence", *J. Fluid Mech.*, 389, pp. 229-254.
- [22] Kellnerova, R., Kukacka, L., Jurcakova, K., Uruba, V., Janour, Z., 2011, "Comparison of wavelet analysis with velocity derivatives for detection of shear layer and vortices inside a turbulent boundary layer", *J. Phys: Confrence series*, 318.
- [23] White, F. M., 2003, *Fluid mechanics*, 5th edition, Mc Graw Hill, New York, USA, ISBN: 0-07-20217-2.
- [24] Jørgensen, F. E., 2002, *How to measure turbulence with hot-wire anemometers - a practical guide*, Dantec Dynamics.

[25] Percival, D. B., and Walden, A. T., 2000, "Wavelet Methods for Time Series Analysis", Cambridge University Press.

[26] Luo, G. Y., Osypiw, D. and Irle, M., 2003, "On-Line Vibration Analysis with Fast Continuous Wavelet Algorithm for Condition Monitoring of Bearing", J. Vibration and Control, 9(8), pp. 931-947.

[27] Abry, P., 1997, Ondelettes et turbulence. Multirésolutions, algorithmes de décomposition, invariance d'échelles, Diderot Editeur, Paris.

[28] Figliola, R.S., and Beasley, D.E., 2011, Theory and Design for Mechanical Measurements, 5th edition, John Wiley and Sons, Inc., New York, USA

## VITA AUCTORIS

NAME: Fama Fouladi

PLACE OF BIRTH: Sary, Iran

YEAR OF BIRTH: 1982

EDUCATION: Farzanegan High School, Sary, Iran, 2000

Isfahan University of Technology, B.Sc., Isfahan, Iran, 2005

Mazandaran University, M.Sc., Babol, Iran, 2009

University of Windsor, Windsor, ON, 2017